Dissertation

submitted to the

Combined Faculties of the Natural Sciences and Mathematics

of the Ruperto-Carola-University of Heidelberg, Germany

for the degree of

Doctor of Natural Sciences

Put forward by

Rainer Weinberger

born in: Augsburg

Oral examination: 17.01.2018

Supermassive black holes and their feedback effects in galaxy formation

Referees: Prof. Dr. Volker Springel

Prof. Dr. Friedrich Röpke

Zusammenfassung

Superschwere schwarze Löcher spielen eine essenzielle Rolle in der heutigen Forschung zur Galaxienentstehung. Es wird vermutet, dass diese Objekte in fast allen massereichen Galaxien zu finden sind und durch die Freisetzung enormer Energiemengen bei der Gasakkretion die Eigenschaften der Galaxie signifikant verändern. In wie weit und durch welche Interaktions-Mechanismen dies geschieht ist jedoch unklar. In dieser Doktorarbeit fasse ich den aktuellen Forschungsstand zur Galaxienentstehung zusammen, wobei ich mich auf Simulationen zur kosmologischen Strukturentstehung und grundlegende Theorien zu superschweren schwarzen Löchern, soweit sie für Galaxienentstehung von Bedeutung sind, beschränke. Anschließend beschreibe ich ein neues Modell für das Wachstum superschwerer schwarzer Löcher sowie deren Rückkopplungs-Effekte auf das umgebende Gas in kosmologischen Simulationen und zeige, wie superschwere schwarze Löcher die Entstehung und Entwicklung von Galaxien, aber auch ihr eigenes Wachstum beeinflussen. Des Weiteren stelle ich ein Modell vor, welches zur Modellierung von Jets von superschweren schwarzen Löchern in Simulationen von Galaxienhaufen dient. Mit Hilfe dieses Modells untersuche ich den Effekt von Jets auf das umgebende Gas in Galaxienhaufen.

Abstract

Supermassive black holes play a key role in modern galaxy formation research. They are conjectured to be present in almost all massive galaxies, and through the release of enormous amounts of energy triggered by gas accretion, they are able to substantially change the properties of the host galaxy. To which extent and how the interaction mechanisms work is an open question. In this thesis, I review the current state of galaxy formation research with a focus on cosmological simulations of structure formation as well as the basic theories of supermassive black holes as far as they are important for galaxy formation. Subsequently, I discuss a new model for black hole growth and feedback in cosmological simulations, along with its application in large cosmological volume simulations. I show how supermassive black holes affect the formation and evolution of their host galaxy as well as their own growth. Furthermore, I present a model for supermassive black hole jets in a galaxy cluster environment. Applying this model, I study the coupling between the jet and the surrounding intra-cluster gas.

Contents

List of abbreviations

AGN active galactic nucleus

CMB cosmic microwave background radiation

FLRW Friedmann-Lemaitre-Robertson-Walker

FR I Fanaroff-Riley type I

FR II Fanaroff-Riley type II

ICM intra-cluster medium

ISM interstellar medium

ΛCDM lambda cold dark matter

LSS large scale structure

MHD magnetohydrodynamics

SMBH supermassive black hole

UV ultraviolet

Part I

Context and theoretical background

1

Fundamentals of galaxy formation

Modern galaxy formation research is able to link the theories of cosmology, in particular large scale structure, to the formation of stars, supermassive black holes (SMBHs) and interstellar medium (ISM) physics in individual galaxies, covering an enormously large dynamical range. This also implies that a detailed understanding of galaxy formation requires at least a basic knowledge about these aspects, which I briefly outline in the following. For a more in depth discussion about cosmology, Dodelson (2003) is a good reference. The book by Mo et al. (2010) covers a large range of topics in galaxy formation including all aspects mentioned in this chapter.

1.1 Cosmological structure formation

The currently favoured theory of the evolution of the Universe is called lambda cold dark matter (ΛCDM). After a hot big bang, the very early universe is in a dense and compact state and rapidly expanding. These very early times are still poorly understood, but we know that the matter distribution in the Universe is uniform at a redshift $z \sim 1100$. This is the case even at scales that, form their physical separation and the speed of light limit of information propagation, cannot be in causal contact with each other at that time. Furthermore, we know that there are small fluctuations of the otherwise homogenous distribution of matter. A possible explanation for both these properties is given by a theoretical concept called inflation (Guth, 1981; Linde, 1982; Albrecht and Steinhardt, 1982). According to this hypothesis, the very early universe has undergone a phase of rapid expansion, which has causally disconnected elements in space-time that have been previously interacting. Invoking quantum fluctuations during this epoch, this model predicts a specific shape of the primordial density fluctuations, which are the seed inhomogeneities for the structure growth in the Universe. After this initial phase of rapid expansion, an even less understood process called reheating (Albrecht et al., 1982) provides thermal

energy to the matter content which at that point has cooled down due to the expansion during inflation.

From this point on, the universe is in a hot, still relatively dense state with tiny seed fluctuations in density. Yet, space-time continues to expand and consequently the hot, optically thick plasma cools down. Once the mean temperature of the universe reaches values comparable to the binding energy in nucleons, light elements form in a process called big-bang nucleosynthesis (Hoyle and Tayler, 1964; Wagoner et al., 1967; Peebles, 1968). In this process, protons combine to form helium with a hydrogen to helium ratio of about $3:1$, and to a tiny amount of lithium. The ratio of the primordial elements, combined with the fact that a single neutron is unstable gives a very good estimate of the timescales and conditions under which the primordial elements have formed. The book by Kolb and Turner (1994) contains a detailed discussion on this topic.

Once the binding energy is significantly higher than the surrounding temperature, nuclei are stable. However, the thermal energy is still high enough to keep the electrons unbound. This implies that the medium is optically thick to very abundant thermal photons. At a redshift of $z \sim 1100$, nuclei and electrons recombine and the matter in the Universe becomes optically thin to electromagnetic radiation. These photons from the early Universe are still observable today as the cosmic microwave background radiation (CMB) (Penzias and Wilson, 1965; Dicke et al., 1965). The radiation is uniform on the sky with only small fluctuations of the order of $\frac{\delta T}{T} \sim 10^{-5}$, which indicates density fluctuations of the same order (Planck Collaboration et al., 2016). Up to this point, the tight coupling of photons, electrons and nucleons has caused so called baryon acoustic oscillations, but otherwise kept the fluid from gravitational collapse in the over-dense regions (e.g. Dodelson, 2003, for a derivation). After the decoupling of photons and atoms, however, there is no restoring force anymore and gravitational collapse sets in. Given that we can derive the growth time of the gravitational collapse of structures and we know the magnitude of seed perturbations at redshift $z \sim 1100$, it is possible to deduce that the age of the universe is not long enough for gravitational instability to grow the structures such as galaxy clusters that we observe today. A possible way to overcome this problem is the introduction of a second matter component, consisting of a collisionless component. The most favoured realisation is the so-called cold dark matter, which is commonly believed to consist of massive elementary particles which consequently have a slow streaming velocity and interact only gravitationally with each other and the visible component. This has the consequence that dark matter structures in the Universe start growing earlier than the visible component and consequently the expected structure

formation up to the present epoch is in agreement with observations (e.g. Springel et al., 2005b)[1].

Describing the large scale evolution of a homogenous universe, as well as the behaviour of perturbations via linear theory is an understood problem, however mathematically a bit lengthy and therefore only briefly outlined here. The line of reasoning follows the textbook of Dodelson (2003), which covers the complete calculation in detail and also provides a link to CMB and large scale structure (LSS) observations.

Evolution equation of a smooth universe

The expansion of an isotropic, homogenous universe can be described by the Friedmann-Robertson-Walker metric $g_{\mu\nu}$ (in flat space-time, with implied summation over doubly occurring indices as commonly used in the field), in which the squared line element is given by

$$ds^2 = g_{\mu\nu}dx^\mu dx^\nu = -c^2dt^2 + a^2(t)\left(dr^2 + r^2\left(d\vartheta^2 + \sin^2\vartheta d\varphi^2\right)\right). \quad (1.1)$$

The Ricci tensor $R_{\mu\nu}$ and Ricci scalar R are defined as

$$\Gamma^\mu_{\alpha\beta} = \frac{g^{\mu\nu}}{2}\left[\frac{\partial g_{\alpha\nu}}{\partial x^\beta} + \frac{\partial g_{\beta\nu}}{\partial x^\alpha} - \frac{\partial g_{\alpha\beta}}{\partial x^\nu}\right], \quad (1.2)$$

$$R_{\mu\nu} = \frac{\partial\Gamma^\alpha_{\mu\nu}}{\partial x^\alpha} - \frac{\partial\Gamma^\alpha_{\mu\alpha}}{\partial x^\nu} + \Gamma^\alpha_{\beta\alpha}\Gamma^\beta_{\mu\nu} - \Gamma^\alpha_{\beta\nu}\Gamma^\beta_{\mu\alpha}, \quad (1.3)$$

$$R = g^{\mu\nu}R_{\mu\nu}. \quad (1.4)$$

General relativity links the geometry of space-time, parameterised via the Einstein-tensor $G_{\mu\nu}$, which is a combination of Ricci tensor and Ricci scalar, to the matter and energy content described by the stress-energy tensor $T_{\mu\nu}$ via the Einstein equation

$$G_{\mu\nu} = R_{\mu\nu} - \frac{1}{2}g_{\mu\nu}R = \frac{8\pi G T_{\mu\nu}}{c^4} - g_{\mu\nu}\Lambda, \quad (1.5)$$

where G is the gravitational constant and c the vacuum speed of light. Throughout this work, we use Λ as a cosmological constant. Using a stress-energy tensor for a universe filled with radiation and non-relativistic matter, the time evolution equation for the scale factor a in a homogeneously expanding universe is given by the so-called Friedmann equation (derived from the $\mu = 0$, $\nu = 0$ component of the Einstein equation)

$$H^2(a) = H_0^2\left(\Omega_r a^{-4} + \Omega_m a^{-3} + \Omega_\Lambda\right), \quad (1.6)$$

[1]This was, however, not the original motivation for the introduction of this concept (Zwicky, 1933).

where $H = \dot{a}a^{-1}$ is the Hubble rate, $H_0 = \left(\frac{8\pi G\rho_c}{3}\right)^{1/2}$ the Hubble constant and ρ_c the critical density. Ω_m is the matter (i.e. particles with non-relativistic velocities) density in the universe in units of ρ_c at $a = 1$, Ω_r the respective density of radiation (zero rest-mass component) and $\Omega_\Lambda = \frac{\Lambda c^2}{3H_0^2}$ can be interpreted as the density of a dark energy component.

Cosmological linear theory

To describe the onset of structure formation, it is necessary to include first-order perturbations in both the metric and the matter component. The evolution equation for these perturbations can then be derived from the Boltzmann equation

$$\frac{df}{dt} = \frac{\partial f}{\partial t} + \frac{\partial x^i}{\partial t}\frac{\partial f}{\partial x_i} + \frac{\partial p^i}{\partial t}\frac{\partial f}{\partial p_i} = C[f] \tag{1.7}$$

for each elementary particle species in the Universe (dark matter, photons, baryonic matter, neutrinos). Realising that $\frac{\partial p^i}{\partial t}$ is given by the laws of gravity, i.e. in general relativity linked to a (perturbative) metric via the geodesic equation, it is possible to link metric perturbations with the phase space distribution function of different components. For the non-relativistic components (i.e. dark matter and baryons), the zeroth and first moments in velocity of the Boltzmann equation link the density and velocity perturbations of the respective component with the metric perturbations. For the relativistic component (photons), the Ansatz of a perturbed Bose-Einstein distribution yields an equation that links temperature fluctuations to the metric fluctuations. Using the resulting equations as well as the perturbed Einstein equation, one can (numerically) solve the evolution of the density and velocity perturbations as well as the temperature perturbations of the photon field, provided one assumes an initial power spectrum for matter fluctuations motivated by inflation theories

$$P_\phi(k) \propto k^{n_s - 1}, \tag{1.8}$$

where $n_s \sim 1$ is one of the cosmological parameters.

Zel'dovich approximation

To first order, it is possible to parameterise the time dependent matter perturbation δ as

$$\delta(x, a) = \Delta\rho/\rho_0 = \delta_i(x)D(a), \tag{1.9}$$

where ρ_0 is the average density and $\Delta\rho$ its perturbation at a given position x. This way the time (scale factor) dependence is absorbed in the so-called growth function $D(a)$ which can be derived using linear perturbation theory, while $\delta_i(x)$ is the perturbation at some earlier time.

It is now possible to extrapolate the evolution of the matter density field by linearly extrapolating the evolution of the matter to a given epoch. This procedure was first suggested by Zel'dovich (1970) and is widely applied in cosmological simulations because it relates a power spectrum with velocity and position perturbations which are needed as initial conditions in particle-based numerical techniques to solve the problem of structure formation (see Mo et al., 2010, for a more detailed discussion). Formally, these equations are

$$v = -\frac{1}{4\pi G\rho_m a}\frac{\dot{D}}{D}\nabla\phi_i, \tag{1.10}$$

$$x = x_i - \frac{D(a)}{4\pi G\rho_m a^3}\nabla\phi_i. \tag{1.11}$$

1.2 Collapse of halos

The initial density fluctuations of the dark matter component lead to a collapse of structure in sheets and filaments, forming the so-called cosmic web. Matter in these filaments is then attracted to the intersections of the cosmic web, which form the loci for the collapse of halos (e.g. Springel et al., 2005b). In these halos, the matter virialises, which means that the dark matter reaches a balance between its kinetic motion and gravitational binding. Generally, structure formation timescales are larger for larger halos, which implies that small objects from first and merge to gradually from larger halos, i.e. structure forms hierarchically. Figure 1.1 illustrates this growth of halos over cosmic time, showing the halo mass function at different redshifts in a cosmological simulation (the IllustrisTNG simulation, which will be introduced later in this thesis). The negative logarithmic slope of each curve at fixed mass reduces over time, indicating that low-mass halos are already fairly frequent at high redshift, while the most massive halos being are only present at redshift zero.

It is therefore also important to keep in mind that matter accretion into a virialised halo is not necessarily smooth, but happens preferentially in discrete mergers of smaller halos, which has important consequences for galaxy formation (Hernquist, 1989; Barnes and Hernquist, 1996; Mihos and

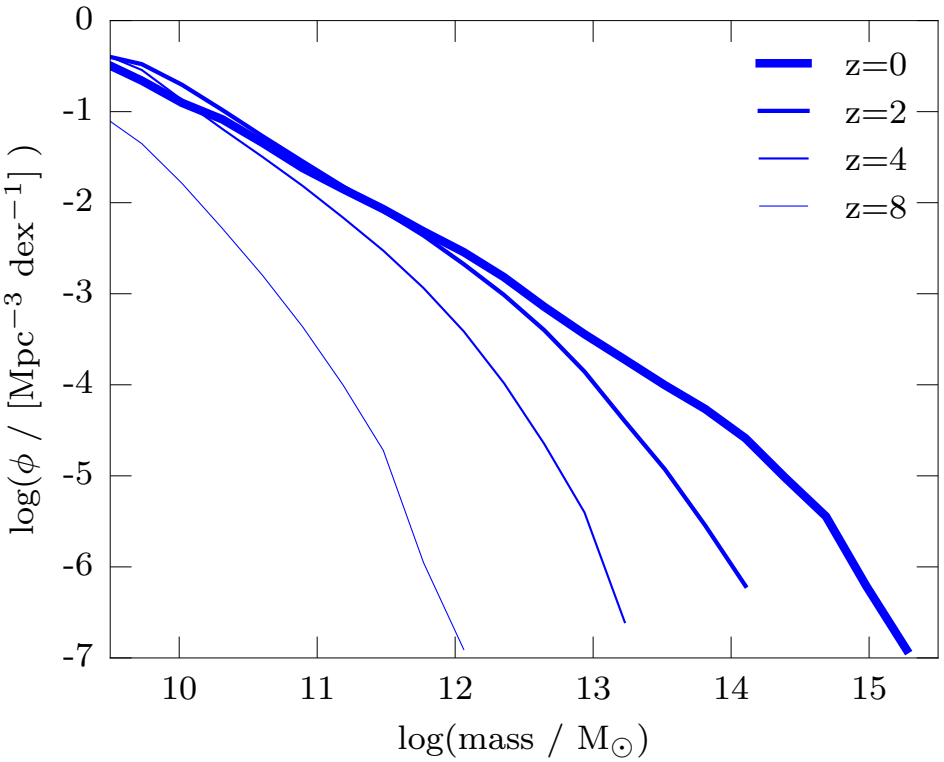

Figure 1.1: Comoving number density of halos binned in mass vs their mass in a cosmological simulation at different redshift. While the number density of low-mass halos already at place at $z \sim 4$, higher mass halos form at later times.

Hernquist, 1996), which will be discussed in more detail when talking about the co-evolution of galaxies and SMBHs.

1.3 Gas in halos

Being the dominant matter component, dark matter drives the gravitational collapse of the initially very homogenous density field. The gas initially follows the dark matter component, but at some point its pressure forces as well as radiative cooling become important and the dynamics differs. In particular, while dark matter virialises, but generally does not dissipate energy, gas will fall into the halos and heat up. This heat, however, can be lost due to radiative processes, which reduces the energy budget of the gas component and therefore its pressure support, causing further gravitational

collapse. This leads to the fact that every (isolated) galaxy lives in a more extended dark matter halo (White and Rees, 1978).

The important aspect for the further dynamics is whether the collapsing gas can get rid of its pressure support via radiative cooling quickly enough to allow a radiative collapse or not. If radiative cooling times are shorter than the free-fall time, the gas will directly collapse, fragment and form stars. If this is not the case, the gas will simply heat up and form a hot, hydrostatic atmosphere. Which of the two scenarios is realised depends on the mass of the collapsing object (Silk, 1977). While low-mass systems ($< 5 \times 10^{11}$ $M_\odot$) can collapse directly, higher mass systems build up a hydrostatic halo, which successively cools (Rees and Ostriker, 1977).

1.3.1 Star formation in galaxies

The collapse of gas in halos is a runaway process which ultimately leads to the formation of stars. The precise mechanism of gravitational collapse depends on the timescales at which the gas is able to cool down, which is likely significantly different for the first generation of stars, so-called population III stars. Therefore, these stars are likely more massive than the present day stellar population.

Massive stars are very short lived, as they burn their hydrogen supply quickly and evolve rapidly, ending their lives as core-collapse supernovae. In the late stages of stellar evolution and in particular in supernovae, these stars loose a significant fraction of their gas to the surroundings. As the gas in stars gets chemically enriched as a product of nuclear fusion, the gas that gets ejected enriches the surrounding ISM, which has important consequences for the further evolution of the ISM: the main effect is that the radiative losses, i.e. the cooling channels of the gas change and gas can also cool via so-called metal-line emission (Wiersma et al., 2009). This has important consequences, both, for star-formation itself, as well as for the further evolution of galaxies. Due to the presence of additional cooling channels, very massive population III stars can no longer form, as the gas would rather fragment and collapse into multiple smaller population II stars than forming one giant star. From this moment on, star formation occurs exclusively via the present-day star formation channel with a seemingly universal initial mass function (Salpeter, 1955).

1.3.2 Global efficiency of star formation

From this early times, after the first stars reionized the gas in the Universe, stars can form via the cooling of galactic gas and the collapse under the

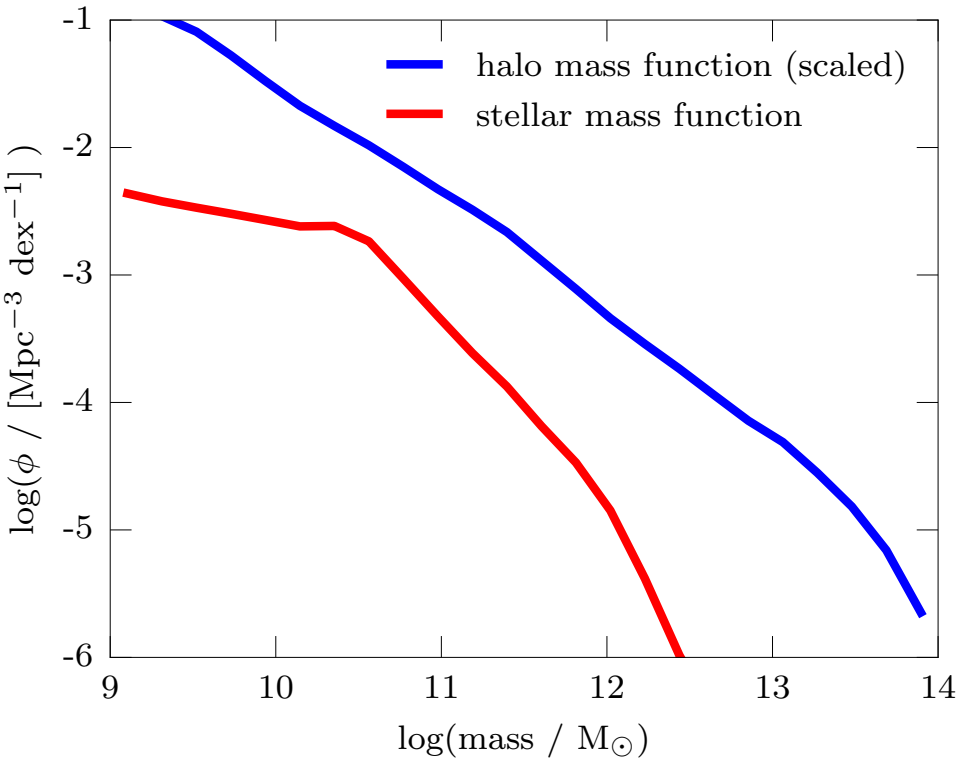

Figure 1.2: Comoving number density of halos binned by their central galaxy's stellar mass (red) and halo mass scaled by the cosmic baryon fraction (blue) at redshift $z = 0$ in a cosmological simulation. If all the gas that is initially in a halo would convert into stars, the red and blue line would overlap. The stellar mass function diverges from the scaled halo mass function both at the low- and high mass end, indicating that star formation is inefficient in both regimes, and most efficient in galaxies of around $10^{10.5}$ $M_\odot$.

influence of its own gravity. However, star formation in galaxies does not occur on the cooling time that one would expect, but is overall much slower. This has to do with the fact that the stellar populations in the galaxies have an important impact on the energetics of the ISM. The main contributions are violent core-collapse supernova explosions setting free a considerable amount of energy, driving shocks into the ISM and thereby heating the surrounding gas. Other channels of this stellar feedback are stellar winds of asymptotic giant branch stars and ionising photons emitted from massive stars.

Because of stellar feedback, the average baryon conversion efficiency in galaxies of a given halo mass does not exceed 30% (Moster et al., 2013; Behroozi et al., 2013b). On top of this, the stellar mass fraction peaks at about the mass scale of Milky-Way halos and drops towards both ends significantly, which means that star formation, or more precisely turning gas into stars on galactic scales, is an inefficient process. This process seems to have a sweet-spot of maximum efficiency at Milky-Way mass halos, and star formation in both more and less massive halos is suppressed by some mechanism. Figure 1.2 illustrates this, showing the comoving number density of halos with a given halo mass, scaled by the baryon over total matter fraction, in blue and the stellar mass function in red. If the halos would be capable of turing all gas in the halos into stars, the two lines would overlap. It is obvious that this is not the case at any mass scale, however, the stellar mass function approaches the scaled halo mass function at stellar masses of around $10^{10.5}$ $M_\odot$, which is roughly the mass of the Milky Way. For both lower and higher mass halos, the two mass functions diverge.

The explanation for low-mass halos lies in the shallower gravitational potentials these galaxies live in. This means that it is easier for one (or multiple) supernova explosions to drive gas out of the halo, leaving behind only relatively hot, dilute gas which does not cool efficiently. Thus, an equilibrium between cooling, star formation and stellar feedback is established at much lower star formation rates than in more massive galaxies.

The stellar feedback scenario qualitatively explains why the overall star-formation efficiency is quite low and why it further drops towards lower mass galaxies. However, stellar feedback would imply that the stellar mass over halo mass fraction in halos more massive than the Milky-Way increases further or at most declines weakly due to longer cooling times in larger halos. However, there is compelling evidence that the efficiency instead decreases drastically, indicating the presence of another mechanism to provide energy. By now it is largely accepted that this additional source of energy are accreting SMBHs in the centres of galaxies which is the main topic of this thesis.

2

Properties of supermassive black holes

The presence of SMBHs is one of the mysteries of structure formation in the universe, but by now there is convincing evidence for their existence. The most stringent test that SMBHs are actual space-time singularities is the measurement of stellar orbits in the Milky-Way's galactic centre close to its SMBH Sagittarius A*. The orbits of the surrounding stars probe the gravitational potential around the centre to radii of about 125 AU, indicating that a mass of around 4×10^6 $M_\odot$ is enclosed in a sphere with at most this radius (e.g. Genzel et al., 2010, for a review).

At high redshift, so-called quasars were first discovered and identified as extragalactic in the 1960s (Schmidt, 1963, 1968). Comparing their observed spectra to a model of a geometrically thin, optically thick accretion disk, Shakura and Sunyaev (1973) showed that these objects are consistent with being rapidly accreting SMBHs. The infalling gas radiates a significant fraction of the accreted rest mass equivalent energy before crossing the event horizon, in some cases outshining their host galaxy. Recent observations show that these quasars are already present at redshift > 6.5 and have masses well above 10^9 $M_\odot$ (Bañados et al., 2016; Mazzucchelli et al., 2017), which raises the question how these SMBHs could grow to these masses in the comparably short time of less than a billion years. To understand why this is a problem it is useful to discuss the formation of SMBHs and their growth via gas accretion first.

2.1 Supermassive black hole formation

It is still unclear how SMBHs form. As massive SMBHs are already observed at redshift > 6.5 (Mazzucchelli et al., 2017), their formation has to happen significantly before this time. Dating back to Rees (1978), there are 3 possible scenarios how SMBHs might form: via direct collapse of a gas cloud, as a remnant of a massive (population III) star, or via formation of a dense star cluster and runaway collisions. In principle, each of these scenarios is

testable, however, due to the limitations of high-redshift observations, none can be ruled out yet. The review by Volonteri (2010) provides a detailed explanation about these scenarios, which I only briefly summarise here.

One theoretical scenario to form supermassive black holes is via direct collapse of gas in a proto-halo with virial temperature of $T \sim 10^4$ K. However, this only works if the ordinary ways of gravitational collapse and star formation are inhibited. This implies that the environment has to be very metal-poor in order to ensure that the cooling of the gas is not too efficient, which means that this process can only happen at very high redshift. In the absence of metal-line cooling, the gas will loose its pressure support comparably slowly, which inhibits fragmentation. In fact, additionally to the absence of metal-line cooling, also cooling via molecular hydrogen has to be suppressed. This can be achieved by the presence of a strong ultraviolet (UV) source nearby which inhibits the formation of hydrogen molecules. If all these criteria are fulfilled, a gas cloud of 10^6 $M_\odot$ can collapse to a single object. One additional challenge in this collapse is to remove the residual angular momentum of the collapsing gas, possibly transported outward via bar instabilities which are forming in the center. Eventually, a supermassive star will form, which will turn into a supermassive black hole of a mass of $M_{\rm BH} \sim 10^5$ $M_\odot$ on a short timescale.

As an alternative, SMBHs might be formed from the first generation of (massive), so-called population III stars. These form when primordial gas which is free of metals gathers in dark matter mini-halos of masses of around 10^6 $M_\odot$, forms molecular hydrogen and cools via emission of radiation from these molecules (Tegmark et al., 1997). Simulations of gas collapse (e.g. Yoshida et al., 2006) show that these collapsing clouds might result in very massive stars of around 100 $M_\odot$ at a redshift of around $z \sim 20$. Depending on the mass loss during its evolution, these massive stars might end up as a black hole with masses of the same order. In principle, this channel seems very elegant, especially because it is a byproduct of theories of early star formation which was not developed to explain SMBH formation. However, it is also important to note that this channel of star formation is still a purely theoretical construct and solid observational evidence supporting a first generation of very massive stars is still missing.

As a third scenario, it is also possible that the (nuclear) star clusters that formed in the early phases of star formation are very compact. If this is the case, collisional effects and three-body interactions become important in these systems, which evaporate some stars from the system. This ejection of stars from the cluster leads to a loss of energy and consequently to a contraction of the remaining stars, which further enhances the frequency of three-body interactions. In the cores of these star clusters, where pre-

dominantly massive stars are present, this might lead to a runaway effect and eventually to stellar collisions and very massive stars which, towards the end of their lifetime, will end up as a black hole with $M \sim 10^2 - 10^4$ $M_\odot$.

In principle these three scenarios produce SMBH seeds with different masses. Thus, it should be possible to observationally constrain the scenarios. However, with current observations it is not possible to detect anything else but very high mass SMBHs at high redshift, which can only indirectly constrain seeding scenarios. Future gravitational wave detectors might be of great help in this respect, as they are sensitive to lower mass SMBHs out to high redshift (Amaro-Seoane et al., 2012)

2.2 Growth of supermassive black holes

The early universe has a high mean density and gas falling into the halos can quickly cool and turn into stars. Part of the gas is able to fuel the central SMBHs, which grow quickly at this epoch and are observable as so-called high-redshift quasars (Fan et al., 2001).

From a theoretical point of view, one can put an upper limit on the accretion rate of supermassive black holes known as the Eddington-limit. This theoretical limit assumes spherically symmetric, non-rotating accretion. The resulting maximum luminosity is

$$L_{\mathrm{E}dd} = \frac{4\,\pi\,G\,M\,m_p\,c}{\sigma_T}, \tag{2.1}$$

where G is the gravitational constant, M the mass of the black hole, m_p the proton mass and σ_T the cross-section of the emitted light with the accreted gas (usually assumed to be the Thomson scattering cross-section). This luminosity can be converted into an accretion rate assuming a conversion to radiation with a radiative efficiency $\epsilon_r = L\dot{M}^{-1}c^{-2}$. This results in the so-called Eddington accretion rate

$$\dot{M}_{\mathrm{E}dd} = \frac{4\,\pi\,G\,M\,m_p}{\epsilon_r\,c\,\sigma_T}, \tag{2.2}$$

which is inversely proportional to the radiative efficiency. The radiative efficiency can be approximated by assuming all the gravitational energy of the infalling gas up to the innermost stable orbit is radiated. This innermost stable circular orbit depends on the spin of the black hole, implying that ϵ_r can be as high as 0.4 for maximally spinning black holes (Novikov and Thorne, 1973; Fanidakis et al., 2011). This significantly increases the growth time of the supermassive black hole and would make it impossible to

reach the needed growth rates. A smooth, continuos feeding via an aligned accretion disc will inevitably spin up the black hole to its maximum spin. This, however, does not happen if the supermassive black hole is fed by a series of clouds that are infalling at random orientations (King et al., 2008). In this case, the spin of the SMBH would be low and therefore the SMBH could grow fast enough.

Another way to resolve the problem is to note that this Eddington limit is an oversimplified picture. In particular, it assumes spherically symmetric accretion without angular momentum, an assumption which will break down at some scale in any real black hole. Ultimately, there will be a disk forming which redistributes the angular momentum and thereby feeds the black hole. However, in this configuration, the assumption of radiation stopping the accretion flow is no longer true, as radiation can escape perpendicular to the disc. Therefore, one might argue that black holes are actually able to exceed the Eddington accretion rate and thereby grow faster, provided there is sufficient gas supply. For recent work on this topic, see Pezzulli et al. (2017), and references therein.

2.3 Black hole demographics

2.3.1 X-ray background and black hole density

Another observational signature of the growth of SMBHs is the so-called cosmic X-ray background. Its spectrum peaks at around 30 keV, which, to a large extent consists of the cumulative emission of active galactic nuclei (AGNs), together with a small contribution from X-ray clusters and starburst galaxies (Gilli et al., 2007). Using this measurement of the radiation density from AGNs, it is possible to deduce a density of SMBHs, assuming a specific radiative efficiency and using the fact that SMBHs can only grow in time. This argument has first been applied by Soltan (1982) and provides an observational limit to the black hole density in the Universe of $\rho_{BH} \sim 4 \times 10^5$ $M_\odot$ Mpc^{-3} (Marconi et al., 2004).

2.3.2 Luminosity function

The demographics of AGNs is most easily described by the luminosity function. This can be inferred from multiple wavelengths, ranging from mid-infrared to hard X-ray, each technique with their own strengths and weaknesses. While the exact shape, in particular of the low-luminosity end of the AGNs luminosity function is still unclear, mainly due to the uncertain

fraction of obscured and Compton-thick AGNs (Buchner et al., 2015), the general evolutionary trend is well-established and highly informative (Hopkins et al., 2007). The luminosity function is commonly described as a double power-law and increases with time until redshift $z \sim 2$. After this redshift AGN become less luminous, which implies a decreasing number density of AGNs at fixed luminosity towards $z = 0$.

Physically, this so-called downsizing trend can be explained by an anti-hierarchical growth of supermassive black holes. While the most massive black holes formed at early times and are by now no longer strongly accreting, the less massive black holes continue to accrete at reasonably high Eddington ratios (see Hirschmann et al., 2014, and references therein). This is different from the hierarchical growth of structure in the Universe, in which small objects from first and more massive objects later.

2.4 Accretion disks around black holes

The growth of SMBHs happens largely via accretion, which leads to the release of considerable amounts of energy. This energy is radiated and gives rise to observable AGNs. How in detail, gas is funnelled into the SMBH is still not completely clear. The main problem is how gas with a given (generally nonzero) amount of angular momentum can get close enough to cross the event horizon of a SMBH. For this to be possible, angular momentum transport in the gas has to be efficient. One of the early successes of SMBH research was based on the realisation that the observed quasars (Schmidt, 1968) are of extragalactic origin and have spectra one would expect from a geometrically thin accretion disc around a massive compact object (Shakura and Sunyaev, 1973). This theory of thin accretion disks still is one of the key theories of SMBH accretion discs today, though it has been realised that this is not the only configuration in which SMBHs can accrete gas. A more in-depth discussion of SMBH accretion discs can be found in Netzer (2013, chapter 4 and references therein). Here, I only briefly mention the main aspects.

2.4.1 Optically thick accretion disks

Luminous SMBH with luminosities from 10^{-2} to 0.3 times the Eddington luminosity are generally believed to have accretion discs that are geometrically thin and optically thick to their emitted radiation. These discs can be treated as a thin disc of gas in vertical pressure equilibrium with radial velocities which are much smaller than their circular component. A

so-called α parameter quantifying a disc viscosity of not further specified origin is commonly used for these disks (Shakura and Sunyaev, 1973). Further assuming that the luminosity of a parcel of gas is equal to its loss of gravitational potential energy while falling in and assuming a black-body radiation, it is possible to calculate a temperature profile of the accretion disk, as well as a spectrum of the overall accretion disk by integrating up individual blackbody spectra of all gas parcels, which yields spectra that are in remarkable agreement with the continuum emission of observed quasars.

For SMBHs accreting at higher rates than 0.3 times the Eddington limit, the mass inflow becomes faster than the radiation diffusion. In this way, a geometrically thick, optically thick accretion disk forms in which photons can be trapped and transported into the black hole. The radiative efficiency of such accretion discs can be much lower than for the geometrically thin discs.

2.4.2 Optically thin accretion disks

In the other extreme, with very low accretion rates relative to the Eddington limit, accretion discs can have cooling times lower than the inflow time, in which case infalling gas parcels retain their dissipated gravitational energy far longer, thus becoming hotter, up to the virial temperature. In this case, it is possible that hot gas parcels can be advected into the SMBH without emitting substantial amounts of radiation, also resulting in low radiative efficiencies. Such accretion flows are generally referred to as advection dominated accretion flows or radiatively inefficient accretion flows. A detailed review on this topic is given in Yuan and Narayan (2014).

2.5 Jets from supermassive black holes

About 10% of the AGN population have significant amounts of radio-emission. These so-called radio-loud AGN generally show a radio-jet or a radio-core. A brief review of the observational perspective of AGN jets can be found in Netzer (2013, section 7.9), while Boettcher et al. (2012) provides a detailed discussion about AGN driven jets. Here, I only briefly mention some of the main aspects which are important to keep in mind for for the work presented in this thesis.

2.5.1 Fanaroff-Riley Classification

According to the location of the peak of the radio emission, one can distinguish two different types of radio-loud AGN (Fanaroff and Riley, 1974): Fanaroff-Riley type I (FR I) objects show a centrally peaked radio emission and in most cases two counter-aligned jets originating from the SMBH, while Fanaroff-Riley type II (FR II) objects are in general more luminous, have the peak of the radio-emission off centre and usually show one jet more prominent due do relativistic beaming effects.

2.5.2 Jet launching theory

Jets are common phenomena in astrophysics. They occur on all kind of scales, from protostellar jets to jets from AGNs, and most of them have a related accretion disk, which indicates that it might be connected to its formation.

Indeed, scenarios of jet formation commonly require a rotating disk and magnetic fields. The exact mechanism how jets can be launched is still an active field of research, but there are analytic models which link the presence of a rotating disk threaded by a magnetic field and its winding to the launching of an accretion disk driven wind, such as the work by Blandford and Payne (1982).

For rapidly spinning black holes, there is in principle another source of energy originating from the fact that particles within the black holes ergosphere can have a negative redshifted energy, i.e. the sum of all energies and the particle rest mass energy. These particles can even exist outside the event horizon, which means that there is energy that can be extracted from the black hole. This process can power AGN jets very efficiently (Blandford and Znajek, 1977).

2.5.3 Simulations of AGN jets

Going beyond the idealised setups for which analytic solutions exist, numerical calculations solving the equations of general relativistic magnetohydrodynamics are employed (e.g. Tchekhovskoy and Bromberg, 2016), usually using a fixed space-time metric. In recent years, it has become possible to perform calculations in 3 dimensions, though 2 dimensional calculations are still widely employed and define the state-of-the-art in this field. One question these simulations address is in which state an accretion disk has to be in order to allow the formation of a jet, and ultimately, how energetic the jet will be. If this connection could be made, the observationally more

easily accessible jet could give important insights into accretion disk theory. Other questions of interest are the origin of the FR I/FR II dichotomy, the stability of jets in general and their composition.

3

The black hole – galaxy connection

One of the key questions of galaxy formation is which role SMBHs play in the evolution of their host galaxy or galaxy cluster. From a theoretical perspective, the accreted rest-mass energy,

$$E = M_{\rm BH}c^2 \sim 10^{63}{\rm erg\ s^{-1}}\ \frac{M_{\rm BH}}{10^9\,{\rm M_\odot}}, \tag{3.1}$$

is of the same order as the gravitational binding energy of the central gas in a galaxy cluster (assuming a 10^9 $M_\odot$ SMBH). If just a small fraction of the accreted rest mass energy is radiated away and deposited in the surrounding gas, the gas properties will be affected significantly, thereby altering the star formation rate in the host galaxy (King, 2003). However, while the radiative efficiency is known within an order of magnitude ($\epsilon_r \sim [0.02 - 0.4]$, depending on SMBH spin, see Fanidakis et al. 2011), the coupling efficiency of the radiated energy to the surroundings is completely unknown and theoretically very challenging to determine reliably. Therefore, it is so far not possible to determine theoretically and from first principles if feedback from AGN is important in galaxies or not.

3.1 Observational challenges

Observationally, connecting SMBH activity with host galaxy properties is a challenging question, in particular because of the different timescales at which SMBHs and galaxies evolve. The very short duty cycles of quasars (Schawinski et al., 2015; King and Nixon, 2015) induce a large scatter in any possible correlation between a galactic quantity and an instantaneous measure of AGN activity. However, it is possible to observe a sufficiently large sample and study observational correlations of integrated properties, which should, in principle, resolve this problem by averaging either over an ensemble or over time.

For galaxy clusters, it is possible to directly study the hot intra-cluster medium (ICM) via X-ray observations and thereby probe the effects of AGNs more directly (e.g. Hitomi Collaboration, 2016, for a recent study of the Perseus cluster).

3.2 Black hole - galaxy scaling relations

One of the at first surprising findings about supermassive black holes is the correlation of their mass with properties of their host galaxy, such as the host's stellar bulge mass (Magorrian et al., 1998) or velocity dispersion (Tremaine et al., 2002). Observationally, this can be measured from local galaxies (Kormendy and Ho, 2013; Reines and Volonteri, 2015, and references therein). The obvious question that arises is how the black hole "knows" about its host galaxy or vice versa. We do not expect this to happen via gravitational interaction, as the gravitational sphere of influence of a SMBH is orders of magnitude smaller than galactic scales, and the mass is around 10^{-3} times the total host galaxy mass. This means that the gravitational forces of a black hole have no substantial effect on the dynamics of gas and stars in the host galaxy.

But the AGN might be able to impact the gas properties of the host galaxy which means that it might be able to limit, or regulate, both its own growth and the growth of the stellar bulge (King, 2003). This theoretical possibility is frequently invoked as the explanation for the black hole mass-bulge mass relation. However, it is important to keep in mind that a correlation does not necessarily imply a causation and a number of authors (e.g. Peng, 2007; Hirschmann et al., 2010; Jahnke and Macciò, 2011, and references therein) argued that hierarchical structure formation naturally produces a correlation simply because of a common formation history without the need of any causal black hole-bulge connection. The interpretation of this correlation thus still remains a topic of debate, and possibly both effects might be important (Graham and Scott, 2013).

3.3 Galaxy mergers and black hole activity

The tidal interactions during the merger of two galaxies strongly affect the gas in the galaxies, triggering instabilities and subsequent collapse and star formation, as well as possible black hole activity (Hernquist, 1989). Simulations of merging galaxies that include models for star formation and supermassive black hole accretion and feedback find a characteristic star

formation rate history for the galaxies and correlate the post-merger drop in star formation rate with an increased black hole accretion rate (Springel et al., 2005a; Di Matteo et al., 2005). Using such merger simulations combined with empirical halo occupation models to connect the theoretical idea with observations of galaxies with different morphologies, star formation rates and AGN luminosities shows that the quasar luminosity density and luminosity function and their evolution with redshift can be explained by merger-driven fuelling of the central SMBH (Hopkins et al., 2008a,b). However, recent cosmological hydrodynamical simulations yield conflicting results whether gas rich galaxy mergers and subsequent AGN activity is actually able to quench a galaxy (Sparre and Springel, 2016, 2017; Pontzen et al., 2017).

3.4 Signatures in galaxy clusters

Galaxy clusters are the most massive collapsed objects in the universe. Because of their large mass, the gas falling into galaxy clusters gets shock-heated to temperatures of $T \geq 10^7$ K. The gas, which mainly cools via bremsstrahlung, emits X-ray photons, which are detectable by space based X-ray observatories, allowing the diffuse ICM to be probed directly. In particular, one can determine the bolometric luminosity of a galaxy cluster, as well as its density profile and derive a cooling rate of the ICM. The corresponding mass drop-out rate can be several hundred up to 1000 $M_\odot$/yr, which means that gas should cool down and, in principle eventually form stars. Surprisingly though, the present star formation rate in local clusters is at most a few tens to 100 $M_\odot$/yr. From the mass and colours of central cluster galaxies it is also clear that this was not significantly higher at earlier epochs. This apparent mystery is called the cooling flow problem (e.g. Fabian, 1994), and can only be explained by a source of heating in the centres of galaxy clusters. Several possible mechanism have been suggested to provide this heat.

One candidate would be for example transport of heat from the cluster outskirts to the centre. The cumulative heat in the cluster gas would be sufficient to "hide" the cooling losses in the centre and thereby resolve the mystery. Such an explanation requires the efficient transport of heat, which is possible in two ways: first, via thermal conduction, i.e. the transport of heat mediated via electrons. This becomes feasible at high mass clusters because of the efficient thermal conduction in high temperature plasmas (Zakamska and Narayan, 2003; Voit et al., 2015). However, the temperature dependence of the conduction coefficient also poses a problem for this

explanation. In particular, thermal conduction would cause an unstable equilibrium solution between heating and cooling, and once cooling is dominating, the heating is reduced because of a reduced temperature, while cooling becomes more efficient, leading to a runaway effect. Second, one could also imagine that the heat is transported via advection processes, i.e. the ICM is mixed continuously. This mechanism requires a process causing large-scale flows, and the gas would have to cross the cooling radius (~ 100 kpc) in less than the cooling time (~ 300 Myr), which implies a flow velocity of several hundred km/s. Recent measurements of the gas velocities in the Perseus cluster, the X-ray brightest cluster on the sky, indicate velocities of around 70 km/s (Hitomi Collaboration, 2016), which disfavour this mechanism as the sole explanation. Yet, both, thermal conduction (Yang and Reynolds, 2016b; Kannan et al., 2017) and systematic gas motions (Yang and Reynolds, 2016a) might contribute to the energetic balance.

The currently favoured mechanism to explain the heating of the central ICM are jets from SMBHs (see McNamara and Nulsen, 2007; Fabian, 2012). This is supported observationally by the fact that most galaxy clusters with short central cooling times show signatures of underdense cavities, showing up as dark regions in X-ray maps (Boehringer et al., 1993) or radio-emission, a signature of magnetised AGN jets. Furthermore, the energy injection rate measured from these cavities correlates with the cooling losses of the corresponding cluster (Dunn and Fabian, 2006; Fabian, 2012).

Yet, one of the most important parts to provide an explanation for the balance of cooling losses by AGN jets remains unclear: the mechanism to distribute the energy from the collimated jet isotropically in the galaxy cluster. There are a number of suggested mechanisms, including the heating of the surrounding material by sound waves and weak shocks (Li et al., 2016; Fabian et al., 2017), the mixing of lobe material with the surrounding gas (Hillel and Soker, 2016), heating by cosmic-ray protons (Jacob and Pfrommer, 2017a,b; Ruszkowski et al., 2017), the dissipation of turbulence (Zhuravleva et al., 2014) or mixing by turbulence (Kim and Narayan, 2003). Recent X-ray measurements of the core region of the Perseus Cluster by the Hitomi satellite indicate that turbulence, assuming it is produced locally at the cavity surface at an energy rate of the cooling rate, cannot be distributed isotropically across the cluster, as this would require an energy density in turbulent motions that is higher than the observed one (Hitomi Collaboration, 2016; Fabian et al., 2017), and theoretically, the turbulent dissipation picture has been challenged by numerical simulations that indicate that turbulence cannot be distributed in a volume-filling fashion throughout the cooling radius (Reynolds et al., 2015). Testing some of these scenarios in simulations of jets interacting with an idealised ICM is part of this thesis.

4

Simulations of galaxy formation

Cosmological simulations of structure formation play an essential role in modern galaxy formation research. Our comparatively detailed knowledge about the early universe through observations of the CMB and the corresponding theoretical description via linear theory of a homogeneously expanding spacetime allow a statistical prescription of the universe at redshifts of around 1100 to remarkable accuracy. Due to several generations of ever more accurate measurements of the CMB, mainly through space-based all-sky surveys (Smoot et al., 1992; Spergel et al., 2003; Planck Collaboration, 2011), the statistical errors of the free parameters of the ΛCDM model are now at a percent level (Planck Collaboration et al., 2016).

This accuracy is sufficient to use cosmological perturbation theory assuming these parameters as initial conditions in numerical simulations of the non-linear collapse of structure. Commonly, a particle based approach is used to discretise the matter field, implying that the simulation starts out with a homogenous distribution of particles, to which small perturbations are applied. The initial perturbations are then calculated using linear (possibly also higher order, but not in this work) perturbation theory and the Zel'dovich approximation is used to link the initial power spectrum to displacements in position and velocity in the initial conditions (see e.g. Springel et al., 2005b).

Having set up the initial conditions of the matter, the dark matter component can be separated from the gas component, according to the cosmic matter and cosmic baryon fraction in the corresponding cosmology. Both components start out with the same power spectrum at a redshift of $z = 127$ in the simulations presented here. Note that strictly speaking, the gas and dark matter components have a slightly different evolution until redshift $z = 127$, which means that their power spectrum is slightly different. We neglect this effect in the simulations presented here, as this effect is of no importance for the relatively massive halos which this work focuses on.

In the following, the gas component is evolved under the laws of mag-

netohydrodynamics and gravity, while the dark matter only interacts via gravitational forces, which can be approximated by a Newtonian interaction on an expanding background spacetime.

4.1 Gravitational forces

The dynamics of collisionless particles can be described by the Vlasov-equation

$$\frac{df}{dt} = \frac{\partial f}{\partial t} + v_i \frac{\partial f}{\partial x_i} - \frac{d\phi}{dx_j}\frac{\partial f}{\partial v_j} = 0, \tag{4.1}$$

where $f = f(x, v, t)$ is the phase-space distribution function. The density is given by

$$\rho = m \int f \, dv, \tag{4.2}$$

where m is the mass of an individual particle. Together with the Poisson equation (assuming $\bar{\rho}$ is the mean density of the universe)

$$\nabla^2 \phi(x) = 4\pi G \left(\rho - \bar{\rho}\right), \tag{4.3}$$

this forms the so-called Vlasov-Poisson system which needs to be solved to compute the gravitational forces of collisionless particles in a cosmological simulation. This is commonly achieved by coarse-graining the equations by introducing a large number of simulation particles which sample f. The Poisson equation can then be solved by summing up individual forces for each simulation particle or by computing approximations thereof, as for example by force-tree (Barnes and Hut, 1986) or fast-multipole methods (Dehnen, 2000, 2002). Alternatively it is possible to use iterative (Guillet and Teyssier, 2011) or Fourier based techniques to solve the Poisson equation on a grid.

4.2 Ideal magnetohydrodynamics

The (magnetised) gaseous component of the Universe can be modelled using the laws of ideal magnetohydrodynamics (MHD). The associated equations are (e.g. Pakmor and Springel, 2013)

$$\frac{\partial \rho}{\partial t} + \nabla \cdot (\rho \mathbf{v}) = 0 \tag{4.4}$$

$$\frac{\partial \rho \mathbf{v}}{\partial t} + \nabla \cdot \left(\rho \mathbf{v}\mathbf{v}^T + p_{\rm tot} - BB^T \right) = 0 \tag{4.5}$$

$$\frac{\partial E}{\partial t} + \nabla \cdot \left[\mathbf{v} \left(E_c + p_{\rm tot} \right) - \mathbf{B} \left(\mathbf{v} \cdot \mathbf{B} \right) \right] = 0 \tag{4.6}$$

$$\frac{\partial \mathbf{B}}{\partial t} + \nabla \cdot \left(\mathbf{B}\mathbf{v}^T - \mathbf{v}\mathbf{B}^T \right) = 0, \tag{4.7}$$

where $\mathbf{v}$ is the velocity of the fluid element, $p = p_{th} + 0.5\mathbf{B}^2$ the total pressure and $E = \rho u_{\rm th} + 0.5\rho\mathbf{v}^2 + 0.5\mathbf{B}^2$ the total energy density, while $u_{\rm th}$ is the thermal energy per unit mass. This systems of equations can be solved on a grid using a finite-volume approach, computing fluxes through the cell-interfaces with a Riemann-solver (see Toro, 1997, for more details).

In MHD, there is an additional constraint that $\mathbf{B}$ is a divergence-free vector-field

$$\nabla \cdot \mathbf{B} = 0, \tag{4.8}$$

which is, mathematically speaking, automatically fulfilled at all times assuming the initial conditions fulfil it. When solving these equations numerically, however, this is not automatically the case due to numerical errors. This problem can be addressed either via dedicated divergence cleaning schemes (Powell et al., 1999; Dedner et al., 2002) or via a staggered-grid discretisation in a so-called constraint transport algorithm (Evans and Hawley, 1988).

4.3 Radiative cooling

One of the key processes in galaxy formation is the ability of gas to radiate energy and cool down. However, most simulations to date do not follow radiation explicitly, but merely model its most important effects, such as the local cooling, or the heating by a spatially uniform UV background. To model this, a cooling loss term $\Lambda(\rho, u, \{X\})$ has to be applied to the energy equation (eq. 4.6). In general, this function depends on the exact physical process that is responsible for the radiation and can depend on density, temperature, chemical composition and external radiation fields of the gas. The cooling function in general can vary over many orders of magnitude and therefore, in extreme cases, the cooling time can be very short and

require a correspondingly short timestepping if computed via an explicit discretisation in time. To avoid this, cooling losses are often calculated via implicit time integration, solving the adiabatic changes at any given timestep $\dot{u}_{\mathrm{ad}}$ first and subsequently solving the implicit equation (Springel et al., 2001b)

$$\hat{u}_i^{n+1} = u_i^n + \dot{u}_{\mathrm{ad}}\Delta t - \frac{\Lambda\left(\rho_i^n, \hat{u}_i^{n+1}, \left\{X_i^n\right\}\right)\Delta t}{\rho_i^n} \tag{4.9}$$

which calculates the rate of change of the specific internal energy as

$$\dot{u}_i = \left[\hat{u}_i^{n+1} - u_i^n\right]/\Delta t, \tag{4.10}$$

Often this is additionally limited such that a cell is at most allowed to loose half of its internal energy in a single timestep.

4.3.1 The cooling function

The cooling function Λ in general is a superposition of many different radiative processes, all having individual efficiencies depending on density, temperature and chemical composition. One generally distinguishes between primordial cooling (Cen, 1992; Katz et al., 1996; Sutherland and Dopita, 1993), metal-line and Compton cooling (Wiersma et al., 2009), and molecular cooling (e.g. Glover and Abel, 2008). Depending on environment and simulated system, only a subset of these cooling losses are relevant.

4.3.2 Reionization modelling /UV background

Convolved with the cooling function, there are also some heating effects due to ionising radiation, in particular during the time of reionization (Haardt and Madau, 1996, 2012; Faucher-Giguère et al., 2009). This radiation mainly originates from early star formation and quasars (to which degree is an topic of ongoing research), and is usually modelled, as a rough approximation to be a uniform background acting on the gas.

4.3.3 UV flux from AGN and young stars

Apart from the uniform background field, one can also model the effect of ionising radiation from young stars (Hopkins et al., 2017) and AGN (Vogelsberger et al., 2013) explicitly. This is usually done by imposing a predefined radiation flux on surrounding gas cells, which alters their heating/cooling balance.

4.4 Modelling of stars

Cooling gas will loose its pressure support, collapse via gravitational instability, become denser and cool even faster. This gravitational instability will ultimately lead to the formation of stars. In cosmological simulations, where an individual gas cell has masses of around 10^6 $M_\odot$, it is not possible to follow this collapse to scales of individual proto-stars. Instead, sub-resolution models of star formations can be employed that convert moderately cold gas into stars with some conversion efficiency (Springel and Hernquist, 2003; Schaye and Dalla Vecchia, 2008).

4.4.1 Stellar feedback

The massive end of the stellar population generally has significant interactions with the surrounding ISM via stellar winds, the already mentioned ionising radiation as well as via supernova explosions. Recent simulations indicate that feedback from supernovae is the dominant feedback channel (Hopkins et al., 2017), however, large uncertainties regarding the individual channels remain. The modelling of stellar feedback is ambiguous due to the fact that individual explosions are unresolved. Simulations use different classes of models, sometimes injecting the feedback energy thermally, sometimes via kinetic kicks, and generally produce different results (Rosdahl et al., 2017; Smith et al., 2017).

4.4.2 Metallicity and its impact on cooling

Apart from depositing energy into the ISM, stellar winds and supernova explosions also pollute the surrounding gas with stellar ejecta, which, in general, contain more heavy elements (in the following referred to as metals) than the primordial gas. These elements are able to change the cooling function significantly, as enriched gas is able to radiate via line transitions of the metals, which is substantial at intermediate and low temperatures (Wiersma et al., 2009).

4.5 Black hole modelling

Apart from stars, an additional, important component of the universe that need to be modelled in cosmological simulations are SMBHs. This includes models for SMBH seed formation, the growth of SMBHs, both via accretion and mergers, their dynamics and feedback effects. Many of these processes

are either poorly understood or very difficult to model at the resolutions available in cosmological simulations.

4.5.1 Seed formation

An explicit modelling of seed formation is not possible with the resolution employed in cosmological simulations. However, one choice one has to make is to decide which seed scenario to employ, and depending on this, different initial seed masses are employed. Assuming that SMBHs form from remnants of population III stars, seeds of around 10^2 to 10^3 $M_\odot$ would be appropriate. If one favours the direct-collapse scenario, the seed masses are around 10^5 $M_\odot$. The latter case is a bit easier to handle in cosmological simulations, as the seed mass of the black hole is not too different from the mass of an individual gas cell. The criterion of introducing a new SMBH seed in the simulation might be tied to a particular halo, seeding a new SMBH whenever a halo exceeds a given mass (e.g. used in Sijacki et al., 2007), or alternatively to local gas properties such as gas density and metallicity (see Tremmel et al., 2017b, and references therein).

4.5.2 Accretion rate estimate

Once a SMBH is seeded, one needs to estimate a gas accretion rate. Commonly, simple analytic models that translate large-scale gas properties and black hole masses to an accretion rate are employed in the simulations. One popular choice is the Bondi-Hoyle formula (Hoyle and Lyttleton, 1939; Bondi and Hoyle, 1944; Bondi, 1952) for spherically symmetric accretion onto a central object. This model generally does neither take angular momentum, nor self-gravity and gas cooling into account. Some modifications to this formula exist, for example taking into account angular momentum (Rosas-Guevara et al., 2015), the torques by non-axisymmetric stellar potentials (Anglés-Alcázar et al., 2015) or a cooling-limited accretion, which is frequently used in simulations of idealised galaxy clusters (Meece et al., 2017, for a comparison of different accretion models). Furthermore tanking into account the radiation pressure that emerges from rapidly accreting black holes, it is often assumed that the accretion rate is limited by the Eddington accretion rate, which is indeed a limiting factor for massive black holes at high redshift.

4.5.3 Black hole dynamics and mergers

In addition to accretion, SMBHs also grow substantially through mergers with other SMBHs. These can be modelled e.g. using an instantaneous merger approximation once two black holes approach each other. This certainly is a very crude approximation, neglecting the complicated dynamics and multi-physics nature of SMBH mergers, yet, it eventually will give roughly the correct outcome and is numerically robust.

Modelling the dynamics of SMBHs in a cosmological simulation is a difficult problem. In general, black holes feel the gravitational potential of all other particles, yet, the dynamical friction a black hole would feel in a sea of dark matter is drastically underestimated due to the discrete nature of the dark matter simulation particles. In principle, it is possible to estimate the drag force due to this dynamical friction (Hirschmann et al., 2014; Tremmel et al., 2017b). In practice, however, this estimate is uncertain and subject to numerical noise, which makes a robust and resolution independent prediction a challenging task. Alternatively, as a simplified model, one can tie the black holes to the centres of identified halos, which is a more numerically robust, but physically less motivated way of treating this problem.

4.5.4 Feedback

Feedback from SMBHs can be implemented in various different ways. In general, one assumes a specified fraction of the accreted rest-mass energy to be converted to feedback energy, which is then injected in the black hole surroundings. Similar to the implementation of stellar feedback, this can be done via dumping thermal or kinetic energy, both, in discrete events or continuously. The exact implementation furthermore depends on the resolution, where higher resolution generally allows for a more diverse and physically motivated implementation, while low-resolution models often just try to inject the correct amount of energy without creating obvious spurious effects from it. Two new implementations for these feedback effects, one kinetically driven AGN wind model for cosmological simulation, and a second implementation modelling AGN jets in higher resolution simulations, will be introduced as part of this thesis.

Part II

Cosmological simulations

5

Modelling black hole driven feedback

In this chapter, I describe the implementation of a new model for SMBHs and its performance in cosmological hydrodynamical simulations. This work is published in Monthly Notices of the Royal Astronomical Society, Volume 465, Issue 3, p.3291-3308.

5.1 Introduction

In simulations of galaxy formation, feedback from active galactic nuclei (AGNs) is the most commonly invoked physical mechanism to explain the suppression of star formation in massive galaxies, and the observed correlations between black hole masses and properties of their host galaxies. In particular, feedback from luminous quasars has been suggested to limit black hole growth and star formation during mergers at high redshift (Di Matteo et al., 2005; Springel et al., 2005a; Hopkins et al., 2006; Debuhr et al., 2010; Choi et al., 2014). Interacting galaxies trigger a redistribution of angular momentum and thus gas inflows into the nuclear region of galaxies (Hernquist, 1989; Barnes and Hernquist, 1996; Mihos and Hernquist, 1996). These gas inflows then generate a cascade of gravitational instabilities (Hopkins and Quataert, 2010; Emsellem et al., 2015), through which the supermassive black hole (SMBH) is fuelled and a fraction of the gravitational binding energy is released. This energy is sufficient to lower the star formation rate by several orders of magnitude (Di Matteo et al., 2005). However, it is not yet clear whether the released energy has a lasting effect on the whole galaxy and its star formation rate, or just affects the innermost regions (Debuhr et al., 2011; Roos et al., 2015).

By applying semi-analytic modelling, Croton et al. (2006) pointed out that 'radio-mode' feedback, which provides an efficient source of energy in systems with hot, hydrostatic atmospheres, can simultaneously explain the low mass drop-out rate in cooling flows, the exponential cutoff at the bright end of the galaxy luminosity function and the increased mean stellar

age in massive elliptical galaxies. Bower et al. (2006) used a similar approach in their semi-analytic model. Sijacki et al. (2007) presented a unified sub-resolution model with energy input from both quasars and radio-mode feedback in hydrodynamical simulations and applied it to galaxy cluster formation. In this model, the second mode of feedback is active once the black hole accretion rate relative to the Eddington limit, $\dot{M}_{\rm BH}/\dot{M}_{\rm Edd}$, drops below a given value. The feedback energy injection is modelled by heating up spherical bubbles of gas in galaxy haloes, mimicking the observed radio lobes in galaxy clusters.

There are various implementations of 'quasar mode' feedback in the literature. Debuhr et al. (2011, 2012) use feedback from radiation pressure from luminous AGN, modelled by depositing momentum in surrounding simulation particles in idealized mergers. Choi et al. (2012, 2014, 2015) included mechanical and thermal energy and pressure from X-rays in their AGN feedback prescription and studied the effect on idealized mergers of disc galaxies and in cosmological "zoom" simulations of elliptical galaxies while Wurster and Thacker (2013) performed a comparative study of these AGN models in merger simulations.

Likewise, many different approaches for 'radio mode' activity have been taken, often using bipolar outflows in idealized simulations of hydrostatic haloes (Reynolds et al., 2002; Basson and Alexander, 2003; Omma et al., 2004; Ruszkowski et al., 2004; Zanni et al., 2005; Brighenti and Mathews, 2006; Brüggen et al., 2007; Cattaneo and Teyssier, 2007; Sternberg et al., 2007; Sternberg and Soker, 2009; Gaspari et al., 2011b,a, 2012; Li and Bryan, 2014a,b; Li et al., 2015; Hillel and Soker, 2016; Yang and Reynolds, 2016a,b), or in cosmological simulations (Dubois et al., 2010, 2012, 2016). These methods assume that quenching is caused by the energy that is released from collimated jets and their associated radio lobes, which can be found in massive systems (Dunn and Fabian, 2006). However, Meece et al. (2017) show that these kinetic feedback implementations have a different impact in an idealized galaxy cluster setup compared to pure thermal injection.

The extensive body of literature on coupled AGN-galaxy evolution (including Granato et al., 2004; Kawata and Gibson, 2005; Sijacki et al., 2007; Di Matteo et al., 2008; Hopkins et al., 2008a,b; Okamoto et al., 2008; Somerville et al., 2008; Booth and Schaye, 2009; Ciotti et al., 2010; Debuhr et al., 2010; Teyssier et al., 2011; Dubois et al., 2012; Hirschmann et al., 2014; Choi et al., 2014; Khandai et al., 2015; Somerville and Davé, 2015; Rosas-Guevara et al., 2015; Steinborn et al., 2015; Trayford et al., 2016, among others) has recently been complemented by a new generation of high-resolution cosmological simulations of galaxy formation in large volumes, such as Eagle (Schaye et al., 2015) and Illustris (Vogelsberger et al.,

2014b). The corresponding implementations for black hole feedback in massive galaxies (in Illustris the radio-mode, while Eagle does not distinguish between modes) gather energy up to a predetermined threshold value, which parametrizes its burstiness and inject it instantaneously as thermal energy (see Sijacki et al., 2007; Booth and Schaye, 2009, for Illustris and Eagle, respectively).

While the Illustris simulation – which forms the starting point of our work – has been remarkably successful in matching a wide range of galaxy properties, its results are in tension with a number of properties of observed haloes and galaxies. An important discrepancy arising from the AGN feedback model is the gas fraction of groups of galaxies and poor clusters, which is substantially too low in Illustris (Genel et al., 2014). At the same time, the stellar masses of the central galaxies in the simulated systems are too high. Employing a yet higher feedback efficiency of the BH radio mode to suppress star formation further would expel even more gas, and hence does not represent a viable solution. Alternatively, as part of our study, we made numerous attempts to improve the impact of the bubble model by adopting different choices for the parameters or by adding non-thermal pressure support in the form of magnetic fields, but without success. We therefore conclude that the particular AGN feedback model in Illustris is disfavoured, and a more radical change is in order.

This suggestion is supported by recent observational findings about the possible importance of kinetic winds driven during BH accretion. For example, Cheung et al. (2016) find bisymmetric emission features in the centres of quiescent galaxies of stellar mass around $2 \times 10^{10}\,\mathrm{M}_{\odot}$, from which they infer the presence of centrally driven winds in typical quiescent galaxies that host low-luminosity active nuclei. They show that such 'red geyser' galaxies are very common at this mass scale, and that the energy input from the low activity of the SMBHs of these galaxies is capable of driving the observed winds, which contain sufficient mechanical energy to suppress star formation. This appears to be a feedback channel that is distinct from the radio galaxies at the centres of clusters, but as it affects many more galaxies at lower mass scales, it could well be more important for global galaxy evolution. Recently, Pontzen et al. (2017) found hot, AGN-driven outflows in post-merger galaxies, using the single-mode thermal AGN feedback model of Tremmel et al. (2017b). Interestingly however, Genzel et al. (2014) and Förster Schreiber et al. (2014) have discovered wide-spread, powerful AGN-driven outflows in the majority ($\sim 70\%$) of massive $z \sim 1-2$ star-forming galaxies. Because this phenomenon is so common, it likely arises from low-luminosity AGN with low Eddington ratios and thus appears consistent with a kinetic wind mode. Also, theoretically there is good motivation for hot

coronal winds from BH accretion flows. For example, Yuan and Narayan (2014) discuss such a scenario, which can be viewed as a small-scale version of the jet model of Blandford and Znajek (1977).

The motivation of our work is therefore to develop a revised model for black hole growth and feedback that takes these considerations into account. It is important to realize that the relevant time and length scales of the detailed black hole physics are by far not resolved in cosmological simulations. Hence, the corresponding feedback models can only be implemented as so-called sub resolution treatments that mimic the net effect of feedback on resolved scales. Besides the theoretical uncertainties involved, this approach comes with the drawback that the behaviour of the models can vary between different numerical methods, because the scales at which the gas state is affected by the subgrid treatment are only marginally resolved. This is demonstrated for example in Sijacki et al. (2015) for the bubble heating model of Sijacki et al. (2007). We thus also aim to take recent improvements in the accuracy of the hydrodynamical modelling into account (Bauer and Springel, 2012; Kereš et al., 2012; Sijacki et al., 2012; Vogelsberger et al., 2012; Pakmor et al., 2016).

The model presented here conjectures two modes of feedback from AGN in thermal and kinetic form, and in this sense is similar to Dubois et al. (2012). While the kinetic part of their model is inspired by the subrelativistic jet simulations of Omma et al. (2004), our approach does not directly aim to represent jets from AGNs that act on marginally resolved scales. Rather we assume that the physical mechanisms that provide energy and momentum transport from black holes to their surroundings are reasonably efficient, and that their impact on large scales can be captured by depositing energy and momentum in small regions around halo centres. This approach does not address the microphysics of the origin of AGN feedback but aims to arrive at a robust parametrization of the effects of black holes on galaxy and galaxy cluster formation even at coarse resolution.

In what follows, we present a new model for SMBH growth and AGN feedback in cosmological simulations of structure formation implemented in the moving-mesh magnetohydrodynamics code AREPO (Springel, 2010; Pakmor et al., 2011, 2016). In Section 5.2, we describe the model and its free parameters. Because the main modification to previous works lies in feedback injection at low accretion rates, in Section 5.3 we discuss idealized tests of how the energy couples in this mode to the gas. We then continue in Section 5.4 with an investigation of its impact on cosmological simulations of galaxy formation. Section 5.5 is dedicated to a systematic exploration of the influence of the different model parameters on the results. Section 5.6 specifies, for definiteness, details of our supernova feedback model, and Sec-

tion 5.7 discusses numerical resolution dependencies. Finally, we describe our findings and present our conclusions in Section 5.8.

5.2 Black Hole Model

Modelling AGNs in cosmological simulations poses several fundamental challenges. First, the detailed physical mechanisms of both accretion on to SMBHs (Hopkins and Quataert, 2010, 2011; Anglés-Alcázar et al., 2013; Gaspari et al., 2013; Anglés-Alcázar et al., 2015, 2017a; Curtis and Sijacki, 2015, 2016; Emsellem et al., 2015; Rosas-Guevara et al., 2015) and the AGN-gas interaction (Huarte-Espinosa et al., 2011; Gaibler et al., 2012; Cielo et al., 2014; Costa et al., 2014; Roos et al., 2015; Bieri et al., 2017; Hopkins et al., 2016) are poorly understood, which makes it at present impossible to formulate a 'correct' treatment for simulations, independent of their resolution. Secondly, the extreme dynamic range posed by the problem, where a comparatively tiny accretion region around the black hole influences an entire galaxy or even a galaxy cluster and the surrounding intergalactic medium, vastly exceeds the capabilities of current numerical techniques so that much of the physics on the smallest scales needs to be coarsely approximated with sub-resolution models. Thirdly, the nonlinear nature of galaxy formation intimately couples black hole accretion with other aspects of feedback, chiefly the regulation of ordinary star formation (Puchwein and Springel, 2013). This makes it difficult to disentangle the impact of different astrophysical processes. While we first examine the behaviour of our model in well-defined idealized tests, we will primarily assess its performance through studies of its consequences in the full cosmological context.

Similar to Sijacki et al. (2007), we distinguish between states of high and low accretion rates. This follows the theoretical notion that there exist (at least) two physically distinct types of accretion flows on to massive black holes (e.g. Begelman, 2014, and references therein): one at comparatively high rates in a classic disc mode (Shakura and Sunyaev, 1973), the other at lower rates in a more spherical and hotter accretion flow (Shapiro et al., 1976; Ichimaru, 1977). These regimes have loosely been identified with "quasar" and "radio" modes in previous simulation work. The observed phenomenology of radio jets in galaxy clusters has often been interpreted as providing the dominant source of feedback, at least in the low-accretion radio mode regime (McNamara and Nulsen, 2007). This has also motivated, e.g., the bubble heating model in Sijacki et al. (2007) that was applied in the Illustris simulation and in other works. However, there are also

theoretical indications pointing to the existence of kinetic winds in the low-accretion state (Igumenshchev and Abramowicz, 1999; Stone et al., 1999; Yuan and Narayan, 2014; Yuan et al., 2015; Bu et al., 2016; Sądowski et al., 2016). These would be difficult to observe but could constitute an even more important feedback mechanism than the radio jets themselves. A central motivation of our work is to test this idea by replacing radio bubble feedback with a kinetic wind.

5.2.1 Accretion mode

We follow previous work and use the Eddington ratio as the criterion for deciding the accretion state of the black hole. Specifically, we assume SMBHs to be in the high accretion state as long as their Bondi-Hoyle-Lyttleton accretion rate $\dot{M}_{\rm Bondi}$ (Hoyle and Lyttleton, 1939; Bondi and Hoyle, 1944; Bondi, 1952) exceeds a fraction χ of the Eddington accretion rate $\dot{M}_{\rm Edd}$:

$$\frac{\dot{M}_{\rm Bondi}}{\dot{M}_{\rm Edd}} \geq \chi, \tag{5.1}$$

where

$$\dot{M}_{\rm Bondi} = \frac{4\pi G^2 M_{\rm BH}^2 \rho}{c_s^3}, \tag{5.2}$$

$$\dot{M}_{\rm Edd} = \frac{4\pi G M_{\rm BH} m_p}{\epsilon_r \sigma_{\rm T} c}. \tag{5.3}$$

Here, G denotes the gravitational constant, c the vacuum speed of light, m_p the proton mass and $\sigma_{\rm T}$ the Thompson cross-section. The factor ϵ_r is the radiative accretion efficiency. $M_{\rm BH}$ is the black hole mass, and ρ and c_s are the density and sound speed[1] of the gas near the black hole, respectively. They are obtained by averaging over a sphere with radius h in a kernel-weighted fashion around the black hole such that the enclosed number of cells in this sphere is approximately equal to a prescribed number:

$$n_{\rm ngb} \approx \sum_i \frac{4\,\pi\,h^3\,m_i}{3\,m_{\rm baryon}} w(r_i). \tag{5.4}$$

Here, $m_{\rm baryon}$ is the target mass of a gas cell, i.e. the gas mass resolution enforced by the refinement and derefinement operations of the hydrodynamic

[1] We use an effective sound speed, taking into account both thermal and magnetic signal propagation $c_{\rm s}^2 = c_{\rm s,therm}^2 + c_{\rm A}^2$, where $c_{\rm A} = \left(\mathbf{B}^2/4\pi\rho\right)^{1/2}$ is the Alfven speed.

code, $n_{\rm ngb}$ is the prescribed number of neighbouring cells in this averaging and $w(r)$ is an SPH weighting kernel.

A sensible value for χ is expected to lie in the range $\sim 0.001 - 0.1$, by analogy with X-ray binaries (e.g. Dunn et al., 2010). Previous works (Sijacki et al., 2007, 2015) have employed a fixed value of χ. Black holes at low redshift located in massive systems show clear signatures of being in a 'radio' feedback state, (Dunn and Fabian, 2006) which indicates low Eddington ratios. However, as we will show in Section 5.4, this does not occur in our simulations *unless* the black holes transition to the kinetic mode in the first place, which is not guaranteed. To favour this transition for the most massive black holes at late times (which tend to be found in the most massive haloes), we scale the threshold with black hole mass,

$$\chi = \min\left[\chi_0 \left(\frac{M_{\rm BH}}{10^8\,{\rm M}_\odot}\right)^\beta, 0.1\right] \tag{5.5}$$

with χ_0 and β as parameters. The pivot mass $10^8\,{\rm M}_\odot$ is degenerate with χ_0 and is therefore not set independently. We limit the threshold χ to a maximum of 0.1 to always allow any black hole (including the most massive ones) to reach the high accretion state provided there is a large enough gas supply to fuel them. This would be expected for high redshift quasars that have very massive black holes.[2] For $\beta > 0$, our scaling makes it more difficult for low mass black holes to be in the kinetic mode, and vice versa. We expect this to support the occurrence of a rapid quenching transition in massive galaxies, and make it unlikely that low-mass galaxies will be strongly affected by kinetic feedback. The physics of the accretion mode transitions of SMBHs is poorly understood, making it difficult to parametrize it adequately in a coarse cosmological model. We have here opted for a heuristic model that is based on the only intrinsic black hole property we keep track of, the black hole mass, and which is selected pragmatically based on how well it reproduces observational trends. We note that it appears physically plausible that there are systematic trends with black mass scale in the accretion mode transition, given that radiative cooling physics breaks the scale invariance.

5.2.2 Accretion estimate and seeding of black holes

Note that in the above calculation of the Bondi accretion rate we omit a boost-factor α that was used in older models to account for the unresolved

[2]Note that the volume of the simulations presented in this work (Section 5.4) is too small to host these kind of objects.

ISM structure. When the latter is treated with a sub-resolution model that prescribes a high mean thermal support and an effective pressure, the Bondi rate is artificially biased low, slowing down especially the early growth of black holes. The boost factor was primarily introduced in the older models to compensate for this problem by ensuring that the Bondi growth time-scale for small mass seed black holes does not exceed the Hubble time. Since the actual accretion rate was however anyway limited to the Eddington rate, the latter is ultimately the governing rate for most of the growth. Furthermore, applying a boost factor for massive black holes in the low accretion state, when their feedback generates a low-density, hot gas phase around them (that can be resolved, unlike the ISM), appears questionable. We therefore simplify our treatment by assuming that the black holes are always accreting at the pure Bondi rate, limited by the Eddington rate:

$$\dot{M}_{\rm BH} = \min\left(\dot{M}_{\rm Bondi}, \dot{M}_{\rm Edd}\right). \tag{5.6}$$

We note that for massive black holes at late times, the accretion rate is self-regulated, thus an additional factor in the accretion rate estimate has no overall effect in this regime apart from systematically shifting the black hole masses, i.e. here the boost factor is largely degenerate with the black hole masses reached. Only the early growth phase is strongly affected by the boost factor, but this phase depends sensitively on the black hole seed mass as well (see discussion below), and we use this dependence to make up for the omission of a boost factor.

Note that Vogelsberger et al. (2013) lowered the accretion rate estimate by a factor of $(P_{\rm ext}/P_{\rm ref})^2$ whenever $P_{\rm ext} < P_{\rm ref}$. Here, $P_{\rm ext}$ is the kernel-weighted gas pressure surrounding the black hole and $P_{\rm ref}$ is a reference pressure (Vogelsberger et al., 2013, their equation 23). While this was used in the Illustris simulation, we omit such a factor in this work. We ran simulations both with and without this factor and found no significant difference in the properties presented in this work. However, as this serves as a protection against rare cases of overly heated, underdense regions in galaxy centres we plan to use it in future simulations that contain a larger sample of galaxies.

In our cosmological simulations, a black hole with mass $M_{\rm seed}$ is placed at the centre of a halo whenever the on-the-fly friend-of-friends halo finder identifies a halo more massive than a threshold mass $M_{\rm FOF}$ that does not yet contain a black hole. We note that to offset a potentially sluggish growth of black holes at high redshift, one can resort to a slightly larger seed mass, which then produces a similar result as using a boost factor α. In order to remain close to our previous models, we use this here and

adopt a black hole seed mass of $8 \times 10^5\, h^{-1}\, \mathrm{M}_\odot$ in our default model, which leads to a similarly fast growth at early times as our older models with $\alpha = 100$. Given the significant theoretical uncertainties in the early growth of SMBHs (e.g. Volonteri, 2010), we consider the seed mass as a poorly constrained free parameter. We note that there are other models for back hole seed formation in cosmological simulations (e.g. Bellovary et al., 2011; Tremmel et al., 2017b) that use thresholds of local gas properties such as metallicity, density and temperature. However, we decided for a seeding prescription depending solely on halo mass because of its simplicity and numerical robustness.

At the limited numerical resolution available in cosmological simulations, two-body discreteness effects and numerical N-body noise can displace black hole particles from halo centres. At the same time, the dynamical friction forces that should allow massive black holes to sink to the centres of dark matter haloes are not captured accurately by the simulation. To prevent black holes from artificially leaving the centres of haloes for long periods of time due to these effects, we resort to an ad hoc centring prescription designed to keep black holes very close to the potential minimum of their host dark matter haloes. To this end, at every global integration timestep (i.e. when the longest timesteps occurring in the whole simulation are synchronized in the nested time integration scheme), we determine the minimum gravitational potential in a region around the BH containing the equivalent of 1000 mass resolution elements. The BH particle is then shifted to this potential minimum (if not at the location of the BH already, which frequently happens), and its velocity is set to the mean mass-weighted velocity of the region. The latter minimizes any motion of the BH with respect to the central region of the halo. This method robustly prevents haloes from losing their central black hole, and it further adopts a scenario in which BH binaries are assumed to merge promptly. We use this approach here because of its numerical robustness and independence of resolution. However, there are more sophisticated treatments in the recent literature that use sub-resolution models for dynamical friction (e.g. Wurster and Thacker, 2013; Hirschmann et al., 2014; Tremmel et al., 2017b). We aim to use such a scheme in future high-resolution extensions of the present model.

5.2.3 Feedback

For the high accretion state, we calculate the liberated feedback energy as

$$\Delta \dot{E}_{\mathrm{high}} = \epsilon_{\mathrm{f,high}} \epsilon_{\mathrm{r}} \dot{M}_{\mathrm{BH}}\, c^2, \tag{5.7}$$

where $\dot{M}_{\rm BH}$ is the estimated black hole mass accretion rate of the black hole with mass $M_{\rm BH}$, $\epsilon_{\rm r}$ is the radiative efficiency (i.e. the canonical 0.1-0.2 of the accreted rest-mass energy that is released in the accretion process and not vanishing in the black hole), while $\epsilon_{\rm f,high}$ is the fraction of this energy that couples to the surrounding gas. For the low accretion state, the feedback energy is parameterized as

$$\Delta\dot{E}_{\rm low} = \epsilon_{\rm f,kin}\dot{M}_{\rm BH}c^2. \tag{5.8}$$

Note that we use different coupling efficiencies, $\epsilon_{\rm f,kin}$ and $\epsilon_{\rm f,high}$, for the two modes, motivated by the different physical nature of the accretion modes; namely that the low accretion state is thought to be radiatively inefficient. We keep the coupling efficiency in the high accretion state at a constant value of $\epsilon_{\rm f,high} = 0.1$, resulting in an overall efficiency $\epsilon_{\rm r}\epsilon_{\rm f,high} = 0.02$, while we set a maximum value of $\epsilon_{\rm f,kin} = 0.2$ in the low accretion mode, which assumes that the released rest-mass energy appears primarily in kinetic outflows. We note that our choice of $\epsilon_{\rm f,kin} = 0.2$ is within the physically plausible range, depending on the underlying physical mechanism. If, for example, the energy is delivered by small-scale jets produced by the Blandford-Znajek mechanism, the jet energy can be a factor of 10 or more larger than our adopted value for $\epsilon_{\rm f,kin}$ because of black hole spin (Yuan and Narayan, 2014). In the opposite case, for non-spinning black holes, small-scale simulations of accretion (Yuan et al., 2015) provide a theoretical lower limit to $\epsilon_{\rm f,kin}$ of about 10^{-3}.

To protect against a potential runaway of the kinetic feedback mode that may drive the density to ever lower values (see also section 2.6.2 of Vogelsberger et al., 2013, for further discussion), we conjecture that at very low densities the coupling efficiency $\epsilon_{\rm f,kin}$ eventually becomes weak. For simplicity, we assume that such a weakening occurs below a density $f_{\rm thresh}\rho_{\rm SFthresh}$, where $f_{\rm thresh}$ is a free parameter and $\rho_{\rm SFthresh}$ is the density threshold for star formation. If the surrounding density ρ drops below this value we reduce the coupling proportional to density. This then formally corresponds to a variable coupling efficiency in the low accretion state,

$$\epsilon_{\rm f,kin} = \min\left(\frac{\rho}{f_{\rm thresh}\rho_{\rm SFthresh}}, 0.2\right). \tag{5.9}$$

Our standard value for this prescription is $f_{\rm thresh} = 0.05$, and we will show in Section 5.5 that the exact value of $\epsilon_{\rm f,kin}$ has hardly any impact on galaxy properties.

In the high accretion state, we inject the feedback as pure thermal energy in a small local environment around the black hole, as in Springel et al.

(2005a) and our subsequent work (including Vogelsberger et al., 2013, as well as Illustris), while using our new model of kinetic feedback in the low accretion state. In the latter case, we inject the energy as pure kinetic energy. Unlike in the high accretion state, we hence input momentum but no immediate thermal energy to the gas. Technically, we inject both forms of feedback in a kernel-weighted manner into a prescribed number of gas neighbouring the BH, as determined by equation. (5.4). This region is identical for imparting feedback and the calculation of the gas properties used in the accretion estimate.

Because we cannot spatially resolve small-scale jets and the accretions flows in our cosmological simulations, we add the momentum in a random direction. We have found that this approach is most robust for avoiding possible numerical artefacts that can be produced at poor resolution by more elaborate approaches for adding the momentum. For example, one may impart the momentum in a spherically symmetric fashion, radially away from the black hole, with zero total momentum (as vector sum) added per injection event. However, this can produce an artificial suppression of the gas density at the position of the black hole at the resolution we achieve here. Similarly, a biconical injection in opposite directions at the position of the black hole can create artificially depressed gas densities unless the 'jets' are well enough resolved. We therefore prefer random injection directions that change for every injection event, which we found to be least resolution dependent. In this case detailed energy and momentum conservation is only obtained as a time average over the injection events.

Specifically, for an available kinetic feedback energy ΔE, we kick each gas cell j in the feedback region by

$$\Delta \mathbf{p}_j = m_j \sqrt{\frac{2\,\Delta E\, w(\mathbf{r}_j)}{\rho}}\,\mathbf{n}, \tag{5.10}$$

where $\Delta \mathbf{p}_j$ is the change in momentum of gas cell j, m_j denotes its mass, and $\mathbf{r}_j$ is the distance vector from the black hole to the respective cell. The factor $\mathbf{n}$ is the unit vector in a randomly chosen injection direction, $w(\mathbf{r}_j)$ the value of the smoothing kernel, and ρ is the density estimate of the surrounding gas, as described in Section 5.2.1. The total momentum injection per feedback event is thus

$$\mathbf{p}_{\rm inj} = \sum_j m_j \sqrt{\frac{2\,\Delta E\, w(\mathbf{r}_j)}{\rho}}\,\mathbf{n}, \tag{5.11}$$

and the corresponding change in total energy of the gas (relative to the lab frame) is

$$E_{\rm inj} = \Delta E + \sum_j \left(\mathbf{p}_j \cdot \mathbf{n}\right) \sqrt{\frac{2\,\Delta E\, w(\mathbf{r}_j)}{\rho}}, \tag{5.12}$$

where $\mathbf{p}_j$ is the momentum of cell j before the injection event.

For a single injection event, this violates strict momentum conservation and will generally not increase the total energy by precisely ΔE. However, the average over many injection events leads to the desired energy injection and assures momentum conservation (i.e. $\left\langle \mathbf{p}_{\rm inj} \right\rangle = 0$), as the injection direction $\mathbf{n}$ is randomly chosen for each injection event and does not correlate with the flow direction of the surrounding gas. To make the occurrence of these injection events independent of the timestepping, and also to make them powerful enough individually, we discretize the kinetic feedback mode by imposing a minimum energy that needs to accumulate in the kinetic accretion mode before the feedback is released. This is similar to the approach adopted in Illustris and Eagle for the BH feedback in large haloes.

In this work, we choose to parametrize the adopted energy threshold for the kinetic feedback in terms of a fiducial energy computed from the mass of the feedback region and the surrounding dark matter velocity dispersion. This identifies an energy per unit mass that is tied to the virial temperature of the halo. In fact, we could also construct the energy scale from the temperature of the surrounding gas. But the latter can be affected strongly by local cooling or previous feedback events, hence we prefer to use the dark matter velocity dispersion for increased robustness. We note that the velocity dispersion is also used for our supernova-driven wind feedback from star formation, which we adopt from Illustris in only a slightly modified form (see Appendix 5.6). We parametrize the kinetic feedback threshold by

$$E_{inj,min} = f_{\rm re} \frac{1}{2} \sigma_{\rm DM}^2\, m_{\rm enc} \tag{5.13}$$

where $\sigma_{\rm DM}$ is the 1D dark matter velocity dispersion, $m_{\rm enc}$ is the gas mass in the feedback region, and $f_{\rm re}$ is a free parameter that specifies the burstiness and thus the frequency of the reorientation of the kinetic feedback. If a larger value is chosen for $f_{\rm re}$, fewer feedback events occur, but they are individually stronger. Choosing this scaling is partly numerically motivated, as it ensures that the resulting shocks are strong enough to be accurately captured by our finite-volume scheme. Without this threshold, low-luminosity black holes would drive very weak flows that would thermalize mainly via

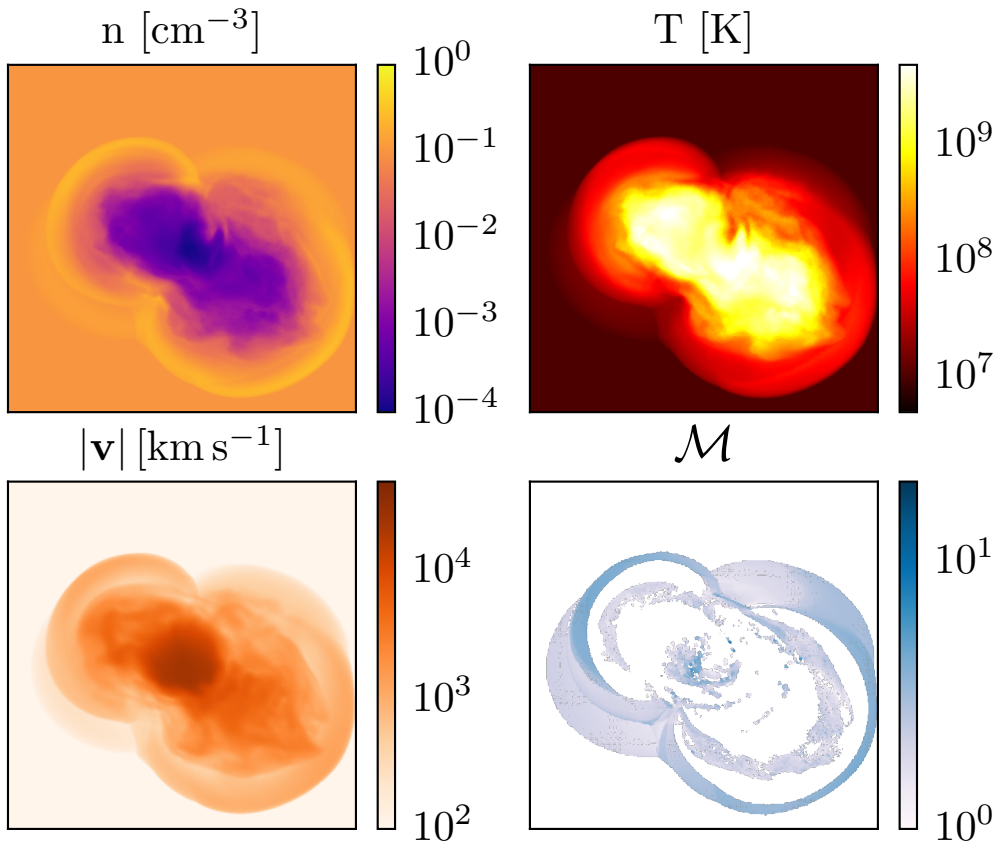

Figure 5.1: Thin projection (5 kpc in depth, 25 kpc on a side) of the 256^3, $n = 10^{-1}\,\mathrm{cm}^{-3}$, $T = 10^7\,\mathrm{K}$ simulation after 5 Myr of evolution. The panels show volume weighted density (top left), volume-weighted temperature (top right), absolute velocity (bottom left), and energy dissipation weighted Mach number (bottom right).

numerical dissipation effects, which is clearly undesirable. Part of the motivation is also physical, because this scaling ensures that the specific energy of the wind does not significantly exceed the specific binding energy of the halo, and thus should not unbind a large amount of gas or overly disturb the thermodynamic state of the intrahalo gas.

5.3 Kinetic wind dissipation tests

To examine the dissipation mechanisms of the kinetic feedback model, we use idealized test simulations in a cubic box with constant density, temperature and pressure and a side length of 25 kpc. The fiducial values for

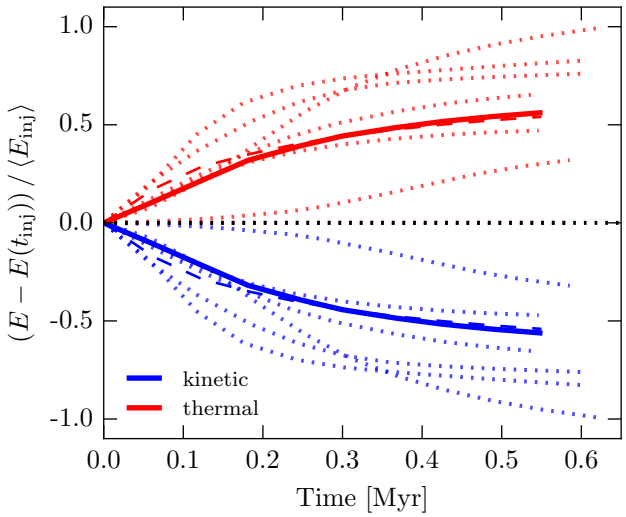

Figure 5.2: Evolution of the different energy components after kinetic energy injection. The dotted lines show individual injection events, the solid line their average, both in the simulation initially with 32^3 cells. The dashed line shows the average of the high resolution test with 256^3 initial cells. On average, half of the feedback energy that was initially in kinetic form is thermalized after 0.5 Myr. This behaviour is converged at the resolution of cosmological simulations.

density and temperature are $n = 10^{-1}\,\mathrm{cm}^{-3}$ and $T = 10^7\,\mathrm{K}$. We place a black hole at the centre and inject energy at a fixed rate of $10^{45}\,\mathrm{erg\,s}^{-1}$ in the kinetic mode. We run the simulations for 5 Myr, only solving the equations of hydrodynamics, switching off self-gravity, gas cooling and all galaxy formation sub-grid prescriptions such as star-formation and feedback, metal enrichment, black hole seeding, etc. We run the simulations at two different resolutions: 32^3 initial cells, which roughly corresponds to the resolution of cosmological simulations (for $\rho = 10^{-1}\,\mathrm{cm}^{-3}$, the average mass of a gas cell is $7 \times 10^5\,\mathrm{M}_\odot$), and 256^3, to show the convergence properties.

Unlike in cosmological simulations, where we keep the number of neighbours in the feedback injection region roughly constant, we here fix the radius of the sphere in which the feedback is injected. We have tested both approaches and found that there is no substantial difference, except that tying the injection region to the number of neighbouring gas cells (equation. 5.4) leads in this particular setup – in which self-regulation is disabled – to a slowly growing injection region, as the gas around the black hole is heated up by previous feedback events. To promote a clean study of

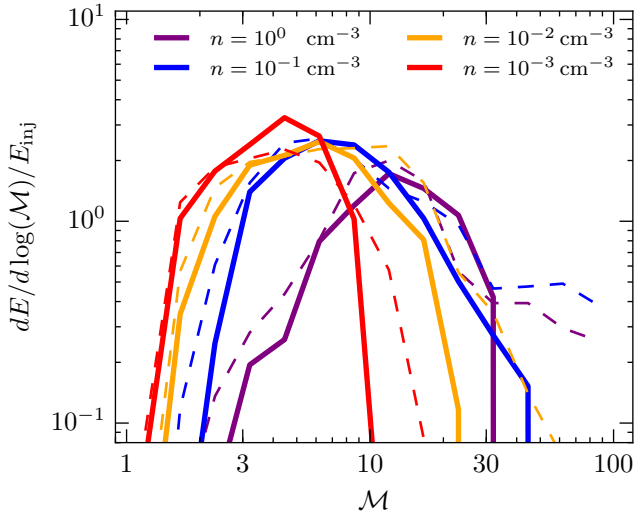

Figure 5.3: Energy dissipation as a function of shock Mach number $\mathcal{M}$ summed up over a simulation time of 5 Myr. The different colours denote different isobaric variations of the gas from relatively cool, dense (1 cm^{-3}, $T = 10^6$ K) to hot, dilute ($\rho = 10^{-3}$ cm^{-3}, $T = 10^9$ K). The solid lines show the simulation with an initial grid of 32^3 cells, comparable to the resolution of cosmological simulations, while the dashed lines indicate simulations with 256^3 cells to show the convergence of the analysis.

the impact of the kinetic pulses on the gas, we prefer to keep the feedback injection region fixed to a sphere of 3.5 kpc radius around the black hole. We ensure that there is always a sufficient number of cells in this region by setting a maximum volume per cell, above which they are refined[3]. The physical size of the feedback injection region is kept the same for the 256^3 simulations, allowing a study of discretization effects in the gas. We note, however, that in cosmological simulations there are additional resolution dependences such as the scaling of the feedback injection region, which is discussed in Appendix 5.7. As there is no dark matter in the present test simulations, we replace equation (5.13) with

$$E_{inj,min} = f_{\rm re}\, u_{\rm init}\, m_{\rm enc}, \tag{5.14}$$

where $u_{\rm init}$ is the initial specific thermal energy. This means that we are assuming that the temperature of the gas in the initial state is equal to the virial temperature of the dark matter halo. Using this threshold, the

[3]Note that in cosmological simulations, we do not impose such a volume limit.

total energy injected in 5 Myr suffices for seven injection events within the simulated timespan.

Fig. 5.1 shows a volume weighted projection of the gas density, temperature, absolute velocity and the energy dissipation weighted Mach number of the shocks present after 5 Myr. For the temperature and density, we average over the logarithm of the corresponding quantity, while we average over the absolute value of the velocity to highlight the maximum velocities involved in the projection. The projected maps show that the model is very efficient in diluting the central regions near the black hole. This means that the accretion rate estimated in this regime would decrease immediately by orders of magnitude, resulting in a very tight self-regulation. As the projections were made shortly after the seventh injection occurred, we reach gas flows with very high velocities in the injection region, which slow down after leaving this immediate vicinity of the black hole.

Fig. 5.2 shows the time evolution of the thermal and kinetic energy after individual injection events, as well as the average evolution with time. We can detect an injection event simply by a jump in total energy of the system owing to very frequent simulation outputs. The first output after this jump defines the zero-point in Fig. 5.2, which means that the thermal energy increases and the kinetic energy decreases subsequently. The initial energy injection is purely kinetic; however within ~ 0.5 Myr about half is dissipated into thermal energy, mostly via shock dissipation. As the direction of the momentum kicks change after every injection event, the AGN model does not build up a coherent gas flow that could reach several tens to a hundred kpc.

As a further analysis tool, we use the shock finder described in Schaal and Springel (2015) to detect shocks and calculate their Mach number $\mathcal{M}$ and energy dissipation rate for each snapshot. The bottom right panel in Fig. 5.1 shows the energy dissipation weighted Mach number projection, which excludes all cells that do not belong to a shock, and Fig. 5.3 shows the corresponding energy dissipation as a function of Mach number. For a hot, dilute gas, the shock Mach number mostly remains below 10, while the shock strength increases with higher densities and correspondingly lower temperatures and sound speeds. Summing up all the energy that is dissipated in shocks, we are, up to a factor of order unity, able to reconstruct the feedback energy purely through post-processing analysis of the surrounding gas. This is possible for even moderate resolution, which opens up the possibility of studying the effects of shocks from AGNs on their surroundings even in cosmological simulations of galaxy formation, so that their behaviour can be compared to observations (e.g. Dopita et al., 2015; Medling et al., 2015). However, there are some technical challenges

to this (see Schaal et al., 2016), in particular concerning the treatment of the unresolved ISM structure in these simulations. Therefore, for now we restrict our analysis to the idealized setup and leave the study of shocks from AGN winds in cosmological simulations to future work.

The test simulations demonstrate that our kinetic feedback model can accelerate the gas in the injection region to several tens of thousands of $\mathrm{km\,s^{-1}}$. This gas flow hits the surrounding medium and heats it via shock dissipation within time-scales of a Myr. A fraction of the energy will remain kinetic and ultimately decay via turbulent dissipation. This behaviour of the feedback injection is well converged, showing that our deposition of energy is not subject to significant numerical limitations on marginally resolved scales.

5.4 Cosmological simulations

Idealized test simulations such as those above cannot address the dynamics of self-regulated black hole growth. As this can only be meaningfully studied in calculations that follow cosmic structure formation and that also account for star formation, we now move on and examine the impact of our new model in hydrodynamical simulations of galaxy formation. This requires the full black hole model as described in Section 5.2, including the seeding of SMBHs and the estimate of their accretion rates. Also, because gas cooling and heating, star formation, stellar evolution and feedback, as well as the chemical enrichment of the interstellar medium, are all crucial ingredients of galaxy formation, we account for these processes using the respective models described in Vogelsberger et al. (2013). These are modified and extended as follows:

- We use isotropic winds from star formation with 10% of the energy injected thermally (Marinacci et al., 2014), instead of purely kinetically with a bipolar orientation as in Illustris.

- We slightly adjust the scaling of the stellar wind model with redshift, metallicity and halo mass.

- Updated chemical yields and an improved metal advection algorithm are used, which has however negligible influence on the results discussed here.

- Ideal magnetohydrodynamics is included based on a Powell cleaning scheme (Pakmor et al., 2011; Pakmor and Springel, 2013).

- An improved gradient estimator and time integration scheme for the hydrodynamics is used (Pakmor et al., 2016), which improves the accuracy of the AREPO code.

We briefly summarize the changes due to the modifications in the stellar wind model (i.e. the first two items) in Section 5.6, as the interplay between stellar and AGN feedback affects the overall galaxy population (Puchwein and Springel, 2013) as well as black hole growth rates (Dubois et al., 2015). The other modifications have a minor effect on the quantities examined in this work. We therefore focus this study on the black hole model and its parameters, and illustrate the relevance of the feedback efficiency, the accretion rate estimate and the black hole seeding model for the formation and evolution of galaxies as a function of their mass. A more detailed analysis of the other changes will be subject of a forthcoming paper (Pillepich et al., 2017b).

5.4.1 The simulations

We run a number of cosmological simulations of a periodic box with a side length of $30\,h^{-1}$ Mpc. As the large-scale modes of the matter power spectrum cannot be sampled in this comparatively small volume, our simulation does not contain structures as massive as the largest galaxy clusters observed in our Universe. However, we still follow the formation of 13 objects more massive than $10^{13}\,\mathrm{M}_\odot$ and more than 100 haloes in the mass range between $10^{12}\,\mathrm{M}_\odot$ and $10^{13}\,\mathrm{M}_\odot$. This makes the simulations well-suited for testing the AGN model and for studying its impact on the formation and evolution of massive galaxies at the resolution of the Illustris simulation.

We adopt the cosmological parameters from the *Planck* intermediate results (Planck Collaboration et al., 2016), $\Omega_\mathrm{M} = 0.3089$, $\Omega_\Lambda = 0.6911$, $\Omega_\mathrm{b} = 0.0486$, $h = 0.6774$ and $\sigma_8 = 0.8159$ and use an Eisenstein and Hu (1998) matter power spectrum to produce initial conditions at redshift $z = 127$. The initial conditions contain 384^3 dark matter particles and the same number of gas cells at our default resolution. This implies an average gas cell and dark matter particle mass of $6.7 \times 10^6\,h^{-1}\,\mathrm{M}_\odot$ and $3.4 \times 10^7\,h^{-1}\,\mathrm{M}_\odot$, respectively, which is similar to the intermediate resolution Illustris simulation (Illustris-2 in Vogelsberger et al., 2014c). The corresponding softening length is 2 comoving kpc with a maximum value of 1 proper kpc for dark matter and stars. The softening for the gas cells depends on their volume and has a minimum of 0.25 comoving kpc. The moderate number of simulation particles allows us to study the effect of each parameter of the black hole model individually, but it also comes with

a severe drawback: At this resolution, the star formation rate predicted by the employed Springel and Hernquist (2003) model is not fully converged for haloes below $10^{12.5}\,\mathrm{M}_\odot$ (Pillepich et al., 2014; Sijacki et al., 2015), as also shown in Section 5.7. This entails important limitations, especially with regard to the comparison to observations.

To get a better idea of the behaviour at the low mass end of AGN host galaxies, we run an additional simulation with 2×768^3 particles and cells and the same box size. In this run, all softening lengths are reduced by a factor of 2 compared to the fiducial setup. The implied resolution corresponds to the Illustris-1 high resolution run. Additionally, we run a low-resolution test with 2×192^3 particles and the same side length of the simulation box. The softening is increased by a factor of 2 compared to the fiducial run. For each of the different resolutions, we also computed a dark matter only version to quantify the role of baryonic physics on the halo mass function.

We have also carried out a suite of simulations with 2×384^3 particles in which the parameters of the black hole model were systematically varied by a factor of 4 each in the direction that seemed most interesting. Table 5.1 gives an overview of these simulations and their parameters. The set of simulations also includes one simulation in which the black holes are always in the quasar-mode, independent of their Eddington rate (labeled '`no kin.`'). Using identical initial conditions in our simulations allows a halo-by-halo comparison of all galaxy properties, facilitating a clean comparison of globally averaged properties and an interpretation of small changes in a meaningful way. We do so by matching the friend-of-friends groups in the different simulations in position space, followed by a verification that they are indeed the same structures by ensuring that they have at least half of their dark matter particles in common.[4] We discard the few percent of haloes that could not be matched by these criteria and ignore them for the analysis; they are for the most part borderline cases where the friend-of-friends algorithm links two haloes across a feeble particle bridge in one simulation but not in the other. In addition to the matching of haloes across simulations at identical redshifts, we also match haloes of a given simulation at different times. We define the progenitor as the halo in the previous snapshot that contributes the most dark matter particles to a given halo, which allows us to study the evolution of individual haloes.

We base a substantial part of our analysis on a comparison of the same haloes in different simulations, thereby avoiding uncertainties due to the

[4]This is done by checking their particle IDs, which are unique identifiers set in the initial conditions.

absolute halo abundance, which is affected significantly by box size and resolution effects. However, a detailed comparison to observational data requires a larger simulated volume and higher resolution. Achieving both at the same time is a computational challenge and is clearly beyond the scope of this paper. Simulations that reach this statistical power will be presented in future work.

Name	$n_{\rm particles}$ in initial conditions	$m_{\rm DM}$,$m_{\rm baryon}$ $[10^5\,{\rm M}_\odot\,h^{-1}]$	$\epsilon_{\rm f,kin}$	ϵ_r	χ_0	β	$M_{\rm seed}$ $[{\rm M}_\odot\,h^{-1}]$	$M_{\rm FOF}$ $[{\rm M}_\odot\,h^{-1}]$	$n_{\rm ngb}$	$f_{\rm re}$
Fid	2×384^3	340, 67	0.2	0.2	0.002	2.0	8×10^5	5×10^{10}	128	20
No kin.	2×384^3	340, 67	0.2	0.2	**0.000**	2.0	8×10^5	5×10^{10}	128	20
High res	$\mathbf{2 \times 768^3}$	**42.5, 8.4**	0.2	0.2	0.002	2.0	8×10^5	5×10^{10}	**256**	20
Low res	$\mathbf{2 \times 192^3}$	**2720, 536**	0.2	0.2	0.002	2.0	8×10^5	5×10^{10}	**64**	20
Low ϵ_f	2×384^3	340, 67	**0.05**	0.2	0.002	2.0	8×10^5	5×10^{10}	128	20
Low ϵ_r	2×384^3	340, 67	**0.05**	**0.05**	0.002	2.0	8×10^5	5×10^{10}	128	20
High χ	2×384^3	340, 67	0.2	0.2	**0.008**	2.0	8×10^5	5×10^{10}	128	20
Low β	2×384^3	340, 67	0.2	0.2	0.002	**0.5**	8×10^5	5×10^{10}	128	20
Low $M_{\rm seed}$	2×384^3	340, 67	0.2	0.2	0.002	2.0	$\mathbf{2 \times 10^5}$	5×10^{10}	128	20
High $M_{\rm FOF}$	2×384^3	340, 67	0.2	0.2	0.002	2.0	8×10^5	$\mathbf{2 \times 10^{11}}$	128	20
High $n_{\rm ngb}$	2×384^3	340, 67	0.2	0.2	0.002	2.0	8×10^5	5×10^{10}	**512**	20
Low $f_{\rm re}$	2×384^3	340, 67	0.2	0.2	0.002	2.0	8×10^5	5×10^{10}	128	**5**

Table 5.1: Overview of our primary simulations. All simulations, except for high res and low res are started from the same initial conditions. The only differences between the simulations and the fiducial case are the parameter values marked in bold. All simulations have a comoving volume of $(30\,h^{-1}{\rm Mpc})^3$.

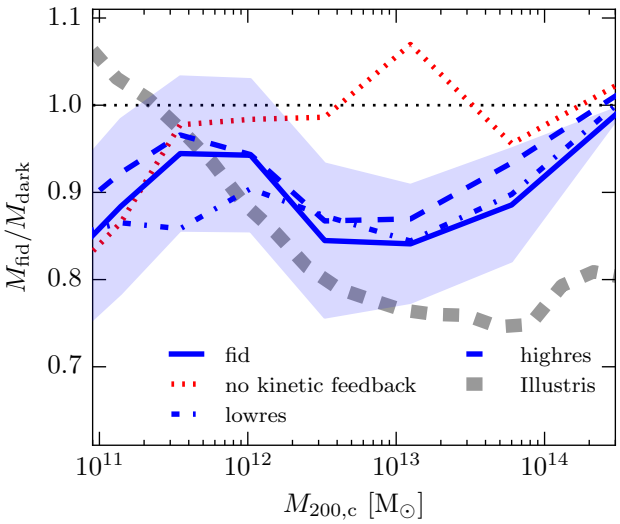

Figure 5.4: Average ratio of the mass of haloes in the full physics simulation to the mass of the corresponding halo in the dark matter only run, as a function of halo mass. The shaded region indicates the 1σ scatter of the results of our default simulation. The dashed grey line represents the result for the Illustris simulation (Vogelsberger et al., 2014c).

5.4.2 Galaxy properties

Halo masses

We start by looking at the overall baryonic effect on the masses of individual haloes. Fig. 5.4 shows the mass of the haloes in our fiducial baryonic simulation in units of the mass of the corresponding halo in the dark matter only simulation, as a function of $M_{200,\rm c}$. The average mass fraction does not exceed unity for any halo mass, unlike in Vogelsberger et al. (2014c) for haloes of $M_{200,c} \sim 10^{11}\,\rm M_\odot$. However, also in our simulations, the mass of some individual haloes can scatter above the mass of their dark matter only counterparts. The masses of haloes with $M_{200,c} < 10^{11}\,\rm M_\odot$ are suppressed more than those of $10^{12}\,\rm M_\odot$ haloes, independent of the black hole feedback implementation. This is hence presumably caused by stellar feedback. A mild decline in the halo masses relative to the dark matter only run occurs for haloes more massive than $10^{12}\,\rm M_\odot$. This drop can be clearly associated with the kinetic AGN feedback, as it is not present in the simulation without this mode. However, it is not as pronounced as in Vogelsberger et al. (2014c), which confirms that our feedback implementation is not as violent. The upturn at $10^{14}\,\rm M_\odot$ indicates a return to the universal baryon fraction

for the most massive haloes but is based only on very few haloes. Better statistics will be needed to reliably establish the behaviour at these mass scales.

Black holes

As mentioned in Section 5.2.2, a black hole with mass $M_{\rm seed}$ is placed into a halo whenever the on-the-fly friend of friends halo finder identifies a structure that is more massive than a threshold mass $M_{\rm FOF}$ and does not yet contain a black hole. At seeding, the surrounding gas is usually dilute and the black hole accretes at low rates with a long Bondi growth time-scale. This means that the growth is slower than the growth in stellar mass and therefore, the corresponding galaxy evolves horizontally in the $M_{\rm BH} - M_{\rm bulge}$ diagram (Fig. 5.5, upper plot). After some time, enough gas piles up around the black hole and produces higher accretion rates, allowing the black hole to eventually grow more rapidly, aided also by the runaway character of Bondi growth due to its $\dot{M}_{\rm BH} \propto M_{\rm BH}^2$ scaling. Consequently, the slope in the $M_{\rm BH} - M_{\rm bulge}$ diagram steepens. This second phase continues until the feedback injection of the black hole into its surroundings becomes significant, at which point the black hole gas supply becomes self-regulated. In this final stage, the black holes grow less rapidly and are mostly in the low accretion state again.

However, the slight change in slope in the $M_{\rm BH} - M_{\rm bulge}$ relation at $M_{\rm bulge} \approx 10^{10}\,{\rm M}_\odot$ is not due to the change of accretion mode, but rather due to the bulge-to-disc decomposition. We define the bulge mass as twice the stellar mass of the counterrotating star particles within $0.1\,R_{200,c}$. Galaxies with $M_{\rm bulge} \approx 10^{10}\,{\rm M}_\odot$ have a large fraction of corotating stars (i.e. a disc) and correspondingly our estimate of the bulge mass is reduced, which shifts the corresponding points to the left in the upper plot of Fig. 5.5. In the $M_{\rm BH} - M_*$ plot (Fig 5.5, lower plot), with M_* being the mass of all the stars within twice the stellar half-mass radius, such a change in slope does not show up.

Generally speaking, our systems with $M_* < 10^{10.5}\,{\rm M}_\odot$ tend to have slightly overly massive black holes compared to the observed relation, which indicates too early growth of the black holes, possibly caused by the increased seeding mass we use compared to earlier work (Sijacki et al., 2015). However, Volonteri et al. (2016) showed that the shape and scatter of the low-mass end changes significantly for different ways to measure $M_{\rm bulge}$. Considering this effect and the observational uncertainties, the discrepancy is not particularly worrisome. For high-mass systems, we follow the observed relation more closely, seemingly with little scatter. We leave a de-

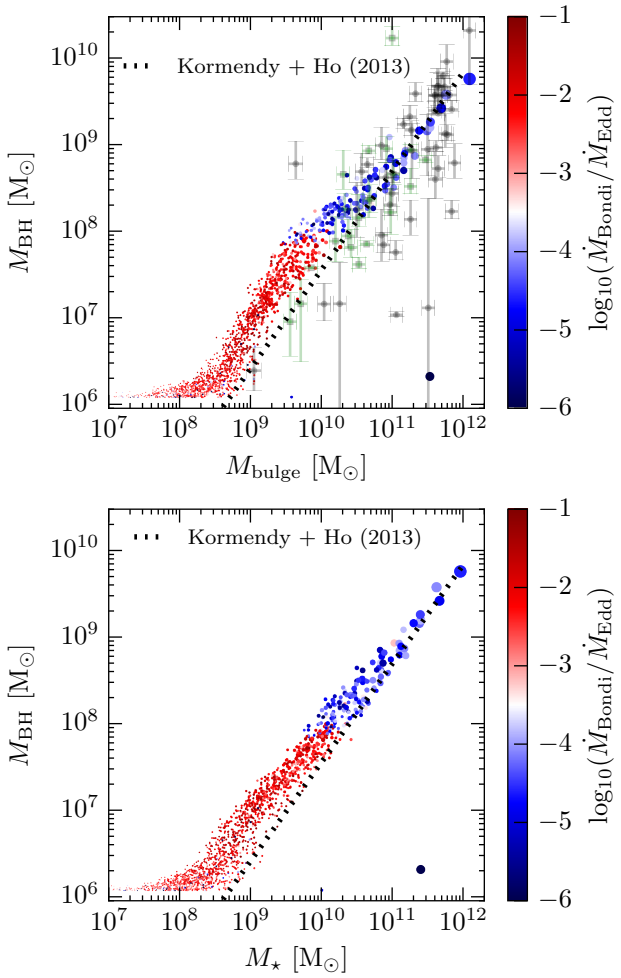

Figure 5.5: Black hole mass as a function of bulge mass (upper plot) and stellar mass within twice the half mass radius (lower plot) for central galaxies in the high-resolution simulation. The size of the symbols is scaled with bulge mass for better visibility, and the assigned colour scale encodes the Eddington ratio. The dotted line is the fit to observational data. The symbols with error bars are observed ellipticals (black), and spirals or S0 galaxies with normal bulges (green), taken from Kormendy and Ho (2013). The bulge mass is estimated as twice the mass of the counter-rotating fraction of stars within $0.1\,R_{200,c}$. We note that this might slightly underestimate the bulge mass in the case of rotating bulges.

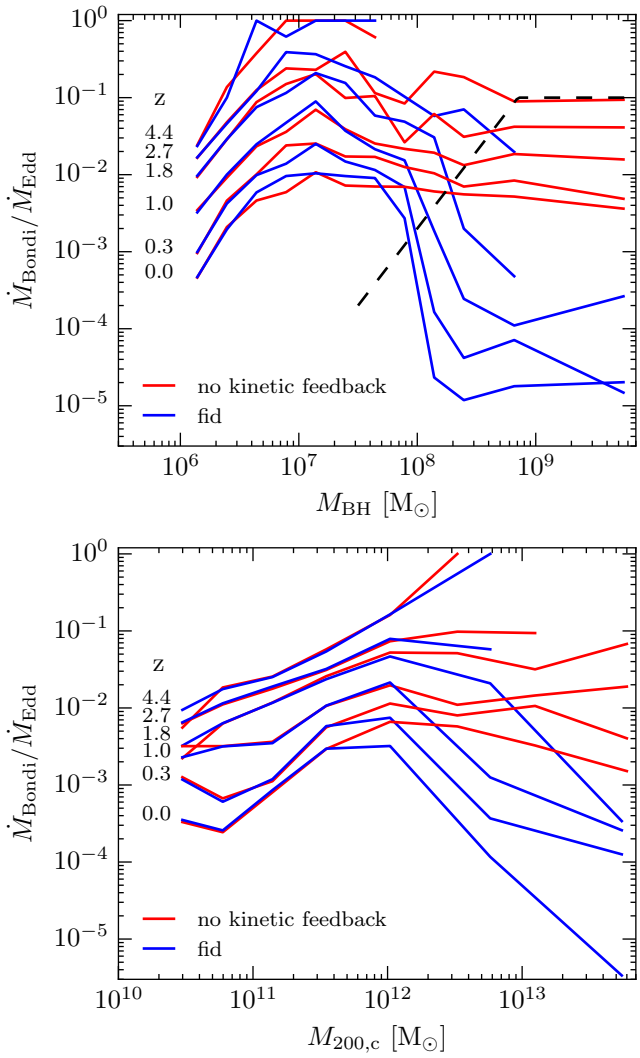

Figure 5.6: Median Eddington ratio as a function of black hole mass (top) and halo mass (bottom). The different lines show different redshifts. The dashed line in the top plot indicates our imposed transition point between low and high accretion states.

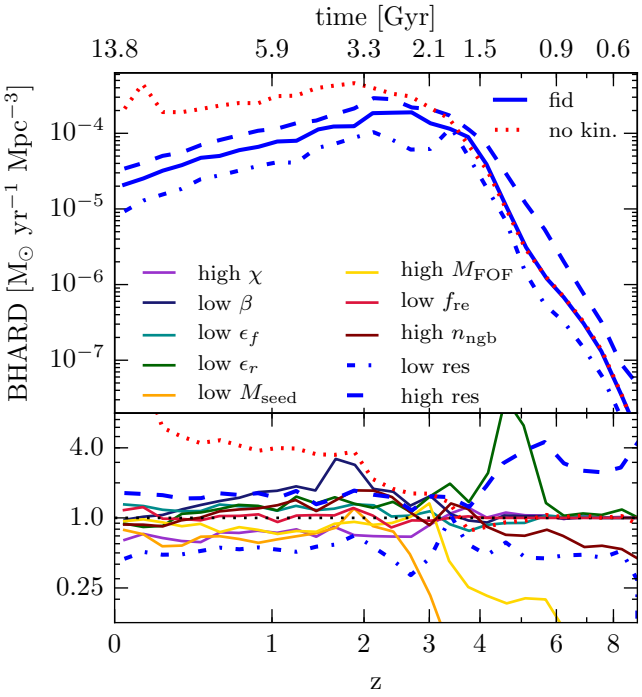

Figure 5.7: BHARD as a function of redshift for different runs. The lower panel shows the ratio relative to the fiducial run.

tailed analysis of the high mass end to future work as it requires a larger sample of black holes.

The black hole population has a clear change in accretion rate at black hole masses of around $10^8\,\mathrm{M}_\odot$ (colour coded in Fig. 5.5). Fig. 5.6 shows the accretion rate in units of $\dot{M}_{\rm Edd}$ as a function of black hole mass for different redshifts. For comparison, we also show the Eddington factors in the run without kinetic feedback. One clear trend is the drop of the Eddington ratio with redshift, which is consistently present over the complete range of black hole masses. This is expected, as the black hole accretion rate density (BHARD) (Fig. 5.7) in $\mathrm{M}_\odot\,\mathrm{yr}^{-1}\mathrm{Mpc}^{-3}$ decreases significantly towards low redshifts. The downturn towards the low black hole mass end shows the relatively slow initial growth of the black holes. This is partially due to a smaller amount of cold gas and partially due to the fact that in our implementation the Eddington ratio depends linearly on the black hole mass. A perhaps unexpected feature is that, without kinetic feedback, the Eddington factor does not significantly vary with black hole mass for black holes more massive than $10^7\,\mathrm{M}_\odot$. This means that even the most massive black holes in galaxy group and cluster environments would have a good

chance of accreting at high Eddington ratios, which is almost invariably also associated with high star formation rates.

This can be prevented by the kinetic feedback of the low accretion mode, which is more efficient than the feedback in the high accretion state. To ensure that a black hole and its surrounding gas transition to a self-regulated state with lower accretion rate, and to prevent newly seeded low-mass black holes from remaining in the low accretion state, we employ a black hole mass dependent quasar threshold χ, shown as the dashed line in the top panel of Fig. 5.6. Once a black hole transitions to the kinetic feedback mode, its Eddington factor drops significantly as a consequence of the stronger feedback, making it likely to remain in this regime for an extended period of time. Note that the deviation of the median curve starts slightly to the left of the dashed line due to the scatter in the black hole properties, allowing some lower mass black holes to make the transition earlier than the mean.

The drop in Eddington ratio for high-mass systems also has an effect on the overall BHARD, shown in Fig. 5.7. In fact, for the simulations without kinetic feedback, there is no significant drop of the BHARD towards lower redshifts. There is an increased BHARD with higher resolution, which is related to the fact that the region in which the accretion rate is estimated is intentionally reduced with increasing resolution, which leads to systematically higher density estimates. Especially at early times, this leads to earlier and thus faster accretion, and consequently more massive black holes.

Stellar component

We now turn to the effect of black hole feedback on the stellar properties of galaxies. Fig. 5.8 shows the average star formation rate density (SFRD) as a function of redshift. At redshifts lower than $z = 3$ the fiducial simulation differs from the observed SFRD by about 0.3 dex. For our higher resolution simulation (dashed line), the SFRD is in better agreement with the observations. At low redshifts, the contribution from Milky Way-sized galaxies dominates, which indicates a relatively poor convergence in their star formation rates. In Section 5.7, we discuss this in more detail.

From an AGN-feedback point of view, galaxy formation can be divided into three epochs. At redshift $z > 5$, there are either no or only slowly accreting black holes with no significant impact on the host galaxy. During this stage, only stellar feedback regulates the star-formation rate (e.g. Vogelsberger et al., 2013, their fig. 15). Correspondingly, changes in the black hole parameters have no effect on the SFRD. After this initial phase, the black holes enter the high accretion regime and grow quickly, releasing

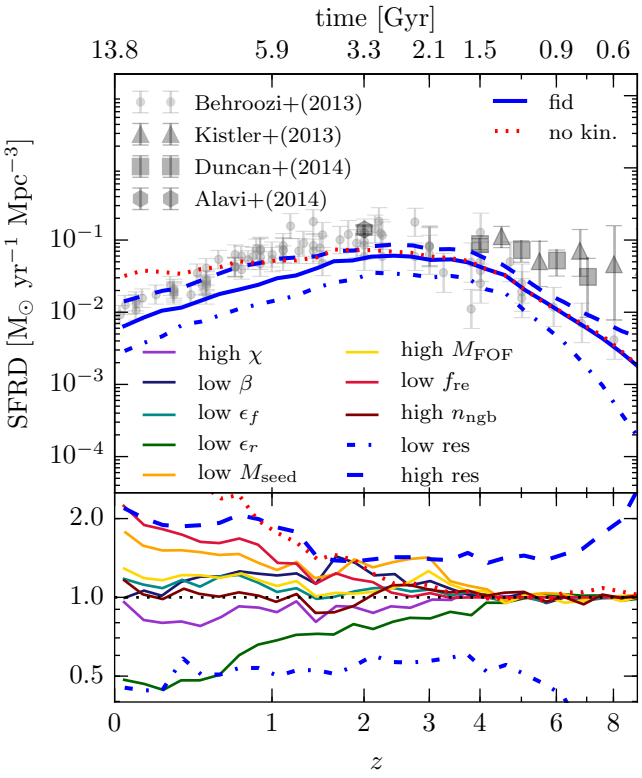

Figure 5.8: SFRD as a function of redshift. The grey dots, triangles, squares and hexagons are observational data from Behroozi et al. (2013a,a), Kistler et al. (2013), Duncan et al. (2014) and Alavi et al. (2014), respectively. The lower panel shows the ratio of the SFRD relative to the fiducial run.

a considerable amount of thermal feedback energy that suppresses star formation, in particular in galaxies with a final halo mass $> 10^{12}\,\mathrm{M}_\odot$. At late times, from redshift $z = 2$ to the present day, the black holes switch to the low-accretion regime again, remaining in a self-regulated state in which both the stellar and AGN feedback balance cooling. The relative importance of AGN over stellar feedback depends on halo mass. While stellar feedback dominates in haloes up to the size of the Milky Way, more massive haloes are mainly regulated through AGN feedback.

The stellar mass fraction as a function of halo mass (Fig. 5.9) clearly shows the decrease in star formation efficiency with halo mass at the massive end, in good agreement with observations. We find it useful to compare the stellar mass including the diffuse intra-cluster light in the high mass end in observations and theory. In this way, we are less sensitive to the choice of the

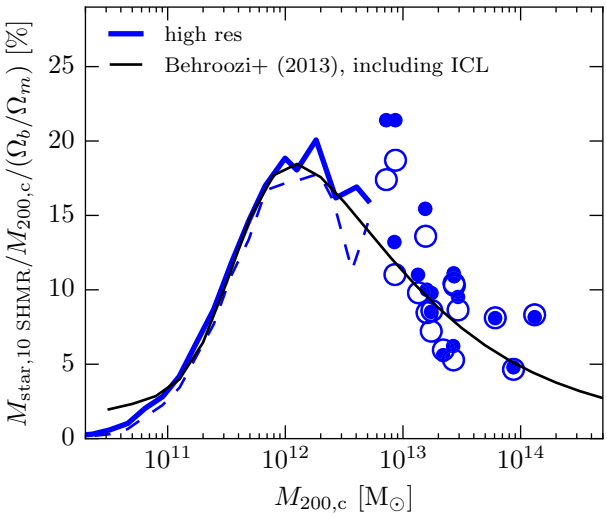

Figure 5.9: Stellar mass fraction as a function of halo mass for the high-resolution simulation. The stellar mass is calculated as the mass of all star particles within 10 stellar half-mass radii that do not belong to a subhalo. The black line is the corresponding fit to observations from Behroozi et al. (2013a,b) including the intracluster light. We use the simulation values of $\Omega_{\rm b}$ and $\Omega_{\rm m}$ for both simulation and literature data. The dashed line and open circles correspond to the same simulation data, but the halo mass $M_{\rm 200,c}$ is taken from the corresponding halo in the dark matter only simulation (see Munshi et al., 2013, for a discussion).

aperture within which stellar masses are estimated. At the high halo-mass end, the data shown here are in reasonable agreement with Kravtsov et al. (2014) who pointed out the importance of outer stellar profiles in high-mass haloes in this type of analysis. Additionally, we plot both the halo mass from the full physics simulation as well as the halo mass of the corresponding halo in the dark matter only run, where the latter, i.e. the dashed line and open circles, should be compared to the results from abundance-matching. Fig. 5.4 shows the ratio of these two masses as a function of halo mass. In particular at around $M_{\rm 200,c} \approx 10^{13}\,\rm M_\odot$ it turns out to be crucial to take this effect into account.

One of the conjectured effects of AGN is that they can prevent the most massive galaxies from being blue and star forming, instead making them red and having an old stellar population. We use *B*-*V* colour and mean stellar age (Fig. 5.10) as a measure for the efficiency of the feedback in the low accretion state to accomplish this. To probe the relevance of the

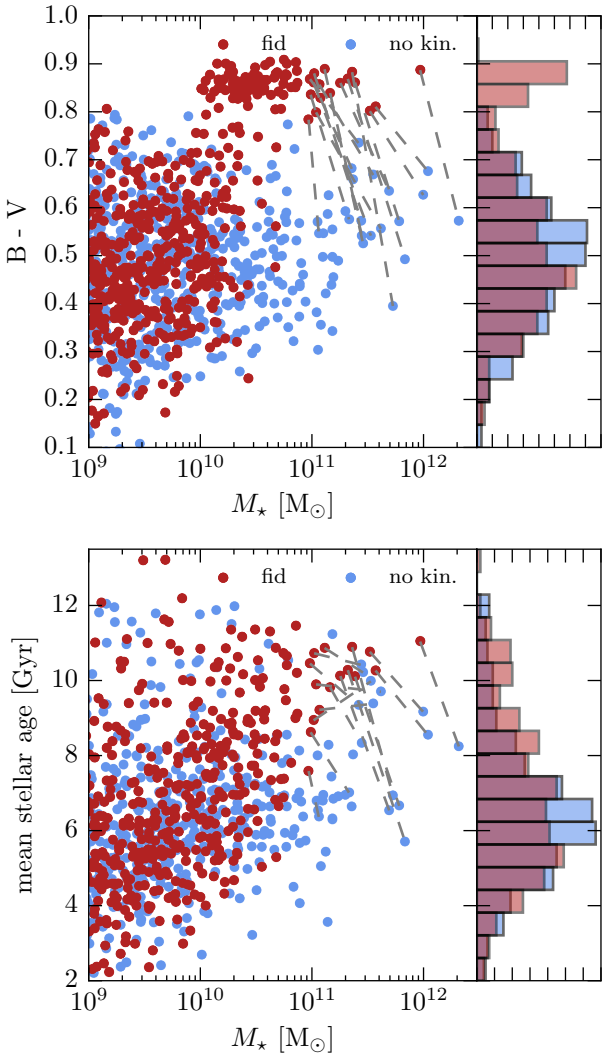

Figure 5.10: Top panel: *B*-*V* colours as a function of stellar mass within twice the stellar half mass radius. The red dots are from the fiducial simulations. The blue dots represent the haloes in the run without kinetic feedback. For the most massive systems, the dashed lines link the same haloes in the two different runs to emphasize the effect of the kinetic feedback mode on a halo-by-halo basis. The histogram on the side clearly shows the emergence of a red (larger *B*-*V* values) population of galaxies due to the kinetic feedback model. Bottom panel: mass-weighted stellar age as a function of stellar mass within twice the stellar half mass radius. Note that the choice of colours differs from the other figures.

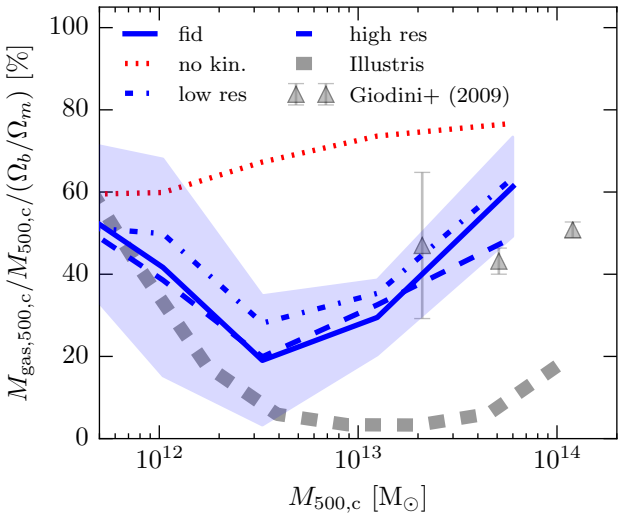

Figure 5.11: Gas mass fraction in $R_{500,c}$ as a function of halo mass $M_{500,c}$. The triangles show the binned data from Giodini et al. (2009). The dashed grey line represents the gas fractions in the Illustris simulation (Genel et al., 2014).

kinetic feedback mode for this, we compare our fiducial simulation with a simulation without the kinetic mode. The panels of Fig. 5.10 clearly show the need for this efficient mode to get 'red and dead' galaxies with old stellar populations on the massive end of the galaxy population.

Gas component

The low gas fraction of haloes around $10^{13}\,M_\odot$ has been identified as one of the main shortcomings of the Illustris simulation (Genel et al., 2014). The gathering of substantial amounts of feedback energy invoked in the bubble model of Illustris, and its explosive release once enough energy is available, does prevent the feedback energy from being quickly lost due to cooling, but it also expels a significant fraction of gas from the inner halo. This resulted in a gas fraction which is factor of a few too low in systems where the feedback is most efficient. In Fig. 5.11, we show the gas fractions within $R_{500,c}$ as a function of their mass $M_{500,c}$, obtained with our new kinetic feedback model. Reassuringly, it does not expel too much gas from the inner halo, but rather heats it via shocks and drives turbulence in the halo core, leading to an overall good agreement with observations.

To further investigate the effect of AGN feedback on the gas properties it is instructive to look at the radial profiles of the gas distribution. To this

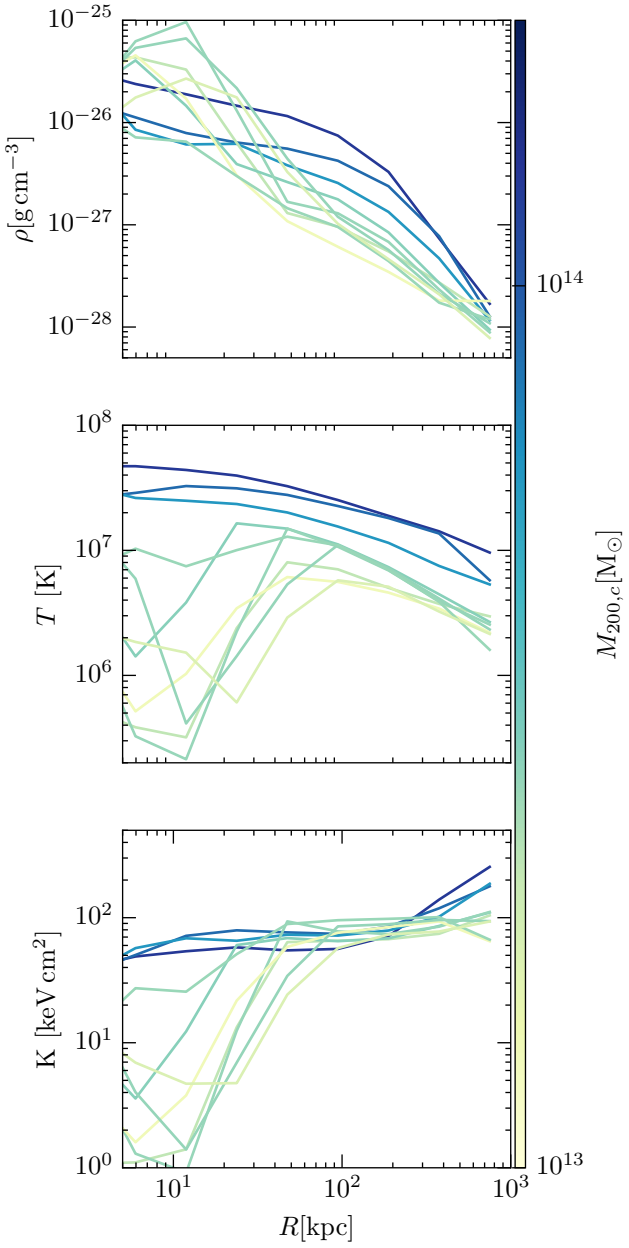

Figure 5.12: Mass-weighted density (top), temperature (middle) and entropic function (bottom) of the 10 most massive haloes in the high-resolution simulation. The line colour encodes $M_{200,c}$ of the halo.

end, we use the high resolution simulation and plot the density, temperature and entropic function profiles in Fig. 5.12. For the most massive haloes with a mass around $10^{14}\,\mathrm{M}_\odot$, the temperature profiles are almost flat in the centre and the central entropic function $K = k_\mathrm{B} T n^{-2/3}$ has a value of around $50\,\mathrm{keV\,cm^2}$. This confirms that the efficient quenching of star formation is not due to overly heating and diluting the central gas. For haloes less massive than $10^{13.5}\,\mathrm{M}_\odot$, the density profiles are more centrally peaked and the temperatures in the centres are lower, which indicates that these haloes might have some residual star formation. As the volume is relatively small, our simulations do not contain massive galaxy clusters for which we could compare the thermodynamic profiles with observations of local galaxy clusters. Such simulations of galaxy clusters and how they are impacted by different AGN models are analysed in detail in forthcoming work (Popa et al., in preparation).

5.5 Dependence on model parameters

We now investigate how robust the findings discussed in Section 5.4 are against changes in the parameters of our new black hole model. As we run identical initial conditions with several different parameter settings, we can compare their effects on a halo-by-halo basis. Figure 5.13 shows the relative changes in the gas-, stellar- and black hole masses binned with respect to halo mass, as well as the star formation rate as a function of redshift for systems with different halo mass at $z = 0$. We shall first discuss the variations due to modifications of the efficiency parameters ϵ_f and ϵ_r, and then consider the other parameters in turn.

5.5.1 Global properties

For all the investigated changes of model parameters, there is generally only a weak change in the late time accretion rate density (Fig. 5.7). At higher redshift, the seeding parameters have however a significant impact on the accretion and growth history of the black holes. In our tests, we lower the seed mass M_seed or increase the halo mass M_FOF at which black holes are seeded, which both delay black hole growth. Lowering the radiative efficiency ϵ_r leads to a higher Eddington accretion limit and therefore an increased accretion rate at $z = 5$. As soon as the accretion rate is feedback regulated, it drops back to the fiducial rate. There is also an increase in the BHARD around $z = 2$ for the simulation with low quasar threshold slope

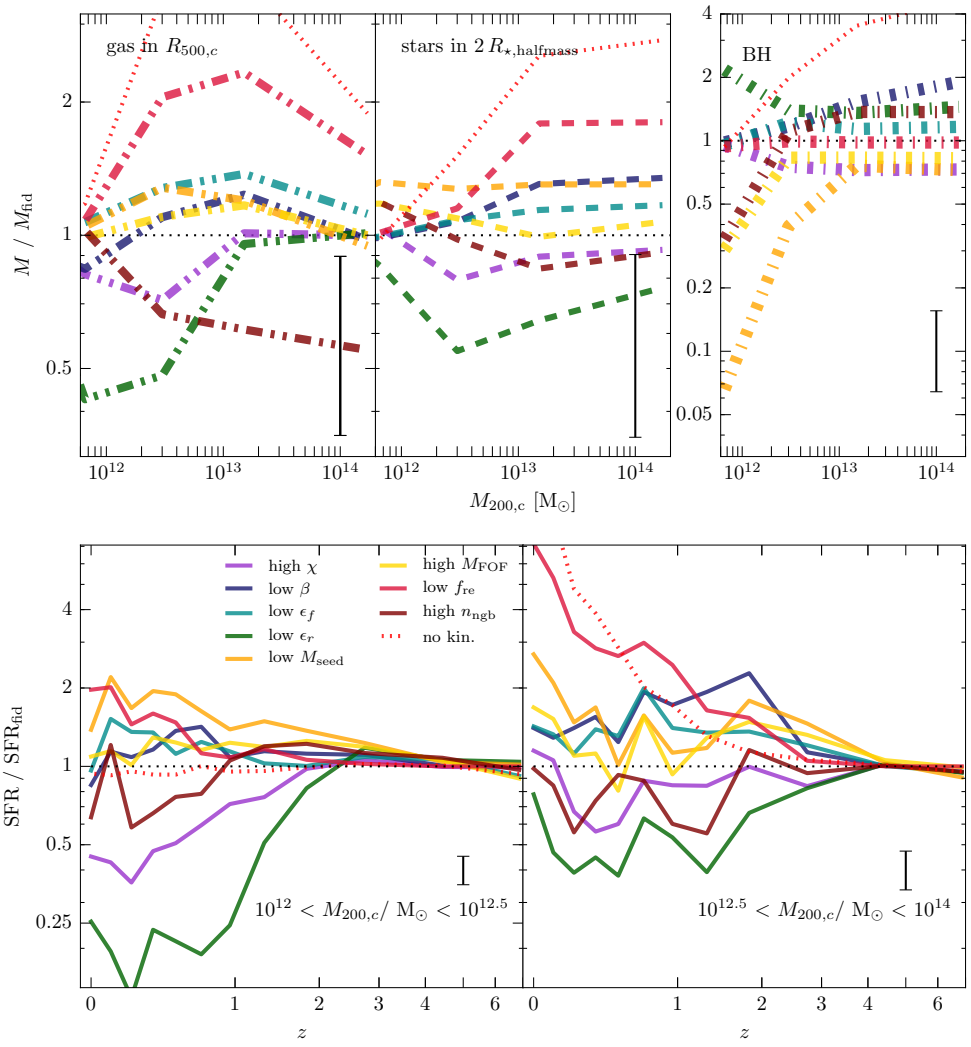

Figure 5.13: Upper panels (from left to right): gas mass in $R_{500,c}$, stellar mass in twice the stellar half-mass radius and black hole mass relative to their values in the fiducial run, compared on a halo-by-halo basis and binned as a function of the fiducial $M_{200,c}$. For clarity, we do not plot the individual scatter, but indicate with the black error bar the average scatter. Lower panels: average star formation rate of systems of different final mass (in the fiducial run) in units of their star formation rate in the fiducial simulation at a given redshift, on a halo-by-halo basis as a function of redshift. The error bar indicates the uncertainty of the mean.

β. This can be explained by a delayed transition to kinetic feedback for the black hole population.

We now focus on the change in the SFRD for different parameter settings, shown in Fig. 5.8. The most significant variations occur for the simulations with modified values of $M_{\rm seed}$, ϵ_r or f_{re}. Changes in these parameters manifest themselves in the global SFRD after redshift $z = 4$, and the effect increases at later times. However, it is also evident that a factor of 2 change in spatial resolution has a stronger impact on the global SFRD than a factor of 4 change in any of the black hole parameters. The significant decline in SFRD for a lower ϵ_r can be explained by the increased accretion rate due to the lower feedback energy per accreted mass. The over-massive black holes in turn have a significantly larger impact on the star formation rate in the host galaxies. This will be further investigated in Section 5.5.2.

5.5.2 Halo-by-halo comparison

Efficiency parameters

The feedback efficiency $\epsilon_{\rm f,}{}_{kin}$ is defined as the fraction of accreted rest mass energy that appears kinetically in the kinetic wind mode. Lowering this efficiency by a factor of 4 reduces the amount of feedback energy, which leads to an increase in the gas fraction and stellar mass, in particular in the high-mass systems. Having a higher gas fraction and star formation rate indicates that the central gas is denser and has lower temperatures than in the fiducial run. This leads to slightly increased black hole masses. Overall, the effect of this drastic change in kinetic feedback efficiency is rather small, which can be explained by the self-regulated nature of the feedback cycle.

The radiative efficiency ϵ_r determines how much of the accreted mass is converted to AGN luminosity in the quasar mode. To achieve a reduction of feedback energy for all black holes independent of accretion mode, we also reduce $\epsilon_{\rm f,kin}$ in the corresponding test. Lowering the overall feedback efficiency by a factor of 4 also increases the Eddington limit by the same factor, which leads to a significantly faster growth of the black holes (bump at $z = 5$ in Fig. 5.7), but leaves the injected feedback energy for a black hole accreting at that limit constant, given the same black hole mass. As the black holes accrete more, they become more massive and have therefore a more significant impact on their surroundings. This increases the quenching in all systems and expels gas from Milky Way-sized galaxies. As the mass of the black hole increases, the threshold for them to be in the kinetic feedback mode also increases; i.e. more energy is injected in this mode. This might

be an additional amplifying factor for the low gas fractions and the efficient quenching of these systems. The fact that a lowering of the quasar-threshold has similar effects (see below) indicates that this is indeed the case.

Accretion rate dependences

The quasar threshold χ determines whether a black hole is associated with the low or high accretion rate state. This means that in our test simulation (higher χ) the Bondi accretion estimate is four times higher when it transitions from the high accretion state to the low accretion state. This seems to have no effect on the initial growth of the black holes, which indicates that the black holes easily exceed the threshold at early times and accrete most of their mass in the high accretion state. At lower redshift, however, the average Eddington rates decrease to a level where the increase of the threshold by a factor of four matters. As our model involves a mass dependence of χ, the higher Eddington rate threshold can also be interpreted as a lowering of the black hole mass for which, at a fixed Eddington factor, a black hole transitions between thermal and kinetic feedback modes. As the black hole mass correlates with halo mass, this means that the mass scale at which black holes are predominantly in the kinetic mode is effectively shifted to lower masses. And because the kinetic feedback mode is comparatively more efficient at quenching a halo, this explains the dip in gas and stellar mass at around $3 \times 10^{12}\,\mathrm{M}_{\odot}$. The lowered black hole masses above this mass scale can be explained by the fact that the black holes only grow significantly in the quasar mode. When the kinetic mode is switched on earlier, the black holes end up systematically less massive, provided they reach the transition threshold in the first place.

The slope β influences the adopted scaling of the Eddington ratio with black hole mass for setting the transition between quasar- and kinetic mode. Reducing it by a factor of four as done in our test means that low mass black holes (below $10^8\,\mathrm{M}_{\odot}$) will be found more often in the kinetic mode, and higher mass black holes more often in the quasar mode, compared to our default run. This explains the relative increase in black hole mass towards high mass haloes, keeping in mind that black holes predominantly grow in the quasar mode. Knowing that the quasar mode is less efficient at quenching, this also explains the larger stellar masses for high-mass systems as well as the fact that the additional stars form mainly at higher redshift, at the time when the haloes are delayed in switching to the kinetic mode.

Black hole seeding parameters

The black halo seed mass $M_{\rm seed}$ is the initial mass given to the black holes when they are inserted in newly emerging haloes. If the black holes begin their evolution with smaller masses as in our test, their growth time-scale is considerably longer, because the Bondi accretion rate scales as $\dot{M}_{\rm Bondi} \propto M_{\rm BH}^2$. This means that the black holes grow significantly later, as more gas needs to accumulate in the halo centres to start a rapid growth. This delayed growth implies that the black holes in $10^{12}\,{\rm M}_\odot$ systems have not yet ended their rapid accretion phase at $z = 0$. This explains why the mean black hole mass is an order of magnitude below the mass in the fiducial run. For the more massive haloes, the black holes formed earlier and already had enough time to catch up; however, they are still about 25% less massive. The delayed growth also implies that there is less feedback energy injected into the galaxies at all times, which increases the star formation rates and the stellar masses over the whole mass range of haloes. The fact that the gas fraction is comparatively higher, particularly at $3 \times 10^{12}\,{\rm M}_\odot$, is again due to the mass-dependent switch from quasar to the kinetic mode. As the black holes are less massive in the modified run, they mostly remain in the quasar mode, keeping a relatively high gas fraction while the corresponding black holes in the fiducial run have switched to kinetic feedback which lowers the gas fractions by $20 - 30\%$.

The halo mass $M_{\rm FOF}$ at which black holes are seeded has a similar effect: lowering $M_{\rm seed}$ and increasing $M_{\rm FOF}$ both lead to a delayed black hole growth. In our test simulation, we place the black holes only in haloes that have grown a factor of 4 more in mass compared to our fiducial simulation. This produces similar trends, but the effect is much weaker. The delay of the black hole growth is not as severe as in the previous case, which can be explained by the accretion rate dependence $\dot{M}_{\rm Bondi} \propto M_{\rm BH}^2$, which means that the black holes have a 16 times higher accretion rate for the same gas properties but are seeded in four times more massive haloes. This means that they do not need a similarly severe change of gas properties as the low mass seeds to eventually grow into the Eddington limited accretion phase.

All in all, the dependence on the seeding prescription reveals one of the most important theoretical uncertainties of the black hole modelling in cosmological simulations. The formation and the early growth of SMBHs are observationally as well as theoretically very poorly understood (see Volonteri, 2010, for a review). However, as we just showed, they have a major impact on the evolution of galaxy properties. One way to reduce these uncertainties from a simulation point of view is to constrain the model with

observations that also crucially depend on the seeding and early growth phase, such as the low mass end of the $M_{\rm BH} - \sigma$ and $M_{\rm BH} - M_{\rm bulge}$ relations, or the abundance of high redshift quasars.

Other parameter dependences

The reorientation factor f_{re} determines the energy threshold at which a new kinetic feedback event along a new direction is injected. The specific parameterization we adopted sets the magnitude of the velocity kicks relative to the local dark matter velocity dispersion. The remarkable thing about lowering this parameter by a factor of 4 is that the black hole mass does not change at all, while the star formation rate and correspondingly the stellar masses as well as the gas mass increase significantly. This means that this factor substantially changes the efficiency of the kinetic feedback and therefore the properties of the high-mass haloes. The fact that the burstiness of the feedback has such a dramatic impact is in agreement with other works (e.g. Le Brun et al., 2014; Sijacki et al., 2015) and can in our case be explained by the fact that the velocity kicks directly determine the strength of the resulting shocks as well as the post shock temperature. The faster the velocity, the higher the post-shock temperature and the lower the cooling losses during the process. With the adopted parameters, we reach velocity kicks up to several tens of thousand $\mathrm{km\,s^{-1}}$ in the largest haloes, which are realistic speeds for winds from optically thin accretion discs. This means that one could in principle try to constrain this parameter, both theoretically from small-scale GRMHD simulations of hot accretion flows (Yuan et al., 2015) as well as from observations (Tombesi et al., 2014).

The number of neighbours $n_{\rm ngb}$ sets the number of cells used for the density, sound speed and velocity estimates, as well as for the injection region of feedback energy. Increasing this number means that, at a fixed resolution, the radius out to which the gas properties are probed increases. As the gas properties change with radius, the accretion rate estimate tends to change as well. This has important consequences for the black holes in low mass systems, because here the black hole growth is delayed when we average over a four times larger number of cells, which can be seen in Fig. 5.7. This leads to a lower black hole mass for galaxies in $10^{12}\,\mathrm{M}_\odot$ haloes. For more massive haloes, the black hole mass increases by about 25%, and correspondingly lower gas and stellar mass fractions are reached. However, Fig. 5.7 also reveals a higher BHARD between redshifts $z = 3$ and 0.5, which is responsible for the more massive black holes. This is because the quasar mode distributes the energy over more mass, leading to lower

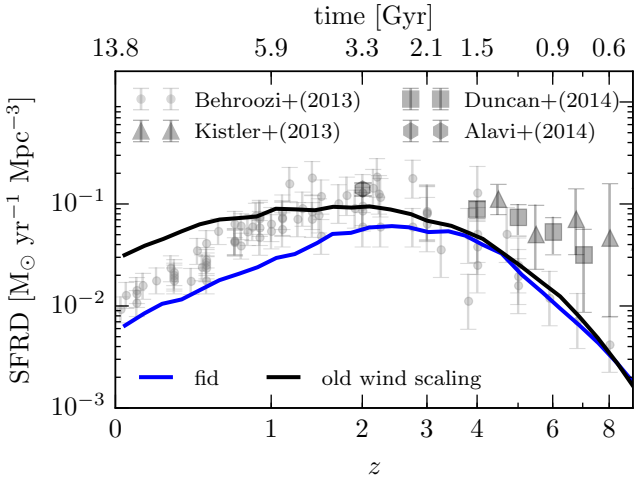

Figure 5.14: SFRD versus redshift for the fiducial run and a run with the old wind scaling.

temperatures in the heated gas and higher radiative cooling losses. In the kinetic mode, the larger injection volume means that we implicitly increase the burstiness of the model, which increases its efficiency at quenching star formation. This explains the lower star formation rate for the most massive haloes and the lower star formation rate after $z = 1$ for haloes in the mass range $10^{12}\,\mathrm{M}_\odot < M_{200,c} < 10^{12.5}\,\mathrm{M}_\odot$.

5.6 Changes in the wind model

In addition to the changes in the AGN model, we have implemented some alterations to the stellar wind feedback compared to the model described in Vogelsberger et al. (2013). They are introduced to address some of the shortcomings of the Illustris simulation in low-mass systems, such an excessive number of galaxies with blue star forming rings, a too high stellar mass fraction in systems with halo masses $M_{200,c} < 10^{11.5}\,\mathrm{M}_\odot$ and a too mild decline in SFRD at low redshift (Vogelsberger et al., 2014c). We summarize these changes here for completeness and refer to Pillepich et al. (2017b) for a detailed discussion.

First, we now use an isotropic wind injection with 10% of the energy injected thermally and not the bipolar, purely kinetic approach employed in the Illustris project (Vogelsberger et al., 2014b). Furthermore, we slightly changed the wind velocity. We still use the scaling with local dark mat-

ter velocity dispersion as in equation 14 of Vogelsberger et al. (2013), but introduce an additional redshift dependent factor $[H_0/H(z)]^{1/3}$, which effectively yields a scaling of the wind velocity that depends purely on halo mass. Additionally, we set a minimum wind velocity of $v_{\rm min} = 350\,{\rm km\,s^{-1}}$ to prevent unrealistically high mass-loading factors in low-mass haloes. Taken together, the equation for the wind velocity is hence

$$v_w = \max\left[\kappa\,\sigma_{\rm DM}^{\rm 1D}\,(H_0/H(z))^{1/3}\,, v_{\rm min}\right]. \tag{5.15}$$

We choose the parameters such that the wind velocity of a given halo equals that of the previous Illustris model at a redshift $z \simeq 5$, implying that it then tends to increase slightly towards lower redshifts compared to Vogelsberger et al. (2014c). This is the main reason for the different scaling of the SFRD with redshift (Fig. 5.14). The minimum wind velocity is partially responsible for the sharp decline in star formation efficiency towards lower masses in Fig. 5.9. A summary of the adopted wind parameters and a comparison to those used in Illustris is given in Table 5.2.

Moreover, we use a higher baseline wind energy for gas of primordial abundance but now reduce the available energy with metallicity Z on the grounds that higher metallicity galaxies plausibly have larger radiative cooling losses of the supernova energy. A similar factor has also been used in the Eagle project (Schaye et al., 2015). The energy of the winds is reduced by a factor

$$f + (1-f)/\left[1 + (Z/Z_{\rm red})^{\gamma}\right] \tag{5.16}$$

where $f = 0.25$, $\gamma = 2$ are free parameters and $Z_{\rm red} = 0.002$. This effectively lowers the efficiency of the supernova feedback in metal-enriched galaxies, and since most of the stars form there, the total injected wind energy is comparable to Illustris. However, the metal dependence leads to a higher relative efficiency of the wind feedback in low-mass systems, suppressing them more in comparison to Milky Way-sized galaxies, which is an effect that seems required by the observational data and the low abundance of luminous dwarf galaxies.

All in all, our stellar feedback is somewhat stronger than in the Illustris simulation (Vogelsberger et al., 2014c), particularly at late times and in low-mass haloes. At high redshift, the strength of the stellar feedback is comparable, which also means that the $z = 0$ black hole masses are not significantly affected by the changes.

Parameter	New	V13	Note
κ	7.4	3.7	Same velocity at $z \approx 5$
egy_w /egy_{0w}	3.6	1.09	Reduced through metallicity Dependence

Table 5.2: Comparison of wind parameters with Vogelsberger et al. (2013, 2014a) (V13).

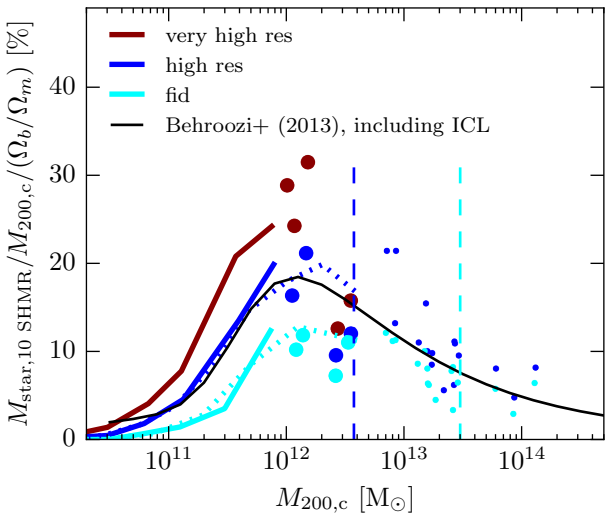

Figure 5.15: Stellar mass fraction as a function of halo mass for simulations of different resolution. The dotted lines and small dots indicate the simulations with $30\,h^{-1}$Mpc side length, the solid lines and large dots test simulations with $7.5\,h^{-1}$Mpc side length. Note that the colour coding is different compared with results presented in the main text. The dashed vertical lines are at $5\times10^5\,(m_{\mathrm{gas}}+m_{\mathrm{dm}})$, i.e. these haloes would have 5×10^5 simulation particles within $R_{200,\mathrm{c}}$ if their baryon content was equal to the cosmic baryon fraction.

5.7 Numerical convergence

Achieving numerical convergence is a major challenge for full physics cosmological volume simulations due to the multi-scale, multi-physics nature of the problem. Normally, convergence cannot be fully established, and hence the lack thereof represents an additional source of systematic uncertainty in the predictions. We attempt to quantify the magnitude of resolution effects here, using simulations with a box side length of $7.5\,h^{-1}$Mpc with $2 \times 384^3, 2 \times 192^3$ and 2×96^3 simulation particles and cells (dark matter + gas). In this small simulation volume, only low-mass haloes form, which makes an analysis of the global SFRD and BHARD meaningless, but it still allows us to estimate the uncertainties due to numerical convergence for the galaxies that happen to be present, especially because we can simulate them at resolutions higher than our standard high-resolution simulation with box side length of $30\,h^{-1}$Mpc.

We focus on the bias due to resolution effects at the low-mass end, as this regime has been the most severely affected when increasing the resolution in the Illustris simulation (Pillepich et al., 2014, fig. A1, upper panel). This is not surprising as the AREPO code ensures that the individual gas cells have approximately equal mass and consequently the number of gas cells within a halo decreases rapidly with decreasing halo mass. Fig. 5.15 shows the star formation efficiency as a function of halo mass for different resolutions. The vertical dashed lines correspond to $5 \times 10^5 (m_{\rm gas} + m_{\rm dm})$, which, depending on the gas fraction in the halo, translates to a few times 10^5 gas cells within $R_{200,c}$. Decreasing the number of gas cells in a halo, individual cells become so large that they average over significant regions of the ISM, producing lower average densities and hence longer gas consumption time-scales. This results in a numerically suppressed star formation rate and, over time, in a lower stellar mass fraction. As this convergence issue is present for the haloes at the peak of the star formation efficiency, it also manifests itself in the global SFRD.

A second resolution problem, related to black holes, is the radius h over which the gas properties are averaged to derive an accretion rate estimate and to inject the feedback energy. We adjust this radius such that it contains approximately a constant number of cells $n_{\rm ngb}$. In Section 5.5, we presented the effect of increasing $n_{\rm ngb}$ by a factor of 4. Changing the particle number per dimension by a factor of 2, h also decreases, assuming constant $n_{\rm ngb}$. This means that the volume over which the gas properties are averaged is a smaller volume at the centre of the galaxy and therefore usually denser, which leads to higher accretion rate densities, as seen in Fig. 5.7. If we increased $n_{\rm ngb}$ to keep approximately the same volume to average over,

this effect would be smaller, but we would not benefit from the increased spatial resolution in the centre. For our simulation sequence, we aimed for a compromise by increasing $n_{\rm ngb}$ by a factor of 2 whenever the particle number per dimension is increased by a factor of 2.

5.8 Conclusions

In this study, we introduced a new model for SMBH growth and the associated feedback in cosmological simulations of galaxy formation. We distinguish between a state of high and a state of low accretion, which are associated with pure thermal or pure kinetic feedback, respectively. Unlike in previous work, we omit an artificial boost factor α in the accretion rate estimate to account for unresolved ISM structure, and instead adopt an accretion rate given by the Bondi formula throughout. The feedback energy in the high accretion rate state is released with a continuous thermal feedback prescription. In the low accretion state, we instead use pulsed kinetic feedback injection in random directions, which is the primary new element adopted in this study. We have shown in idealized simulations that this mode drives shocks in the surrounding gas, thermalizing a significant fraction of the AGN energy within a Myr.

In simulations of cosmological structure formation, our new model is able to significantly reduce star formation in the most massive haloes, leading to a stellar mass fraction in excellent agreement with observations, without overly heating and diluting the central gas. This resolves one of the central problems in the Illustris simulation. It also leads to massive galaxies with a red, old stellar population, living in haloes that have gas fractions in agreement with observations.

The star formation efficiency peaks in haloes with a few times $10^{12}\,{\rm M}_\odot$, in very good agreement with abundance matching expectations once we use the halo masses from dark matter only simulations for the comparison, as also used in the fits to observations on which the abundance models are based. The key to sustained quenching of massive haloes in our simulations is to ensure that the black holes in these systems transition to the low accretion state and remain in it for most of their subsequent evolution. We encourage this behaviour by employing a BH mass-dependent Eddington ratio threshold for determining the accretion state, making it progressively easier for high-mass black holes to be in the kinetic mode. Once the black holes reach this mode, the more efficient coupling of the kinetic feedback and the self-regulated nature of gas accretion will typically keep the black holes accreting at low Eddington rates. Brief interruptions of this with

episodes of quasar activity, triggered for example by significant inflows of cold gas during a galaxy merger, may nevertheless occur.

We analysed the impact of each of our black hole model parameters on the cosmic star formation rate history and the stellar, gas and black hole masses. To this end we varied each parameter by a factor of 4 and carried out otherwise identical simulations to our default model. We found that most of the parameters do not alter the global properties severely, but some of them can have a significant impact on a subset of haloes and galaxies over particular mass ranges. In these cases, the changes can be readily understood in terms of the tightly self-regulated nature of black hole growth that occurs in our models. We would like to emphasize that the assumption of the existence of a low accretion rate state with efficient kinetic feedback is more important than the precise value of any of the model parameters.

The new AGN feedback model discussed here significantly improves the galaxy formation model explored previously in the Illustris simulation project, particularly at the high-mass end of the galaxy population. It therefore promises to be an excellent starting point for a new generation of hydrodynamical simulations of galaxy formation that allow much improved predictions for the bright end of the galaxy population, and for groups and clusters of galaxies, as well as their thermodynamic scaling relations. Future work with this model in high-resolution simulations of galaxy formation could potentially also shed light on the physical origin of observed centrally concentrated radio emission (Baldi et al., 2015, 2016), AGN driven nuclear outflows (Förster Schreiber et al., 2014; Tombesi et al., 2014) and related phenomena.

6

Black hole feedback in simulations

In this chapter, I describe the connection between SMBH and their host galaxies in the large-volume cosmological magnetohydrodynamical simulation IllustrisTNG. This work is submitted for publication in Monthly Notices of the Royal Astronomical Society and available online as a pre-print under arXiv:1710.04659.

6.1 Introduction

It is now well established that most if not all massive galaxies host supermassive black holes (SMBHs). If the growth of SMBHs is dominated by gas accretion, the corresponding energy released per unit volume is quite substantial (Soltan, 1982) and matches the integrated emission from the quasar luminosity function, supporting that this is the primary growth channel. If only a small fraction of the released energy couples to the gas of the host galaxy, the impact of SMBHs on their host galaxies can be significant (King, 2003; Di Matteo et al., 2005). The relatively tight scaling relations between supermassive black hole masses and properties of their host galaxies (e.g. Ferrarese and Merritt, 2000) furthermore point towards a mutual influence on each other, thereby establishing some form of co-evolution.

Recent simulations that model the formation of massive galaxies rely on feedback effects from SMBHs to reproduce the properties of massive galaxies (Springel et al., 2005a; Bower et al., 2006; Croton et al., 2006; Dubois et al., 2013; Martizzi et al., 2014; Choi et al., 2015; Somerville and Davé, 2015). However, even with presently available computational resources, it is not possible to model these effects from first principles. Instead, sub-resolution models are applied which typically measure gas properties at resolved scales, translate them via simplified analytic models to a black hole accretion rate, and inject feedback energy with some assumed efficiency into the surrounding gas on resolved scales. While these models contain tuneable parameters

which are usually set such that the simulations reproduce the stellar properties of simulated galaxies and the relation between black hole mass and stellar mass, the calculations are able to *additionally* reproduce a variety of other (unconstrained) observable properties of active galactic nuclei (AGNs) (e.g. Sijacki et al., 2015; Volonteri et al., 2016). In this way, such models allow detailed insights into how the different growth and feedback processes of galaxies and their SMBHs are intertwined.

Observationally, a number of important properties of the SMBH population can be inferred. First, the luminosity function, which can be measured up to high redshift, gives insights about the mass growth via gas accretion over cosmic time (Hopkins et al., 2007; Shankar et al., 2009; Ueda et al., 2014; Lacy et al., 2015). Using estimates for black hole masses and accretion rates, it is also possible to infer the distribution of Eddington ratios (Schulze et al., 2015; Georgakakis et al., 2017), or alternatively, the specific accretion rate distribution (Aird et al., 2017a,b), which constrains the state of the accretion disc over cosmic time (Weigel et al., 2017b). Furthermore, relating the SMBH properties to the galaxy properties, e.g. the SMBH mass with the bulge mass (or velocity dispersion) of the host (Magorrian et al., 1998; Tremaine et al., 2002; Häring and Rix, 2004; McConnell and Ma, 2013; Kormendy and Ho, 2013; Graham and Scott, 2015; Reines and Volonteri, 2015; Savorgnan et al., 2016), indicates a connection between the two objects. Yet it remains debated whether this is an indication for the feedback regulated nature of SMBH growth (King, 2003), or just a manifestation of a common assembly history (Peng, 2007; Hirschmann et al., 2010; Jahnke and Macciò, 2011; Anglés-Alcázar et al., 2013).

The comparatively accurate description of hierarchical structure formation obtained by cosmological simulations can be used to turn the statistical properties of the predicted SMBH population into powerful tests of the SMBH model adopted in a simulation (Di Matteo et al., 2008; DeGraf et al., 2012; Hirschmann et al., 2014; Sijacki et al., 2015; Volonteri et al., 2016), even though the observations are subject to large uncertainties and selection biases. In addition, it is possible to exploit the rich information contained in simulations to test specific scenarios for the SMBH – galaxy coevolution, such as the role of major mergers (Springel et al., 2005a; Di Matteo et al., 2005; Hopkins et al., 2006; Sparre and Springel, 2016, 2017; Pontzen et al., 2017) or the interplay with other effects, like stellar feedback in galaxies of specific masses (Dubois et al., 2015; Habouzit et al., 2016, 2017; Bower et al., 2017).

In high-resolution simulations of representative cosmological volumes (Vogelsberger et al., 2014c; Schaye et al., 2015; Dubois et al., 2016; Khandai et al., 2015; Anglés-Alcázar et al., 2017a; Tremmel et al., 2017b) it is possible

to track the evolution of SMBHs and their host galaxies through cosmic time and relate the host galaxy transformations, for example quenching or changes in morphology, to the SMBH properties. Using a large number of simulated systems, it is possible to obtain statistical information about the diversity of the evolutionary paths of galaxies, which can reveal new insights about the SMBH – galaxy coevolution.

In this paper, we use "The Next Generation Illustris" (IllustrisTNG) simulations to study the co-evolution of SMBHs and galaxies. In the introductory papers of the project (Marinacci et al., 2017; Naiman et al., 2017; Nelson et al., 2017; Pillepich et al., 2017a; Springel et al., 2017), we have shown that IllustrisTNG reproduces a diverse range of observables remarkably well, in particular massive galaxies have significantly improved stellar (Nelson et al., 2017; Pillepich et al., 2017a; Genel et al., 2017) and gas properties (Vogelsberger et al., 2017; Marinacci et al., 2017; Weinberger et al., 2017a) compared to the predecessor Illustris simulation (Vogelsberger et al., 2014c; Genel et al., 2014). Based on this encouraging progress, we study the origin of the quenched, massive central galaxies and the role of SMBHs for their evolution. We focus in particular on the energetics of the AGN feedback and investigate the role of (major) mergers for quenching, black hole mass growth, and AGN activity.

In Section 6.2, we present the IllustrisTNG simulations and briefly describe the numerical methods and astrophysical models used. The galaxy population of IllustrisTNG in terms of star formation rate and energetics of different feedback modes is presented in Section 6.3, and linked to the SMBH population in Section 6.4. We discuss the results in Section 6.7, and conclude in Section 6.8.

6.2 The Illustris TNG Simulations

The simulations used in this study are part of the IllustrisTNG project (Marinacci et al., 2017; Naiman et al., 2017; Nelson et al., 2017; Pillepich et al., 2017a; Springel et al., 2017). These are high-resolution simulations of cosmological structure formation in a representative part of the universe. The primary simulation used for the present analysis has a side length ~ 300 comoving Mpc (TNG300) and follows the formation and evolution of structure governed by the laws of gravity and magnetohydrodynamics from the early universe to redshift zero. We also use a simulation of higher resolution but smaller volume (TNG100) as well as a lower resolution version of the large box (TNG300-2) to test for numerical convergence. The main numerical parameters of these simulation can be found in Table 6.1. For a

Simulation name		TNG100	TNG300	TNG300-2
N_{cells}		1820^3	2500^3	1250^3
L_{box}	[Mpc]	111	303	303
$m_{target,gas}$	[10^6 $M_\odot$]	1.4	11	88
m_{dm}	[10^6 $M_\odot$]	7.5	59	470
$\epsilon^{z=0}_{DM,stars}$	[kpc]	0.75	1.48	2.95

Table 6.1: Primary simulation parameters of the IllustrisTNG runs analysed in this study. The TNG300 simulation is used in the main study, while TNG100 and TNG300-2 are used in Section 6.6 for a resolution study. For a more extensive overview of the parameters of the simulation suite we refer to Nelson et al. (2017, their Table A1).

more detailed list of parameters, see Nelson et al. (2017, their Table A1).

6.2.1 Initial conditions

The simulations were initialised at redshift $z = 127$ using the Planck Collaboration et al. (2016) cosmological parameters (i.e. a matter density $\Omega_m = 0.3089$, baryon density $\Omega_b = 0.0486$, dark energy density $\Omega_\Lambda = 0.6911$, Hubble constant $H_0 = 67.74$ km s^{-1} Mpc^{-1}, power spectrum normalisation $\sigma_8 = 0.8159$ and a primordial spectral index $n_s = 0.9667$) and the Zel'dovich approximation for the initial displacement field, which is applied to glass initial conditions (White, 1994). The simulations start out with a uniform magnetic seed field with comoving field strength of 10^{-14} Gauss. A suite with several different box sizes at different numerical resolutions were computed as part of IllustrisTNG.

The highest resolution version of TNG300, which has the largest box size, contains 2500^3 dark matter particles and the same number of gas cells in the initial conditions. Additionally, we analyse a lower resolution counterpart (TNG300-2) which has the same volume but a factor of 2^3 reduced particle number, and two times worse spatial resolution with all softenings increased by a factor of 2. We furthermore analyse the TNG100 simulation from the IllustrisTNG set, which has 2×1820^3 resolution elements, and a factor of 2^3 higher mass and a factor of 2 higher spatial resolution than TNG300, but covers only a volume of $\sim 110^3$ Mpc^3 and consequently does not contain rare objects such as rich galaxy clusters.

6.2.2 Methods

The simulations are evolved with the Arepo code, i.e. using a finite-volume approach where the equations of ideal magnetohydrodynamics are solved on a quasi-Lagrangian, moving, unstructured mesh (Springel, 2010; Pakmor et al., 2011, 2016). The divergence constraint of the magnetic field is taken care of by an 8-wave Powell-cleaning scheme (Pakmor and Springel, 2013). The gravitational forces are calculated using a tree-particle-mesh method with an operator-split, hierarchical time integration, allowing for efficient calculations of gravitational forces in systems with large dynamic range in time.

We employ a cooling function using primordial and metal line cooling, a time-dependent ultraviolet background from stars and luminous AGN, prescriptions for star-formation, stellar feedback and metal enrichment, as well as a model for SMBHs, including their formation, growth and feedback effects. The approaches used in the IllustrisTNG simulations (with identical parameter choices), as well as the impact of variations of model parameters, are presented in two separate method papers, Pillepich et al. (2017b) for the stellar feedback, enrichment and the low mass end of the galaxy stellar mass function (GSMF), and Weinberger et al. (2017a) for the AGN feedback model and the high mass end of the GSMF. Here, we only briefly summarize the aspects of the model that are most relevant to this study.

6.2.3 Modelling of supermassive black holes

We identify friend of friends (FOF) groups on the fly during the simulation (Springel et al., 2001a). A SMBH with mass 1.18×10^6 $M_\odot$is seeded whenever a FOF halo exceeds a mass of 7.38×10^{10} $M_\odot$and does not yet contain a SMBH. These black holes are then accreting according to an Eddington-limited Bondi accretion rate

$$\dot{M}_{\rm Bondi} = \frac{4\pi G^2 M_{\rm BH}^2 \rho}{c_s^3}, \tag{6.1}$$

$$\dot{M}_{\rm Edd} = \frac{4\pi G M_{\rm BH} m_p}{\epsilon_r \sigma_{\rm T}} c, \tag{6.2}$$

$$\dot{M} = \min\left(\dot{M}_{\rm Bondi}, \dot{M}_{\rm Edd}\right), \tag{6.3}$$

where G is the gravitational constant, $M_{\rm BH}$ the mass of the black hole, ρ the kernel-weighted ambient density around the SMBH, c_s the kernel-weighted ambient sound speed including the magnetic signal propagation speed, m_p

the proton mass, c the speed of light, $\epsilon_r = 0.2$ the black hole radiative efficiency and $\sigma_{\rm T}$ the Thompson cross section. We emphasize that, unlike previous work (e.g. Springel et al., 2005a), this model does not use an artificial boost factor in the accretion rate. We enforce the SMBH to be located at the potential minimum of its host halos at every global integration timestep, and assume a prompt merging of SMBH binaries. Note that the SMBH merger rates, which will be discussed in this paper, are not affected by our neglect of delay times in the merging process (assuming all pairs eventually merge).

Feedback from SMBHs is injected in two different channels, where the dividing line is the accretion rate in units of the Eddington accretion limit. Whenever the Eddington ratio exceeds a black hole mass dependent threshold of

$$\chi = \min\left[0.002\left(\frac{M_{\rm BH}}{10^8\,{\rm M}_\odot}\right)^2, 0.1\right], \tag{6.4}$$

the feedback energy is injected continuously as thermal energy ('thermal mode') into the surroundings of the black holes with a rate of $\dot{E}_{therm} = 0.02\,\dot{M}\,c^2$, while for lower accretion rates the feedback energy is injected into the surroundings as pure kinetic feedback ('kinetic mode') in a pulsed, directed fashion with the rate $\dot{E}_{\rm kin} = \epsilon_{f,\rm kin}\,\dot{M}\,c^2$, where

$$\epsilon_{f,\rm kin} = \min\left(\frac{\rho}{0.05\,\rho_{\rm SFthresh}}, 0.2\right), \tag{6.5}$$

and $\rho_{\rm SFthresh}$ is the star formation threshold density. The factor (6.5) means that we assume that at low environmental densities, the coupling of the AGN feedback energy to the surroundings becomes weak. We employ a similar scaling in the thermal mode, where we use the approach of Vogelsberger et al. (2013) and reduce the accretion rate by a factor of $\left(P_{ext}/P_{ref}\right)^2$ whenever $P_{ext} < P_{ref}$. P_{ext} is the kernel weighted pressure of the gas surrounding the black hole and P_{ref} is a reference pressure defined in Vogelsberger et al. (2013, their equation 23).

6.2.4 Feedback energetics

The stellar feedback parametrisation is described in Pillepich et al. (2017b, their section 2.3.2). The energy of the stellar feedback is given by their equation 3, which can be rewritten as

$$\dot{E}_{stellar} = 3.41 \times 10^{41} erg\, s^{-1} \left(\frac{\mathrm{SFR}}{\mathrm{M}_\odot\, yr^{-1}} \right) f(Z), \tag{6.6}$$

$$f(Z) = 1 + \frac{3}{1 + (Z/0.002)^2}, \tag{6.7}$$

where Z is the metallicity (metal mass fraction) and SFR the star formation rate in a gas cell. With this parameterisation, $f(Z)$ is usually close to unity, but for very low metallicity it can increase up to a value of 4 to account for reduced cooling losses in this regime, which happens preferentially at high redshift for low-mass systems.

The maximum AGN feedback energy rate (i.e. not limited due to the lower efficiencies at low surrounding densities) can be written as

$$\dot{E}_{thermal\,AGN} = 5.66 \times 10^{42} erg\, s^{-1} \frac{\dot{M}}{5 \times 10^{-3}\, \mathrm{M}_\odot\, \mathrm{y} r^{-1}}, \tag{6.8}$$

$$\dot{E}_{\mathrm{max.}\,kinetic\,AGN} = 5.66 \times 10^{43} erg\, s^{-1} \frac{\dot{M}}{5 \times 10^{-3}\, \mathrm{M}_\odot\, \mathrm{y} r^{-1}}, \tag{6.9}$$

where the different reference value for gas accretion compared to the star formation rate in equation (6.6) is inspired by the black hole mass–stellar bulge mass relation (Kormendy and Ho, 2013). Comparing equations (6.6) and (6.8), it becomes clear that a system which is located on the black hole mass – stellar bulge mass relation will have experienced significantly more energy injection from AGN feedback than from stellar feedback (provided the contribution from black hole seeds to the SMBH mass is subdominant).

However, this does not automatically imply that AGN feedback is the dominant feedback channel in these galaxies, i.e. is mainly responsible for regulating the star formation rate in these systems. The feedback efficiency depends on the precise way the feedback energy is injected into the surrounding medium (e.g. Rosdahl et al., 2017; Smith et al., 2017). In the employed stellar feedback model, cells are attributed a probability (proportional to the star formation rate) to launch a 'wind particle' with a given velocity that is temporarily hydrodynamically decoupled. The particles recouple to the gas as soon as they reach a cell with a density lower than 0.05 times the star formation threshold (Springel and Hernquist, 2003; Pillepich et al., 2017b). This means that the coupling of the stellar wind feedback to the gas is slightly non-local and hence different from the AGN feedback, which is directly injected to the surrounding gas cells. Therefore, relating the energetics of the different feedback channels to their overall importance

for galaxy formation requires a careful analysis of the simulation results and is not possible from simple analytic considerations alone.

What is clear, however, is that the kinetic AGN feedback channel is significantly more efficient than the thermal AGN feedback mode, which is one of the key features of the employed AGN feedback implementation. Besides the higher efficiency parameter in the kinetic mode (equations 6.8 and 6.9), this is due to the fact that a pulsed injection of feedback energy (as used in the kinetic mode) heats up the affected gas to higher temperatures and consequently reduces the cooling losses compared to a continuous injection (used in the thermal mode).

6.2.5 Definition of quenched galaxies

Throughout this paper, we analyse the main, central halos (excluding satellites) of the TNG300 simulation, the largest volume simulation box of the IllustrisTNG project. We mainly focus on halos with redshift $z = 0$ stellar masses (measured within twice the stellar half mass radius) larger than $10^{10.5}\,\mathrm{M}_\odot$, and use the relation

$$\log \mathrm{SFR}_{\mathrm{SFMS}} = -7.4485 + \log M_* \times 0.7575 \tag{6.10}$$

adopted from (Ellison et al., 2015), where SFR is the star formation rate in $\mathrm{M}_\odot\ \mathrm{yr}^{-1}$ and M_* the stellar mass within twice the stellar half mass radius in $\mathrm{M}_\odot$, to define the star forming main sequence (SFMS) at redshift $z = 0$. We define quenched galaxies as systems with an instantaneous star formation rate (measured from gas cells within the same radius) of at least 1 dex below $\mathrm{SFR}_{\mathrm{SFMS}}$, independent of their redshift. We consider all systems above this cut as star-forming. The use of the instantaneous star formation rate measured from the star-forming gas cells (given as an output of the model of Springel and Hernquist, 2003) is helpful for this study, as it just depends on the present state of the gas in the galaxy and not on its history. However, we also emphasize that this instantaneous star formation rate is not an observable quantity and it can vary on rather short timescales, which increases the scatter in its distribution function. Therefore, we leave a detailed comparison to the numerous observations in this area (e.g. Noeske et al., 2007; Rodighiero et al., 2011; Wuyts et al., 2011; Whitaker et al., 2012; Speagle et al., 2014; Renzini and Peng, 2015; Schreiber et al., 2015; Tasca et al., 2015) to future work, and use the star formation rate in this paper only as a proxy for classifying a galaxy to be either in a quenched or star-forming state.

6.3 The galaxy population

Because of its large volume and high number of resolution elements, the TNG300 simulation contains an unprecedented number of resolved galaxies in a single hydrodynamic simulation, ranging from isolated Milky Way-sized galaxies to massive brightest cluster galaxies. In particular, there are 19090 redshift $z = 0$ galaxies with a stellar mass larger than $10^{10.5}\,\mathrm{M}_\odot$. In this paper, we focus mainly on these massive galaxies that host a supermassive black hole and are significantly affected by its feedback energy. In particular, we want to answer the question how the massive end of the galaxy population was driven off the SFMS and became quiescent, and how this relates to observables of black hole activity.

6.3.1 Feedback at different galaxy masses

To understand the behaviour of galaxies of different masses in the simulation, we first show the energetics of the gas phase of these systems. To this end, we select central galaxies in different redshift $z = 0$ stellar mass bins and trace back their main progenitor. Throughout this paper, we define the stellar mass as the mass within twice the stellar half-mass radius. As in previous work (e.g. Nelson et al., 2017; Genel et al., 2017), we use the merger-tree algorithm described in Rodriguez-Gomez et al. (2015) to track the central galaxies identified by the SUBFIND algorithm (Springel et al., 2001a) to high redshift. In the following, we refer to a 'galaxy' as the subhalo identified by SUBFIND. We calculate the instantaneous cooling rate of all non-star-forming cells in the galaxy[1] as well as the instantaneous feedback energy rates of stellar feedback, thermal AGN feedback and kinetic AGN feedback in the respective subhalos. The stellar feedback is calculated via the star formation rate and gas metallicity on a cell-by-cell basis using equation (6.6), and the AGN feedback energy by using the black hole accretion rate and applying the appropriate formulae for either thermal or kinetic feedback given in Section 6.2.3, using the most massive SMBH in the subhalo (using all black holes in a subhalo instead does not change the results). Note that an individual SMBH can only be in either of the two modes, which means that the average, i.e. the sum over all active SMBH divided by the total number of galaxies in this stellar mass bin, can suddenly drop to zero whenever the SMBHs in these subhalos are not in the corresponding mode.

[1] The thermodynamic state of all star forming cells is described by an 'effective equation of state' model (Springel and Hernquist, 2003), which makes it difficult to define an unambiguous cooling rate for them.

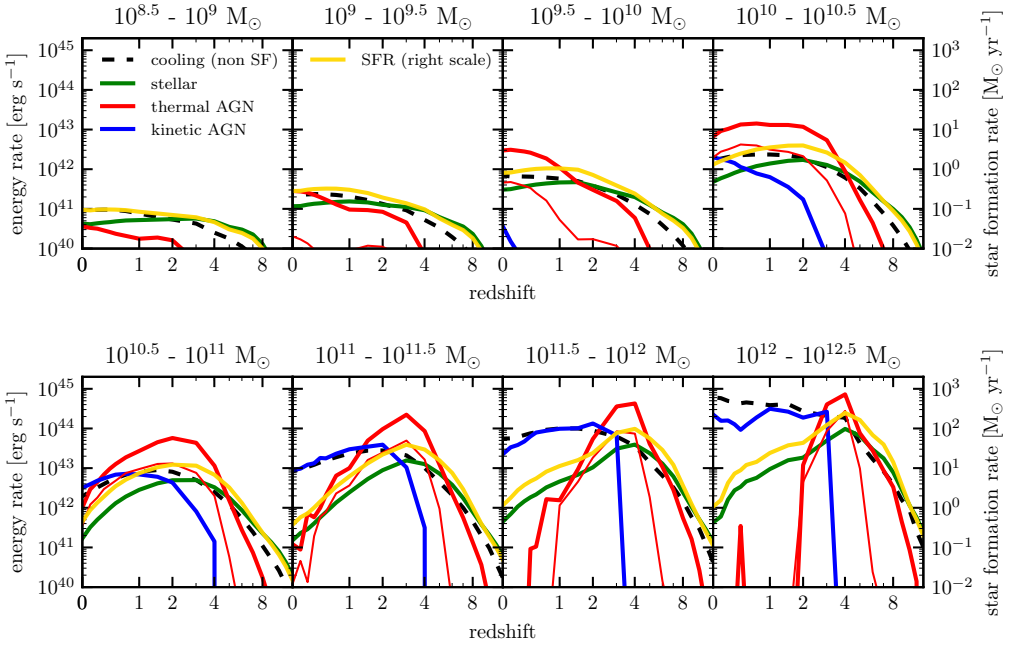

Figure 6.1: Average instantaneous feedback energy rates (thermal AGN feedback in red, kinetic AGN feedback in blue, stellar feedback in green) and non-star-forming gas cooling rate (dashed black) within each galaxy as a function of redshift for central galaxies with different redshift $z = 0$ stellar mass. The yellow line indicates the star formation rate in $M_\odot$ yr^{-1} (right scale). Independent of galaxy mass, stellar feedback always dominates at high redshift, followed by thermal AGN feedback. In massive halos, the kinetic AGN feedback takes over at late times, approximately compensating the cooling losses and keeping the star formation rate low. The thin line indicates the effective thermal AGN feedback energy rate (see text), which is substantially lower than the nominal value, in particular in low-mass systems. Note that there is an additional heating channel via gravitational infall of gas, which we do not account for here.

We show the redshift evolution of the average energy rates and the average star formation rate in the corresponding galaxies in Figure 6.1. For galaxies of all masses, stellar feedback dominates at high redshift. For the lowest mass bin shown here ($10^{8.5}$ – 10^{9} $M_{\odot}$), stellar feedback (green line) stays the dominant feedback channel until redshift $z = 0$, while in the most massive galaxies, the thermal AGN feedback (red line) becomes dominant over stellar feedback already at $z = 6$. Note that the stellar feedback becomes sub-dominant in part because the AGN feedback reduces star-formation, so one needs to be aware that the AGN feedback indirectly reduces the stellar feedback energy. At low redshifts, the AGN feedback energy dominates for all but the least massive galaxies shown here. We emphasise, however, that this does not necessarily mean that it is the most important feedback channel in these systems. In particular, in our model, the stellar feedback energy, by construction, only couples to non-star forming gas which has comparably low density and consequently low cooling losses, while the thermal AGN feedback is continuously injected around the SMBH. As the region around the SMBH can contain very dense, star forming gas, large fractions of the injected feedback energy can be radiated away immediately. We expect the kinetic AGN feedback to be less affected by this effect due to the kinetic, pulsed injection of momentum, and therefore to be more efficient than the thermal mode at equal energy rates.

The cooling rate in the non-star-forming phase (dashed black line) is of the same order as the feedback energy of stellar and kinetic AGN feedback. The thermal AGN feedback energy can significantly exceed this rate without having any dramatic effect on the star formation rate (yellow line), indicating that large amounts of this energy are lost in the star forming gas phase. To illustrate this point further, the thin red lines in Figure 6.1 show the effective thermal AGN feedback energy rate. This quantity is calculated by summing up the contribution of thermal AGN feedback of each individual gas cell in the surroundings of a SMBH. We then subtract the cooling losses if the gas cell is in the star-forming regime. If the cooling losses exceed the feedback energy in a particular cell, its contribution to the feedback energy neglected. This means that we only take the energy injection in gas cells that are not in the star-forming regime in the subsequent timestep into account. The energy difference between the nominal and the effective thermal AGN feedback is de facto never injected, as the respective gas cells stay on the effective equation of state, thus have a pre-defined pressure given their density. In this way, we obtain the actual thermal feedback energy that is not immediately lost to cooling, which is a more realistic estimate of the feedback energy from this channel.

Thus, thermal AGN feedback energy only becomes an important feed-

back channel in galaxies with stellar masses of around $10^{10}\,M_\odot$. Wherever the kinetic AGN feedback takes over, i.e. in galaxies more massive than $10^{10.5}\,M_\odot$ at low redshift, the star formation rate is significantly reduced and the shape of the star formation rate curve no longer follows the cooling curve, but is significantly suppressed. We now investigate how this suppression in star formation rate impacts the specific star formation rate – stellar mass diagram and we examine on a galaxy-by-galaxy basis what triggers the quenching initially.

6.3.2 Star formation in galaxies

Figure 6.2 shows the specific star formation rate (defined as the star formation rate divided by the stellar mass) within twice the stellar half mass radius as a function of stellar mass for all central galaxies in the simulation. At redshift $z = 0$, there is a well-defined star forming population up to stellar masses of around $5 \times 10^{10}\,M_\odot$, following the dashed line which denotes the observed SFMS from Ellison et al. (2015). Starting at $3 \times 10^{10}\,M_\odot$, there is a significant population of galaxies off the SFMS. The different panels show the same range of specific star formation rate vs stellar mass at redshifts $z = 4$, 2, 1 and 0. At redshift $z = 4$, the bulk of the galaxy population at all masses is star-forming. At $z = 2$, a significant fraction of the high-mass galaxies have already quenched, while the main sequence still shows a very high level of specific star formation rate. This changes towards $z = 1$, where the lower mass population also has a larger low specific star formation rate tail, which is even more pronounced at $z = 0$.

The colour coding in this plot shows the fraction of systems that experienced a major merger ($> 1:4$ in stellar mass ratio[2]) since redshift $z = 4$. For the $z = 0$ massive galaxies, most systems experienced at least one major merger. Looking at the onset of the population of quenched galaxies at $z = 2$, however, a significant fraction of the quenched galaxies have not undergone such a major merger, and no significant enhancement of mergers can be seen in this population relative to the SFMS galaxies. This means, in particular, that a large fraction of galaxies that are quenched by $z = 2$ did not undergo a major merger since $z = 4$, which indicates that a scenario in which a system needs to undergo a gas-rich major merger leading to a starburst in order to trigger subsequent quenching by AGN activity (Di Matteo et al., 2005; Springel et al., 2005a; Hopkins et al., 2008b) does not

[2]We measure the merger masses as the stellar mass of the galaxy at the time of maximum mass of the low-mass progenitor (see Rodriguez-Gomez et al., 2015).

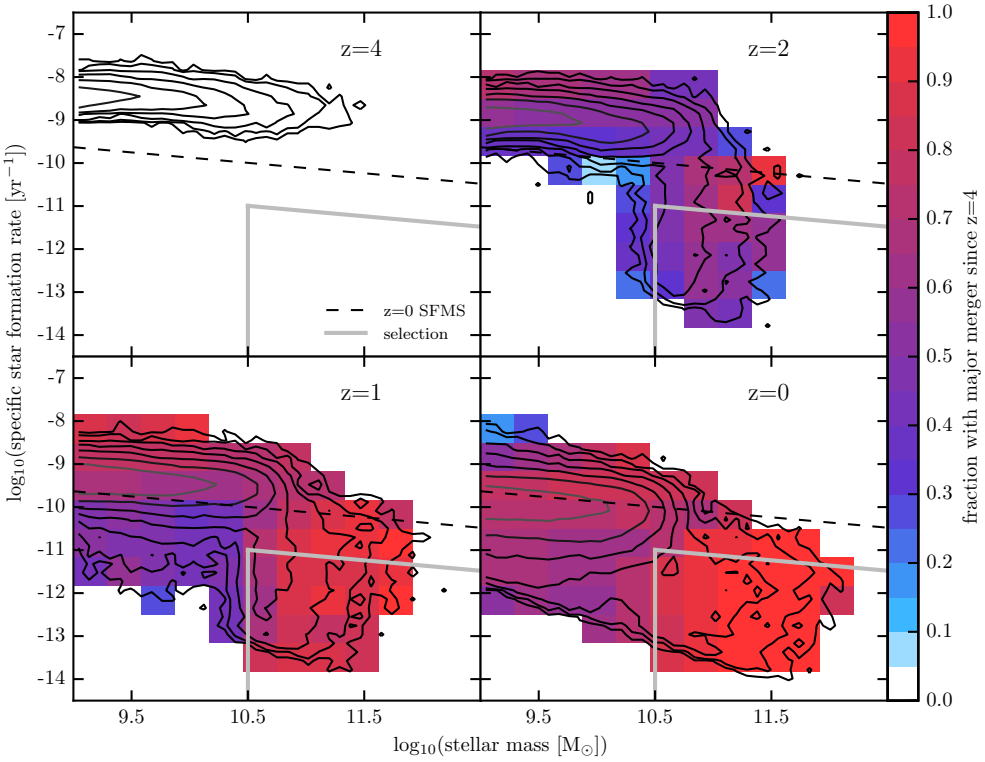

Figure 6.2: Specific star formation rate vs stellar mass in the TNG300 simulation. The contours indicate number density (the outermost contour encloses a density of $10^{-5.5}$ comoving Mpc^{-3} dex^{-2}, the other contours show a density increase by 0.5 dex each) in this plane, the colours indicate the fraction of systems in the corresponding bin which have had a major merger (subhalo stellar mass ratio >1:4) since $z = 4$, i.e. within the past ~ 12.3 Gyr. The dashed line shows the star forming main sequence at $z = 0$, adopted from Ellison et al. (2015). Most massive, quenched galaxies, have undergone at least one major merger by $z = 0$. However, this is not the case for quenched galaxies at higher redshift, where, e.g. at $z = 2$, only about half of the quenched galaxies have undergone at least one major merger. Therefore, major mergers cannot be the sole reason for quenching. The grey lines indicate the selection for quenched massive central galaxies.

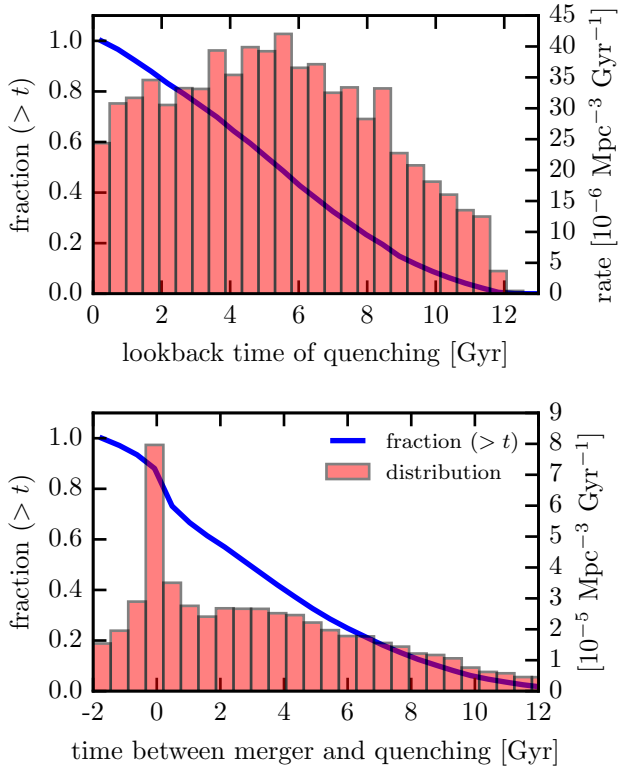

Figure 6.3: *Top panel*: Distribution of the lookback time when the (last) quenching happens for more than 17000 quenched central galaxies with a redshift $z = 0$ stellar mass larger than $10^{10.5}$ $M_\odot$ and a star formation rate at least 1 dex below the star forming main sequence. *Bottom panel*: Distribution of time between last quenching and last major merger prior to quenching (see text for precise definition). The scale of the histogram is shown on the right axis, while the cumulative distribution function is shown on the left axis.

apply to all quenched galaxies in IllustrisTNG (but it might still do to a sub-population).

To investigate this further, we select all central galaxies more massive than $10^{10.5}\,M_\odot$ in stars and that are at least 1 dex below the SFMS (equation 6.10) at redshift $z = 0$. Because of the large volume of the simulation, we find more than 17000 such systems. After tracing the main progenitor branch back in time, we define the (last) time of quenching as the snapshot after they were located above this selection threshold for the last time[3]. The distribution function of the quenching times is shown in the top panel of Figure 6.3. We then identify major mergers prior to the time of quenching and measure the time between the last merger and the quenching. The resulting distribution function of this time difference is shown in Figure 6.3, bottom panel. We note that we perform this analysis in post-processing on 100 snapshots which are roughly equally spaced in scalefactor, which gives a time-resolution of around 200 Myr at low redshift. In practice, we also include mergers that, according to the merger-tree algorithm, happen up to 2 Gyr after quenching, as these not yet merged galaxies might have tidal interactions with the host, which can cause AGN activity. Increasing this time does not change the result. There is an excess of systems that had experienced a recent merger prior to quenching, but, more significantly, a tail which extends all the way to 12 Gyrs. This means that for the majority of the quenched galaxies in IllustrisTNG, we cannot relate their quenching to a particular major merger event.

To determine what happens during quenching, we use the identified quenching events and evaluate the time-averaged AGN feedback energy injection during the period in which the galaxies transition to the quenched population. Technically, we derive this quantity by using the cumulative energy injected in the thermal and in the kinetic AGN mode (these are kept track of in the simulation and are part of the output for every SMBH) from all SMBHs in a given galaxy at the snapshot directly after quenching. We then use the SMBH merger tree to identify all progenitors of those SMBHs in the last snapshot where the host galaxy was still star forming, i.e. the star formation rate was larger than 0.1 times the corresponding observed $z = 0$ SFMS value (equation 6.10), and subtract the cumulative energy up to this snapshot from the final one. We then divide the remaining energy differences by the time elapsed between the two snapshots (typically around 200 Myr), and therefore get an average feedback energy rate.

We plot the cumulative distribution function (CDF) of this average feedback rate, i.e. the fraction of systems with a feedback energy lower than

[3]The precise value of the threshold does not change the conclusions drawn here.

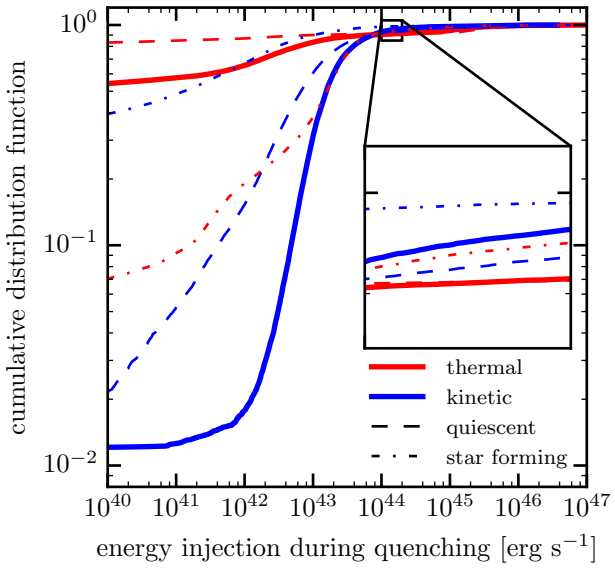

Figure 6.4: Cumulative distribution function of the average energy injected between the last snapshot when galaxies are found above 0.1 times the SFMS and the first time below this threshold. We consider the same galaxies here as in Figure 6.3. Note that the spacing between two snapshot outputs is around 200 Myr. The dashed and dash-dotted lines measure the same quantity for a sample of quiescent and star forming galaxies, respectively, with the same distribution in redshift as the quenching events.

the given value, both for the thermal (solid red line) and kinetic (solid blue line) modes, in Figure 6.4. From this figure, it becomes clear that more than 90% had an average kinetic AGN feedback energy larger than $10^{42.5}\,\mathrm{erg\,s^{-1}}$, whereas more than 50% of the galaxies had an average thermal feedback energy of less than $10^{40}\,\mathrm{erg\,s^{-1}}$. We speculate that the $1-2\%$ of galaxies without significant kinetic feedback are redshift $z = 0$ central galaxies that were satellites at quenching, but leave an explicit confirmation of this to future work.

Additionally, we select a sample of star forming and a sample of quenched galaxies with the same redshift $z = 0$ mass cut and the same redshift distribution, and compare the feedback energy during star forming (dash-dotted) and quiescent (dashed) phases. The comparison shows that galaxies that are quenching have a higher kinetic AGN feedback rate than quiescent systems (except for a very small sub-population, which likely originates in an implicit mass-selection effect when selecting for quiescent galaxies), and that kinetic AGN feedback is energetically unimportant for more than half of the

star-forming systems even in these high mass systems ($> 10^{10.5}\,M_\odot$). We therefore conclude that kinetic mode AGN feedback causes the quenching (as well as quiescence) of massive central galaxies in IllustrisTNG.

By construction, it becomes easier for the AGN to enter the kinetic mode once the SMBHs are massive (around $10^8\,M_\odot$) and have a low accretion rate relative to the Eddington limit (Weinberger et al., 2017a). To study the connection between quenching and the supermassive black hole mass, we plot the star formation efficiency (SFE), defined as the star formation rate divided by the gas mass in twice the stellar half mass radius, as a function of black hole mass. We bin the distribution, colour-coded by average stellar over black hole mass, in the top panel of Figure 6.5. In case there is more than one black hole in the galaxy, we use the mass of the most massive one. The grey line indicates the average star formation efficiency.

There is a sharp increase in the SFE with stellar mass for galaxies with black holes with a mass close to the seed mass, as well as a steep drop above $\sim 2 \times 10^8\,M_\odot$. At these high masses, there is also a significant number of galaxies with zero star formation rate which do not enter this plot. We note, however, that there are also individual systems that have a SFE of around $10^{-10}\,yr^{-1}$. Apart from the highest SFE values at black hole masses of around $10^{7.5}\,M_\odot$, which seem to have a particularly low-mass black hole for their stellar mass, there is no significant trend of SFE with stellar mass in this plot. The ratio of stellar mass over black hole mass has a noticeable drop at around $10^{7.5}\,M_\odot$, with significantly under-massive SMBH at lower black hole masses due to a delayed growth of SMBHs after seeding, and a roughly constant stellar mass to black hole mass ratio of ~ 200 at higher SMBH masses, which will be discussed in the next section.

Looking at the black hole mass – stellar mass plane in Figure 6.5 (bottom panel, colour-coded by the average of the star-formation efficiency), it becomes clear that the change in star formation efficiency at black hole masses of a few times $10^8\,M_\odot$ is even more significant for systems with over-massive black holes and stellar masses around $10^{10.5}\,M_\odot$, manifesting itself in a population with zero mean star formation rate (within the contours but no colour-coding).

6.4 The connection to the black hole population

In general, the black hole mass – stellar mass relation (Figure 6.5, bottom panel) agrees well with observational data from Savorgnan et al. (2016), in

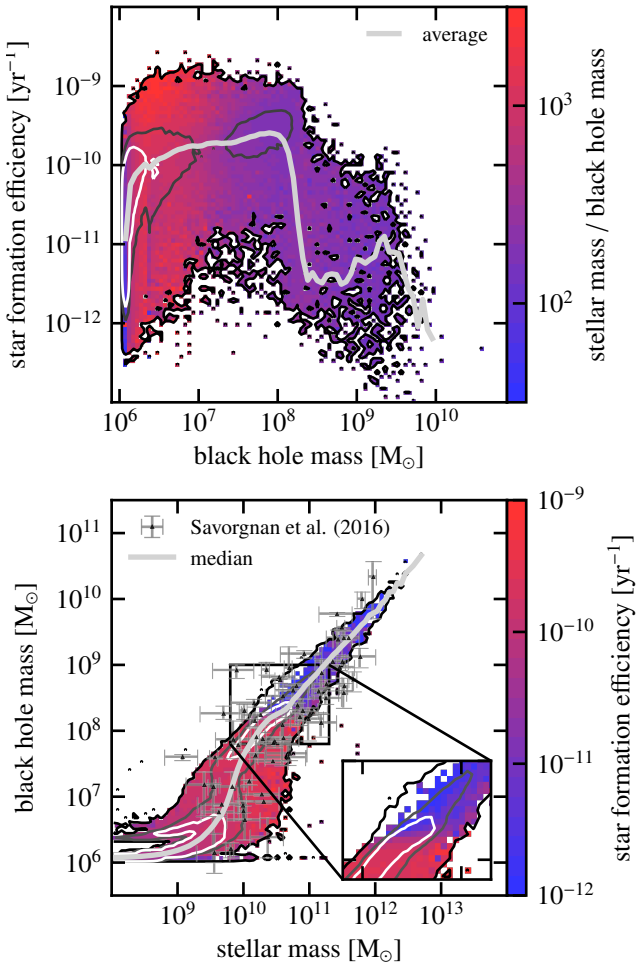

Figure 6.5: *Top panel*: 2d histogram of star formation efficiency, defined as the star formation rate divided by the gas mass within twice the stellar half mass radius, vs black hole mass, colour coded by average stellar over black hole mass. The solid grey line shows the average. *Bottom panel*: Black hole masses vs stellar mass colour coded by the star formation efficiency. The solid grey line shows the median. The symbols with errorbars are observational data taken from Savorgnan et al. (2016).

the sense that the observational data could be drawn as a subset of the simulated objects. We note, however, that due to a lack of resolution we do not perform a decomposition of each galaxy to derive a mass for the bulge component in our simulation data. This aspect, as well as the resolution dependence of both stellar (e.g. Weinberger et al., 2017a, their Appendix B) and black hole mass (Section 6.6), leads to some uncertainties in the theoretical prediction. The scatter in the simulation prediction is smaller than in the observational sample, which is a generic feature of many simulation models (e.g. Volonteri et al., 2016, their Section 3.3 and references therein). To quantify our comparison of the scatter, we added Gaussian random noise with a standard deviation equal to the average measurement errors of Savorgnan et al. (2016) to the simulation data (all in log-space), and measured the root mean square distance from the mean of the logarithm of the black hole mass over stellar mass fraction in stellar mass bins of 1 dex width (ranging from $10^9\,\mathrm{M}_\odot$ to $10^{12}\,\mathrm{M}_\odot$). The resulting scatter is around 0.4 dex at $10^{9.5}\,\mathrm{M}_\odot$ and 0.3 dex at $10^{11.5}\,\mathrm{M}_\odot$. This is significantly smaller than in the observations (0.7 dex and 0.4 dex, for $10^{9.5}\,\mathrm{M}_\odot$ and $10^{11.5}\,\mathrm{M}_\odot$, respectively). On top of this, the fact that the observational sample is highly biased means that the discrepancy is probably even more severe, because it is hard to imagine how the complete sample could have a smaller dispersion than a specific sub-selection (see e.g. Reines and Volonteri, 2015).

Another interesting prediction of the simulation is that there are no significantly over-massive black holes (more than ~ 0.5 dex above the median). A few such systems do exist in the simulation, but they are all satellite galaxies, which are excluded from the plot shown here (see also Barber et al., 2016; Volonteri et al., 2016). We now focus on the question why this is the case, or conversely, why there are no massive central galaxies that have over-massive black holes. It turns out that this question is intimately linked to how black holes grow and how this relation gets established in the first place.

6.4.1 The black hole mass growth

Figure 6.6 shows the overall contribution of accretion in thermal (red) and kinetic mode (blue), as well as the contribution of SMBH seeds to the final black hole mass. The latter is also a measure for the number of mergers of the SMBH and all its progenitors, which increases from an average of 1 for black holes less massive than $10^{7.5}$ $\mathrm{M}_\odot$ to more than 1000 for the most massive black holes in the simulation ($> 10^{10}$ $\mathrm{M}_\odot$). Consequently, the seed mass contribution of the most massive black holes reaches about 10%. Apart from the least massive black holes, accretion in the thermal

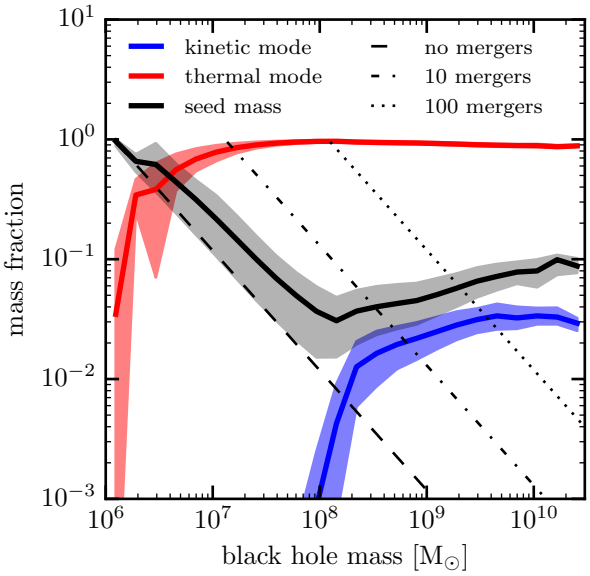

Figure 6.6: Fraction of mass growth of all progenitors of a redshift zero SMBH via different channels as a function of their redshift $z = 0$ mass. The solid lines show the averages, the shaded regions the 10th and 90th percentiles. Red and blue lines denote the growth in thermal and kinetic mode, respectively, and the black line indicates the contribution of seed masses to the final black hole mass. Note that the three lines add up to unity by construction. The intersection of the black lines with the dashed, dash-dotted and dotted lines gives the number of mergers the black hole and all its progenitors experienced. The mass growth is dominated by the thermal mode, with a 10 percent contribution from black hole seeds. Mass growth in the kinetic mode never contributes more than a few percent of a SMBH's mass.

mode always dominates the mass growth of black holes, while growth in the kinetic mode is completely subdominant at all masses.

Note however that Figure 6.6 does not distinguish whether the mass growth in the thermal mode was taking place in-situ or by merging with lower mass SMBHs, which themselves grew via accretion in the thermal mode (the number of progenitors for high-mass black holes shows that the latter scenario is plausible for them). To investigate this in detail, we plot the instantaneous accretion rates in the thermal and kinetic modes as well as the mass accretion rate through SMBH merging as a function of redshift and for SMBHs with different final masses in Figure 6.7. Note that, here, we do not use the subhalo merger tree, but rather the merger tree of

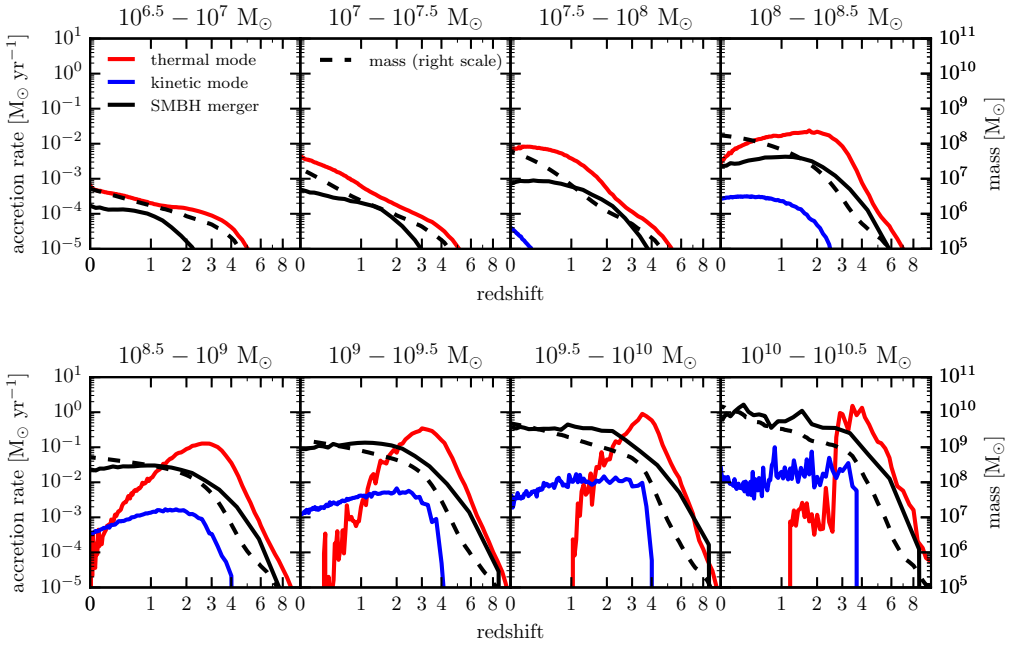

Figure 6.7: Mean mass growth history of SMBHs of different final masses, split up by gas accretion in thermal (red) and kinetic (blue) feedback mode, as well as via mergers with lower-mass SMBHs (solid black). The more massive progenitor in a SMBH merger defines the main branch of a SMBH, while the less massive SMBH contributes to the merger (solid black) line. The dashed black lines indicate the average mass of the SMBHs at a given redshift. Low mass black holes grow via accretion in the thermal mode, while high mass black holes have a rapid accretion phase at high redshift, until they reach a mass of $\sim 10^{8.5}$ M$_\odot$, and build up most of their mass via mergers at later times.

the SMBHs themselves. For every binary BH merger, we define the more massive progenitor as the main branch, while the less massive progenitor is considered to be a contribution to the mass growth via merging. We use this tree because it is, unlike the galaxy merger tree, unambiguous and does not require additional definitions apart from the one just stated (all SMBH mergers and masses at the time of merging of the two SMBHs involved are part of the simulation output). Additionally, we show the average black hole mass as a function of redshift (black dashed line, right scale) in Fig. 6.6 to emphasize the relative importance of different redshifts.

Low mass SMBHs are at all times dominated by the growth via accretion in the thermal mode, with mergers being a second, sub-dominant channel

of growth. For SMBHs more massive than $10^{8.5}$ $M_\odot$, however, the growth in the thermal mode gets increasingly suppressed as more and more SMBHs switch to the kinetic mode. The accretion rate in the kinetic mode is always subdominant, however, even with respect to the growth by mergers. Thus, switching to kinetic mode implies that the mass growth starts to become entirely dominated by mergers, because the in-situ growth via gas accretion is reduced by up to two orders of magnitude.

We therefore conclude that SMBHs more massive than $10^{8.5}$ $M_\odot$ grow most of their mass via mergers with lower mass black holes. The trend that mergers become more important for the mass growth of SMBHs is in qualitative agreement with other work (Fanidakis et al., 2011; Dubois et al., 2014), however, it is significantly more pronounced in IllustrisTNG. This is likely caused by the very efficient feedback in our simulations, and not due to more frequent mergers per se, which is discussed further in Section 6.5.

A second, interesting aspect is the average accretion rate in the kinetic mode. For SMBHs less massive than 10^9 $M_\odot$, it reaches at most $\dot{M} \approx 10^{-3}$ $M_\odot$ yr^{-1}. As the accretion rate translates to a bolometric luminosity of

$$L_{bol} \approx 1.4 \times 10^{43} erg\, s^{-1} \frac{\dot{M}}{10^{-3}\, M_\odot\, yr^{-1}}, \tag{6.11}$$

assuming a radiative efficiency of 0.2 (which is highly optimistic for a SMBH accreting at low Eddington ratios), and keeping in mind that the number density of SMBHs drops steeply for SMBHs more massive than $10^{8.5}$ $M_\odot$ (not shown here), it becomes clear that AGN in the kinetic mode are not expected to play a significant role in the quasar luminosity function, i.e. the quasar luminosity function only probes the growth in the thermal mode.

6.4.2 The quasar luminosity function

The bolometric quasar luminosity function (QLF) encodes information about the instantaneous state of accretion of the SMBH population, however, in practice it just probes the most luminous black holes. In Figure 6.8, we show the QLF at different redshifts (blue line). We also show the contribution from SMBHs in different mass bins to facilitate the theoretical interpretation. We calculate the bolometric luminosity as

$$L = \begin{cases} \epsilon_r \dot{M} c^2 & \text{for} \quad \dot{M} \geq 0.1\, \dot{M}_{Edd}, \\ \left(10\, \frac{\dot{M}}{\dot{M}_{Edd}}\right)^2 0.1\, L_{Edd} & \text{for} \quad \dot{M} < 0.1\, \dot{M}_{Edd}, \end{cases} \tag{6.12}$$

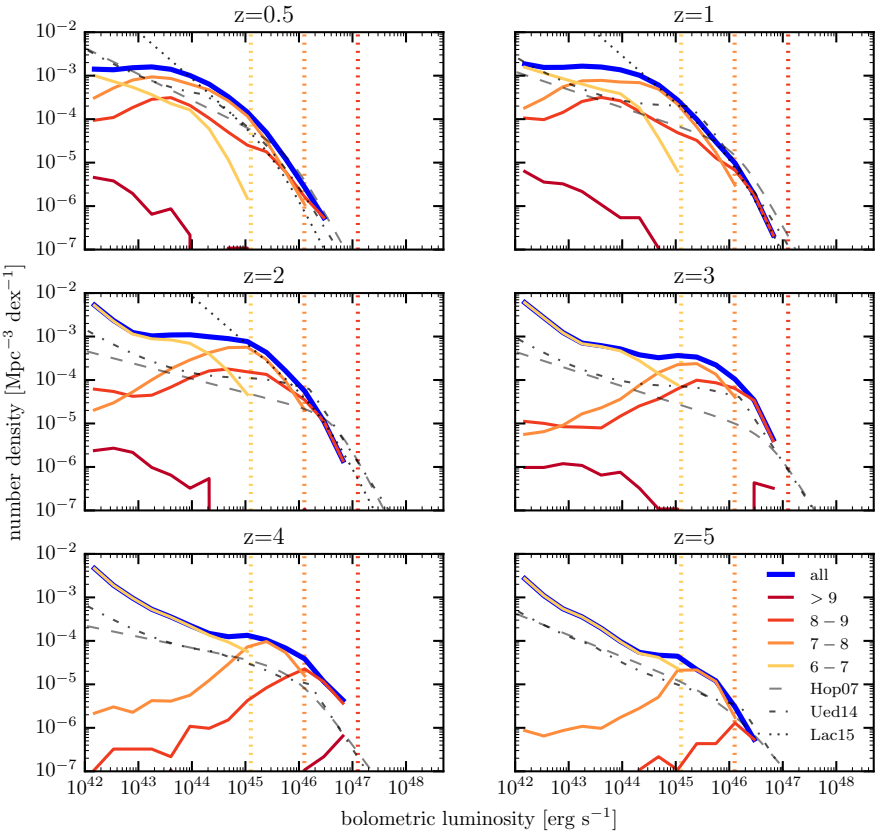

Figure 6.8: Quasar luminosity function at different redshifts (blue) as well as the contribution from SMBHs in different mass bins. The numbers in the legend signify the $\log(M_{\mathrm{SMBH}}\mathrm{M}_{\odot}^{-1})$ limits of the respective mass bin. The dotted vertical lines show the Eddington luminosity of black holes in the respective mass bin. We also show observational fits from Hopkins et al. (2007, Hop07), Ueda et al. (2014, Ued14) and Lacy et al. (2015, Lac15).

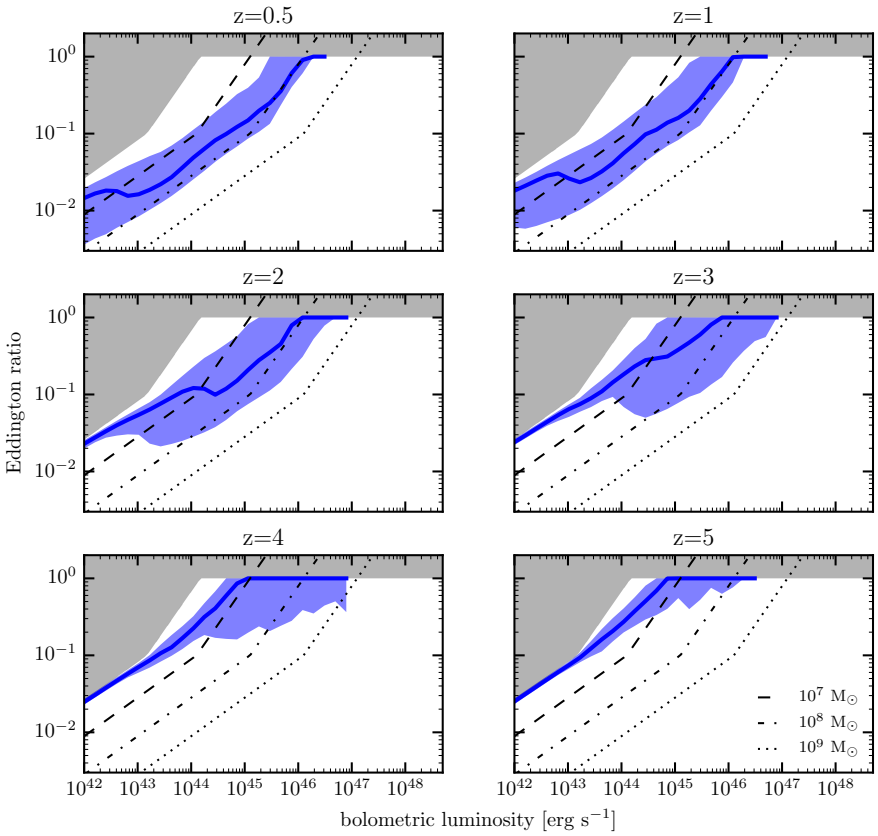

Figure 6.9: Median (solid line) and 10th to 90th percentile of the Eddington ratio distribution as a function of bolometric luminosity. The upper left corner (grey region) cannot be populated because our seed mass is $\sim 10^6$ M$_\odot$. The dashed, dash-dotted and dotted lines are lines of equal SMBH mass, 10^7,10^8 and 10^9 M$_\odot$, respectively.

assuming a decreasing radiative efficiency at low accretion rates relative to the Eddington limit (Churazov et al., 2005; Hirschmann et al., 2014). At high accretion rates, $\epsilon_r = 0.2$, consistent with the parameters used in the simulation. We do not model effects of obscuration, but present the QLF as a theoretical prediction of the simulation.

At low redshifts, up to $z = 2$, the QLF is in good agreement with the observational fit from Lacy et al. (2015), overshooting at around 10^{44} erg s^{-1} relative to Hopkins et al. (2007); Ueda et al. (2014). We note however that the exact number of Compton-thick AGN at low luminosities is uncertain (Buchner et al., 2015), thus the observational uncertainties in this regime are substantial. An additional theoretical caveat for the low-luminosity end of the QLF is that it depends significantly on the assumed radiative efficiency at low Eddington ratios (Hirschmann et al., 2014), which might be a more complicated relation than the one assumed here (Sądowski and Gaspari, 2017). Note that the conversion to bolometric luminosity used here, in particular the cut at 0.1 times the Eddington accretion rate is different from the cut used to separate the thermal from the kinetic feedback mode. It assumes that the radiative efficiency of SMBHs in the thermal mode that are accreting with lower rates than 0.1 times the Eddington limit is lower than the value we use in the simulation. We note, however, that even assuming a constant radiative efficiency of 0.2 for all SMBHs, which is clearly an upper limit, only affects the low luminosity end of the QLF but does not change the high luminosity regime. Keeping all the uncertainties in mind, we conclude that the simulation is in good agreement with observations at low redshift.

At high redshift, $z \geq 3$, the simulation over-predicts the QLF with respect to observations (Hopkins et al., 2007; Ueda et al., 2014) also at the high luminosity end. We note in particular that we compare to the results from the TNG300 simulation here, i.e. the largest volume IllustrisTNG model, because it is the only volume that probes the very rare, high-luminosity AGN. The resolution convergence of the high redshift QLF is relatively poor, with higher resolution simulations generally yielding a higher number density at fixed bolometric luminosity due to their better tracking of faster accreting black holes. This means that the discrepancy between simulation and observation at high redshift is likely alleviated by numerical resolution effects. We discuss the resolution dependence of the SMBH growth in more detail in Section 6.6.

All in all, we find that the number of luminous quasars is significantly higher in IllustrisTNG than in the Illustris simulation (Sijacki et al., 2015), in particular at bolometric luminosities between 10^{44} and 10^{46} erg s^{-1}. Future observations will need to answer the question whether IllustrisTNG

over-predicts the number of quasars in this luminosity range also at low redshifts, or whether the low-luminosity end of the real QLF is indeed steeper than originally inferred. Obtaining an answer to these questions will give significant constraints on SMBH seed formation and the growth of SMBHs in the low-mass regime.

To investigate the origin of the discrepancy at the high luminosity end of the high redshift QLF, we plot the contribution of SMBHs with different masses to the QLF, as well as the corresponding Eddington luminosities (vertical lines). As already indicated in the previous section, black holes more massive than 10^9 $M_\odot$ are unimportant for the QLF. The large number of high-luminosity SMBHs at $z = 3$ and $z = 4$ are caused by SMBHs between 10^7 $M_\odot$ and 10^9 $M_\odot$, accreting at a significant fraction of the Eddington accretion rate. We confirm this with Figure 6.9, in which we show the median (solid blue) and 10th and 90th percentiles (shaded blue) of the Eddington ratio distribution vs bolometric luminosity. The grey regions show the area of the parameter space that is not allowed by our model. More than half of the SMBHs at $z = 4$ that are more luminous than 10^{45} erg s^{-1} are experiencing Eddington-limited accretion. The only parameter that enters the Eddington luminosity is the mass of the SMBH, in particular, it is independent of the radiative efficiency. Therefore, a large number of luminous SMBHs at high redshift indicates a large number of massive SMBHs at high redshift, and an overall too early build-up of massive SMBHs at high redshift.

Comparing the Eddington ratio distribution in Figure 6.9 with the lines of equal SMBH mass (black dashed, dash-dotted and dotted lines) shows which black holes impact different regimes of the QLF. While the high luminosity end is always dominated by black holes with masses of about $10^{8.5}$ $M_\odot$, the low luminosity end is dominated by SMBHs close to the seed mass at high redshift, and by SMBHs between 10^7 $M_\odot$ and 10^8 $M_\odot$ at redshift zero. This trend shows that the choice of comparably massive SMBH seeds within the model causes accretion at considerable rates after seeding in particular at high redshift, which is different compared to the scenario described in Bower et al. (2017).

6.5 Black hole merger rates

As shown in Figures 6.6 and 6.7, mergers of SMBHs are important for their mass growth at the high mass end. We quantify the SMBH merger rates for different massive progenitors and at different redshifts in Figure 6.10. The top panel shows the SMBH merger event rates, which is also a prediction

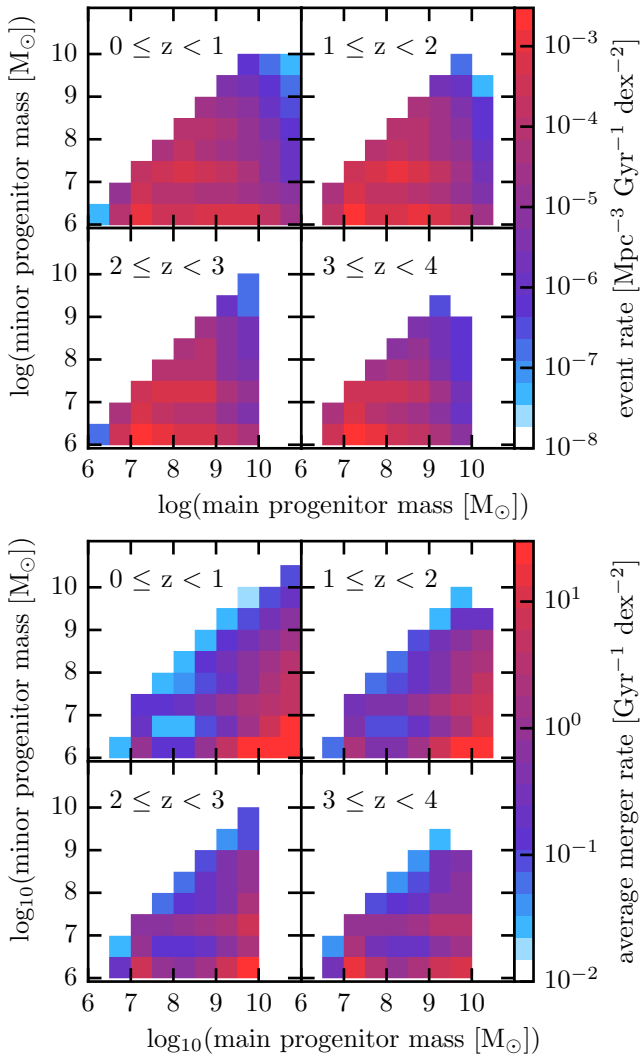

Figure 6.10: SMBH merger rates at different redshifts, event rate (top panel) and the average rate per SMBH (bottom panel). The rate per SMBH is calculated using the merger rate divided by the arithmetic mean of the mass functions at the start and end of the redshift interval. Overall, the merger rates are only mildly evolving, with slightly more frequent low-mass mergers at high redshift, but fewer high-mass mergers. Even though the event rate of high mass SMBH mergers is low, the rate per SMBH is very high.

for gravitational wave events. We note that the simulation uses an instantaneous merger approach, i.e. time delays between a galaxy merger and the merger of the associated SMBH pair are not modelled here and are assumed to be negligibly short. To predict the inspiral time accurately, higher resolution simulations with explicit dynamical friction treatments (Tremmel et al., 2017a) or more sophisticated post-processing analysis (Kelley et al., 2017a,b) would have to be employed. However, due to the remarkably constant event rate in different redshift bins, this is likely not going to alter the global event rate in a significant way.

In total, there are around 740000 SMBH merger events in the TNG300 simulation, which corresponds to a merger density of 2.7×10^{-2} Mpc^{-3} and an average event rate of 1.9×10^{-3} Mpc^{-3} Gyr^{-1}. We note that this is about a factor of two smaller than in the 100 Mpc EAGLE simulation, which contains $\sim$ 55000 SMBH mergers (Salcido et al., 2016). This difference can be explained by the seeding of less massive halos with lower mass SMBH in the EAGLE simulation (Schaye et al., 2015) and the resulting larger number of SMBHs.

Comparing the merger rates in Figure 6.10 with Salcido et al. (2016, their Figure 4), it is obvious that IllustrisTNG, unlike EAGLE, does not predict an excess of mergers of seed mass black holes with each other. In IllustrisTNG the merger growth is more evenly distributed, indicating that SMBH seeds do not have a delayed growth compared to their host systems, unlike in EAGLE. These differences in merger rates at black hole masses up to $10^{7.5}$ M$_\odot$imply that future space-based gravitational wave detectors such as eLisa (Amaro-Seoane et al., 2012) will be able to differentiate between different models for the SMBH growth. The need for observational constraints on this quantity can also be appreciated when comparing our inferred SMBH merger rate with the prediction of the formation rate of SMBH pairs from Tremmel et al. (2017a), which is 1.3×10^{-2} Mpc^{-3} Gyr^{-1} and therefore almost an order of magnitude larger than our prediction. These large discrepancies are due to the significant uncertainties about the environment in which SMBHs can form, and due to the different approaches for seeding that are adopted in different models.

The lower panel of Figure 6.10 shows the merger rate divided by the SMBH mass function of the more massive progenitor (calculated as the mean of the mass functions at the start and end point of a given redshift interval). Thus, this figure shows the average SMBH merger rate for SMBHs with a given mass. We emphasize in particular that the merger rate at the high-mass end can be quite substantial, in particular due to the contribution of mergers with small mass ratios. This means that, depending on inspiral time, high-mass SMBHs might commonly occur in binaries.

6.6 Resolution dependence

The predictive power of the SMBH demographics in cosmological simulations is mostly limited by the fact that they cannot model gas accretion from first principles. Consequently, sub-resolution models that estimate the accretion rate using gas properties at resolved scales need to be employed. The main problem with this approach is that the gas properties around a SMBH, i.e. in the centre of a halo, are resolution dependent. Usually, higher densities are reached with increased resolution due to a finer sampling of the potential minimum. As a result, the estimated mass growth rate for SMBHs also increases with resolution, which leads to a more rapid growth at higher resolution. In the Bondi-Hoyle formula for the accretion rate, which is adopted in our simulations, the mass accretion rate depends on the square of the black hole mass. This means that the black hole masses of high- and low-resolution simulations will diverge with time, even in logarithmic space. This diverging behaviour can be seen not just in the time-evolution, but also in the black hole mass–total mass and the black hole accretion rate–total mass relations, which are shown in Figure 6.11 for different redshifts. Because a black hole is seeded at a fixed halo mass, the halo mass can be considered as a measure of the evolutionary stage of a SMBH. The masses differ significantly in the different resolution runs at intermediate halo masses, due to the effect described above.

The diverging of black hole masses is however stopped by the fact that systems will become self-regulated at a black hole mass determined by global halo and galaxy properties. This means that once this regime is reached, the black hole masses in low- and high-resolution simulations tend to converge again to a common final value. We emphasize that the black hole masses for which the resolution effect is strongest corresponds to the regime of SMBHs that contribute to the high luminosity end of the quasar luminosity function (Figure 6.8). Therefore, we caution to over-interpret the results on the QLF, as the theoretical uncertainties are substantial.

6.7 Discussion

It is a widely held conjecture that the inefficiency of star formation in high mass galaxies is caused by feedback from AGN. We show in Figure 6.1 that this is indeed the case in the IllustrisTNG simulations, where kinetic AGN feedback provides a sufficient amount of energy to balance the cooling losses of the surrounding gas and thereby maintains low star formation rates.

However, this does not answer the question what triggers this low star

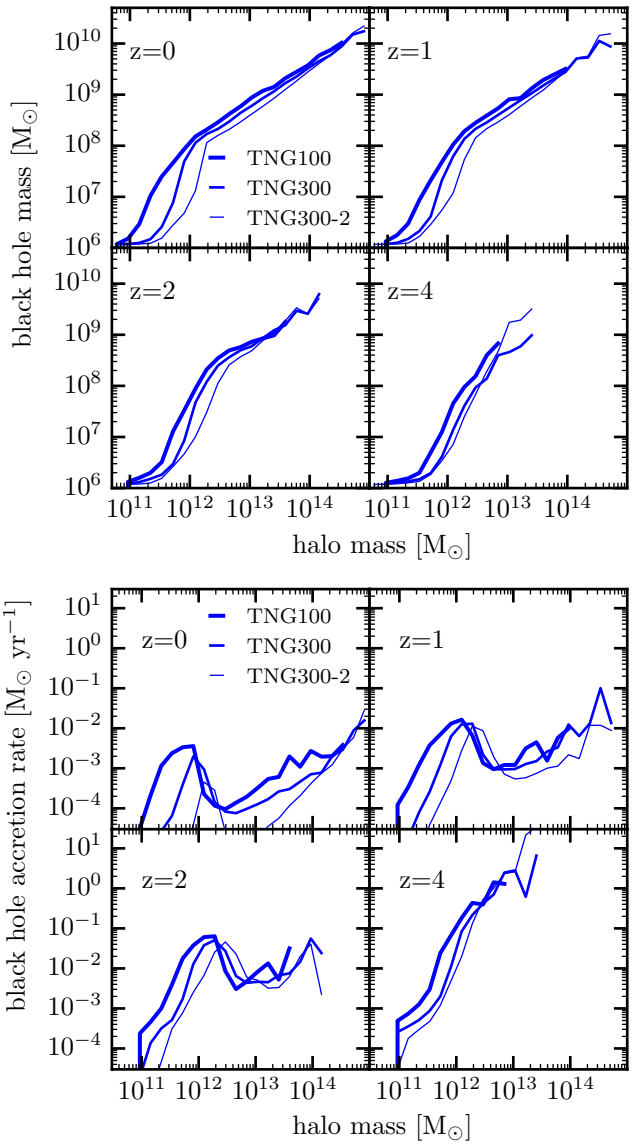

Figure 6.11: Resolution study with the TNG100 (high resolution), TNG300 (intermediate resolution, used in the main study) and TNG300-2 (low resolution) simulations. *Top panel*: Median SMBH mass as a function of host halo mass for simulations of different resolution at different redshifts. *Bottom panel*: Median SMBH accretion rate vs host galaxy mass. The host halo mass is a well-converged quantity, which means that the discrepancy of the simulations with different resolutions is due to the resolution dependence of the SMBH model.

formation rate in the first place and steers galaxies off the star forming main sequence, as shown in Figure 6.2. There have been a number of simulations showing that gas rich major mergers are able to drive gas to the galactic center (Hernquist, 1989) and trigger both, a starburst and AGN quasar activity that subsequently quenches the galaxy (see e.g. Springel et al., 2005a; Di Matteo et al., 2005; Hopkins et al., 2008a; Debuhr et al., 2012; Pontzen et al., 2017). However, there is no definite agreement whether this scenario is responsible for the majority of quenching events (e.g. Wurster and Thacker, 2013; Roos et al., 2015; Sparre and Springel, 2017). In IllustrisTNG, the key factor for quenching is the mass of the SMBH (Figure 6.5) and the associated energy from kinetic AGN feedback (Figure 6.4). This leaves us with a large population ($> 60\%$) of galaxies that are quenched unrelated to a major merger (Figure 6.3). We note that there is an increase in quenching events that have a preceding major merger, however, it is not clear whether this is due to an increased SMBH mass growth during this merger, or whether there is a sub-population that quenches via quasar activity and switches to the kinetic mode as a consequence. In this sense, our findings do not contradict the studies of isolated systems that see this happening, but in IllustrisTNG this quenching path appears subdominant, which is also in agreement with recent observational findings (Weigel et al., 2017a).

The SMBH model in IllustrisTNG reproduces the black hole mass–stellar mass relation (Figure 6.5) and does so for the following reason: low-mass SMBHs grow mainly via thermal mode accretion (Figure 6.7), with their growth being stopped on the power-law relation due to their own feedback. The kinetic feedback mode becomes important for more massive SMBH, at masses of around 10^8 $M_\odot$ and beyond. It not only shuts off star formation, but also lowers the accretion rate by several orders of magnitude (Figure 6.7 and Weinberger et al., 2017a, their Fig. 6). Indeed, it lowers the accretion rate by a large enough amount that mergers of SMBHs become the dominant growth channel from this mass onwards. It has been shown (Peng, 2007; Jahnke and Macciò, 2011) that hierarchical merging of galaxies and their SMBHs naturally causes a correlation close to the observed black hole mass–stellar mass relation, so this "dry merging" of massive black holes tends to maintain the (already established) relation. We note that this behaviour is in agreement with the scenario proposed by Graham and Scott (2013). However, the scatter in the black hole mass–stellar mass relation is smaller than in the observations and cannot be explained by the measurement errors alone.

The low accretion rates in the kinetic mode imply that SMBHs in this mode do not affect the bolometric quasar luminosity function (Figure 6.8).

Instead, the QLF probes SMBHs radiating at their Eddington luminosity at high redshift and SMBHs between 10^7 and $10^{8.5}$ $M_\odot$ at lower redshift (Figure 6.9). Generally, we reproduce the low redshift QLF, which implies that the transition to a kinetic mode (for which black holes 'vanish' from the QLF) is allowed by the observations of the QLF. At the high redshift regime, we over-predict the number of luminous SMBHs. One might argue that the employed radiative efficiency of $\epsilon_r = 0.2$ is rather large, and a smaller value might lower the instantaneous luminosity. However, lowering this value self-consistently in the simulation would also lead to a more rapid mass growth (Weinberger et al., 2017a, their Figure 13), and consequently to an even stronger discrepancy at slightly lower redshift (as more massive black holes in general accrete at larger rates, given the same external conditions).

A more likely explanation lies in an over-efficient early growth of the SMBHs, which might happen for a variety of reasons. One possibility is that the seeding of SMBHs happens too early and/or with too massive seeds, thereby boosting the early growth of SMBHs. An alternative solution is that some other mechanism delays the growth of low-mass SMBHs. Figure 6.1 shows that at early times, stellar feedback is energetically dominant. It has been shown in a number of studies (Dubois et al., 2014; Volonteri et al., 2016; Anglés-Alcázar et al., 2017b; Habouzit et al., 2017) that stellar feedback can have a large impact on the accretion rates of SMBHs. Thus, more efficient, local coupling of the stellar feedback energy at early times could delay the SMBH growth by the necessary amount and thereby lower the predicted QLF to the observed one. This possibility is in particular interesting because Grand et al. (2017) (using a similar, but not identical model) calls for an increased early stellar feedback for a completely different reason, namely to reduce bulge-formation at high redshift in Milky Way-sized galaxies.

The SMBH model in IllustrisTNG has been changed substantially compared to the one used in Illustris. In particular, SMBHs are seeded at higher masses, the 'boost factor' in the accretion formula is abandoned, and, via a BH mass dependent threshold, it becomes more difficult for low-mass SMBHs to enter the low accretion state. All these changes affect the growth of SMBHs substantially, thus it is not surprising that the resulting QLF is different. In fact, SMBHs contribute to it very differently in IllustrisTNG compared to Illustris (Sijacki et al., 2015). Overall, we consider the results of our comparison of the IllustrisTNG predictions for SMBHs with observations of AGN encouraging. The discrepancies we found at high redshift can help to refine the model once more detailed comparisons with observational data have been carried out, for example of the observed distributions of Eddington ratios, the occupation fractions and of the quasar

clustering.

6.8 Conclusion

The IllustrisTNG simulations reproduce a wide range of observations (Genel et al., 2017; Marinacci et al., 2017; Naiman et al., 2017; Nelson et al., 2017; Pillepich et al., 2017a; Springel et al., 2017; Vogelsberger et al., 2017) and arguably represent the currently best model for galaxy formation physics in hydrodynamical simulations of cosmological volumes. We here studied the relative importance of stellar and AGN feedback channels in IllustrisTNG as a function of galaxy mass and redshift. At high redshifts, stellar feedback dominates the energy release in all galaxies. At lower redshifts, depending on galaxy mass, thermal AGN feedback takes over and becomes dominant. While the energy injected via thermal AGN feedback is formally remarkably high, only a small fraction of the energy actually acts onto the host galaxies, whereas large parts are immediately lost due to the large cooling rates of the gas surrounding the SMBHs, reducing the efficiency of this feedback channel. For massive galaxies with a redshift $z = 0$ stellar mass larger than $10^{10.5}$ $M_\odot$, kinetic AGN feedback takes over at late times, which is coincident with quenching of the host galaxies and keeping them in a state of inefficient star formation.

Alongside with quenching, the kinetic feedback also self-regulates and equilibrates at accretion rates that are orders of magnitude below the average mass growth rate of mergers. This means that high mass SMBHs are formed predominantly via mergers of lower mass SMBHs. This leads to a buildup of the black hole mass – stellar mass relation according to the scenario outlined in Graham and Scott (2013).

Another consequence of this behaviour is that the bolometric quasar luminosity function only probes black holes in the thermal mode, i.e. SMBHs less massive than $10^{8.5}$ $M_\odot$. In general, SMBHs in IllustrisTNG seem to grow too fast at high redshift which might have a number of reasons. One mechanism that could alleviate this discrepancy would be a more efficient (or possibly additional e.g. Stinson et al. 2013; Hopkins et al. 2017) stellar feedback channel at high redshift, as proposed by Grand et al. (2017) for an entirely independent reason. Another would be to consider smaller SMBH seed masses, which would slow their high redshift growth substantially due to the sensitive dependence of the Bondi growth time on the black hole mass.

Finally, we note that another important consequence of our two mode model of thermal and kinetic feedback, as described in Weinberger et al.

(2017a), is a partial decoupling of both the AGN luminosity and events that might trigger AGN activity (such as mergers) from the quenching of massive central galaxies. This leads to a scenario that may make it observationally very difficult to establish a simple AGN–galaxy quenching connection. We showed in this paper how such a model behaves in a cosmological framework. A collection of other works has compared different aspects of the IllustrisTNG simulations with observational data, showing that it – as far as we tested so far – represents a viable scenario for galaxy formation. One critical ingredient of this model is a mass dependent switch in feedback mode at SMBH masses of around 10^8 $M_\odot$, which is so-far only poorly motivated. Investigating possible physical explanations why such a change of modes exists will therefore be a particularly interesting topic of future research.

Part III

High-resolution idealized simulations

7

Modelling black hole driven jets

Having investigated the effect of AGN feedback in a statistical sense on the galaxy population, it is now instructive to focus on the detailed interaction mechanisms at work in individual systems. In the following, I study the interaction of AGN jets on the surroundings in an idealized galaxy cluster environment. This work is published in Monthly Notices of the Royal Astronomical Society, Volume 470, Issue 4, p.4530-4546.

7.1 Introduction

The short cooling times in galaxy clusters, combined with the paucity of cold gas and star formation (e.g. Fabian, 1994; Peterson and Fabian, 2006, and references therein), suggest the presence of a central heating source. The energy from jets driven by the central supermassive black hole (SMBH) is widely considered to be a promising candidate to balance the cooling losses (Quilis et al., 2001; McNamara and Nulsen, 2007, 2012). This is observationally supported by the fact that most galaxy clusters with short cooling times show signatures of jet activity, and their jet power correlates with the cooling rate (Bîrzan et al., 2004; Dunn and Fabian, 2006; Fabian, 2012).

Yet, how the highly collimated jets distribute energy in a volume-filling fashion to the cluster gas still remains a topic of debate. Suggested mechanisms include heating by weak shocks and sound waves (e.g. Ruszkowski et al., 2004; Li et al., 2016; Fabian et al., 2017), mixing of the lobe with surrounding material (Hillel and Soker, 2016), cosmic rays (Loewenstein et al., 1991; Guo and Oh, 2008; Enßlin et al., 2011; Fujita and Ohira, 2011; Pfrommer, 2013; Jacob and Pfrommer, 2017a,b; Ruszkowski et al., 2017), turbulent dissipation (Fujita, 2005; Enßlin and Vogt, 2006; Kunz et al., 2011; Zhuravleva et al., 2014), and mixing by turbulence (Kim and Narayan, 2003; Ruszkowski and Oh, 2011) which may be promoted by anisotropic thermal conduction (Kannan et al., 2017). Recent X-ray spectroscopic observations

of the Perseus cluster (Hitomi Collaboration, 2016) however indicate that turbulence is unlikely to distribute the energy in a volume filling fashion if it is generated close to the lobe, because it would then dissipate on a much shorter timescale than needed to advect the energy to the cooling gas (Fabian et al., 2017).

An important aspect of the jet–intra-cluster medium (ICM) interaction is the dynamics and lifetime of the jet-inflated cavities. To quantify this, a number of idealised simulations have been carried out, typically starting with idealised under-dense structures. Churazov et al. (2001) performed such hydrodynamical simulations in 2D to explain the observed X-ray and radio morphology in M87. Brüggen and Kaiser (2001) and Brüggen et al. (2002) present a generalised study of hydrodynamical and magnetohydrodynamical simulations of buoyant cavities of different shapes. One result of their work is that the cavities need to have some favoured direction initially to rise buoyantly without being disrupted by Rayleigh-Taylor instabilities. Reynolds et al. (2005) find that buoyant cavities in idealised 3D hydrodynamical simulations get disrupted quickly by emerging Rayleigh-Taylor and Kelvin-Helmholtz instabilities, which, however, can be prevented assuming a non-negligible amount of shear viscosity. Sijacki and Springel (2006) come to a similar conclusion using smoothed particle hydrodynamics simulations with physical viscosity. External magnetic fields could in principle have a similar effect (Ruszkowski et al., 2007; Dursi and Pfrommer, 2008).

More recently, a number of studies have been published on the efficiency of different coupling mechanisms. Reynolds et al. (2015) show in an idealised simulation that the turbulent driving via explosively injected, buoyantly rising bubbles is not efficient enough to balance cooling losses via turbulent dissipation. Hillel and Soker (2016, 2017) find in simulations of jet-inflated lobes that turbulent mixing is the main energy distribution channel, dominating over turbulent dissipation and shocks. Studying the effect of a clumpy interstellar medium on the early phases of jet propagation, Mukherjee et al. (2016) show that low-power jets get dispersed by high-density clouds, and distribute their energy at small radii.

Simulations that include a self-regulated cycle of gas cooling, black hole accretion and gas heating (e.g. Sijacki et al., 2007; Cattaneo and Teyssier, 2007; Sijacki et al., 2008; Dubois et al., 2010) were generally able to prevent excessive cooling of gas, yet sometimes at the cost of dramatically changing the thermodynamic profiles (Cattaneo and Teyssier, 2007). Using a different estimate for the accretion rate, a steady state can also be reached, maintaining a cool-core temperature structure (Gaspari et al., 2011b; Li and Bryan, 2014a,b; Li et al., 2015). More recent results indicate that this discrepancy is due to insufficient numerical resolution (Meece et al., 2017). In

high-resolution simulations, cold clumps form along the outflows via thermal instability, which plays an important role in the overall heating-cooling cycle (Li and Bryan, 2014b; Li et al., 2015; Prasad et al., 2015; Voit et al., 2017). The dominant mechanism of energy dissipation in these simulations are weak shocks (Li et al., 2016). This is particularly the case in the external regions at large angles from the jet direction, while in the 'jet cones', mixing of lobe material is energetically dominant (Yang and Reynolds, 2016a). Yang and Reynolds (2016a) also find that a large-scale circulation and associated advective transport of energy is an important ingredient for the isotropic distribution of the feedback energy in the cluster core.

Jets from SMBHs that interact with the ICM cover an enormous dynamic range in space and time, being launched at several Schwarzschild radii, and propagating outwards to tens, sometimes even 100 kpc. Given this dynamic range challenge, there are a number of different techniques to model jets in simulations, depending on the topic of investigation. In particular, the implementation of how the jet is injected has to be adjusted to the available resolution of the simulation, and some simplifications are inevitable. Recently, some studies (Tchekhovskoy and Bromberg, 2016; Barniol Duran et al., 2017) used a magneto-centrifugal launching of jets, which is likely closest to the real jet launching. However, this technique requires a quite high resolution and strong magnetic fields.

In lower resolution studies that target only hydrodynamical jets, other techniques have to be applied. A widely used method for injecting a collimated outflow on kpc scales, as presented in Omma et al. (2004), is based on adding a predefined momentum and energy in a kernel-weighted fashion to all cells in a given region. This approach is also used in the model of Li and Bryan (2014a). Gaspari et al. (2011b) place all available energy in kinetic form in the injection region, which implies a variable momentum input. In an alternative approach, the thermodynamic and kinetic state of an injected region is explicitly modified instead of adding a given flux to the cells, i.e. a predefined density, velocity and energy density is set (e.g. Gaibler et al., 2009; Hardcastle and Krause, 2014; English et al., 2016). This gives full control over the jet properties at the injection scale and has been shown to produce low-density cavities, yet has the disadvantage that the injected energy depends on the external pressure, which implies that such a scheme is difficult to use in simulations with self-regulated feedback. Alternatively to preparing individual simulation cells, the jet can also be set up by using an inflow boundary condition (e.g. Norman et al., 1982).

In this paper, we analyse a new set of high-resolution magnetohydrodynamical simulations of jets from SMBHs and their interaction with the surrounding medium. We use idealised magnetohydrodynamical simula-

tions which conserve, apart from the energy injection from the jet, the total energy of the gas in a stationary spherically symmetric gravitational potential. This simple setup allows us to simulate the evolution of the jet inflating a low-density cavity in the surrounding ICM and the subsequent lobe evolution and disruption after a few hundred Myr at unprecedented resolution.

This paper is structured as follows. We describe the simulation methodology and our implementation of the jet injection in Section 7.2, followed by the details of the simulation setup in Section 7.3. We discuss the results in Section 7.4, and give our conclusions in Section 7.7.

7.2 Methodology

We carry out 3D magnetohydrodynamic (MHD) simulations in a prescribed external gravitational potential using the moving-mesh code Arepo. The equations of ideal MHD are discretised on an unstructured, moving Voronoi mesh (Springel, 2010; Pakmor et al., 2011). The MHD Riemann problems at cell interfaces are solved using an HLLD Riemann solver (Pakmor et al., 2011), and the divergence-constraint of the magnetic field is addressed by a Powell eight-wave cleaning scheme (Pakmor and Springel, 2013). The gravitational acceleration is imparted in the same way as in Springel (2010), using the local gradient of the analytic potential and ignoring gas self-gravity.

In addition to ideal MHD, we include a cosmic ray (CR) component in a two-fluid approximation (Pakmor et al., 2016; Pfrommer et al., 2017). The CR component has an adiabatic index of $\gamma_{\rm CR} = 4/3$ and is injected as part of the jet. Throughout this paper, we restrict ourselves to an advective transport of the CR component, leaving a study of CR transport relative to the gas as well as energy dissipation from the CR to the thermal component to future work.

7.2.1 Jet model

In this work, we study jets from SMBHs in simulations that reach resolutions better than 200 pc (target cell size). However, the model is designed such that it is still applicable for simulations with 10 times coarser (spatial) resolution. We do not model the actual jet launching, or early propagation effects such as self-collimation, but instead set up the thermodynamic, magnetic and kinetic state of the jet at a distance of a few kpc from the black hole. In practice, this means that we want to create in a numerically

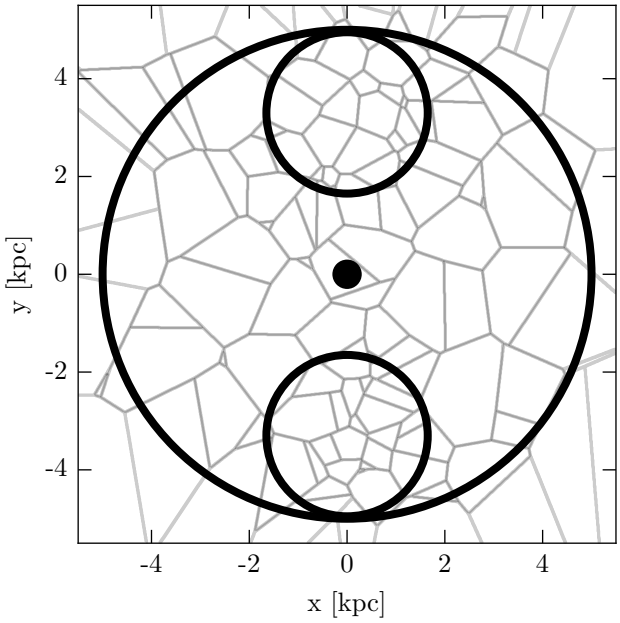

Figure 7.1: Division of the volume around a black hole (central dot) into jet regions (upper and lower small circle) and a buffer region (rest enclosed by large circle). The jet regions are always chosen in the direction of the kinetic energy injection. The contours are a slice through a 3D mesh of one of the low-resolution simulations. Note that a slice through a 3D Voronoi mesh is in general not a valid 2D Voronoi mesh.

robust way a kinetically dominated, low density, collimated outflow in pressure equilibrium with its surroundings. If desired, this outflow can contain a predefined fraction of the pressure in a (toroidal) magnetic field and in cosmic rays.

To enforce an overall mass conservation in the system while simultaneously keeping a well-specified thermodynamic state in the jet, we apply a redistribution of mass and internal energy from the jet region to the surroundings (or vice versa) according to criteria that will be specified in the following.

Throughout this work, we use a single continuous injection event, which ceases after a specified time. Numerically, however, the injection, as well as all other equations of MHD are discretised in time. For the remainder of this section, we therefore refer to one of these discretised events as an injection event.

We only set up the thermodynamic state of this 'effective jet' if the required energy, composed of the energy $\Delta E_{\mathrm{redist}}$ (including thermal and

CR component) for redistributing the gas and the energy ΔE_B connected to the magnetic field change, is smaller than the energy available from the black hole, viz.

$$\Delta E = \int_{t_{\rm last}}^{t} \dot{E}_{\rm jet}\, {\rm d}t' = \Delta E_{\rm kin} + \Delta E_B + \Delta E_{\rm redist}. \tag{7.1}$$

Here t is the current time, $t_{\rm last}$ is the time of the last injection event, and $\dot{E}_{\rm jet}$ is the jet power, a free parameter in our setup[1]. In other words, the injected kinetic energy $\Delta E_{\rm kin}$ in the jet region has to be positive. Due to this criterion, the injection is not necessarily happening every (local) hydrodynamical timestep. During a jet injection phase over 50 Myr, there are typically several thousand small injection events that effectively yield a continuous launching of the jet.

Jet thermodynamic state

To achieve the targeted thermodynamic state of the jet, we select a spherical region around the black hole with a given radius h (5 kpc throughout the paper). We split this volume into two spherical sub-volumes, located off-center along the jet-direction $\hat{\mathbf{n}}$ (see Figure 7.1). The union of all cells that have their mesh-generating points within these spherical sub-volumes is referred to as jet regions $(1, 2)$ in the following. In these regions, we set the jet thermodynamic state. The third volume, outside of the jet regions, will be referred to as the buffer region (3), to which we add (or from which we take) the mass to set up a desired thermodynamic state in the jet region while simultaneously ensuring overall mass conservation.

The density in jet region $1, 2$ is calculated as

$$\rho_{1,2} = \rho_{\rm target}\, \frac{V_1 + V_2}{2V_{1,2}}, \tag{7.2}$$

respectively, where $\rho_{\rm target}$ is treated as a free parameter. V_1 and V_2 are the volumes of the jet regions 1 and 2. We emphasise that these two volumes can be slightly different due to the nature of the unstructured computational grid in Arepo. The volume factor in the density ensures equal mass in both jet regions. The specific thermal energy u in this region is

$$u_{1,2} = \frac{P_{\rm target}}{(1 + \beta_{\rm jet}^{-1} + \beta_{\rm CR,\,jet}^{-1})\,(\gamma - 1)\,\rho_{1,2}}, \tag{7.3}$$

[1] $\dot{E}_{\rm jet}$ can be computed using a black hole accretion rate estimate in future work.

where $\gamma = 5/3$ is the adiabatic index of the gas and $P_{\rm target}$ is the kernel-weighted pressure in the buffer region. We use an SPH-smoothing kernel of the form

$$w(r,h) = \frac{8}{\pi h^3} \begin{cases} 1 - 6\left(\frac{r}{h}\right)^2 + 6\left(\frac{r}{h}\right)^3 & \text{for } 0 \leq \frac{r}{h} \leq \frac{1}{2} \\ 2\left(1 - \frac{r}{h}\right)^3 & \text{for } \frac{1}{2} < \frac{r}{h} \leq 1 \\ 0 & \text{for } \frac{r}{h} > 1, \end{cases} \tag{7.4}$$

where r is the distance from the black hole. Note that we use the same kernel, centred around the injection region and with a different value of h, for the kinetic energy injection to the jet gas.

$$\beta_{\rm jet}^{-1} = \frac{\mathbf{B}^2}{8\,\pi\,P_{\rm th}} \quad \text{and} \tag{7.5}$$

$$\beta_{\rm CR,\,jet}^{-1} = \frac{P_{\rm CR}}{P_{\rm th}} \tag{7.6}$$

are the magnetic and cosmic ray pressure contributions relative to the thermal pressure $P_{\rm th}$ in the jet region, respectively, and are treated as free parameters[2]. The cosmic ray specific energy $u_{\rm CR}$ is

$$u_{\rm CR,1,2} = \frac{P_{\rm target}}{(1 + \beta_{\rm CR,jet} + \beta_{\rm CR,jet}\,\beta_{\rm jet}^{-1})\,(\gamma_{\rm CR} - 1)\,\rho_{1,2}}, \tag{7.7}$$

where $\gamma_{\rm CR} = 4/3$ is the adiabatic index of the cosmic ray component.

The mass that is removed from the jet regions is added adiabatically to the buffer region (or the mass which is added in the jet regions is removed adiabatically from the buffer region, depending on the initial density of the jet region) in a mass weighted fashion, adding the total momentum associated with this redistribution to the buffer cells. Additionally, we make sure that the total thermal energy change in the jet regions is added (or subtracted) from the buffer region in a mass-weighted fashion, which ensures that the overall thermal energy change is only due to adiabatic contraction or expansion in the buffer region. This means that the thermal energy change in the buffer region $\Delta E_{\rm therm,\,3}$ is given by

$$\begin{aligned} \Delta E_{\rm therm,\,3} = & \sum_{\text{region 3}} \left(\frac{\rho_{\rm final}}{\rho_{\rm init}}\right)^{\gamma-1} \\ & + \sum_{\text{regions 1,2}} (u_{i,\rm init} m_{i,\rm init}) - (u_{i,\rm final} m_{i,\rm final}), \end{aligned} \tag{7.8}$$

[2]We use β^{-1} to be consistent with the nomenclature of the commonly used plasma-beta parameter.

where $u_{i,\mathrm{init}}$, $m_{i,\mathrm{init}}$, $u_{i,\mathrm{final}}$ and $m_{i,\mathrm{final}}$ are the specific thermal energy and mass of cell i before and after the redistribution, respectively.

We denote the overall energy change due to this redistribution as

$$\begin{aligned}\Delta E_{\mathrm{redist}} = \sum_{\text{regions } 1,2,3} \Bigg[& \frac{1}{2}\, m_{i,\mathrm{final}}\, \mathbf{v}_{i,\mathrm{final}}^2 \\ & + \left(u_{i,\mathrm{final}} + u_{\mathrm{CR},i,\mathrm{final}}\right) m_{i,\mathrm{final}} \\ & - \frac{1}{2}\, m_{i,\mathrm{init}}\, \mathbf{v}_{i,\mathrm{init}}^2 \\ & - \left(u_{i,\mathrm{init}} + u_{\mathrm{CR},i,\mathrm{init}}\right) m_{i,\mathrm{init}} \Bigg] , \end{aligned} \tag{7.9}$$

where $u_{\mathrm{CR},i,\mathrm{init}}$ and $u_{\mathrm{CR},i,\mathrm{final}}$ are the CR specific energy of cell i before and after the redistribution, respectively.

Magnetic field

In addition to the thermal and cosmic ray specific energy, we determine the magnetic energy injection ΔE_B needed to reach a specified magnetic pressure relative to the thermal pressure $\beta_{\mathrm{jet}}^{-1}$ by

$$\beta_{\mathrm{jet}}^{-1} = \frac{\sum\limits_i \mathbf{B}_{i,\mathrm{init}}^2 V_i\, (8\pi)^{-1} + \Delta E_B}{(\gamma - 1) \sum\limits_i u_i m_i}, \tag{7.10}$$

where the sum includes all cells in both jet regions. Note that we set $\Delta E_B = 0$ if the magnetic field energy is already exceeding the desired value.

The injected magnetic field is purely toroidal with the direction

$$\hat{\mathbf{B}}_i = \frac{\mathbf{r}_i \times \hat{\mathbf{n}}}{|\mathbf{r}_i \times \hat{\mathbf{n}}|}, \tag{7.11}$$

where $\mathbf{r}_i$ is the position of the cell i relative to the black hole. We parametrise the injected magnetic field as

$$\Delta \mathbf{B}_i = w_{B,i}\, f_B\, \hat{\mathbf{B}}_i, \tag{7.12}$$

insert this parametrisation in the energy equation

$$\Delta E_B = \sum_i (\mathbf{B}_{i,\mathrm{init}} + \Delta \mathbf{B}_i)^2 V_i\, (8\pi)^{-1} - \sum_i \mathbf{B}_{i,\mathrm{init}}^2 V_i\, (8\pi)^{-1} , \tag{7.13}$$

and solve it for f_{B}. $\mathbf{B}_{i,\mathrm{init}}$ and V_i are the magnetic field and volume of the cell i before injection.

$$w_{B,i} = w(|\mathrm{d}\mathbf{r}_i|\,, 0.33\, h) \left(\frac{\mathrm{d}r_i^2 - (\mathrm{d}\mathbf{r}_i \cdot \hat{\mathbf{n}})^2}{(0.33\, h)^2} \right)^4 \tag{7.14}$$

is a weighting kernel for the magnetic field, and $\mathrm{d}\mathbf{r}_i$ the position of the cell i relative to the center of its jet region. Note that the radius of the jet regions is $0.33\,h$.

Momentum injection

The momentum kick for each cell $\Delta\mathbf{p}_i$ is given by

$$\Delta\mathbf{p}_i = w_i\, m_i\, f\, \frac{\hat{\mathbf{n}}\cdot\mathbf{r}_i}{|\hat{\mathbf{n}}\cdot\mathbf{r}_i|} \tag{7.15}$$

where $w_i = w(|\mathrm{d}\mathbf{r}_i|\,, 0.33\,h)$. f is determined by the desired kinetic energy input,

$$\Delta E_{\mathrm{kin}} = \sum_i \frac{(\mathbf{p}_{i,\mathrm{old}} + \Delta\mathbf{p}_i)^2}{2m_i} - \frac{\mathbf{p}_{i,\mathrm{old}}^2}{2m_i}. \tag{7.16}$$

7.2.2 Local time-stepping

Collimated outflows can have a very high velocity. Also, in the early phase of a jet, the velocity in the jet region, which dominates over the sound speed, changes rapidly with time. This has consequences for the Courant-Friedrich-Levy condition in the jet region, as well as in neighbouring cells, and demands very fine timestepping.

For the jet region itself, this can be accounted for at any timestep by choosing a smaller timestep instead (which is usually the case after an injection event). However, it is also important to ensure that the neighbouring cells are evolved on timesteps that are short enough to handle an incoming jet. This is in general a problem for simulations that operate with local timesteps and include such source terms. To overcome this problem, we use a tree-based nonlocal timestep criterion (section 7.2 in Springel, 2010), setting the signal speed of the cells in the jet region as

$$c_j = \max(2\,v_{\mathrm{jet}}, 0.1\,c, c_s + v_{\mathrm{jet}}), \tag{7.17}$$

where v_{jet} is the gas velocity of the respective cells relative to the velocity of the mesh-generating point, c is the speed of light, c_s the speed of sound[3] and c_j the signal speed of a cell as in Springel (2010, their eq. 111). We do not have a good way yet for reliably predicting the precise values required for the parameters involved, but practical experience shows that the choice

[3]Here, we use the effective sound speed of thermal gas, magnetic fields and cosmic rays, $c_s^2 = \gamma\, P_{\mathrm{th}}\,\rho^{-1} + \gamma_{\mathrm{CR}}\, P_{\mathrm{CR}}\,\rho^{-1} + \mathbf{B}^2\,(4\pi\rho)^{-1}$.

we made works well and enforces neighbouring cells outside the jet regions $(1, 2)$ to be on low enough timesteps for properly modelling the incoming supersonic flows.

In practice, we do not apply this procedure to all cells in the jet regions (1,2), but only to those that are at most a specified distance away from the spherical shell defining the corresponding jet region. This distance is specified for each cell individually as the radius of the largest circumsphere of the Delaunay tessellation involved in the generation of the Voronoi cell. This ensures that at least the outermost layer of cells in the jet regions is considered, while the inner cells are not. In this way, we considerably reduce the computational cost of the timestep calculations.

7.3 Simulation setup

To study the interaction between jets and the ICM, we set up a halo in the form of an analytic Navarro-Frenk-White (NFW) profile (Navarro et al., 1996, 1997) with mass $M_{200,\mathrm{c}} = 10^{15}\,\mathrm{M}_\odot$, concentration $c_{\mathrm{NFW}} = 5.0$ and virial radius $R_{200,\mathrm{c}} = 2.12\,\mathrm{Mpc}$. We use a fit to the Perseus cluster electron number density profile from Pinzke and Pfrommer (2010), originally from Churazov et al. (2003), and scale with a constant factor such that the gas fraction within $R_{200,\mathrm{c}}$ reaches 16 %:

$$n = 26.9 \times 10^{-3} \left(1.0 + \left(\frac{r}{57\,\mathrm{kpc}}\right)^2\right)^{-1.8} \mathrm{cm}^{-3} + 2.80 \times 10^{-3} \left(1.0 + \left(\frac{r}{200\,\mathrm{kpc}}\right)^2\right)^{-0.87} \mathrm{cm}^{-3} \tag{7.18}$$

The energy density is derived from the pressure needed for hydrostatic equilibrium, and the assumption of a vanishing pressure at a radius of 3 Mpc. The dotted black lines in Figure 7.2 show the initial density, temperature and entropy profiles, respectively.

At the center of the halo, we consider a black hole which injects energy at a constant rate $\dot{E}_{\mathrm{jet}}$ for a given amount of time. Apart from the energy injection in the jet, the simulation is non-radiative and does not include gravitational interactions between gas cells or from the black hole itself. Thus the gravitational force originates purely from the analytic NFW potential. We choose this approach to maximise the possible hydrodynamic resolution with moderate computational resources. The magnetic field strength in the initial conditions is zero. Throughout the analysis, we assume a constant chemical composition with 76% hydrogen and 24% helium.

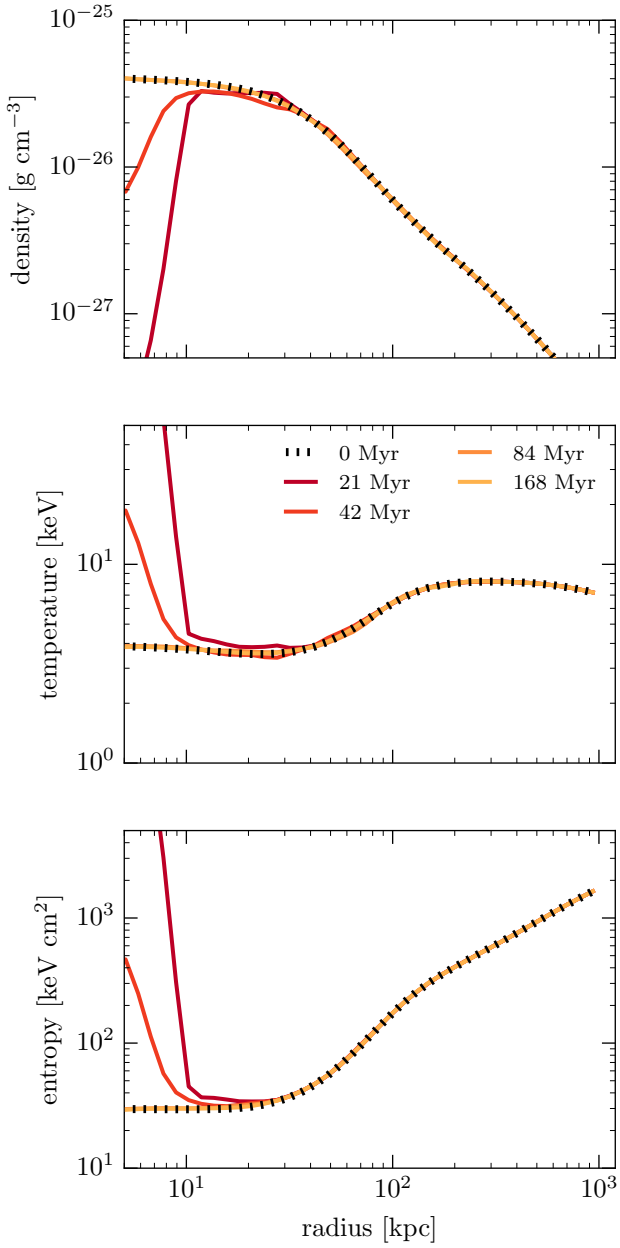

Figure 7.2: Radial profiles of the gas in the initial conditions (black dotted line) and at later times for the simulations with a jet power of 3×10^{44} erg s^{-1}. The density is volume-weighted, the temperature mass-weighted, and the entropy is calculated from these weighted quantities. The low densities and high temperatures of the inner regions are associated with the jet and quickly reaches its original value once it is no longer active (after 50 Myr).

7.3.1 Refinement

Simulating jets from active galactic nuclei on the scale of full galaxy clusters represents a challenging numerical problem. Jets operate at scales around a kpc and lower, and involve correspondingly short timescales of a few hundred kyr, while galaxy clusters have typical sizes of a Mpc and dynamical timescales in the range of a Gyr. The aim here is to resolve both simultaneously, which requires a high adaptivity of the resolution, both in space and time.

A standard approach of using Arepo consists of prescribing a fixed target mass $m_{\mathrm{target},0}$ for each cell (Vogelsberger et al., 2012), and refining a cell once it is a factor of two more massive than that this target mass (and derefining it once the cell is a factor two less massive than the target mass). We use this criterion in the region of the unperturbed ICM. But the jets inflate low-density cavities. Using only this criterion would imply that the gas cells in the lobes would attain a volume orders of magnitude larger that in the surrounding medium. This would mean in particular that gas flows within the lobe, and the surface of these lobes, would be very poorly resolved. As this structure is one of the regions of interest in our simulations, we instead apply a refinement criterion based on a target volume to the cells in the lobe. This target volume is significantly lower than the resolution of the surrounding medium. Technically this is done by defining an adaptive target mass for each cell by

$$m_{\mathrm{target},i} = f\,\rho_i V_{\mathrm{target}} + (1-f)\; m_{\mathrm{target},0} \tag{7.19}$$

$$f = 0.5 + 0.5\tanh\left(\frac{x_{\mathrm{jet},i} - 10^{-4}}{10^{-5}}\right), \tag{7.20}$$

where $x_{\mathrm{jet},i}$ is the mass fraction of jet material in cell i. Note that $x_{\mathrm{jet}} = 1.0$ in a jet injection cell and that the mass fraction is advected with the fluid according to the fluxes at the interfaces of each cell. In practice this ensures that the complete jet and lobe structure has uniform spatial resolution. Due to the very low numerical diffusivity of the Arepo code, the outside is not affected.

One region of particular interest is the boundary layer between jet/lobe and surrounding ICM, which we want to resolve as well as possible to study arising hydrodynamic instabilities. To achieve this, we refine a cell whenever

$$V_i^{1/3}\,|\nabla\rho_i| > 0.5\,\rho_i. \tag{7.21}$$

This ensures that we refine boundary layers until they are well resolved, and this criterion replaces the above mentioned criteria whenever applicable. We

note that by construction, this criterion is violated at the boundaries of the jet injection region, where the density contrast between neighbouring cells is significant, and therefore the estimated gradients can be much larger. To avoid a runaway refinement, we employ a minimum cell volume $V_{\rm min}$, irrespective of all other refinement criteria.

Because of these variable refinement criteria and target resolutions, it is important to ensure a smooth transition in resolutions. To achieve this, we enforce that the volume of every cell is at most a factor of 3 larger than the smallest neighbour, refining the cells where this is not satisfied[4].

7.3.2 Mesh-movement and refinement criteria

Because these non-standard refinement and derefinement criteria produce significant changes in the computational mesh as the system evolves, we also change the mesh-regularisation options slightly compared to the standard settings in the Arepo-code, allowing for more aggressive refinement and cell shape changes. To this end, we apply a slightly faster mesh regularisation value of $\xi = 1.0$, in agreement with Springel (2010, eq. 63).

Furthermore, we do not allow for derefinement of a gas cell if

$$\max(\sqrt{A/\pi}\, h^{-1}) > 6.75, \tag{7.22}$$

where A is the area of the interface between two cells, h the distance between mesh generating point and the cell interface. The maximum denotes the maximum over all faces of a cell. Note that, due to the nature of Voronoi cells, this criterion, if satisfied, always applies to a pair of neighbouring cells. This means that the code does not derefine heavily distorted cells (Vogelsberger et al., 2012, use a value of 3.38).

7.3.3 Simulation set

We perform a number of simulations with different jet powers (10^{44} erg s^{-1}, 3×10^{44} erg s^{-1}, and 10^{45} erg s^{-1}). In all runs, the jet is active for 50 Myr, which corresponds to a total energy injection of $\sim 1.6 \times 10^{59}$ erg, 4.7×10^{59} erg, and 1.6×10^{60} erg, respectively. We run the simulation setup at various resolution levels (see Table 7.1), always changing all resolution parameters, i.e. the resolution of the ICM (the target mass per cell, $m_{\rm target,0}$), the target volume in the jet and lobe $V_{\rm target}$, and the minimum volume of a cell $V_{\rm min}$

[4]Note that the jump in resolution between neighbouring cells used here is smaller than usually present in adaptive mesh refinement simulations (factor of 8).

Jet parameters		
Jet density	$\rho_{\rm target}$	10^{-28} g cm^{-3}
Black hole region	h	5 kpc
Magnetic pressure	$\beta_{\rm jet}^{-1}$	MHD: 0.1
		hydro: 0.0
Cosmic ray pressure	$\beta_{\rm CR,jet}^{-1}$	1.0
Jet power	$\dot{E}_{\rm jet}$	1×10^{44} erg s^{-1}
		3×10^{44} erg s^{-1}
		1×10^{45} erg s^{-1}
Jet active for		5×10^7 yr
Resolution		
Target mass	$m_{\rm target,0}$	low res: 1.5×10^7 M$\odot$
		interm. res: 1.5×10^6M$\odot$
		high res: 1.5×10^5M$\odot$
Target volume	$V_{\rm target}^{1/3}$	low res: 872 pc
		interm. res: 405 pc
		high res: 188 pc
Minimum volume	$V_{\rm min}$	$V_{\rm target}/2$

Table 7.1: Simulation parameters.

(always half the target volume) by the same amount (factors of 10). Due to the high computational cost, we do not simulate the high-power jet at the highest resolution level. All runs are performed with a purely hydrodynamic jet ($\beta_{\rm jet}^{-1} = 0$) and with a magnetised jet ($\beta_{\rm jet}^{-1} = 0.1$), both with the same HLLD Riemann solver.

For the further analysis, unless stated otherwise, we focus on the high resolution simulation with a jet power of 3×10^{44} erg s^{-1} and a magnetised jet. This is the simulation with the highest number of simulation cells within the lobes ($\sim 1.7 \times 10^7$ cells in both lobes combined, in total 2.7×10^8 cells in the simulation box after 168 Myr.)

Additionally, we run a set of simulations of the low-resolution target mass $m_{\rm target,0} = 1.5 \times 10^7\,{\rm M}_\odot$ in which we successively abandon or relax the refinement criteria that are special to this simulation (density gradient, neighbour refinement criterion, and target volume). In this way, we evaluate a potential use of the presented model in future cosmological simulations of galaxy cluster formation at much lower resolution[5]. This set of simulations

[5]We note that the used 'low res' target gas mass is larger than the one in some already

has a varying h, determined by the weighted number of neighbouring cells $n_{\mathrm{ngb}} = 64 \pm 20$, as it is usually used in cosmological simulations (Weinberger et al., 2017a). h is then calculated iteratively by solving

$$n_{\mathrm{ngb}} = \sum_i \frac{4\pi h^3 m_i}{3 m_{\mathrm{target},0}} w(r_i, h) \tag{7.23}$$

via bisection. These special simulations, as well as two intermediate resolution runs with 3×10^{44} erg s^{-1} and magnetised jets with varying parameters h and ρ_{target}, are only analysed in Sections 7.5 and 7.6, respectively.

7.4 Results

In this section, we analyse the effect of the jet from the injection scale to successively larger spatial and time scales. Figure 7.3 shows the evolution of both, a magnetised ('MHD') and an unmagnetised ('hydro') jet, where the colormap indicates the mass fraction of jet material. As long as the jet is active, it drills a low-density channel into the ICM and inflates elongated, low density cavities that expand until they reach pressure equilibrium with the surroundings. The buoyant timescale of these cavities is larger than the jet timescales, but a persistent buoyancy force over several hundred Myr changes the shape of the lobe, first reducing its ellipticity and ultimately forming a torus (two disconnected round patches in the slice). This torus structure is gradually diluted and mixed with the surroundings. The magnetised lobe mixes less efficiently with the surroundings.

7.4.1 Jet properties

One of the key properties of a jet is its internal Mach number $|\mathbf{v}|/c_{\mathrm{s}}$ (Figure 7.4). Although we set up a low density jet in pressure equilibrium, i.e. with a high sound speed, we payed attention that the jet actually reaches supersonic speeds (the maximum absolute velocity is $\sim 1.0 \times 10^5$ km s^{-1}) in the black hole rest frame, so that it transports its kinetic energy flux outwards and thermalises in a low-density cavity. The magnetic fields are frozen into the plasma and transported outward with the fluid flow, staying confined within the cavity. Note that the magnetic energy flux here is about two orders of magnitude lower than the kinetic energy flux. In this particular simulation, we choose thermal and cosmic ray pressure in the

published cosmological zoom-in simulations of galaxy clusters (e.g. Kannan et al., 2017).

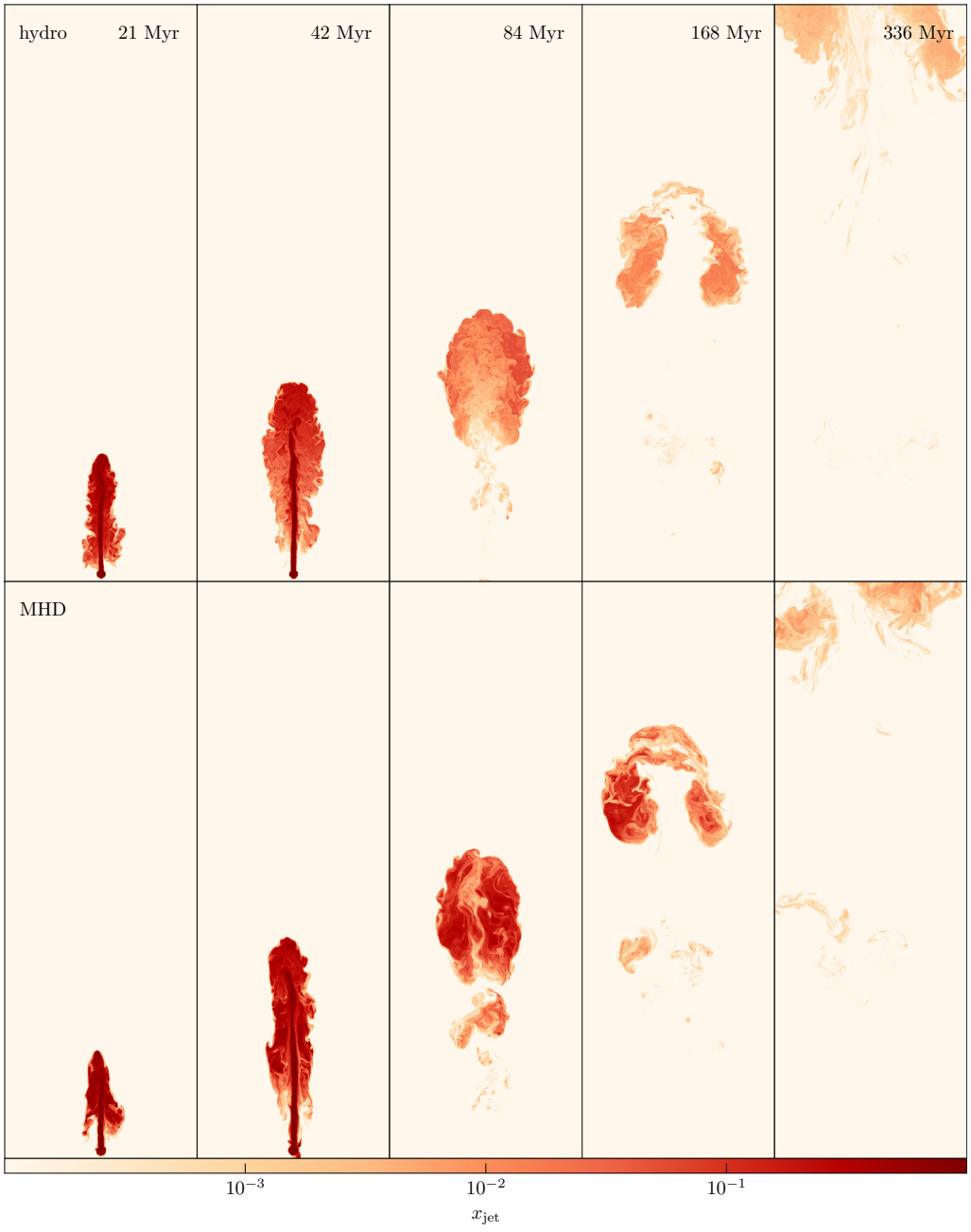

Figure 7.3: Slices through the mid-plane of a jet simulation showing the concentration of jet material at different evolutionary stages of low-density cavities. Top panels show purely hydrodynamical cavities, bottom panel shows magnetised cavities. We only show one of the two lobes in this visualisation. Each panel is 225 kpc high and 75 kpc wide.

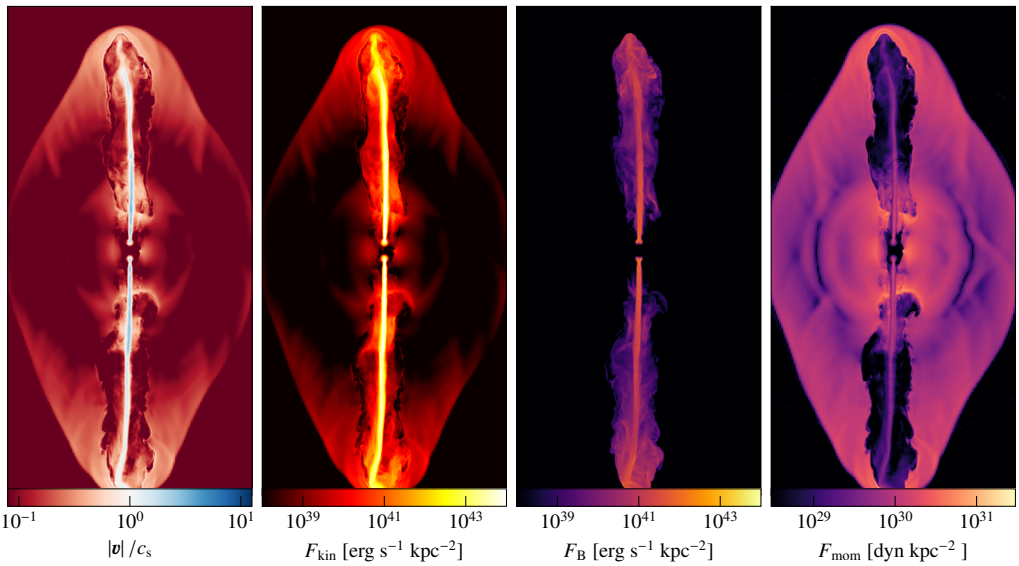

Figure 7.4: Left to right: jet velocity $|v|\,/c_s$, kinetic energy flux, magnetic energy flux and momentum flux of a 3×10^{44} erg s^{-1} jet after 42 Myr, all measured in the black hole rest frame. Each panel is 200 kpc in the vertical, and 100 kpc in the horizontal directions, and shows jet material weighted averaged quantities over a 10 kpc depth.

injection region in equipartition, while the magnetic pressure is 10% of the thermal pressure.

The momentum flux of the jet in the black hole rest frame is lower than the momentum flux of the surrounding medium outside the expanding lobe (in the post bow shock region). This is the case because we have set up a low density jet, which has important consequences for the resulting dynamics as well as for the morphology of the cavity (see also Krause, 2003; Gaibler et al., 2009; Hardcastle and Krause, 2013, 2014; Guo, 2015): the surrounding material is pushed aside by pressure forces of the expanding lobe, which itself is fuelled by the jet, rather than being directly displaced by a jet with high momentum flux. Consequently, the lobe expands in all directions, not just in the jet propagation direction, thereby naturally leading to a considerable horizontal extent. A higher density jet, on the other hand, would propagate further with the same amount of energy (see Section 7.6).

The jet shown here reaches remarkably large distances of more than 75 kpc, which is surprising given its moderate power of 3×10^{44} erg s^{-1}. This is in qualitative agreement with Massaglia et al. (2016), who find that the

transition form Fanaroff-Riley type I to type II type morphology occurs at $\dot{E}_{\rm jet} \sim 10^{43}$ erg s^{-1} for purely hydrodynamic jets. However, there are several effects that could in principle obstruct the jet propagation. First, the surrounding material has in our run a favourable uniform density and no prior fluid motions or magnetic fields. A clumpy medium would be more readily capable of stopping the jet or delaying its propagation (Mukherjee et al., 2016), while large scale density, velocity and magnetic field fluctuations can also redirect and deform the resulting low-density channels (Gan et al., 2017), making it more difficult for a jet to propagate outwards. Second, instabilities of the jet, such as a magnetic kink instability, can help to disperse the jet (Tchekhovskoy and Bromberg, 2016), limiting its range. We avoided such instabilities by choosing a low degree of magnetisation, mainly because we expect their occurrence to be very sensitive to the details of the injection of the magnetic field (which is toroidal in our case, not helical as expected in jets). Because of these reasons, we expect the jet range to be slightly overestimated in our study.

There are also hydrodynamical effects, such as internal recollimation shocks (Norman et al., 1982) and non-axisymmetric modes (Hardee, 1987) that affect the deceleration of the shock. As the target cell size of a computational cell in the jet is $V_{\rm target}^{1/3} = 188$ pc (while the jet width is several kpc) we are able to marginally resolve these effects. A careful quantitative study of these instabilities, however, would require a substantially increased resolution in the jet and a relativistic treatment of MHD, which is beyond the scope of this paper.

Another interesting detail is the absence of a backflow down to the injection base, connecting the two lobes (Cielo et al., 2014, 2017). We note that for some of our simulations, in particular the high-power jets, such backflows are present. We suspect that the absence of the backflows is partially due to the (intentional) separation of the injection regions by a few kpc, as well as possible resolution effects at these small scales. However, we do not expect this to have a large impact on scales of a few tens to a few hundred kpc from the center, which is the main focus of our study.

7.4.2 Lobe properties

After the jet has terminated, the low-density cavities quickly reach pressure equilibrium with their surroundings. Figure 7.5 shows the jet material weighted density, total pressure, plasma-beta parameter $\beta = P_{\rm th}(\mathbf{B}^2/8\pi)^{-1}$ and the thermal over cosmic ray pressure $\beta_{\rm CR} = P_{\rm th}P_{\rm CR}^{-1}$. Note that at injection we chose $\beta = 10$ and $\beta_{\rm CR} = 1$. As the jet inflates the lobe, kinetic energy thermalises, and correspondingly, the thermal pressure content of

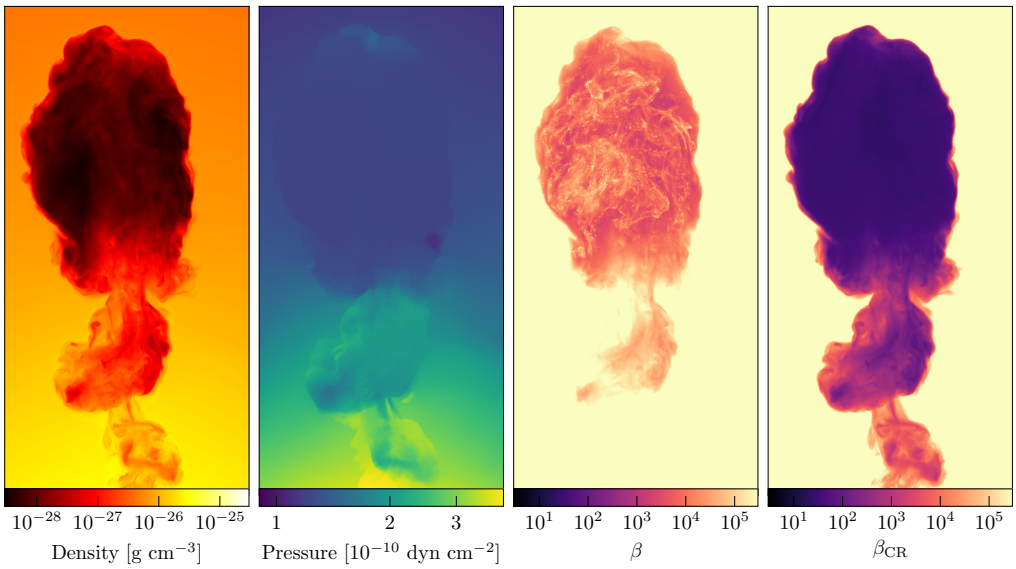

Figure 7.5: Left to right: jet material weighted density, total pressure, plasma beta parameter and thermal over cosmic ray pressure of the resulting radio lobes after 84 Myr, i.e. 34 Myr after the jet became inactive. Each panel is 100 kpc in the vertical and 50 kpc in the horizontal directions, and shows jet material weighted averages over a 50 kpc depth. The projection is centred at a distance of 75 kpc from the black hole.

the lobe exceeds the magnetic and cosmic ray content[6]. This means that about 90% of the lobe thermal energy originates from thermalisation of kinetic energy, not from an initial thermal energy injection[7]. However, even though subdominant, the energies in magnetic fields and cosmic rays are still significant, especially if their dynamics is different than that of an ideal fluid. For example, as seen in Figure 7.3, magnetic fields have a stabilising effect on the lobe with respect to instabilities (Ruszkowski et al., 2007). We furthermore note that the magnetic energy in radio lobes is observed to be close to equipartition with the electron population (Croston et al., 2005, for Fanaroff-Riley type II systems), which implies that we might underestimate the effect of magnetic fields in our simulations. Note, however, that this might not be the case in Fanaroff-Riley type I systems (de Gasperin et al.,

[6]As the density of the lobe at most differs by a factor of a few from the target density $\rho_{\rm target} = 10^{-28}$ g cm^{-3}, this cannot be explained by the different adiabatic expansion behaviour of the thermal, magnetic and CR components.

[7]We neglect diffusive shock acceleration at these shocks that should inject a CR population, which should form a dynamically significant component after adiabatic expansion in the lobe.

2012; Pfrommer, 2013).

The cosmic rays are advected with the thermal fluid throughout this study. This means that the only difference between thermal and cosmic-ray fluid is the adiabatic index (5/3 for the thermal component, 4/3 for the cosmic rays). When CRs are subdominant, the effective adiabatic index stays close to 5/3 in the lobe and its dynamics is not significantly changed. In an astrophysical plasma, however, cosmic rays can propagate along magnetic field lines and thus behave very different from the thermal component (see e.g. Ruszkowski et al., 2017). We will study this in more detail in a forthcoming paper (Ehlert et al., in prep.).

Lobe dynamics

Studying the evolution of an individual lobe with a time-series of slices through the mid-plane showing the mass fraction of jet material (Figure 7.3), it becomes clear that the lobe evolution and disruption is not governed by the onset of Kelvin-Helmholtz (KH) instabilities on ever larger scales, but rather by a Rayleigh-Taylor (RT) like instability which causes surrounding ICM material in the wake of the lobe to rise and shred the lobe inside out. This behaviour has been seen already in previous studies that started out with under-dense lobes at rest (e.g. Reynolds et al., 2005; Sternberg and Soker, 2008). We verified that setting up bubbles at rest in pressure equilibrium in our setup leads to the same dynamics, and therefore conclude that the jet is unimportant for this stage of lobe evolution.

It is important to note that the buoyancy force is proportional to the absolute difference of densities, which means that it does not make a big difference whether the density is reduced by a factor of a few or by ~ 3 orders of magnitude, as in our case. For Kelvin Helmholtz instabilities on the surface layer, however, the growth time depends on the ratio of densities. Because of the large density contrast and the magnetisation, the lobe does not develop Kelvin-Helmholtz instabilities on scales larger than a few kpc.

Quantitatively, the growth timescales for the KH and RT instabilities in ideal hydrodynamics (Chandrasekhar, 1981) are

$$\tau_{\mathrm{KH}} = \frac{\rho_1 + \rho_2}{(\rho_1\,\rho_2)^{0.5}} \frac{1}{\Delta v\, k} \approx \left(\frac{\rho_2}{\rho_1}\right)^{0.5} \frac{1}{\Delta v\, k}, \tag{7.24}$$

$$\tau_{\mathrm{RT}} = \left|\frac{\rho_1 + \rho_2}{\rho_1 - \rho_2} \frac{1}{\dot{v}\, k}\right|^{0.5} \approx \frac{1}{|\dot{v}\, k|^{0.5}}, \tag{7.25}$$

where ρ_1 and ρ_2 are the densities in the lobe and the surrounding ICM, respectively. We assume $\rho_1/\rho_2 \approx 10^{-3}$ (see figure 7.5, left panel). $\Delta v \approx 500$

km s^{-1} is the relative velocity of the shear flow parallel to the surface, $\dot{v} \approx 3.1 \times 10^{-8}$cm s^{-2} is the acceleration of the lobe, and k is the wavenumber of the perturbation. We assume that the acceleration originates purely due to gravitational forces (i.e. that the lobe rises with constant velocity) at a distance of 80 kpc. Using these values, we obtain

$$\tau_{\mathrm{KH}} \approx 600\ (k\,10\,\mathrm{kpc})^{-1}\,\mathrm{Myr}, \tag{7.26}$$

$$\tau_{\mathrm{RT}} \approx 30\ (k\,10\,\mathrm{kpc})^{-0.5}\,\mathrm{Myr}, \tag{7.27}$$

which means that large-scale KH instabilities with $k < (10\ \mathrm{kpc})^{-1}$ do not have enough time to grow. KH eddies on smaller scales, however, do grow (consistent with Fig. 7.3, top panel).

This result differs from the finding by Hillel and Soker (2016), who report that Kelvin-Helmholtz instabilities develop on the lobe surfaces and mix the lobe material significantly. We explain the difference mainly by the different ways the jet is injected. The presence of magnetic fields and a high density contrast might also contribute. Also recall that the simulations are run with ideal MHD. In particular, our modelling does not include any physical viscosity, which would stabilise the lobe further (Reynolds et al., 2005). However, even with our simulations, the lifetime of the lobes can be up to a few times the time the jet is active (Figure 7.3). This implies that, assuming that the jet is active most of the time, the model would naturally produce multiple generations of observable buoyantly rising cavities, as observed in some cool core galaxy clusters.

We note that in cavities filled with a relativistic fluid, the growth time of the associated Kelvin-Helmholtz instability does not depend on the density ratio, but on the ratio of the relativistic enthalpy (see e.g. Reynolds et al., 2002, appendix A)

$$\frac{h_2}{h_1} = \frac{\rho_2 c^2 + \gamma_2 p}{\rho_1 c^2 + \gamma_1 p} \approx \frac{c_{s,1}^2}{c^2} \approx 10^{-4}, \tag{7.28}$$

where it is assumed that the enthalpy in the lobe fluid (2) is completely dominated by the pressure term, while the surrounding ICM (1) is non-relativistic with sound speed $c_{s,1} \approx 3000$ km s^{-1} and the density term dominates. This implies that the growth time of the Kelvin-Helmholtz instability (at fixed shear velocity Δv and wavenumber k) in real lobes has a lower limit independent of lobe density. However, our simulations, using non-relativistic equations, thus $h_2/h_1 = \rho_2/\rho_1$, achieve a similar ratio.

While Kelvin-Helmholtz instabilities require very high numerical resolution of a few hundred parsec, the large-scale nature of the Rayleigh-Taylor

instability, which dominates in our lobes, implies that a resolution of a few kiloparsec is enough to capture the lobe dynamics. This has important consequences for the possible modelling in future (lower resolution) cosmological simulations of galaxy clusters, as will be discussed in detail in Section 7.5.

Lobe mixing

The slow growth time of large-scale KH instabilities gives rise to the question of how fast the lobe material mixes with the surrounding medium. Qualitatively, this is shown in Figure 7.3. We now quantify the degree of mixing in Figure 7.6, which shows the mass fraction of the jet material (normalised by the overall integrated mass flux of the jets) enclosed in a sphere with a given radius as a function of this radius for the different simulations. In all simulations, the dominant part of the jet material ends up (after 336 Myr) at radii larger than 70 kpc, which indicates that the mixing timescale of the jet material is larger than the buoyant timescale. This effect is more pronounced for the high-power jets. For the low-power jet (10^{44} erg s^{-1}), however, a significant fraction of the material stays at distances less than 100 kpc.

Keeping this in mind, we analyse the volume filling fraction of the jet material within the inner 100 kpc in Figure 7.7, where we show the volume fraction of cells with a jet mass contribution higher than $x_{\rm jet}$, as a function of $x_{\rm jet}$. Even accounting for extremely small mass fractions ($x_{\rm jet} \geq 10^{-12}$), the volume fraction stays below 10% after 336 Myr. We note that there might be other transport processes, such as thermal conduction (Kannan et al., 2017), active CR propagation (Ehlert et al., in prep.) or externally induced turbulence, which promote the mixing of the lobe's internal energy, increasing the volume filling factor.

Lobe energetics

Figure 7.8 shows the evolution of the energy in the lobe as a function of time. We split the velocity into a bulk velocity $\mathbf{v}_b$, which is the volume-weighted average velocity in the lobe, and a turbulent component[8] $\mathbf{v}_t$, which is the

[8]All small-scale chaotic motions are referred to as turbulent motions here. We note that, strictly speaking, the decomposition in small-scale and large scale energy contribution can only be done using a mass weighted velocity, which we do not use to avoid contamination from the lobe surface layers. In our case, there is a non-vanishing cross-term between the two velocities, contributing to the energy. We calculate this cross-term and find that it is at least 4 orders of magnitude lower than the other components.

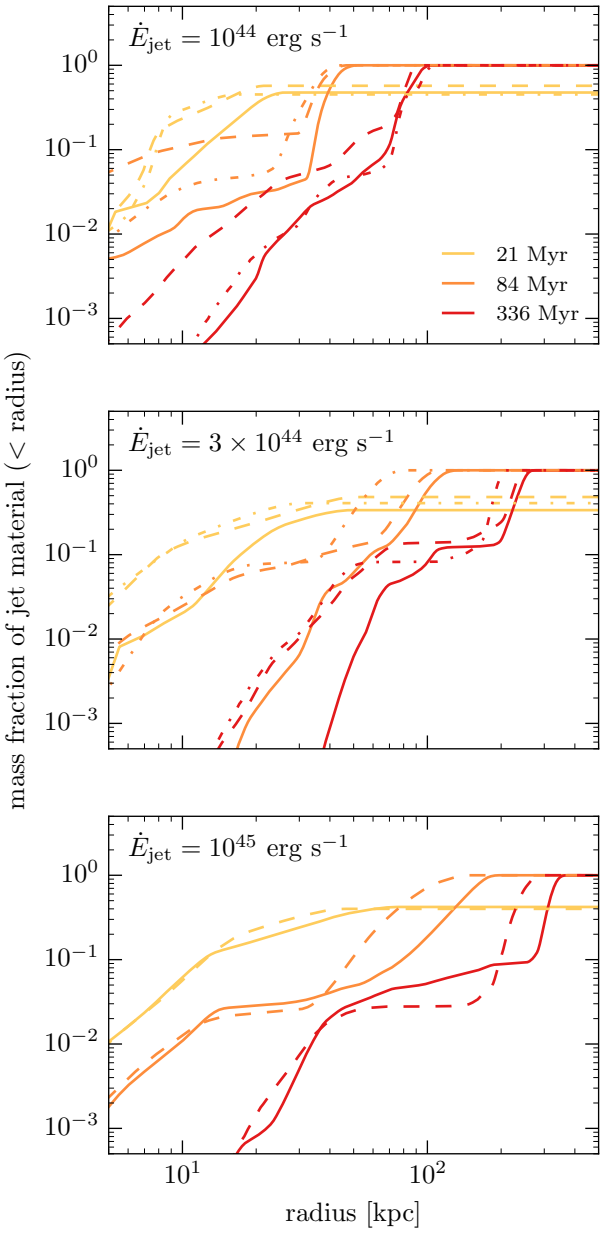

Figure 7.6: Cumulative mass fraction of the jet material as a function of radius for the different jet energies. The dashed and dash-dotted lines indicate the intermediate and low resolution simulations, respectively.

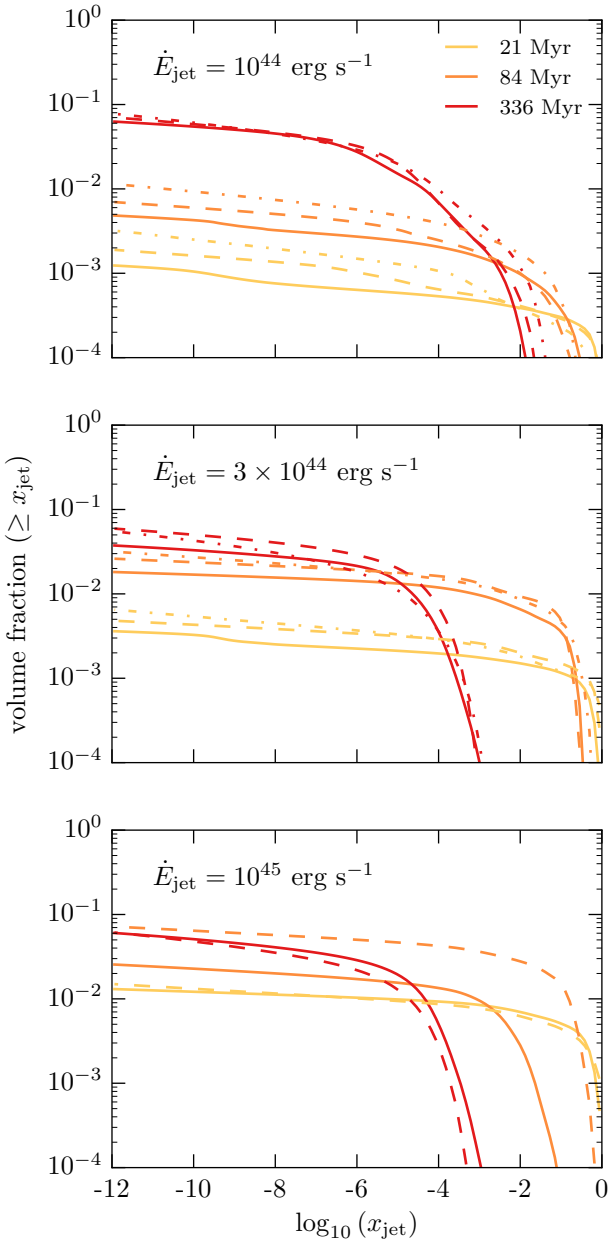

Figure 7.7: Volume filling fraction of the jet material within the central 100 kpc as a function of minimum jet mass fraction. The dashed and dash-dotted lines indicate the intermediate and low resolution simulations, respectively. Note that the discrepancy of the high and low resolution runs at 84 Myr in the lower panel originates from the fact that the lobe height exceeds 100 kpc in the high resolution run, while it is still below 100 kpc in the lower resolution run (see Figure 7.6).

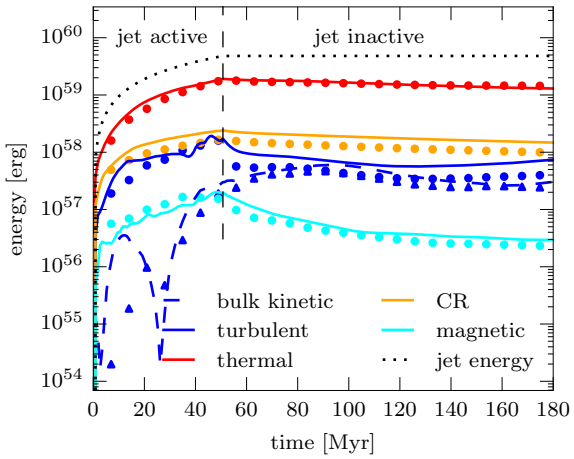

Figure 7.8: Time evolution of different energy components of the lobe. The lobe is defined as all cells that have a mass fraction of jet material higher than 10^{-3}. The vertical dashed line indicates when the jet becomes inactive. The lines indicate the lobe evolution in the intermediate resolution run, for which we have frequent outputs. The dots are the corresponding energies from the high-resolution run.

gas velocity of each cell in the lobe relative to the bulk velocity. This decomposition allows us to study the energies separately. The turbulent kinetic energy in the lobe dominates over the bulk kinetic energy as long as the jet is active. Once the jet has terminated, i.e. to the right of the vertical dashed line in Figure 7.8, the bulk kinetic energy increases due to buoyancy forces, while the turbulent energy decreases. The cosmic ray energy increases at a slightly slower rate compared to the thermal energy, being subdominant by an order of magnitude after the jet terminated. This is consistent with the pressure fractions shown in Figure 7.5. In the jet region, the magnetic pressure is 10% of the cosmic ray pressure. In the further evolution, the ratio of magnetic to cosmic ray energy, as well as the ratio of magnetic to thermal energy, drop, mainly due to a decline in magnetic energy between 50 and 100 Myr (likely due to numerical resistivity). It is remarkable, however, that the magnetic field, though energetically subdominant by a factor of ~ 500 over the thermal component, and even subdominant by an order of magnitude compared to the kinetic energy, still has a significant impact on the lobe morphology and mixing properties (Figure 7.3), which highlights the need for simulations to model MHD in this context. The reason for this behaviour is that in the lobe, the force density due to magnetic tension

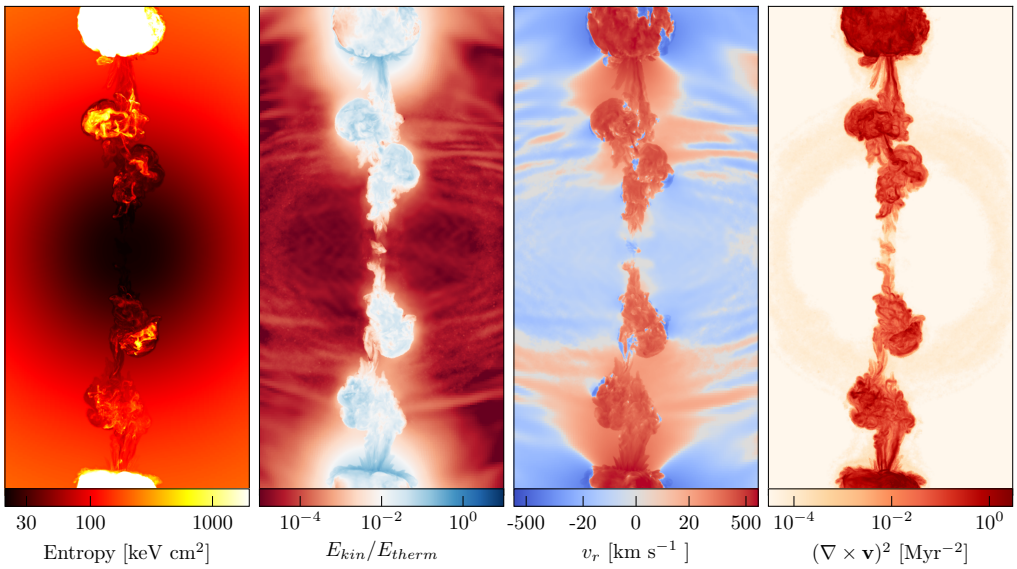

Figure 7.9: Left to right: entropy, kinetic over thermal energy ratio, radial velocity and vorticity squared of the ICM after passage of a magnetised radio-lobe (168 Myr). Each projection is 150 kpc wide, 300 kpc high and 75 kpc deep.

is almost as high as the net force density due to pressure gradients and gravity.

7.4.3 ICM properties

One of the key aspects of AGN jet feedback is the question how the radio lobe interacts with the surrounding ICM. We study this by looking at the entropy and kinetic properties of the gas in Figure 7.9. Excluding lobes, the entropy profile is barely changed, except of a radial feature in the wake of the lobe, in agreement with Figure 7.2. The kinetic energy around the lobe is increased, but does not exceed unity, even in the wake of the lobe where the velocities are highest.

At distances to the lobe surface of more than a few tens of kiloparsec, the kinetic energy fraction drops to sub-per cent level. In the ICM, the kinetic energy fraction stays below a per cent level in our simulations. The map of vorticity squared confirms that the turbulent motions are largely restricted to the wake of the lobe and the cavity itself, but there is a ring-like feature in the ICM at a distance of $\sim$ 75 kpc from the centre. The rising of the lobe induces a systematic outward motion in its wake and a

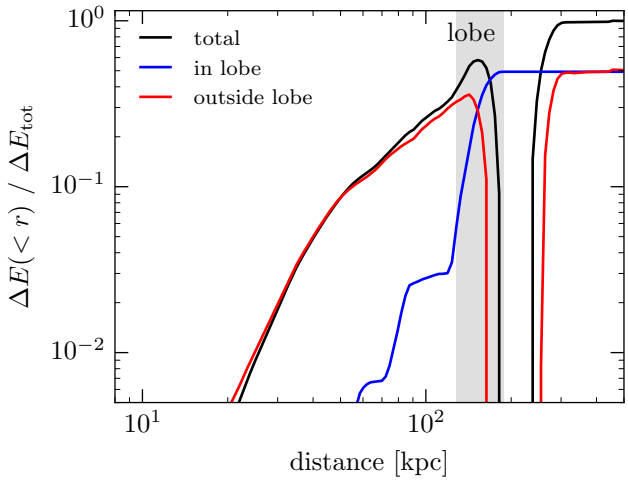

Figure 7.10: Cumulative energy deposition in material enclosed by a given radius vs. radius. The black line shows the total energy, the red line the energy excluding cells with a jet mass fraction of at least 10^{-3}, and the blue line represents the energy in these lobe cells. The shaded region denotes the 10 and 99.9 percentiles of the radio lobe energy, which marks the position of the lobe.

corresponding slow inflow perpendicular to it. This is in agreement with Yang and Reynolds (2016a), who obtain this pattern for a simulation that has a (fixed) directional jet for a simulation time of several Gyr. However, in our case, this happens for each buoyantly rising lobe individually. Another feature are ripples in the radial velocity map and in the kinetic over thermal energy ratio. They seem to be located outside the lobe trajectory, filling a large fraction of the volume. A careful inspection of the entropy map as well as pressure and density maps (not shown here) indicates that these ripples in velocity are coincident with adiabatic fluctuations. This is in qualitative agreement with the idea that sound waves dissipate energy in the ICM in a volume filling fashion (Fabian et al., 2017). We leave a quantitative analysis of the ICM perturbations induced by the jet-lobe system for a future study.

7.4.4 Energy coupling

Figure 7.10 shows the energy gain of gas inside a sphere that encloses a specific mass as a function of the radius this enclosed mass corresponds to in the initial conditions. At small radii, where the lobe already passed, the gain in thermal energy dominates the total energy gain (Figure 7.11). Overall, around 25% of the total energy is deposited in the inner 100 kpc of the

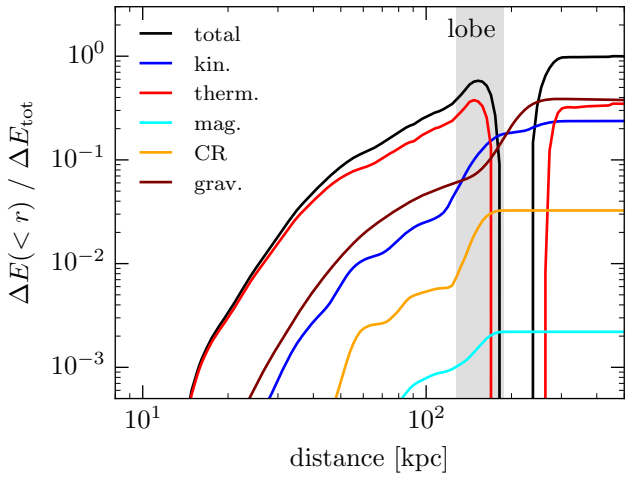

Figure 7.11: Same as figure 7.10, here showing the energy components individually. Note that the range of the vertical axis is changed. We do not make a distinction between lobe and external medium here. The thermal energy clearly dominates the post-lobe energy gain.

ICM. The lobe itself, after having risen buoyantly to a distance of more than 100 kpc, still contains half of the injected energy. The drop and increase in energy change at radii larger than the lobe position can be attributed to the post-shock uplift of the gas (increase in gravitational potential energy in Figure 7.11), an associated adiabatic cooling (simultaneous decrease in thermal energy), and the bow shock (increase of the thermal energy gain to the final value), respectively. The remaining energy is transported outward by a shock to radii of more than 200 kpc. We note that this number does not correspond to the total energy thermalised in shocks.

Overall, about 40% of the energy gain goes into an increase in gravitational energy, about 35% to a thermal energy increase (this includes the thermal energy in the lobe) and more than 20% into kinetic energy, mostly outside the lobe. The energy gains via magnetic fields and cosmic rays ($< 5\%$) are subdominant in this simulation, and mostly confined to the lobe region. The overall energy gain outside the lobe region is about 50%.

This result is in agreement with Reynolds et al. (2002), who find a similar coupling efficiency in their axisymmetric simulations of more energetic jets, as well as a very similar overall dynamics of the system, which shows that the predictions of the simulations are robust against substantial modelling changes.

7.4.5 Shortcomings and missing physics

In this paper, we have introduced a new model for launching jets in magnetohydrodynamical simulations. For the sake of clarity and simplicity, we did not include some additional effects that are known or at least suspected to be important in this context. These include a clumpy interstellar medium, which might significantly change the range and energy deposition of the jets (Mukherjee et al., 2016). Additionally, we only solve the equations of non-relativistic magnetohydrodynamics, which is somewhat inappropriate for the jet velocities reached (English et al., 2016), and treat the jet material and the corresponding lobe, as a thermal fluid with a non-relativistic equation of state (apart from a small contribution of cosmic rays), which is highly approximate at these temperatures (Perucho et al., 2011, 2014) . The jet power is constant for a specific simulation, and not yet linked to the black hole spin and accretion rate, which likely determine the jet power in real systems.

On the galaxy cluster side, potential future improvements include radiative gas cooling and subsequent star formation, stellar feedback and related processes. Furthermore, our simulations do not include the infall of substructure (Mendygral et al., 2012; Bourne and Sijacki, 2017) , a resulting large-scale turbulent velocity, and a self-consistent magnetic field. From a plasma-physics perspective, thermal conduction, viscosity as well as diffusive shock acceleration, transport and interaction processes of CRs with the gas are not included in our set of simulations. Neglecting CR acceleration may be responsible for the artificial dominance of thermal over CR pressure in the lobes.

We leave the systematic study of these effects to future work, though we emphasise that simultaneous improvements in both, small scale jet modelling and galaxy cluster modelling, is restricted by computational and numerical limits. We therefore rather advocate to study, wherever possible, the importance of each of the above listed effects individually at the appropriate level of simplification, *using the same implementation for launching jets* and carefully assessing the possibilities to account for the corresponding effects in larger-scale simulations.

7.5 Resolution dependence

Figure 7.12 shows, as an example, a map of the internal Mach number in simulations with the same jet properties, but different numerical resolution. The three panels on the left hand side correspond to our high resolution,

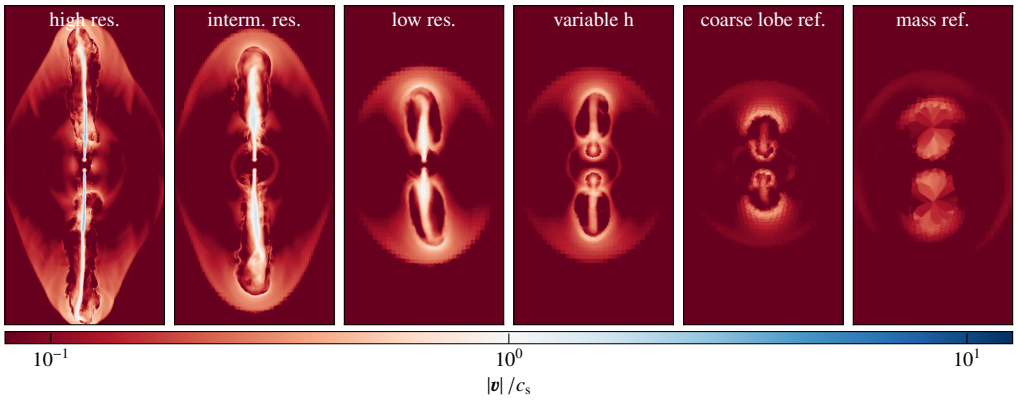

Figure 7.12: Same as Figure 7.4, left panel, for simulations of different resolutions. The three panels on the left show our fiducial high resolution, intermediate resolution, and low resolution simulations, respectively. The three panels on the right are runs with a variable injection kernel size (as used in cosmological simulations), and simulations that successively disable the special refinement criteria used for this study.

intermediate resolution, and low-resolution results, respectively. The first thing to notice is that the propagation distance of the jet increases with resolution. This is likely linked to the fact that a poorly resolved velocity gradient across the jet leads to a widening of the jet. We note that the computational grid does not line up along the jet direction in our case, which causes a numerical widening of the jet if the flow is not sufficiently resolved. For our high-resolution simulation, where the jet diameter is resolved by ~ 25 cells, this effect is significantly reduced, which means that the loss of momentum and kinetic energy flux is small and therefore the jet propagates further.

The three panels on the right-hand side (from centre to right) show simulations with a variable injection kernel, as would be used in cosmological simulations, and successively relaxed refinement criteria. While the first of these panels ('variable h') has the same resolution settings as the low resolution run, the middle one ('coarse lobe ref.') has a reduced target volume ($V_{\rm target}^{1/3} \approx 1.5$ kpc) and no refinement criteria on the gradient of the density or volume limitations. The rightmost panel ('mass ref') shows a run where the only refinement criteria is the target mass of a cell. The change to an injection region which varies in size depending on the surrounding density leads to a less well-defined jet which is in general slower, while the main structure is still captured. Decreasing the resolution in the outflow further to kpc scales, the nature of the outflow changes, as it is no longer

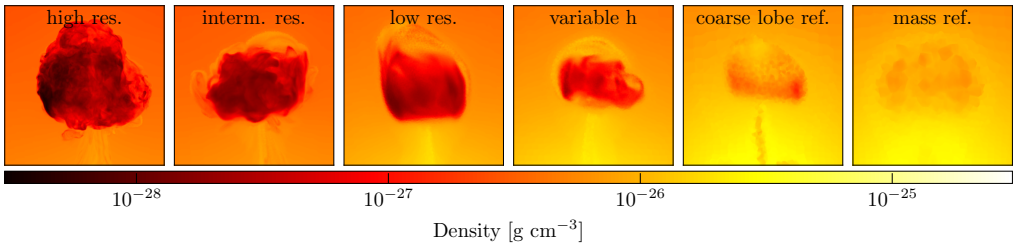

Figure 7.13: Lobe-averaged density after 168 Myr. The panels are 75 by 75 kpc, centred on the upper lobe, and are 50 kpc deep.

reaching supersonic velocities. Having a pure mass criterion for refinement is (as expected) an inappropriate choice for the problem at hand. In particular, the redistribution of mass from the jet region to the buffer region (see Section 7.2.1) leads to low-mass cells in the jet region. Having only a mass criterion for refinement and derefinement, these cells are derefined immediately (causing merging with the surrounding higher density cells) and thus become numerically mixed. Therefore, it is not possible to simulate a low-density outflow in a meaningful way with this numerical treatment.

The morphology of the lobe is more robust to resolution changes than the jet itself. Figure 7.13 shows the jet-material weighted density of the lobe. Each panel is 75 kpc wide and centred on the median lobe position, to compensate for the different height due to the different jet propagation properties discussed previously. The projections are made after 168 Myr, i.e. at a stage where the lobe is already relatively evolved (see Figure 7.3). The left three panels, i.e. the high, intermediate and low resolution lobes, show a similar overall shape and density, which means that we expect a similar dynamics for them. For the runs with a variable injection kernel, we see a successively smaller and denser lobe, forming a less coherent structure, indicating that more material has mixed with the surroundings for numerical reasons. For reasons discussed above, the run using only a refinement criterion based on a target mass never forms a significantly under-dense structure and mixes with its surroundings very efficiently.

One of the key features of a predictive model for AGN jet-mode feedback is the ability to deposit the jet energy radially in the same way, and in the same form as in the high-resolution simulations presented in this work. To assess this issue, we plot the energy change in a sphere with given enclosed mass as a function of the corresponding radius in Figure 7.14. The general shape of this function is preserved for different resolution, indicating that the general structure of the lobe (inner maximum) and the bow shock (maximum at larger distances) is preserved. The position of the bow

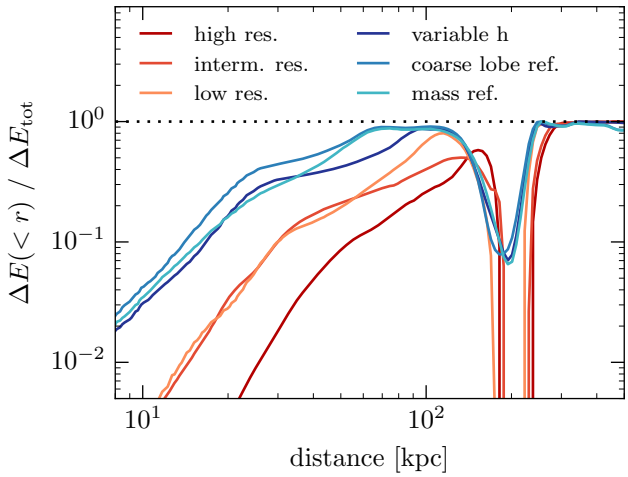

Figure 7.14: Cumulative energy deposition in material enclosed by a given radius vs radius for simulations with different resolutions.

shock is very robust, too, even considering the drastic changes in resolution. This can be explained by the excellent shock-capturing properties of the finite-volume approach used in this study. The lobe structure, however, is located at successively larger distances when going to higher resolution. This can be explained by the different jet propagation properties, as shown in Figure 7.12.

Apart from this change, there is an additional difference concerning the relative height of the first peak, which is lower for the high-resolution simulations. This indicates that the bow-shock is energetically more important in the higher resolution simulations than in the low-resolution run. We note, however, that the relative energies do not indicate the energy dissipated in the bow shock vs the energy retained in the lobe.

For potential use of such a model in cosmological simulations, or in general simulations with lower resolution, this means that the energy deposition is in general too centrally concentrated at low resolution, whereas the radial distribution of the energy up to the height of the lobe is approximately the same. Keeping in mind that simulations of galaxy clusters develop a self-regulated cooling-heating balance, one would expect the black hole accretion rate to drop by the overestimate of central heating, which would further decrease the range of the low-resolution jet. A possible way to compensate for such a propagation effect is to artificially prolong the duty cycle of poorly resolved jets, such that the resulting lobes end up at the same height. Given the uncertainties in both, the duty cycle and the conversion

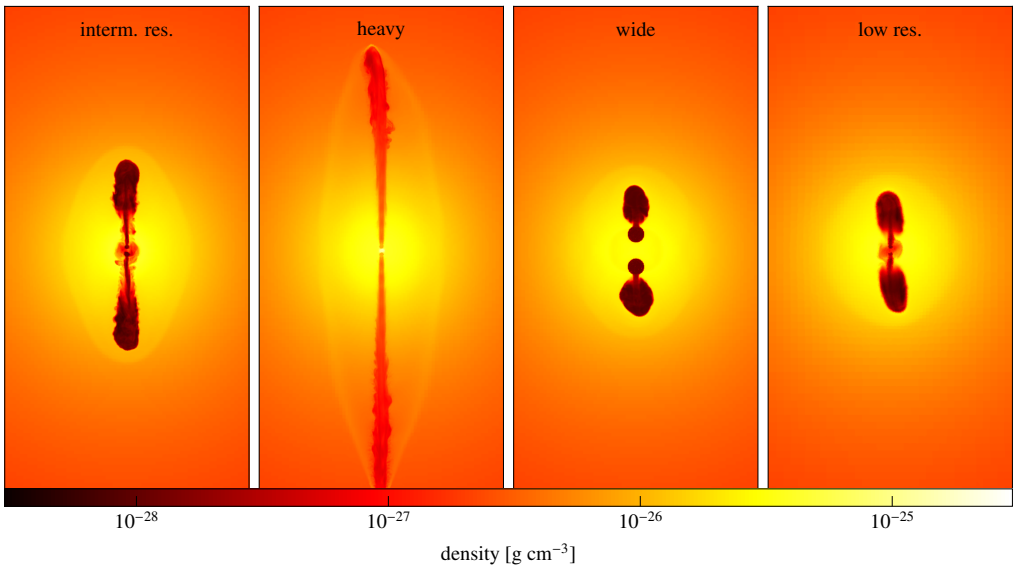

Figure 7.15: Jet material weighted density projection of different model parameter variations. Each panel is 400 kpc high, 200 kpc wide and average over a depth of 20 kpc. The model variation are run with the same resolution as the fiducial run.

efficiency of black hole accretion rate to jet power, this could be an acceptable way to compensate for the above mentioned resolution effects, allowing use of the model in lower resolution simulations.

7.6 Dependence on model parameters

We already discussed the effect of jet magnetisation in the main text. For completeness, we discuss the variations of jet density $\rho_{\rm target}$ and the precise choice of the size of the jet injection region, parameterised by h in this section. Figure 7.15 shows the density projections in panels of $200 \times 400\,{\rm k}pc^2$ for the fiducial ('fid', intermediate resolution) runs as well as for a jet with $\rho_{\rm target} = 10^{-26}$ g cm^{-3}, i.e. 100 times higher initial jet density ('heavy'). Unsurprisingly, the heavy jet, carrying more momentum given the same amount of kinetic energy, propagates further, leading to an extremely elongated cavity extending far beyond 100 kpc. Consequently, such a jet will have a very different impact on the surrounding ICM, which is why we consider this parameter as the main uncertainty in modelling jet-mode feedback by AGN.

The 'wide' panel of Figure 7.15 shows a jet where we increased the parameter h to 20 kpc, i.e. by a factor of 4. This has significant consequences for the width of the jet and consequently its propagation distance. This effect is similar to a decrease in resolution (see 'low res'), however, for a different reason. As already discussed in Appendix 7.5, the precise range of the jet is not converged for all possible resolutions used in this study, and it is subject to additional uncertainties due to the modelled jet and galaxy cluster effects (see discussion in Section 7.4.1). We therefore do not consider the parameter h to be a dominant factor of uncertainty in our model, in particular as the lobe density is largely unaffected by it.

7.7 Conclusions

In this paper, we present a new model for jets in the Arepo code. It is based on the preparation of the thermodynamic state of the jet material on marginally resolved scales close to the SMBH, and a redistribution of material to (or from) the surrounding gas for mass conservation. We study the evolution of light, magnetised jets in idealised simulations of hydrostatic cluster-sized halos. Here, the jet represents a kinetically dominated energy flux which reaches mildly supersonic velocities. At the head of the jet, the low density jet material is slowed down by the ram pressure of the denser, ambient ICM and thermalises most of its kinetic energy via shocks. This leads to an inflation of low-density, hot, magnetised cavities containing a population of CRs, in pressure equilibrium with the surrounding ICM.

The cavities rise buoyantly and get deformed and eventually disrupted by a Rayleigh-Taylor like instability, similarly to what has been seen in previous simulations of idealised radio lobes. In the wake of the lobe, an upward flow is induced which shows high vorticity and a kinetic energy of up to a few percent of the thermal energy. Very close to the cavity, this fraction rises to almost unity. Overall, the rising cavities induce an upward motion in the wake of the cavity, which is compensated by a slow downward motion at the sides and perpendicular to it, similar as reported by Churazov et al. (2001) and Yang and Reynolds (2016a). The shear flow at the lobe surface can cause Kelvin-Helmholtz instabilities, yet, we find that their growth time is sufficiently suppressed with respect to the Rayleigh-Taylor growth time in our simulations.

Consequently, the mixing of lobe material with the surrounding ICM is energetically unimportant in the centre of the halo. Overall, we find that about half of the injected jet energy is deposited in regions outside the lobe. After passage of the lobe, $\sim 25\%$ of the injected energy is deposited in the

inner 100 kpc, which is dominated by an increase in thermal energy, while the remaining energy can be found in material affected by the bow shock at large radii, which mostly gained gravitational energy.

This study of the jet-ICM interaction at very high resolution has allowed us to identify some of the main mechanisms governing lobe dynamics and to quantify the energy coupling efficiency. It also provides guidance for modelling jets from AGN more realistically in simulations of galaxy clusters. We find that the main requirements for such a model are to resolve the (lobe-scale) Rayleigh-Taylor instability and to maintain a large density contrast between lobe and surrounding ICM, which calls for sufficiently good control of numerical mixing in the hydrodynamic scheme. In Section 7.5, we study at which resolution these requirements can be fulfilled. We conclude that, while still highly challenging or beyond reach for present simulations, the corresponding resolutions should be achievable in the next generations of cosmological 'zoom-in' simulations of galaxy clusters.

Part IV

Conclusions and outlook

8

Cosmological simulations

The physics of supermassive black holes is a key ingredient to many state of the art cosmological simulations of galaxy formation. Their feedback effects counteract radiative cooling losses of the gas in massive galaxies and thereby reduce star-formation in these systems significantly. I presented one particular implementation of such a model, which uses a two-mode prescription for AGN feedback with a moderately efficient, continuos thermal injection of energy in phases of rapid accretion relative to the Eddington limit, and an efficient, pulsed, kinetic injection at comparably low accretion rates. The model is able to produce a bimodal galaxy colour distribution, similar to what is observed in galaxy surveys (see also Nelson et al., 2017), with a transition in galaxy colours at stellar masses of about $10^{10.5}$ $M_{\odot}$. The red galaxy population has very little ongoing star formation. We showed that this is coincident with an efficient kinetic feedback which becomes active at comparably low accretion rates relative to the Eddington limit, while SMBHs in the thermal mode are responsible for the growth via gas accretion.

The described implementation for AGN feedback forms one of the key ingredients in the galaxy formation physics model used in the IllustrisTNG simulation. The model produces high mass galaxies that are significantly more realistic compared to previous generations of cosmological hydrodynamical simulations (Vogelsberger et al., 2014c; Genel et al., 2014). This allows more detailed studies of the (satellite) galaxy population around massive central galaxies in galaxy groups and clusters, their hydrodynamical interactions with the host's gaseous halo and consequences such as the enrichment of this hot halo gas in galaxy clusters (Vogelsberger et al., 2017). Furthermore, the model provides a plausible scenario for the co-evolution between SMBHs and their host galaxies. In particular, opposite to the commonly assumed scenario of luminous AGN, triggered by gas rich major mergers, quenching the high-mass galaxy population (Hopkins et al., 2008b), the IllustrisTNG model quenches via feedback from the low accre-

tion state, and consequently predominantly in galaxies that did not have a major merger immediately prior to quenching. I showed that it is possible to create such a model in a self-consistent way in cosmological simulations, while producing a galaxy population in agreement with observations, as far as we tested (Springel et al., 2017; Marinacci et al., 2017; Naiman et al., 2017; Pillepich et al., 2017a; Nelson et al., 2017; Genel et al., 2017; Vogelsberger et al., 2017; Weinberger et al., 2017b). Future observations targeting the correlations between kinematic disturbances (as signs for major mergers) and recent reduction in star formation rate (i.e. quenching) will likely reveal whether this is a viable scenario.

9

Active galactic nucleus jet feedback

One of the remaining open questions that the coarse grained models used in cosmological simulations cannot answer is how efficient AGN feedback, say for example an AGN driven collimated jet in a galaxy cluster, is in distributing its energy into the surrounding medium. To answer this question, I developed a model that injects a bipolar, collimated low-density outflow on kpc scales and follow its evolution in idealised high resolution simulations of hydrostatic halos. With these simulations it is possible to follow the jet propagation, its slow-down and the inflation of low-density lobes in the hydrostatic atmosphere in detail.

Studying the jet-inflated, low-density lobes and their buoyant rising, it is possible to deduce the net effect AGN jets have on their surrounding intra-cluster medium. While the lobe itself stays intact for several hundred Myr, mainly because Kelvin-Helmholtz instabilities are suppressed due to the large density contrast between the lobe and its surrounding, the overall, Rayleigh-Taylor like, flow pattern induced by the rising lobe itself is eventually responsible for the disruption of the lobe via uprising material in the wake of the lobe. However, as this effect acts on a buoyant timescale, the efficiency of mixing of lobe material with the surrounding is very low, indicating that the thermal state of the intra-cluster medium is not significantly affected by mixing. The gas flow patterns in the center of the hydrostatic halo show no significant increase in vorticity and thus turbulence in directions perpendicular to the jet, indicating that the buoyantly rising lobe does not drive significant levels of volume-filling turbulence in the surroundings.

Looking at the overall energy change due to a jet inflated, buoyantly rising lobe in the simulations, I nonetheless find a reasonably high coupling efficiency of up to $\sim 50\%$ to the surrounding gas behind the lobe. Disentangling this in different energy components shows mainly a gain in thermal energy, but also substantial amounts of gravitational and kinetic energy, suggesting that the main coupling originates from the $P\,dV$ work done on the hydrostatic halo and the fall-back of halo gas once the lobe has risen to

the outer parts. Future work will include a large set of such simulations in a more realistic environment to investigate which aspects of the surrounding medium is crucial for the efficiency of the AGN jet–intra-cluster medium interaction.

Publications by Rainer Weinberger

D.J. Barnes, M. Vogelsberger, R. Kannan, F. Marinacci, R. Weinberger, V. Springel, P. Torrey, A. Pillepich, D. Nelson, R. Pakmor, J. Naiman, L. Hernquist, M. McDonald. A census of cool core galaxy clusters in IllustrisTNG. ArXiv:1710.08420, Oct. 2017.

S. Genel, D. Nelson, A. Pillepich, V. Springel, R. Pakmor, R. Weinberger, L. Hernquist, J. Naiman, M. Vogelsberger, F. Marinacci, and P. Torrey. The Size Evolution of Star-forming and Quenched Galaxies in the IllustrisTNG simulation. ArXiv:1707.05327, July 2017.

R. Kannan, M. Vogelsberger, C. Pfrommer, R. Weinberger, V. Springel, L. Hernquist, E. Puchwein, and R. Pakmor. Increasing Black Hole Feedback-induced Quenching with Anisotropic Thermal Conduction. ApJ, 837:L18, Mar. 2017.

F. Marinacci, M. Vogelsberger, R. Pakmor, P. Torrey, V. Springel, L. Hernquist, D. Nelson, R. Weinberger, A. Pillepich, J. Naiman, and S. Genel. First results from the IllustrisTNG simulations: radio haloes and magnetic fields. ArXiv:1707.03396, July 2017.

J. P. Naiman, A. Pillepich, V. Springel, E. Ramirez-Ruiz, P. Torrey, M. Vogelsberger, R. Pakmor, D. Nelson, F. Marinacci, L. Hernquist, R. Weinberger, and S. Genel. First results from the IllustrisTNG simulations: A tale of two elements – chemical evolution of magnesium and europium. ArXiv:1707.03401, July 2017.

D. Nelson, A. Pillepich, V. Springel, R. Weinberger, L. Hernquist, R. Pakmor, S. Genel, P. Torrey, M. Vogelsberger, G. Kauffmann, F. Marinacci, and J. Naiman. First results from the IllustrisTNG simulations: the galaxy color bimodality. ArXiv:1707.03395, July 2017.

A. Pillepich, D. Nelson, L. Hernquist, V. Springel, R. Pakmor, P. Torrey, R. Weinberger, S. Genel, J. Naiman, F. Marinacci, and M. Vogelsberger. First results from the IllustrisTNG simulations: the stellar mass content of groups and clusters of galaxies. ArXiv:1707.03406, July 2017a.

A. Pillepich, V. Springel, D. Nelson, S. Genel, J. Naiman, R. Pakmor, L. Hernquist, P. Torrey, M. Vogelsberger, R. Weinberger, and F. Marinacci. Simulating Galaxy Formation with the IllustrisTNG Model. ArXiv:1703.02970, Mar. 2017b.

V. Springel, R. Pakmor, A. Pillepich, R. Weinberger, D. Nelson, L. Hernquist, M. Vogelsberger, S. Genel, P. Torrey, F. Marinacci, and J. Naiman. First results from the IllustrisTNG simulations: matter and galaxy clus- tering. ArXiv:1707.03397, July 2017.

M. Vogelsberger, F. Marinacci, P. Torrey, S. Genel, V. Springel, R. Weinberger, R. Pakmor, L. Hernquist, J. Naiman, A. Pillepich, and D. Nelson. The uniformity and time-invariance of the intra-cluster metal distribution in galaxy clusters from the IllustrisTNG simulations. ArXiv:1707.05318, July 2017.

* R. Weinberger, V. Springel, L. Hernquist, A. Pillepich, F. Marinacci, R. Pakmor, D. Nelson, S. Genel, M. Vogelsberger, J. Naiman, and P. Torrey. Simulating galaxy formation with black hole driven thermal and kinetic feedback. MNRAS, 465:3291-3308, Mar. 2017.

* R. Weinberger, K. Ehlert, C. Pfrommer, R., V. Springel. Simulating the interaction of jets with the intra-cluster medium. MNRAS, 470:4530-4546, Oct. 2017.

* R. Weinberger, V. Springel, R. Pakmor, D. Nelson, S. Genel, A. Pillepich, M. Vogelsberger, F. Marinacci, J. Naiman, P. Torrey, L. Hernquist. Supermassive black holes and their feedback effects in the IllustrisTNG simulation. ArXiv:1710.04659, Oct. 2017.

* part of this thesis.

Bibliography

J. Aird, A. L. Coil, and A. Georgakakis. X-rays across the galaxy population - I. Tracing the main sequence of star formation. *MNRAS*, 465:3390–3415, Mar. 2017a.

J. Aird, A. L. Coil, and A. Georgakakis. X-rays across the galaxy population - II. The distribution of AGN accretion rates as a function of stellar mass and redshift. *arXiv:1705.01132*, May 2017b.

A. Alavi, B. Siana, J. Richard, D. P. Stark, C. Scarlata, H. I. Teplitz, W. R. Freeman, A. Dominguez, M. Rafelski, B. Robertson, and L. Kewley. Ultra-faint Ultraviolet Galaxies at z ˜ 2 behind the Lensing Cluster A1689: The Luminosity Function, Dust Extinction, and Star Formation Rate Density. *ApJ*, 780:143, Jan. 2014.

A. Albrecht and P. J. Steinhardt. Cosmology for grand unified theories with radiatively induced symmetry breaking. *Physical Review Letters*, 48:1220–1223, Apr. 1982.

A. Albrecht, P. J. Steinhardt, M. S. Turner, and F. Wilczek. Reheating an inflationary universe. *Physical Review Letters*, 48:1437–1440, May 1982.

P. Amaro-Seoane, S. Aoudia, S. Babak, P. Binétruy, E. Berti, A. Bohé, C. Caprini, M. Colpi, N. J. Cornish, K. Danzmann, J.-F. Dufaux, J. Gair, O. Jennrich, P. Jetzer, A. Klein, R. N. Lang, A. Lobo, T. Littenberg, S. T. McWilliams, G. Nelemans, A. Petiteau, E. K. Porter, B. F. Schutz, A. Sesana, R. Stebbins, T. Sumner, M. Vallisneri, S. Vitale, M. Volonteri, and H. Ward. Low-frequency gravitational-wave science with eLISA/NGO. *Classical and Quantum Gravity*, 29(12):124016, June 2012.

D. Anglés-Alcázar, F. Özel, and R. Davé. Black Hole-Galaxy Correlations without Self-regulation. *ApJ*, 770:5, June 2013.

D. Anglés-Alcázar, F. Özel, R. Davé, N. Katz, J. A. Kollmeier, and B. D. Oppenheimer. Torque-limited Growth of Massive Black Holes in Galaxies across Cosmic Time. *ApJ*, 800:127, Feb. 2015.

D. Anglés-Alcázar, R. Davé, C.-A. Faucher-Giguère, F. Özel, and P. F. Hopkins. Gravitational torque-driven black hole growth and feedback in cosmological simulations. *MNRAS*, 464:2840–2853, Jan. 2017a.

D. Anglés-Alcázar, C.-A. Faucher-Giguère, E. Quataert, P. F. Hopkins, R. Feldmann, P. Torrey, A. Wetzel, and D. Kereš. Black Holes on FIRE: Stellar Feedback Limits Early Feeding of Galactic Nuclei. *arXiv:1707.03832*, July 2017b.

E. Bañados, B. P. Venemans, R. Decarli, E. P. Farina, C. Mazzucchelli, F. Walter, X. Fan, D. Stern, E. Schlafly, K. C. Chambers, H.-W. Rix, L. Jiang, I. McGreer, R. Simcoe, F. Wang, J. Yang, E. Morganson, G. De Rosa, J. Greiner, M. Baloković, W. S. Burgett, T. Cooper, P. W. Draper, H. Flewelling, K. W. Hodapp, H. D. Jun, N. Kaiser, R.-P. Kudritzki, E. A. Magnier, N. Metcalfe, D. Miller, J.-T. Schindler, J. L. Tonry, R. J. Wainscoat, C. Waters, and Q. Yang. The Pan-STARRS1 Distant z < 5.6 Quasar Survey: More than 100 Quasars within the First Gyr of the Universe. *ApJS*, 227:11, Nov. 2016.

R. D. Baldi, A. Capetti, and G. Giovannini. Pilot study of the radio-emitting AGN population: the emerging new class of FR 0 radio-galaxies. *A&A*, 576:A38, Apr. 2015.

R. D. Baldi, A. Capetti, and G. Giovannini. The new class of FR 0 radio galaxies. *Astronomische Nachrichten*, 337:114, Feb. 2016.

C. Barber, J. Schaye, R. G. Bower, R. A. Crain, M. Schaller, and T. Theuns. The origin of compact galaxies with anomalously high black hole masses. *MNRAS*, 460:1147–1161, July 2016.

J. Barnes and P. Hut. A hierarchical O(N log N) force-calculation algorithm. *Nature*, 324:446–449, Dec. 1986.

J. E. Barnes and L. Hernquist. Transformations of Galaxies. II. Gasdynamics in Merging Disk Galaxies. *ApJ*, 471:115, Nov. 1996.

R. Barniol Duran, A. Tchekhovskoy, and D. Giannios. Simulations of AGN jets: magnetic kink instability versus conical shocks. *MNRAS*, 469:4957–4978, Aug. 2017.

J. F. Basson and P. Alexander. The long-term effect of radio sources on the intracluster medium. *MNRAS*, 339:353–359, Feb. 2003.

A. Bauer and V. Springel. Subsonic turbulence in smoothed particle hydrodynamics and moving-mesh simulations. *MNRAS*, 423:2558–2578, July 2012.

M. C. Begelman. Accreting Black Holes. *arXiv:1410.8132*, Oct. 2014.

P. S. Behroozi, R. H. Wechsler, and C. Conroy. On the Lack of Evolution in Galaxy Star Formation Efficiency. *ApJ*, 762:L31, Jan. 2013a.

P. S. Behroozi, R. H. Wechsler, and C. Conroy. The Average Star Formation Histories of Galaxies in Dark Matter Halos from z = 0-8. *ApJ*, 770:57, June 2013b.

J. Bellovary, M. Volonteri, F. Governato, S. Shen, T. Quinn, and J. Wadsley. The First Massive Black Hole Seeds and Their Hosts. *ApJ*, 742:13, Nov. 2011.

R. Bieri, Y. Dubois, J. Rosdahl, A. Wagner, J. Silk, and G. A. Mamon. Outflows driven by quasars in high-redshift galaxies with radiation hydrodynamics. *MNRAS*, 464:1854–1873, Jan. 2017.

L. Bîrzan, D. A. Rafferty, B. R. McNamara, M. W. Wise, and P. E. J. Nulsen. A Systematic Study of Radio-induced X-Ray Cavities in Clusters, Groups, and Galaxies. *ApJ*, 607:800–809, June 2004.

R. D. Blandford and D. G. Payne. Hydromagnetic flows from accretion discs and the production of radio jets. *MNRAS*, 199:883–903, June 1982.

R. D. Blandford and R. L. Znajek. Electromagnetic extraction of energy from Kerr black holes. *MNRAS*, 179:433–456, May 1977.

H. Boehringer, W. Voges, A. C. Fabian, A. C. Edge, and D. M. Neumann. A ROSAT HRI study of the interaction of the X-ray-emitting gas and radio lobes of NGC 1275. *MNRAS*, 264:L25–L28, Oct. 1993.

M. Boettcher, D. E. Harris, and H. Krawczynski. *Relativistic Jets from Active Galactic Nuclei*. Jan. 2012.

H. Bondi. On spherically symmetrical accretion. *MNRAS*, 112:195, 1952.

H. Bondi and F. Hoyle. On the mechanism of accretion by stars. *MNRAS*, 104:273, 1944.

C. M. Booth and J. Schaye. Cosmological simulations of the growth of supermassive black holes and feedback from active galactic nuclei: method and tests. *MNRAS*, 398:53–74, Sept. 2009.

M. A. Bourne and D. Sijacki. AGN jet feedback on a moving mesh: cocoon inflation, gas flows and turbulence. *arXiv:1705.07900*, May 2017.

R. G. Bower, A. J. Benson, R. Malbon, J. C. Helly, C. S. Frenk, C. M. Baugh, S. Cole, and C. G. Lacey. Breaking the hierarchy of galaxy formation. *MNRAS*, 370:645–655, Aug. 2006.

R. G. Bower, J. Schaye, C. S. Frenk, T. Theuns, M. Schaller, R. A. Crain, and S. McAlpine. The dark nemesis of galaxy formation: why hot haloes trigger black hole growth and bring star formation to an end. *MNRAS*, 465:32–44, Feb. 2017.

F. Brighenti and W. G. Mathews. Stopping Cooling Flows with Jets. *ApJ*, 643:120–127, May 2006.

M. Brüggen and C. R. Kaiser. Buoyant radio plasma in clusters of galaxies. *MNRAS*, 325:676–684, Aug. 2001.

M. Brüggen, C. R. Kaiser, E. Churazov, and T. A. Enßlin. Simulation of radio plasma in clusters of galaxies. *MNRAS*, 331:545–555, Apr. 2002.

M. Brüggen, S. Heinz, E. Roediger, M. Ruszkowski, and A. Simionescu. Shock heating by Fanaroff-Riley type I radio sources in galaxy clusters. *MNRAS*, 380:L67–L70, Sept. 2007.

D.-F. Bu, F. Yuan, Z.-M. Gan, and X.-H. Yang. Hydrodynamical Numerical Simulation of Wind Production from Black Hole Hot Accretion Flows at Very Large Radii. *ApJ*, 818:83, Feb. 2016.

J. Buchner, A. Georgakakis, K. Nandra, M. Brightman, M.-L. Menzel, Z. Liu, L.-T. Hsu, M. Salvato, C. Rangel, J. Aird, A. Merloni, and N. Ross. Obscuration-dependent Evolution of Active Galactic Nuclei. *ApJ*, 802:89, Apr. 2015.

A. Cattaneo and R. Teyssier. AGN self-regulation in cooling flow clusters. *MNRAS*, 376:1547–1556, Apr. 2007.

R. Cen. A hydrodynamic approach to cosmology - Methodology. *ApJS*, 78: 341–364, Feb. 1992.

S. Chandrasekhar. *Hydrodynamic and Hydromagnetic Stability*. Dover, New York, 1981.

E. Cheung, K. Bundy, M. Cappellari, S. Peirani, W. Rujopakarn, K. Westfall, R. Yan, M. Bershady, J. E. Greene, T. M. Heckman, N. Drory, D. R. Law, K. L. Masters, D. Thomas, D. A. Wake, A.-M. Weijmans, K. Rubin, F. Belfiore, B. Vulcani, Y.-M. Chen, K. Zhang, J. D. Gelfand, D. Bizyaev, A. Roman-Lopes, and D. P. Schneider. Suppressing star formation in quiescent galaxies with supermassive black hole winds. *Nature*, 533:504–508, May 2016.

E. Choi, J. P. Ostriker, T. Naab, and P. H. Johansson. Radiative and Momentum-based Mechanical Active Galactic Nucleus Feedback in a Three-dimensional Galaxy Evolution Code. *ApJ*, 754:125, Aug. 2012.

E. Choi, T. Naab, J. P. Ostriker, P. H. Johansson, and B. P. Moster. Consequences of mechanical and radiative feedback from black holes in disc galaxy mergers. *MNRAS*, 442:440–453, July 2014.

E. Choi, J. P. Ostriker, T. Naab, L. Oser, and B. P. Moster. The impact of mechanical AGN feedback on the formation of massive early-type galaxies. *MNRAS*, 449:4105–4116, June 2015.

E. Churazov, M. Brüggen, C. R. Kaiser, H. Böhringer, and W. Forman. Evolution of Buoyant Bubbles in M87. *ApJ*, 554:261–273, June 2001.

E. Churazov, W. Forman, C. Jones, and H. Böhringer. XMM-Newton Observations of the Perseus Cluster. I. The Temperature and Surface Brightness Structure. *ApJ*, 590:225–237, June 2003.

E. Churazov, S. Sazonov, R. Sunyaev, W. Forman, C. Jones, and H. Böhringer. Supermassive black holes in elliptical galaxies: switching from very bright to very dim. *MNRAS*, 363:L91–L95, Oct. 2005.

S. Cielo, V. Antonuccio-Delogu, A. V. Macciò, A. D. Romeo, and J. Silk. 3D simulations of the early stages of AGN jets: geometry, thermodynamics and backflow. *MNRAS*, 439:2903–2916, Apr. 2014.

S. Cielo, V. Antonuccio-Delogu, J. Silk, and A. D. Romeo. Backflows by active galactic nuclei jets: global properties and influence on supermassive black hole accretion. *MNRAS*, 467:4526–4539, June 2017.

L. Ciotti, J. P. Ostriker, and D. Proga. Feedback from Central Black Holes in Elliptical Galaxies. III. Models with Both Radiative and Mechanical Feedback. *ApJ*, 717:708–723, July 2010.

T. Costa, D. Sijacki, and M. G. Haehnelt. Feedback from active galactic nuclei: energy- versus momentum-driving. *MNRAS*, 444:2355–2376, Nov. 2014.

J. H. Croston, M. J. Hardcastle, D. E. Harris, E. Belsole, M. Birkinshaw, and D. M. Worrall. An X-Ray Study of Magnetic Field Strengths and Particle Content in the Lobes of FR II Radio Sources. *ApJ*, 626:733–747, June 2005.

D. J. Croton, V. Springel, S. D. M. White, G. De Lucia, C. S. Frenk, L. Gao, A. Jenkins, G. Kauffmann, J. F. Navarro, and N. Yoshida. The many lives of active galactic nuclei: cooling flows, black holes and the luminosities and colours of galaxies. *MNRAS*, 365:11–28, Jan. 2006.

M. Curtis and D. Sijacki. Resolving flows around black holes: numerical technique and applications. *MNRAS*, 454:3445–3463, Dec. 2015.

M. Curtis and D. Sijacki. Resolving flows around black holes: the impact of gas angular momentum. *MNRAS*, 463:63–77, Nov. 2016.

F. de Gasperin, E. Orrú, M. Murgia, A. Merloni, H. Falcke, R. Beck, R. Beswick, L. Bîrzan, A. Bonafede, M. Brüggen, G. Brunetti, K. Chyży, J. Conway, J. H. Croston, T. Enßlin, C. Ferrari, G. Heald, S. Heidenreich, N. Jackson, G. Macario, J. McKean, G. Miley, R. Morganti, A. Offringa, R. Pizzo, D. Rafferty, H. Röttgering, A. Shulevski, M. Steinmetz, C. Tasse, S. van der Tol, W. van Driel, R. J. van Weeren, J. E. van Zwieten, A. Alexov, J. Anderson, A. Asgekar, M. Avruch, M. Bell, M. R. Bell, M. Bentum, G. Bernardi, P. Best, F. Breitling, J. W. Broderick, A. Butcher, B. Ciardi, R. J. Dettmar, J. Eisloeffel, W. Frieswijk, H. Gankema, M. Garrett, M. Gerbers, J. M. Griessmeier, A. W. Gunst, T. E. Hassall, J. Hessels, M. Hoeft, A. Horneffer, A. Karastergiou, J. Köhler, Y. Koopman, M. Kuniyoshi, G. Kuper, P. Maat, G. Mann, M. Mevius, D. D. Mulcahy, H. Munk, R. Nijboer, J. Noordam, H. Paas, M. Pandey, V. N. Pandey, A. Polatidis, W. Reich, A. P. Schoenmakers, J. Sluman, O. Smirnov, C. Sobey, B. Stappers, J. Swinbank, M. Tagger, Y. Tang, I. van Bemmel, W. van Cappellen, A. P. van Duin, M. van Haarlem, J. van Leeuwen, R. Vermeulen, C. Vocks, S. White, M. Wise, O. Wucknitz, and P. Zarka. M 87 at metre wavelengths: the LOFAR picture. *A&A*, 547:A56, Nov. 2012.

J. Debuhr, E. Quataert, C.-P. Ma, and P. Hopkins. Self-regulated black hole growth via momentum deposition in galaxy merger simulations. *MNRAS*, 406:L55–L59, July 2010.

J. Debuhr, E. Quataert, and C.-P. Ma. The growth of massive black holes in galaxy merger simulations with feedback by radiation pressure. *MNRAS*, 412:1341–1360, Apr. 2011.

J. Debuhr, E. Quataert, and C.-P. Ma. Galaxy-scale outflows driven by active galactic nuclei. *MNRAS*, 420:2221–2231, Mar. 2012.

A. Dedner, F. Kemm, D. Kröner, C.-D. Munz, T. Schnitzer, and M. Wesenberg. *Journal of Computational Physics*, 175, 2002.

C. DeGraf, T. Di Matteo, N. Khandai, R. Croft, J. Lopez, and V. Springel. Early black holes in cosmological simulations: luminosity functions and clustering behaviour. *MNRAS*, 424:1892–1898, Aug. 2012.

W. Dehnen. A Very Fast and Momentum-conserving Tree Code. *ApJ*, 536: L39–L42, June 2000.

W. Dehnen. A Hierarchical O(N) Force Calculation Algorithm. *Journal of Computational Physics*, 179:27–42, June 2002.

T. Di Matteo, V. Springel, and L. Hernquist. Energy input from quasars regulates the growth and activity of black holes and their host galaxies. *Nature*, 433:604–607, Feb. 2005.

T. Di Matteo, J. Colberg, V. Springel, L. Hernquist, and D. Sijacki. Direct Cosmological Simulations of the Growth of Black Holes and Galaxies. *ApJ*, 676:33-53, Mar. 2008.

R. H. Dicke, P. J. E. Peebles, P. G. Roll, and D. T. Wilkinson. Cosmic Black-Body Radiation. *ApJ*, 142:414–419, July 1965.

S. Dodelson. *Modern cosmology*. 2003.

M. A. Dopita, I.-T. Ho, L. L. Dressel, R. Sutherland, L. Kewley, R. Davies, E. Hampton, P. Shastri, P. Kharb, J. Jose, H. Bhatt, S. Ramya, J. Scharwächter, C. Jin, J. Banfield, I. Zaw, B. James, S. Juneau, and S. Srivastava. Probing the Physics of Narrow-line Regions in Active Galaxies. III. Accretion and Cocoon Shocks in the LINER NGC 1052. *ApJ*, 801:42, Mar. 2015.

Y. Dubois, J. Devriendt, A. Slyz, and R. Teyssier. Jet-regulated cooling catastrophe. *MNRAS*, 409:985–1001, Dec. 2010.

Y. Dubois, J. Devriendt, A. Slyz, and R. Teyssier. Self-regulated growth of supermassive black holes by a dual jet-heating active galactic nucleus feedback mechanism: methods, tests and implications for cosmological simulations. *MNRAS*, 420:2662–2683, Mar. 2012.

Y. Dubois, R. Gavazzi, S. Peirani, and J. Silk. AGN-driven quenching of star formation: morphological and dynamical implications for early-type galaxies. *MNRAS*, 433:3297–3313, Aug. 2013.

Y. Dubois, M. Volonteri, and J. Silk. Black hole evolution - III. Statistical properties of mass growth and spin evolution using large-scale hydrodynamical cosmological simulations. *MNRAS*, 440:1590–1606, May 2014.

Y. Dubois, M. Volonteri, J. Silk, J. Devriendt, A. Slyz, and R. Teyssier. Black hole evolution - I. Supernova-regulated black hole growth. *MNRAS*, 452:1502–1518, Sept. 2015.

Y. Dubois, S. Peirani, C. Pichon, J. Devriendt, R. Gavazzi, C. Welker, and M. Volonteri. The HORIZON-AGN simulation: morphological diversity of galaxies promoted by AGN feedback. *MNRAS*, 463:3948–3964, Dec. 2016.

K. Duncan, C. J. Conselice, A. Mortlock, W. G. Hartley, Y. Guo, H. C. Ferguson, R. Davé, Y. Lu, J. Ownsworth, M. L. N. Ashby, A. Dekel, M. Dickinson, S. Faber, M. Giavalisco, N. Grogin, D. Kocevski, A. Koekemoer, R. S. Somerville, and C. E. White. The mass evolution of the first galaxies: stellar mass functions and star formation rates at $4 < z < 7$ in the CANDELS GOODS-South field. *MNRAS*, 444:2960–2984, Nov. 2014.

R. J. H. Dunn and A. C. Fabian. Investigating AGN heating in a sample of nearby clusters. *MNRAS*, 373:959–971, Dec. 2006.

R. J. H. Dunn, R. P. Fender, E. G. Körding, T. Belloni, and C. Cabanac. A global spectral study of black hole X-ray binaries. *MNRAS*, 403:61–82, Mar. 2010.

L. J. Dursi and C. Pfrommer. Draping of Cluster Magnetic Fields over Bullets and Bubbles –Morphology and Dynamic Effects. *ApJ*, 677:993-1018, Apr. 2008.

D. J. Eisenstein and W. Hu. Baryonic Features in the Matter Transfer Function. *ApJ*, 496:605–614, Mar. 1998.

S. L. Ellison, D. R. Patton, and R. C. Hickox. Galaxy pairs in the Sloan Digital Sky Survey - XII. The fuelling mechanism of low-excitation radio-loud AGN. *MNRAS*, 451:L35–L39, July 2015.

E. Emsellem, F. Renaud, F. Bournaud, B. Elmegreen, F. Combes, and J. M. Gabor. The interplay between a galactic bar and a supermassive black hole: nuclear fuelling in a subparsec resolution galaxy simulation. *MNRAS*, 446:2468–2482, Jan. 2015.

W. English, M. J. Hardcastle, and M. G. H. Krause. Numerical modelling of the lobes of radio galaxies in cluster environments - III. Powerful relativistic and non-relativistic jets. *MNRAS*, 461:2025–2043, Sept. 2016.

T. Enßlin, C. Pfrommer, F. Miniati, and K. Subramanian. Cosmic ray transport in galaxy clusters: implications for radio halos, gamma-ray signatures, and cool core heating. *A&A*, 527:A99, Mar. 2011.

T. A. Enßlin and C. Vogt. Magnetic turbulence in cool cores of galaxy clusters. *A&A*, 453:447–458, July 2006.

C. R. Evans and J. F. Hawley. Simulation of magnetohydrodynamic flows - A constrained transport method. *ApJ*, 332:659–677, Sept. 1988.

A. C. Fabian. Cooling Flows in Clusters of Galaxies. *ARA&A*, 32:277–318, 1994.

A. C. Fabian. Observational Evidence of Active Galactic Nuclei Feedback. *ARA&A*, 50:455–489, Sept. 2012.

A. C. Fabian, S. A. Walker, H. R. Russell, C. Pinto, J. S. Sanders, and C. S. Reynolds. Do sound waves transport the AGN energy in the Perseus cluster? *MNRAS*, 464:L1–L5, Jan. 2017.

X. Fan, V. K. Narayanan, R. H. Lupton, M. A. Strauss, G. R. Knapp, R. H. Becker, R. L. White, L. Pentericci, S. K. Leggett, Z. Haiman, J. E. Gunn, Ž. Ivezić, D. P. Schneider, S. F. Anderson, J. Brinkmann, N. A. Bahcall, A. J. Connolly, I. Csabai, M. xdoi, M. Fukugita, T. Geballe, E. K. Grebel, D. Harbeck, G. Hennessy, D. Q. Lamb, G. Miknaitis, J. A. Munn, R. Nichol, S. Okamura, J. R. Pier, F. Prada, G. T. Richards, A. Szalay, and D. G. York. A Survey of z>5.8 Quasars in the Sloan Digital Sky Survey. I. Discovery of Three New Quasars and the Spatial Density of Luminous Quasars at z˜6. *AJ*, 122:2833–2849, Dec. 2001.

B. L. Fanaroff and J. M. Riley. The morphology of extragalactic radio sources of high and low luminosity. *MNRAS*, 167:31P–36P, May 1974.

N. Fanidakis, C. M. Baugh, A. J. Benson, R. G. Bower, S. Cole, C. Done, and C. S. Frenk. Grand unification of AGN activity in the ΛCDM cosmology. *MNRAS*, 410:53–74, Jan. 2011.

C.-A. Faucher-Giguère, A. Lidz, M. Zaldarriaga, and L. Hernquist. A New Calculation of the Ionizing Background Spectrum and the Effects of He II Reionization. *ApJ*, 703:1416–1443, Oct. 2009.

L. Ferrarese and D. Merritt. A Fundamental Relation between Supermassive Black Holes and Their Host Galaxies. *ApJ*, 539:L9–L12, Aug. 2000.

N. M. Förster Schreiber, R. Genzel, S. F. Newman, J. D. Kurk, D. Lutz, L. J. Tacconi, S. Wuyts, K. Bandara, A. Burkert, P. Buschkamp, C. M. Carollo, G. Cresci, E. Daddi, R. Davies, F. Eisenhauer, E. K. S. Hicks, P. Lang, S. J. Lilly, V. Mainieri, C. Mancini, T. Naab, Y. Peng, A. Renzini, D. Rosario, K. Shapiro Griffin, A. E. Shapley, A. Sternberg, S. Tacchella, D. Vergani, E. Wisnioski, E. Wuyts, and G. Zamorani. The Sins/zC-Sinf Survey of z ˜ 2 Galaxy Kinematics: Evidence for Powerful Active Galactic Nucleus-Driven Nuclear Outflows in Massive Star-Forming Galaxies. *ApJ*, 787:38, May 2014.

Y. Fujita. A Simple Measurement of Turbulence in Cores of Galaxy Clusters. *ApJ*, 631:L17–L20, Sept. 2005.

Y. Fujita and Y. Ohira. Stable Heating of Cluster Cooling Flows by Cosmic-Ray Streaming. *ApJ*, 738:182, Sept. 2011.

V. Gaibler, M. Krause, and M. Camenzind. Very light magnetized jets on large scales - I. Evolution and magnetic fields. *MNRAS*, 400:1785–1802, Dec. 2009.

V. Gaibler, S. Khochfar, M. Krause, and J. Silk. Jet-induced star formation in gas-rich galaxies. *MNRAS*, 425:438–449, Sept. 2012.

Z. Gan, H. Li, S. Li, and F. Yuan. Three-dimensional Magnetohydrodynamical Simulations of the Morphology of Head-Tail Radio Galaxies Based on the Magnetic Tower Jet Model. *ApJ*, 839:14, Apr. 2017.

M. Gaspari, F. Brighenti, A. D'Ercole, and C. Melioli. AGN feedback in galaxy groups: the delicate touch of self-regulated outflows. *MNRAS*, 415:1549–1568, Aug. 2011a.

M. Gaspari, C. Melioli, F. Brighenti, and A. D'Ercole. The dance of heating and cooling in galaxy clusters: three-dimensional simulations of self-regulated active galactic nuclei outflows. *MNRAS*, 411:349–372, Feb. 2011b.

M. Gaspari, F. Brighenti, and P. Temi. Mechanical AGN feedback: controlling the thermodynamical evolution of elliptical galaxies. *MNRAS*, 424: 190–209, July 2012.

M. Gaspari, M. Ruszkowski, and S. P. Oh. Chaotic cold accretion on to black holes. *MNRAS*, 432:3401–3422, July 2013.

S. Genel, M. Vogelsberger, V. Springel, D. Sijacki, D. Nelson, G. Snyder, V. Rodriguez-Gomez, P. Torrey, and L. Hernquist. Introducing the Illustris project: the evolution of galaxy populations across cosmic time. *MNRAS*, 445:175–200, Nov. 2014.

S. Genel, D. Nelson, A. Pillepich, V. Springel, R. Pakmor, R. Weinberger, L. Hernquist, J. Naiman, M. Vogelsberger, F. Marinacci, and P. Torrey. The Size Evolution of Star-forming and Quenched Galaxies in the IllustrisTNG simulation. *arXiv:1707.05327*, July 2017.

R. Genzel, F. Eisenhauer, and S. Gillessen. The Galactic Center massive black hole and nuclear star cluster. *Reviews of Modern Physics*, 82:3121–3195, Oct. 2010.

R. Genzel, N. M. Förster Schreiber, D. Rosario, P. Lang, D. Lutz, E. Wisnioski, E. Wuyts, S. Wuyts, K. Bandara, R. Bender, S. Berta, J. Kurk, J. T. Mendel, L. J. Tacconi, D. Wilman, A. Beifiori, G. Brammer, A. Burkert, P. Buschkamp, J. Chan, C. M. Carollo, R. Davies, F. Eisenhauer, M. Fabricius, M. Fossati, M. Kriek, S. Kulkarni, S. J. Lilly, C. Mancini, I. Momcheva, T. Naab, E. J. Nelson, A. Renzini, R. Saglia, R. M. Sharples, A. Sternberg, S. Tacchella, and P. van Dokkum. Evidence for Wide-spread Active Galactic Nucleus-driven Outflows in the Most Massive z ˜ 1-2 Star-forming Galaxies. *ApJ*, 796:7, Nov. 2014.

A. Georgakakis, J. Aird, A. Schulze, T. Dwelly, M. Salvato, K. Nandra, A. Merloni, and D. P. Schneider. Observational constraints on the specific accretion-rate distribution of X-ray-selected AGNs. *MNRAS*, 471:1976–2001, Oct. 2017.

R. Gilli, A. Comastri, and G. Hasinger. The synthesis of the cosmic X-ray background in the Chandra and XMM-Newton era. *A&A*, 463:79–96, Feb. 2007.

S. Giodini, D. Pierini, A. Finoguenov, G. W. Pratt, H. Boehringer, A. Leauthaud, L. Guzzo, H. Aussel, M. Bolzonella, P. Capak, M. Elvis, G. Hasinger, O. Ilbert, J. S. Kartaltepe, A. M. Koekemoer, S. J. Lilly, R. Massey, H. J. McCracken, J. Rhodes, M. Salvato, D. B. Sanders, N. Z. Scoville, S. Sasaki, V. Smolcic, Y. Taniguchi, D. Thompson, and COSMOS Collaboration. Stellar and Total Baryon Mass Fractions in Groups and Clusters Since Redshift 1. *ApJ*, 703:982–993, Sept. 2009.

S. C. O. Glover and T. Abel. Uncertainties in H_2 and HD chemistry and cooling and their role in early structure formation. *MNRAS*, 388:1627–1651, Aug. 2008.

A. W. Graham and N. Scott. The M_{BH}-$L_{spheroid}$ Relation at High and Low Masses, the Quadratic Growth of Black Holes, and Intermediate-mass Black Hole Candidates. *ApJ*, 764:151, Feb. 2013.

A. W. Graham and N. Scott. The (Black Hole)-bulge Mass Scaling Relation at Low Masses. *ApJ*, 798:54, Jan. 2015.

G. L. Granato, G. De Zotti, L. Silva, A. Bressan, and L. Danese. A Physical Model for the Coevolution of QSOs and Their Spheroidal Hosts. *ApJ*, 600:580–594, Jan. 2004.

R. J. J. Grand, F. A. Gómez, F. Marinacci, R. Pakmor, V. Springel, D. J. R. Campbell, C. S. Frenk, A. Jenkins, and S. D. M. White. The Auriga Project: the properties and formation mechanisms of disc galaxies across cosmic time. *MNRAS*, 467:179–207, May 2017.

T. Guillet and R. Teyssier. A simple multigrid scheme for solving the Poisson equation with arbitrary domain boundaries. *Journal of Computational Physics*, 230:4756–4771, June 2011.

F. Guo. The Shape of X-Ray Cavities in Galaxy Clusters: Probing Jet Properties and Viscosity. *ApJ*, 803:48, Apr. 2015.

F. Guo and S. P. Oh. Feedback heating by cosmic rays in clusters of galaxies. *MNRAS*, 384:251–266, Feb. 2008.

A. H. Guth. Inflationary universe: A possible solution to the horizon and flatness problems. *Phys. Rev. D*, 23:347–356, Jan. 1981.

F. Haardt and P. Madau. Radiative Transfer in a Clumpy Universe. II. The Ultraviolet Extragalactic Background. *ApJ*, 461:20, Apr. 1996.

F. Haardt and P. Madau. Radiative Transfer in a Clumpy Universe. IV. New Synthesis Models of the Cosmic UV/X-Ray Background. *ApJ*, 746: 125, Feb. 2012.

M. Habouzit, M. Volonteri, M. Latif, Y. Dubois, and S. Peirani. On the number density of 'direct collapse' black hole seeds. *MNRAS*, 463:529–540, Nov. 2016.

M. Habouzit, M. Volonteri, and Y. Dubois. Blossoms from black hole seeds: properties and early growth regulated by supernova feedback. *MNRAS*, 468:3935–3948, July 2017.

M. J. Hardcastle and M. G. H. Krause. Numerical modelling of the lobes of radio galaxies in cluster environments. *MNRAS*, 430:174–196, Mar. 2013.

M. J. Hardcastle and M. G. H. Krause. Numerical modelling of the lobes of radio galaxies in cluster environments - II. Magnetic field configuration and observability. *MNRAS*, 443:1482–1499, Sept. 2014.

P. E. Hardee. Spatial stability of jets - The nonaxisymmetric fundamental and reflection modes. *ApJ*, 313:607–622, Feb. 1987.

N. Häring and H.-W. Rix. On the Black Hole Mass-Bulge Mass Relation. *ApJ*, 604:L89–L92, Apr. 2004.

L. Hernquist. Tidal triggering of starbursts and nuclear activity in galaxies. *Nature*, 340:687–691, Aug. 1989.

S. Hillel and N. Soker. Heating the intracluster medium by jet-inflated bubbles. *MNRAS*, 455:2139–2148, Jan. 2016.

S. Hillel and N. Soker. Hitomi observations of Perseus support heating by mixing. *MNRAS*, 466:L39–L42, Mar. 2017.

M. Hirschmann, S. Khochfar, A. Burkert, T. Naab, S. Genel, and R. S. Somerville. On the evolution of the intrinsic scatter in black hole versus galaxy mass relations. *MNRAS*, 407:1016–1032, Sept. 2010.

M. Hirschmann, K. Dolag, A. Saro, L. Bachmann, S. Borgani, and A. Burkert. Cosmological simulations of black hole growth: AGN luminosities and downsizing. *MNRAS*, 442:2304–2324, Aug. 2014.

Hitomi Collaboration. The quiescent intracluster medium in the core of the Perseus cluster. *Nature*, 535:117–121, July 2016.

P. F. Hopkins and E. Quataert. How do massive black holes get their gas? *MNRAS*, 407:1529–1564, Sept. 2010.

P. F. Hopkins and E. Quataert. An analytic model of angular momentum transport by gravitational torques: from galaxies to massive black holes. *MNRAS*, 415:1027–1050, Aug. 2011.

P. F. Hopkins, L. Hernquist, T. J. Cox, T. Di Matteo, B. Robertson, and V. Springel. A Unified, Merger-driven Model of the Origin of Starbursts, Quasars, the Cosmic X-Ray Background, Supermassive Black Holes, and Galaxy Spheroids. *ApJS*, 163:1–49, Mar. 2006.

P. F. Hopkins, G. T. Richards, and L. Hernquist. An Observational Determination of the Bolometric Quasar Luminosity Function. *ApJ*, 654: 731–753, Jan. 2007.

P. F. Hopkins, T. J. Cox, D. Kereš, and L. Hernquist. A Cosmological Framework for the Co-Evolution of Quasars, Supermassive Black Holes, and Elliptical Galaxies. II. Formation of Red Ellipticals. *ApJS*, 175:390-422, Apr. 2008a.

P. F. Hopkins, L. Hernquist, T. J. Cox, and D. Kereš. A Cosmological Framework for the Co-Evolution of Quasars, Supermassive Black Holes, and Elliptical Galaxies. I. Galaxy Mergers and Quasar Activity. *ApJS*, 175:356-389, Apr. 2008b.

P. F. Hopkins, P. Torrey, C.-A. Faucher-Giguère, E. Quataert, and N. Murray. Stellar and quasar feedback in concert: effects on AGN accretion, obscuration, and outflows. *MNRAS*, 458:816–831, May 2016.

P. F. Hopkins, A. Wetzel, D. Keres, C.-A. Faucher-Giguere, E. Quataert, M. Boylan-Kolchin, N. Murray, C. C. Hayward, S. Garrison-Kimmel, C. Hummels, R. Feldmann, P. Torrey, X. Ma, D. Angles-Alcazar, K.-Y. Su, M. Orr, D. Schmitz, I. Escala, R. Sanderson, M. Y. Grudic, Z. Hafen, J.-H. Kim, A. Fitts, J. S. Bullock, C. Wheeler, T. K. Chan, O. D. Elbert, and D. Narananan. FIRE-2 Simulations: Physics versus Numerics in Galaxy Formation. *arXiv:1702.06148*, Feb. 2017.

F. Hoyle and R. A. Lyttleton. The effect of interstellar matter on climatic variation. *Proceedings of the Cambridge Philosophical Society*, 35:405, 1939.

F. Hoyle and R. J. Tayler. The Mystery of the Cosmic Helium Abundance. *Nature*, 203:1108–1110, Sept. 1964.

M. Huarte-Espinosa, M. Krause, and P. Alexander. Interaction of Fanaroff-Riley class II radio jets with a randomly magnetized intracluster medium. *MNRAS*, 418:1621–1639, Dec. 2011.

S. Ichimaru. Bimodal behavior of accretion disks - Theory and application to Cygnus X-1 transitions. *ApJ*, 214:840–855, June 1977.

I. V. Igumenshchev and M. A. Abramowicz. Rotating accretion flows around black holes: convection and variability. *MNRAS*, 303:309–320, Feb. 1999.

S. Jacob and C. Pfrommer. Cosmic ray heating in cool core clusters - I. Diversity of steady state solutions. *MNRAS*, 467:1449–1477, May 2017a.

S. Jacob and C. Pfrommer. Cosmic ray heating in cool core clusters - II. Self-regulation cycle and non-thermal emission. *MNRAS*, 467:1478–1495, May 2017b.

K. Jahnke and A. V. Macciò. The Non-causal Origin of the Black-hole-galaxy Scaling Relations. *ApJ*, 734:92, June 2011.

R. Kannan, M. Vogelsberger, C. Pfrommer, R. Weinberger, V. Springel, L. Hernquist, E. Puchwein, and R. Pakmor. Increasing Black Hole Feedback-induced Quenching with Anisotropic Thermal Conduction. *ApJ*, 837:L18, Mar. 2017.

N. Katz, D. H. Weinberg, and L. Hernquist. Cosmological Simulations with TreeSPH. *ApJS*, 105:19, July 1996.

D. Kawata and B. K. Gibson. Self-regulated active galactic nuclei heating in elliptical galaxies. *MNRAS*, 358:L16–L20, Mar. 2005.

L. Z. Kelley, L. Blecha, and L. Hernquist. Massive black hole binary mergers in dynamical galactic environments. *MNRAS*, 464:3131–3157, Jan. 2017a.

L. Z. Kelley, L. Blecha, L. Hernquist, A. Sesana, and S. R. Taylor. The gravitational wave background from massive black hole binaries in Illustris: spectral features and time to detection with pulsar timing arrays. *MNRAS*, 471:4508–4526, Nov. 2017b.

D. Kereš, M. Vogelsberger, D. Sijacki, V. Springel, and L. Hernquist. Moving-mesh cosmology: characteristics of galaxies and haloes. *MNRAS*, 425:2027–2048, Sept. 2012.

N. Khandai, T. Di Matteo, R. Croft, S. Wilkins, Y. Feng, E. Tucker, C. DeGraf, and M.-S. Liu. The MassiveBlack-II simulation: the evolution of haloes and galaxies to z $\sim$ 0. *MNRAS*, 450:1349–1374, June 2015.

W.-T. Kim and R. Narayan. Turbulent Mixing in Clusters of Galaxies. *ApJ*, 596:L139–L142, Oct. 2003.

A. King. Black Holes, Galaxy Formation, and the M_{BH}-σ Relation. *ApJ*, 596:L27–L29, Oct. 2003.

A. King and C. Nixon. AGN flickering and chaotic accretion. *MNRAS*, 453: L46–L47, Oct. 2015.

A. R. King, J. E. Pringle, and J. A. Hofmann. The evolution of black hole mass and spin in active galactic nuclei. *MNRAS*, 385:1621–1627, Apr. 2008.

M. D. Kistler, H. Yuksel, and A. M. Hopkins. The Cosmic Star Formation Rate from the Faintest Galaxies in the Unobservable Universe. *arXiv:1305.1630*, May 2013.

E. Kolb and M. Turner. *The Early Universe*. Frontiers in physics. Avalon Publishing, 1994. ISBN 9780813346458. URL `https://books.google.de/books?id=Qwijr-HsvMMC`.

J. Kormendy and L. C. Ho. Coevolution (Or Not) of Supermassive Black Holes and Host Galaxies. *ARA&A*, 51:511–653, Aug. 2013.

M. Krause. Very light jets. I. Axisymmetric parameter study and analytic approximation. *A&A*, 398:113–125, Jan. 2003.

A. Kravtsov, A. Vikhlinin, and A. Meshscheryakov. Stellar mass – halo mass relation and star formation efficiency in high-mass halos. *arxiv:1401.7329*, Jan. 2014.

M. W. Kunz, A. A. Schekochihin, S. C. Cowley, J. J. Binney, and J. S. Sanders. A thermally stable heating mechanism for the intracluster medium: turbulence, magnetic fields and plasma instabilities. *MNRAS*, 410:2446–2457, Feb. 2011.

M. Lacy, S. E. Ridgway, A. Sajina, A. O. Petric, E. L. Gates, T. Urrutia, and L. J. Storrie-Lombardi. The Spitzer Mid-infrared AGN Survey. II. The Demographics and Cosmic Evolution of the AGN Population. *ApJ*, 802:102, Apr. 2015.

A. M. C. Le Brun, I. G. McCarthy, J. Schaye, and T. J. Ponman. Towards a realistic population of simulated galaxy groups and clusters. *MNRAS*, 441:1270–1290, June 2014.

Y. Li and G. L. Bryan. Modeling Active Galactic Nucleus Feedback in Cool-core Clusters: The Balance between Heating and Cooling. *ApJ*, 789:54, July 2014a.

Y. Li and G. L. Bryan. Modeling Active Galactic Nucleus Feedback in Cool-core Clusters: The Formation of Cold Clumps. *ApJ*, 789:153, July 2014b.

Y. Li, G. L. Bryan, M. Ruszkowski, G. M. Voit, B. W. O'Shea, and M. Donahue. Cooling, AGN Feedback, and Star Formation in Simulated Cool-core Galaxy Clusters. *ApJ*, 811:73, Oct. 2015.

Y. Li, M. Ruszkowski, and G. L. Bryan. AGN Heating in Simulated Cool-Core Clusters. *arXiv:1611.05455*, Nov. 2016.

A. D. Linde. Scalar field fluctuations in the expanding universe and the new inflationary universe scenario. *Physics Letters B*, 116:335–339, Oct. 1982.

M. Loewenstein, E. G. Zweibel, and M. C. Begelman. Cosmic-ray heating of cooling flows - A critical analysis. *ApJ*, 377:392–402, Aug. 1991.

J. Magorrian, S. Tremaine, D. Richstone, R. Bender, G. Bower, A. Dressler, S. M. Faber, K. Gebhardt, R. Green, C. Grillmair, J. Kormendy, and T. Lauer. The Demography of Massive Dark Objects in Galaxy Centers. *AJ*, 115:2285–2305, June 1998.

A. Marconi, G. Risaliti, R. Gilli, L. K. Hunt, R. Maiolino, and M. Salvati. Local supermassive black holes, relics of active galactic nuclei and the X-ray background. *MNRAS*, 351:169–185, June 2004.

F. Marinacci, R. Pakmor, and V. Springel. The formation of disc galaxies in high-resolution moving-mesh cosmological simulations. *MNRAS*, 437: 1750–1775, Jan. 2014.

F. Marinacci, M. Vogelsberger, R. Pakmor, P. Torrey, V. Springel, L. Hernquist, D. Nelson, R. Weinberger, A. Pillepich, J. Naiman, and S. Genel. First results from the IllustrisTNG simulations: radio haloes and magnetic fields. *arXiv:1707.03396*, July 2017.

D. Martizzi, Jimmy, R. Teyssier, and B. Moore. Brightest cluster galaxies in cosmological simulations with adaptive mesh refinement: successes and failures. *MNRAS*, 443:1500–1508, Sept. 2014.

S. Massaglia, G. Bodo, P. Rossi, S. Capetti, and A. Mignone. Making Faranoff-Riley I radio sources. I. Numerical hydrodynamic 3D simulations of low-power jets. *A&A*, 596:A12, Nov. 2016.

C. Mazzucchelli, E. Bañados, B. P. Venemans, R. Decarli, E. P. Farina, F. Walter, A.-C. Eilers, H.-W. Rix, R. Simcoe, D. Stern, X. Fan, E. Schlafly, G. De Rosa, J. Hennawi, K. C. Chambers, J. Greiner, W. Burgett, P. W. Draper, N. Kaiser, R.-P. Kudritzki, E. Magnier, N. Metcalfe, C. Waters, and R. J. Wainscoat. Physical properties of 15 quasars at $z \gtrsim 6.5$. *arXiv:1710.01251*, Oct. 2017.

N. J. McConnell and C.-P. Ma. Revisiting the Scaling Relations of Black Hole Masses and Host Galaxy Properties. *ApJ*, 764:184, Feb. 2013.

B. R. McNamara and P. E. J. Nulsen. Heating Hot Atmospheres with Active Galactic Nuclei. *ARA&A*, 45:117–175, Sept. 2007.

B. R. McNamara and P. E. J. Nulsen. Mechanical feedback from active galactic nuclei in galaxies, groups and clusters. *New Journal of Physics*, 14(5):055023, May 2012.

A. M. Medling, V. U, J. A. Rich, L. J. Kewley, L. Armus, M. A. Dopita, C. E. Max, D. Sanders, and R. Sutherland. Shocked gas in IRAS F17207-0014: ISM collisions and outflows. *MNRAS*, 448:2301–2311, Apr. 2015.

G. R. Meece, G. M. Voit, and B. W. O'Shea. Triggering and Delivery Algorithms for AGN Feedback. *ApJ*, 841:133, June 2017.

P. J. Mendygral, T. W. Jones, and K. Dolag. MHD Simulations of Active Galactic Nucleus Jets in a Dynamic Galaxy Cluster Medium. *ApJ*, 750: 166, May 2012.

J. C. Mihos and L. Hernquist. Gasdynamics and Starbursts in Major Mergers. *ApJ*, 464:641, June 1996.

H. Mo, F. C. van den Bosch, and S. White. *Galaxy Formation and Evolution*. May 2010.

B. P. Moster, T. Naab, and S. D. M. White. Galactic star formation and accretion histories from matching galaxies to dark matter haloes. *MNRAS*, 428:3121–3138, Feb. 2013.

D. Mukherjee, G. V. Bicknell, R. Sutherland, and A. Wagner. Relativistic jet feedback in high-redshift galaxies - I. Dynamics. *MNRAS*, 461:967–983, Sept. 2016.

F. Munshi, F. Governato, A. M. Brooks, C. Christensen, S. Shen, S. Loebman, B. Moster, T. Quinn, and J. Wadsley. Reproducing the Stellar Mass/Halo Mass Relation in Simulated ΛCDM Galaxies: Theory versus Observational Estimates. *ApJ*, 766:56, Mar. 2013.

J. P. Naiman, A. Pillepich, V. Springel, E. Ramirez-Ruiz, P. Torrey, M. Vogelsberger, R. Pakmor, D. Nelson, F. Marinacci, L. Hernquist, R. Weinberger, and S. Genel. First results from the IllustrisTNG simulations: A tale of two elements – chemical evolution of magnesium and europium. *arXiv:1707.03401*, July 2017.

J. F. Navarro, C. S. Frenk, and S. D. M. White. The Structure of Cold Dark Matter Halos. *ApJ*, 462:563, May 1996.

J. F. Navarro, C. S. Frenk, and S. D. M. White. A Universal Density Profile from Hierarchical Clustering. *ApJ*, 490:493–508, Dec. 1997.

D. Nelson, A. Pillepich, V. Springel, R. Weinberger, L. Hernquist, R. Pakmor, S. Genel, P. Torrey, M. Vogelsberger, G. Kauffmann, F. Marinacci, and J. Naiman. First results from the IllustrisTNG simulations: the galaxy color bimodality. *arXiv:1707.03395*, July 2017.

H. Netzer. *The Physics and Evolution of Active Galactic Nuclei*. Nov. 2013.

K. G. Noeske, B. J. Weiner, S. M. Faber, C. Papovich, D. C. Koo, R. S. Somerville, K. Bundy, C. J. Conselice, J. A. Newman, D. Schiminovich, E. Le Floc'h, A. L. Coil, G. H. Rieke, J. M. Lotz, J. R. Primack, P. Barmby, M. C. Cooper, M. Davis, R. S. Ellis, G. G. Fazio, P. Guhathakurta, J. Huang, S. A. Kassin, D. C. Martin, A. C. Phillips, R. M. Rich, T. A. Small, C. N. A. Willmer, and G. Wilson. Star Formation in AEGIS Field Galaxies since z=1.1: The Dominance of Gradually Declining Star Formation, and the Main Sequence of Star-forming Galaxies. *ApJ*, 660:L43–L46, May 2007.

M. L. Norman, K.-H. A. Winkler, L. Smarr, and M. D. Smith. Structure and dynamics of supersonic jets. *A&A*, 113:285–302, Sept. 1982.

I. D. Novikov and K. S. Thorne. Astrophysics of black holes. In C. Dewitt and B. S. Dewitt, editors, *Black Holes (Les Astres Occlus)*, pages 343–450, 1973.

T. Okamoto, R. S. Nemmen, and R. G. Bower. The impact of radio feedback from active galactic nuclei in cosmological simulations: formation of disc galaxies. *MNRAS*, 385:161–180, Mar. 2008.

H. Omma, J. Binney, G. Bryan, and A. Slyz. Heating cooling flows with jets. *MNRAS*, 348:1105–1119, Mar. 2004.

R. Pakmor and V. Springel. Simulations of magnetic fields in isolated disc galaxies. *MNRAS*, 432:176–193, June 2013.

R. Pakmor, A. Bauer, and V. Springel. Magnetohydrodynamics on an unstructured moving grid. *MNRAS*, 418:1392–1401, Dec. 2011.

R. Pakmor, V. Springel, A. Bauer, P. Mocz, D. J. Munoz, S. T. Ohlmann, K. Schaal, and C. Zhu. Improving the convergence properties of the moving-mesh code AREPO. *MNRAS*, 455:1134–1143, Jan. 2016.

P. J. E. Peebles. Recombination of the Primeval Plasma. *ApJ*, 153:1, July 1968.

C. Y. Peng. How Mergers May Affect the Mass Scaling Relation between Gravitationally Bound Systems. *ApJ*, 671:1098–1107, Dec. 2007.

A. A. Penzias and R. W. Wilson. A Measurement of Excess Antenna Temperature at 4080 Mc/s. *ApJ*, 142:419–421, July 1965.

M. Perucho, V. Quilis, and J.-M. Martí. Intracluster Medium Reheating by Relativistic Jets. *ApJ*, 743:42, Dec. 2011.

M. Perucho, J.-M. Martí, V. Quilis, and E. Ricciardelli. Large-scale jets from active galactic nuclei as a source of intracluster medium heating: cavities and shocks. *MNRAS*, 445:1462–1481, Dec. 2014.

J. R. Peterson and A. C. Fabian. X-ray spectroscopy of cooling clusters. *Phys. Rep.*, 427:1–39, Apr. 2006.

E. Pezzulli, M. Volonteri, R. Schneider, and R. Valiante. The sustainable growth of the first black holes. *MNRAS*, 471:589–595, Oct. 2017.

C. Pfrommer. Toward a Comprehensive Model for Feedback by Active Galactic Nuclei: New Insights from M87 Observations by LOFAR, Fermi, and H.E.S.S. *ApJ*, 779:10, Dec. 2013.

C. Pfrommer, R. Pakmor, K. Schaal, C. M. Simpson, and V. Springel. Simulating cosmic ray physics on a moving mesh. *MNRAS*, 465:4500–4529, Mar. 2017.

A. Pillepich, M. Vogelsberger, A. Deason, V. Rodriguez-Gomez, S. Genel, D. Nelson, P. Torrey, L. V. Sales, F. Marinacci, V. Springel, D. Sijacki, and L. Hernquist. Halo mass and assembly history exposed in the faint outskirts: the stellar and dark matter haloes of Illustris galaxies. *MNRAS*, 444:237–249, Oct. 2014.

A. Pillepich, D. Nelson, L. Hernquist, V. Springel, R. Pakmor, P. Torrey, R. Weinberger, S. Genel, J. Naiman, F. Marinacci, and M. Vogelsberger. First results from the IllustrisTNG simulations: the stellar mass content of groups and clusters of galaxies. *arXiv:1707.03406*, July 2017a.

A. Pillepich, V. Springel, D. Nelson, S. Genel, J. Naiman, R. Pakmor, L. Hernquist, P. Torrey, M. Vogelsberger, R. Weinberger, and F. Marinacci. Simulating Galaxy Formation with the IllustrisTNG Model. *arXiv:1703.02970*, Mar. 2017b.

A. Pinzke and C. Pfrommer. Simulating the γ-ray emission from galaxy clusters: a universal cosmic ray spectrum and spatial distribution. *MNRAS*, 409:449–480, Dec. 2010.

Planck Collaboration. Planck early results. I. The Planck mission. *A&A*, 536:A1, Dec. 2011.

Planck Collaboration, P. A. R. Ade, N. Aghanim, M. Arnaud, M. Ashdown, J. Aumont, C. Baccigalupi, A. J. Banday, R. B. Barreiro, J. G. Bartlett, and et al. Planck 2015 results. XIII. Cosmological parameters. *A&A*, 594:A13, Sept. 2016.

A. Pontzen, M. Tremmel, N. Roth, H. V. Peiris, A. Saintonge, M. Volonteri, T. Quinn, and F. Governato. How to quench a galaxy. *MNRAS*, 465: 547–558, Feb. 2017.

K. G. Powell, P. L. Roe, T. J. Linde, T. I. Gombosi, and D. L. de Zeeuw. *Journal of Computational Physics*, 154:284, 1999.

D. Prasad, P. Sharma, and A. Babul. Cool Core Cycles: Cold Gas and AGN Jet Feedback in Cluster Cores. *ApJ*, 811:108, Oct. 2015.

E. Puchwein and V. Springel. Shaping the galaxy stellar mass function with supernova- and AGN-driven winds. *MNRAS*, 428:2966–2979, Feb. 2013.

V. Quilis, R. G. Bower, and M. L. Balogh. Bubbles, feedback and the intracluster medium: three-dimensional hydrodynamic simulations. *MNRAS*, 328:1091–1097, Dec. 2001.

M. J. Rees. Emission from the nuclei of nearby galaxies - Evidence for massive black holes. In E. M. Berkhuijsen and R. Wielebinski, editors, *Structure and Properties of Nearby Galaxies*, volume 77 of *IAU Symposium*, pages 237–242, 1978.

M. J. Rees and J. P. Ostriker. Cooling, dynamics and fragmentation of massive gas clouds - Clues to the masses and radii of galaxies and clusters. *MNRAS*, 179:541–559, June 1977.

A. E. Reines and M. Volonteri. Relations between Central Black Hole Mass and Total Galaxy Stellar Mass in the Local Universe. *ApJ*, 813:82, Nov. 2015.

A. Renzini and Y.-j. Peng. An Objective Definition for the Main Sequence of Star-forming Galaxies. *ApJ*, 801:L29, Mar. 2015.

C. S. Reynolds, S. Heinz, and M. C. Begelman. The hydrodynamics of dead radio galaxies. *MNRAS*, 332:271–282, May 2002.

C. S. Reynolds, B. McKernan, A. C. Fabian, J. M. Stone, and J. C. Vernaleo. Buoyant radio lobes in a viscous intracluster medium. *MNRAS*, 357:242–250, Feb. 2005.

C. S. Reynolds, S. A. Balbus, and A. A. Schekochihin. Inefficient Driving of Bulk Turbulence By Active Galactic Nuclei in a Hydrodynamic Model of the Intracluster Medium. *ApJ*, 815:41, Dec. 2015.

G. Rodighiero, E. Daddi, I. Baronchelli, A. Cimatti, A. Renzini, H. Aussel, P. Popesso, D. Lutz, P. Andreani, S. Berta, A. Cava, D. Elbaz, A. Feltre, A. Fontana, N. M. Förster Schreiber, A. Franceschini, R. Genzel, A. Grazian, C. Gruppioni, O. Ilbert, E. Le Floch, G. Magdis, M. Magliocchetti, B. Magnelli, R. Maiolino, H. McCracken, R. Nordon, A. Poglitsch, P. Santini, F. Pozzi, L. Riguccini, L. J. Tacconi, S. Wuyts, and G. Zamorani. The Lesser Role of Starbursts in Star Formation at z = 2. *ApJ*, 739:L40, Oct. 2011.

V. Rodriguez-Gomez, S. Genel, M. Vogelsberger, D. Sijacki, A. Pillepich, L. V. Sales, P. Torrey, G. Snyder, D. Nelson, V. Springel, C.-P. Ma, and L. Hernquist. The merger rate of galaxies in the Illustris simulation: a comparison with observations and semi-empirical models. *MNRAS*, 449: 49–64, May 2015.

O. Roos, S. Juneau, F. Bournaud, and J. M. Gabor. Thermal and Radiative Active Galactic Nucleus Feedback have a Limited Impact on Star Formation in High-redshift Galaxies. *ApJ*, 800:19, Feb. 2015.

Y. M. Rosas-Guevara, R. G. Bower, J. Schaye, M. Furlong, C. S. Frenk, C. M. Booth, R. A. Crain, C. Dalla Vecchia, M. Schaller, and T. Theuns. The impact of angular momentum on black hole accretion rates in simulations of galaxy formation. *MNRAS*, 454:1038–1057, Nov. 2015.

J. Rosdahl, J. Schaye, Y. Dubois, T. Kimm, and R. Teyssier. Snap, crackle, pop: sub-grid supernova feedback in AMR simulations of disc galaxies. *MNRAS*, 466:11–33, Apr. 2017.

M. Ruszkowski and S. P. Oh. Galaxy motions, turbulence and conduction in clusters of galaxies. *MNRAS*, 414:1493–1507, June 2011.

M. Ruszkowski, M. Brüggen, and M. C. Begelman. Cluster Heating by Viscous Dissipation of Sound Waves. *ApJ*, 611:158–163, Aug. 2004.

M. Ruszkowski, T. A. Enßlin, M. Brüggen, S. Heinz, and C. Pfrommer. Impact of tangled magnetic fields on fossil radio bubbles. *MNRAS*, 378: 662–672, June 2007.

M. Ruszkowski, H.-Y. K. Yang, and C. S. Reynolds. Cosmic-Ray Feedback Heating of the Intracluster Medium. *ApJ*, 844:13, July 2017.

J. Salcido, R. G. Bower, T. Theuns, S. McAlpine, M. Schaller, R. A. Crain, J. Schaye, and J. Regan. Music from the heavens - gravitational waves from supermassive black hole mergers in the EAGLE simulations. *MNRAS*, 463:870–885, Nov. 2016.

E. E. Salpeter. The Luminosity Function and Stellar Evolution. *ApJ*, 121: 161, Jan. 1955.

G. A. D. Savorgnan, A. W. Graham, A. Marconi, and E. Sani. Supermassive Black Holes and Their Host Spheroids. II. The Red and Blue Sequence in the M_{BH}-$M_{*,sph}$ Diagram. *ApJ*, 817:21, Jan. 2016.

A. Sądowski and M. Gaspari. Kinetic and radiative power from optically thin accretion flows. *MNRAS*, 468:1398–1404, June 2017.

A. Sądowski, J.-P. Lasota, M. A. Abramowicz, and R. Narayan. Energy flows in thick accretion discs and their consequences for black hole feedback. *MNRAS*, 456:3915–3928, Mar. 2016.

K. Schaal and V. Springel. Shock finding on a moving mesh - I. Shock statistics in non-radiative cosmological simulations. *MNRAS*, 446:3992–4007, Feb. 2015.

K. Schaal, V. Springel, R. Pakmor, C. Pfrommer, D. Nelson, M. Vogelsberger, S. Genel, A. Pillepich, D. Sijacki, and L. Hernquist. Shock finding on a moving-mesh - II. Hydrodynamic shocks in the Illustris universe. *MNRAS*, 461:4441–4465, Oct. 2016.

K. Schawinski, M. Koss, S. Berney, and L. F. Sartori. Active galactic nuclei flicker: an observational estimate of the duration of black hole growth phases of $\sim 10^5$ yr. *MNRAS*, 451:2517–2523, Aug. 2015.

J. Schaye and C. Dalla Vecchia. On the relation between the Schmidt and Kennicutt-Schmidt star formation laws and its implications for numerical simulations. *MNRAS*, 383:1210–1222, Jan. 2008.

J. Schaye, R. A. Crain, R. G. Bower, M. Furlong, M. Schaller, T. Theuns, C. Dalla Vecchia, C. S. Frenk, I. G. McCarthy, J. C. Helly, A. Jenkins, Y. M. Rosas-Guevara, S. D. M. White, M. Baes, C. M. Booth, P. Camps, J. F. Navarro, Y. Qu, A. Rahmati, T. Sawala, P. A. Thomas, and J. Trayford. The EAGLE project: simulating the evolution and assembly of galaxies and their environments. *MNRAS*, 446:521–554, Jan. 2015.

M. Schmidt. 3C 273 : A Star-Like Object with Large Red-Shift. *Nature*, 197:1040, Mar. 1963.

M. Schmidt. Space Distribution and Luminosity Functions of Quasi-Stellar Radio Sources. *ApJ*, 151:393, Feb. 1968.

C. Schreiber, M. Pannella, D. Elbaz, M. Béthermin, H. Inami, M. Dickinson, B. Magnelli, T. Wang, H. Aussel, E. Daddi, S. Juneau, X. Shu, M. T. Sargent, V. Buat, S. M. Faber, H. C. Ferguson, M. Giavalisco, A. M. Koekemoer, G. Magdis, G. E. Morrison, C. Papovich, P. Santini, and D. Scott. The Herschel view of the dominant mode of galaxy growth from z = 4 to the present day. *A&A*, 575:A74, Mar. 2015.

A. Schulze, A. Bongiorno, I. Gavignaud, M. Schramm, J. Silverman, A. Merloni, G. Zamorani, M. Hirschmann, V. Mainieri, L. Wisotzki, F. Shankar, F. Fiore, A. M. Koekemoer, and G. Temporin. The cosmic growth of the active black hole population at 1 <z <2 in zCOSMOS, VVDS and SDSS. *MNRAS*, 447:2085–2111, Mar. 2015.

N. I. Shakura and R. A. Sunyaev. Black holes in binary systems. Observational appearance. *A&A*, 24:337–355, 1973.

F. Shankar, D. H. Weinberg, and J. Miralda-Escudé. Self-Consistent Models of the AGN and Black Hole Populations: Duty Cycles, Accretion Rates, and the Mean Radiative Efficiency. *ApJ*, 690:20–41, Jan. 2009.

S. L. Shapiro, A. P. Lightman, and D. M. Eardley. A two-temperature accretion disk model for Cygnus X-1 - Structure and spectrum. *ApJ*, 204:187–199, Feb. 1976.

D. Sijacki and V. Springel. Physical viscosity in smoothed particle hydrodynamics simulations of galaxy clusters. *MNRAS*, 371:1025–1046, Sept. 2006.

D. Sijacki, V. Springel, T. Di Matteo, and L. Hernquist. A unified model for AGN feedback in cosmological simulations of structure formation. *MNRAS*, 380:877–900, Sept. 2007.

D. Sijacki, C. Pfrommer, V. Springel, and T. A. Enßlin. Simulations of cosmic-ray feedback by active galactic nuclei in galaxy clusters. *MNRAS*, 387:1403–1415, July 2008.

D. Sijacki, M. Vogelsberger, D. Kereš, V. Springel, and L. Hernquist. Moving mesh cosmology: the hydrodynamics of galaxy formation. *MNRAS*, 424:2999–3027, Aug. 2012.

D. Sijacki, M. Vogelsberger, S. Genel, V. Springel, P. Torrey, G. F. Snyder, D. Nelson, and L. Hernquist. The Illustris simulation: the evolving population of black holes across cosmic time. *MNRAS*, 452:575–596, Sept. 2015.

J. Silk. On the fragmentation of cosmic gas clouds. I - The formation of galaxies and the first generation of stars. *ApJ*, 211:638–648, Feb. 1977.

M. C. Smith, D. Sijacki, and S. Shen. Supernova feedback in numerical simulations of galaxy formation: separating physics from numerics. *arXiv:1709.03515*, Sept. 2017.

G. F. Smoot, C. L. Bennett, A. Kogut, E. L. Wright, J. Aymon, N. W. Boggess, E. S. Cheng, G. de Amici, S. Gulkis, M. G. Hauser, G. Hinshaw, P. D. Jackson, M. Janssen, E. Kaita, T. Kelsall, P. Keegstra, C. Lineweaver, K. Loewenstein, P. Lubin, J. Mather, S. S. Meyer, S. H. Moseley, T. Murdock, L. Rokke, R. F. Silverberg, L. Tenorio, R. Weiss, and D. T. Wilkinson. Structure in the COBE differential microwave radiometer first-year maps. *ApJ*, 396:L1–L5, Sept. 1992.

A. Soltan. Masses of quasars. *MNRAS*, 200:115–122, July 1982.

R. S. Somerville and R. Davé. Physical Models of Galaxy Formation in a Cosmological Framework. *ARA&A*, 53:51–113, Aug. 2015.

R. S. Somerville, P. F. Hopkins, T. J. Cox, B. E. Robertson, and L. Hernquist. A semi-analytic model for the co-evolution of galaxies, black holes and active galactic nuclei. *MNRAS*, 391:481–506, Dec. 2008.

M. Sparre and V. Springel. Zooming in on major mergers: dense, star-bursting gas in cosmological simulations. *MNRAS*, 462:2418–2430, Nov. 2016.

M. Sparre and V. Springel. The unorthodox evolution of major merger remnants into star-forming spiral galaxies. *MNRAS*, 470:3946–3958, Oct. 2017.

J. S. Speagle, C. L. Steinhardt, P. L. Capak, and J. D. Silverman. A Highly Consistent Framework for the Evolution of the Star-Forming "Main Sequence" from z ˜ 0-6. *ApJS*, 214:15, Oct. 2014.

D. N. Spergel, L. Verde, H. V. Peiris, E. Komatsu, M. R. Nolta, C. L. Bennett, M. Halpern, G. Hinshaw, N. Jarosik, A. Kogut, M. Limon, S. S. Meyer, L. Page, G. S. Tucker, J. L. Weiland, E. Wollack, and E. L. Wright. First-Year Wilkinson Microwave Anisotropy Probe (WMAP) Observations: Determination of Cosmological Parameters. *ApJS*, 148: 175–194, Sept. 2003.

V. Springel. E pur si muove: Galilean-invariant cosmological hydrodynamical simulations on a moving mesh. *MNRAS*, 401:791–851, Jan. 2010.

V. Springel and L. Hernquist. Cosmological smoothed particle hydrodynamics simulations: a hybrid multiphase model for star formation. *MNRAS*, 339:289–311, Feb. 2003.

V. Springel, S. D. M. White, G. Tormen, and G. Kauffmann. Populating a cluster of galaxies - I. Results at [formmu2]z=0. *MNRAS*, 328:726–750, Dec. 2001a.

V. Springel, N. Yoshida, and S. D. M. White. GADGET: a code for collisionless and gasdynamical cosmological simulations. *New Astron.*, 6: 79–117, Apr. 2001b.

V. Springel, T. Di Matteo, and L. Hernquist. Modelling feedback from stars and black holes in galaxy mergers. *MNRAS*, 361:776–794, Aug. 2005a.

V. Springel, S. D. M. White, A. Jenkins, C. S. Frenk, N. Yoshida, L. Gao, J. Navarro, R. Thacker, D. Croton, J. Helly, J. A. Peacock, S. Cole,

P. Thomas, H. Couchman, A. Evrard, J. Colberg, and F. Pearce. Simulations of the formation, evolution and clustering of galaxies and quasars. *Nature*, 435:629–636, June 2005b.

V. Springel, R. Pakmor, A. Pillepich, R. Weinberger, D. Nelson, L. Hernquist, M. Vogelsberger, S. Genel, P. Torrey, F. Marinacci, and J. Naiman. First results from the IllustrisTNG simulations: matter and galaxy clustering. *arXiv:1707.03397*, July 2017.

L. K. Steinborn, K. Dolag, M. Hirschmann, M. A. Prieto, and R.-S. Remus. A refined sub-grid model for black hole accretion and AGN feedback in large cosmological simulations. *MNRAS*, 448:1504–1525, Apr. 2015.

A. Sternberg and N. Soker. Rising jet-inflated bubbles in clusters of galaxies. *MNRAS*, 389:L13–L17, Sept. 2008.

A. Sternberg and N. Soker. Sound waves excitation by jet-inflated bubbles in clusters of galaxies. *MNRAS*, 395:228–233, May 2009.

A. Sternberg, F. Pizzolato, and N. Soker. Inflating Fat Bubbles in Clusters of Galaxies by Wide Jets. *ApJ*, 656:L5–L8, Feb. 2007.

G. S. Stinson, C. Brook, A. V. Macciò, J. Wadsley, T. R. Quinn, and H. M. P. Couchman. Making Galaxies In a Cosmological Context: the need for early stellar feedback. *MNRAS*, 428:129–140, Jan. 2013.

J. M. Stone, J. E. Pringle, and M. C. Begelman. Hydrodynamical non-radiative accretion flows in two dimensions. *MNRAS*, 310:1002–1016, Dec. 1999.

R. S. Sutherland and M. A. Dopita. Cooling functions for low-density astrophysical plasmas. *ApJS*, 88:253–327, Sept. 1993.

L. A. M. Tasca, O. Le Fèvre, N. P. Hathi, D. Schaerer, O. Ilbert, G. Zamorani, B. C. Lemaux, P. Cassata, B. Garilli, V. Le Brun, D. Maccagni, L. Pentericci, R. Thomas, E. Vanzella, E. Zucca, R. Amorin, S. Bardelli, L. P. Cassarà, M. Castellano, A. Cimatti, O. Cucciati, A. Durkalec, A. Fontana, M. Giavalisco, A. Grazian, S. Paltani, B. Ribeiro, M. Scodeggio, V. Sommariva, M. Talia, L. Tresse, D. Vergani, P. Capak, S. Charlot, T. Contini, S. de la Torre, J. Dunlop, S. Fotopoulou, A. Koekemoer, C. López-Sanjuan, Y. Mellier, J. Pforr, M. Salvato, N. Scoville, Y. Taniguchi, and P. W. Wang. The evolving star formation rate: $M_{\hat{a}\acute{N}\c{E}}$ relation and sSFR since z ∼ 5 from the VUDS spectroscopic survey. *A&A*, 581:A54, Sept. 2015.

A. Tchekhovskoy and O. Bromberg. Three-dimensional relativistic MHD simulations of active galactic nuclei jets: magnetic kink instability and Fanaroff-Riley dichotomy. *MNRAS*, 461:L46–L50, Sept. 2016.

M. Tegmark, J. Silk, M. J. Rees, A. Blanchard, T. Abel, and F. Palla. How Small Were the First Cosmological Objects? *ApJ*, 474:1, Jan. 1997.

R. Teyssier, B. Moore, D. Martizzi, Y. Dubois, and L. Mayer. Mass distribution in galaxy clusters: the role of Active Galactic Nuclei feedback. *MNRAS*, 414:195–208, June 2011.

F. Tombesi, F. Tazaki, R. F. Mushotzky, Y. Ueda, M. Cappi, J. Gofford, J. N. Reeves, and M. Guainazzi. Ultrafast outflows in radio-loud active galactic nuclei. *MNRAS*, 443:2154–2182, Sept. 2014.

E. Toro. *Riemann solvers and numerical methods for fluid dynamics*. 1997.

J. W. Trayford, T. Theuns, R. G. Bower, R. A. Crain, C. d. P. Lagos, M. Schaller, and J. Schaye. It is not easy being green: the evolution of galaxy colour in the EAGLE simulation. *MNRAS*, 460:3925–3939, Aug. 2016.

S. Tremaine, K. Gebhardt, R. Bender, G. Bower, A. Dressler, S. M. Faber, A. V. Filippenko, R. Green, C. Grillmair, L. C. Ho, J. Kormendy, T. R. Lauer, J. Magorrian, J. Pinkney, and D. Richstone. The Slope of the Black Hole Mass versus Velocity Dispersion Correlation. *ApJ*, 574:740–753, Aug. 2002.

M. Tremmel, F. Governato, M. Volonteri, T. R. Quinn, and A. Pontzen. Dancing to ChaNGa: A Self-Consistent Prediction For Close SMBH Pair Formation Timescales Following Galaxy Mergers. *arXiv:1708.07126*, Aug. 2017a.

M. Tremmel, M. Karcher, F. Governato, M. Volonteri, T. R. Quinn, A. Pontzen, L. Anderson, and J. Bellovary. The Romulus cosmological simulations: a physical approach to the formation, dynamics and accretion models of SMBHs. *MNRAS*, 470:1121–1139, Sept. 2017b.

Y. Ueda, M. Akiyama, G. Hasinger, T. Miyaji, and M. G. Watson. Toward the Standard Population Synthesis Model of the X-Ray Background: Evolution of X-Ray Luminosity and Absorption Functions of Active Galactic Nuclei Including Compton-thick Populations. *ApJ*, 786:104, May 2014.

M. Vogelsberger, D. Sijacki, D. Kereš, V. Springel, and L. Hernquist. Moving mesh cosmology: numerical techniques and global statistics. *MNRAS*, 425:3024–3057, Oct. 2012.

M. Vogelsberger, S. Genel, D. Sijacki, P. Torrey, V. Springel, and L. Hernquist. A model for cosmological simulations of galaxy formation physics. *MNRAS*, 436:3031–3067, Dec. 2013.

M. Vogelsberger, S. Genel, D. Sijacki, P. Torrey, V. Springel, and L. Hernquist. Erratum: A model for cosmological simulations of galaxy formation physics. *MNRAS*, 438:3607–3607, Mar. 2014a.

M. Vogelsberger, S. Genel, V. Springel, P. Torrey, D. Sijacki, D. Xu, G. Snyder, S. Bird, D. Nelson, and L. Hernquist. Properties of galaxies reproduced by a hydrodynamic simulation. *Nature*, 509:177–182, May 2014b.

M. Vogelsberger, S. Genel, V. Springel, P. Torrey, D. Sijacki, D. Xu, G. Snyder, D. Nelson, and L. Hernquist. Introducing the Illustris Project: simulating the coevolution of dark and visible matter in the Universe. *MNRAS*, 444:1518–1547, Oct. 2014c.

M. Vogelsberger, F. Marinacci, P. Torrey, S. Genel, V. Springel, R. Weinberger, R. Pakmor, L. Hernquist, J. Naiman, A. Pillepich, and D. Nelson. The uniformity and time-invariance of the intra-cluster metal distribution in galaxy clusters from the IllustrisTNG simulations. *arXiv:1707.05318*, July 2017.

G. M. Voit, M. Donahue, G. L. Bryan, and M. McDonald. Regulation of star formation in giant galaxies by precipitation, feedback and conduction. *Nature*, 519:203–206, Mar. 2015.

G. M. Voit, G. Meece, Y. Li, B. W. O'Shea, G. L. Bryan, and M. Donahue. A Global Model for Circumgalactic and Cluster-core Precipitation. *ApJ*, 845:80, Aug. 2017.

M. Volonteri. Formation of supermassive black holes. *A&ARv*, 18:279–315, July 2010.

M. Volonteri, Y. Dubois, C. Pichon, and J. Devriendt. The cosmic evolution of massive black holes in the Horizon-AGN simulation. *MNRAS*, 460: 2979–2996, Aug. 2016.

R. V. Wagoner, W. A. Fowler, and F. Hoyle. On the Synthesis of Elements at Very High Temperatures. *ApJ*, 148:3, Apr. 1967.

A. K. Weigel, K. Schawinski, N. Caplar, A. Carpineti, R. E. Hart, S. Kaviraj, W. C. Keel, S. J. Kruk, C. J. Lintott, R. C. Nichol, B. D. Simmons, and R. J. Smethurst. Galaxy Zoo: Major Galaxy Mergers Are Not a Significant Quenching Pathway. *ApJ*, 845:145, Aug. 2017a.

A. K. Weigel, K. Schawinski, N. Caplar, O. I. Wong, E. Treister, and B. Trakhtenbrot. AGNs and Their Host Galaxies in the Local Universe: Two Mass-independent Eddington Ratio Distribution Functions Characterize Black Hole Growth. *ApJ*, 845:134, Aug. 2017b.

R. Weinberger, V. Springel, L. Hernquist, A. Pillepich, F. Marinacci, R. Pakmor, D. Nelson, S. Genel, M. Vogelsberger, J. Naiman, and P. Torrey. Simulating galaxy formation with black hole driven thermal and kinetic feedback. *MNRAS*, 465:3291–3308, Mar. 2017a.

R. Weinberger, V. Springel, R. Pakmor, D. Nelson, S. Genel, A. Pillepich, M. Vogelsberger, F. Marinacci, J. Naiman, P. Torrey, and L. Hernquist. Supermassive black holes and their feedback effects in the IllustrisTNG simulation. *arXiv:1710.04659*, Oct. 2017b.

K. E. Whitaker, P. G. van Dokkum, G. Brammer, and M. Franx. The Star Formation Mass Sequence Out to z = 2.5. *ApJ*, 754:L29, Aug. 2012.

S. D. M. White. Formation and Evolution of Galaxies: Les Houches Lectures. *astro-ph/9410043*, Oct. 1994.

S. D. M. White and M. J. Rees. Core condensation in heavy halos - A two-stage theory for galaxy formation and clustering. *MNRAS*, 183:341–358, May 1978.

R. P. C. Wiersma, J. Schaye, and B. D. Smith. The effect of photoionization on the cooling rates of enriched, astrophysical plasmas. *MNRAS*, 393:99–107, Feb. 2009.

J. Wurster and R. J. Thacker. A comparative study of AGN feedback algorithms. *MNRAS*, 431:2513–2534, May 2013.

S. Wuyts, N. M. Förster Schreiber, A. van der Wel, B. Magnelli, Y. Guo, R. Genzel, D. Lutz, H. Aussel, G. Barro, S. Berta, A. Cava, J. Graciá-Carpio, N. P. Hathi, K.-H. Huang, D. D. Kocevski, A. M. Koekemoer, K.-S. Lee, E. Le Floc'h, E. J. McGrath, R. Nordon, P. Popesso, F. Pozzi, L. Riguccini, G. Rodighiero, A. Saintonge, and L. Tacconi. Galaxy Structure and Mode of Star Formation in the SFR-Mass Plane from z ˜ 2.5 to z ˜ 0.1. *ApJ*, 742:96, Dec. 2011.

H.-Y. K. Yang and C. S. Reynolds. How AGN Jets Heat the Intracluster Medium – Insights from Hydrodynamic Simulations. *ApJ*, 829:90, Oct. 2016a.

H.-Y. K. Yang and C. S. Reynolds. Interplay Among Cooling, AGN Feedback, and Anisotropic Conduction in the Cool Cores of Galaxy Clusters. *ApJ*, 818:181, Feb. 2016b.

N. Yoshida, K. Omukai, L. Hernquist, and T. Abel. Formation of Primordial Stars in a ΛCDM Universe. *ApJ*, 652:6–25, Nov. 2006.

F. Yuan and R. Narayan. Hot Accretion Flows Around Black Holes. *ARA&A*, 52:529–588, Aug. 2014.

F. Yuan, Z. Gan, R. Narayan, A. Sadowski, D. Bu, and X.-N. Bai. Numerical Simulation of Hot Accretion Flows. III. Revisiting Wind Properties Using the Trajectory Approach. *ApJ*, 804:101, May 2015.

N. L. Zakamska and R. Narayan. Models of Galaxy Clusters with Thermal Conduction. *ApJ*, 582:162–169, Jan. 2003.

C. Zanni, G. Murante, G. Bodo, S. Massaglia, P. Rossi, and A. Ferrari. Heating groups and clusters of galaxies: The role of AGN jets. *A&A*, 429:399–415, Jan. 2005.

Y. B. Zel'dovich. Gravitational instability: An approximate theory for large density perturbations. *A&A*, 5:84–89, Mar. 1970.

I. Zhuravleva, E. Churazov, A. A. Schekochihin, S. W. Allen, P. Arévalo, A. C. Fabian, W. R. Forman, J. S. Sanders, A. Simionescu, R. Sunyaev, A. Vikhlinin, and N. Werner. Turbulent heating in galaxy clusters brightest in X-rays. *Nature*, 515:85–87, Nov. 2014.

F. Zwicky. Die Rotverschiebung von extragalaktischen Nebeln. *Helvetica Physica Acta*, 6:110–127, 1933.

Acknowledgments

Looking back at the last three years, during which the work for this thesis was done, I am very grateful to have worked amongst such remarkable people. Without their support, advice and encouragement, this thesis would not have been possible.

Above all, I would like to thank my advisor Volker Springel for giving me the opportunity to work on this topic, for his faith in my skills and his support in all possible aspects. His modesty, patience and persistence are a great inspiration for my own work. I would also like to thank Friedrich Röpke, who kindly agreed to referee this thesis.

Additionally, I would like to thank my colleagues at HITS for the friendly and welcoming atmosphere. In particular, I would like to thank Rüdiger Pakmor, Jolanta Zjupa, Christian Arnold, Thomas Guillet, Christine Simpson, Dandan Xu, Svenja Jacob, Robert Grand, Martin Sparre, Andreas Bauer, Kevin Schaal, Freeke van de Voort, Sebastian Bustamante and Felipe Goicovic for the excellent working environment in the theoretical astrophysics group at the HITS, which made my time there very enjoyable. I would also like to thank the IllustrisTNG collaboration for the constructive, focused and intense meetings during which we worked together and for their valuable comments and suggestions to my work.

Special thanks go to Christoph Pfrommer, for his help and advice, and to Kristian Ehlert, who, through his fantastic work during his Master-thesis, encouraged me to constantly question and improve my own work. Furthermore, I would like to thank Philipp Girichidis, Matteo Pais and Georg Winner for the valuable discussions about all aspects of physics.

Finally I would like to thank my family for their support.